
# Race to the surface: Developing *in vitro* and *in silico* models of microbial and mammalian cell growth on implant surfaces

By

Sophie E Mountcastle

A thesis submitted to
the University of Birmingham
for the degree of
DOCTOR OF PHILOSOPHY

School of Chemistry
College of Engineering and Physical Sciences
University of Birmingham
December 2021

UNIVERSITY OF
BIRMINGHAM

## University of Birmingham Research Archive

### e-theses repository

This unpublished thesis/dissertation is copyright of the author and/or third parties. The intellectual property rights of the author or third parties in respect of this work are as defined by The Copyright Designs and Patents Act 1988 or as modified by any successor legislation.

Any use made of information contained in this thesis/dissertation must be in accordance with that legislation and must be properly acknowledged. Further distribution or reproduction in any format is prohibited without the permission of the copyright holder.

## ABSTRACT

The "race to the surface" describes the competition between bacteria and eukaryotic cells for colonisation of an implant device. This thesis aimed to address gaps in modelling the oral microenvironment surrounding a dental implant material, specifically focusing on three key elements: identification of a suitable hydrogel scaffold, development of a method for calculating biofilm viability on the surface of implant materials, and exploration of a computational model of surface adhesion.

For strain values up to 30%, the mechanical stiffness of porcine oral mucosa under compression was determined, with porcine as a model tissue. Acellular alginate and alginate-collagen scaffolds were then characterised to determine the concentrations that were most similar to the stiffness of the porcine mucosa. Further investigations included scanning electron microscopy, rheology, and Fourier-transform infrared spectroscopy to fully characterise the surface topography, gelling behaviour, and chemical bonds within the polymers, respectively. Blended collagen-alginate hydrogels of 2.5 mg/mL collagen with 10 mg/mL alginate and 2.5 mg/mL collagen with 5 mg/mL alginate were found to closely match the mechanical stiffness of the native tissue, as well as demonstrating desirable gelling behaviour through the formation of collagen fibrils and low concentrations of cross-linking agent required.

These hydrogels were then shown to support human dermal fibroblast growth upon encapsulation within the scaffold, with high cell viability. Matrix stiffness was found to influence fibroblast morphology, with a higher stiffness resulting in rounded fibroblast morphology

and a lower stiffness resulting in a spindle shape. The presence of a stratified epithelium was not confirmed and therefore further optimisation of this model is required.

Alongside the refinement of this 3D model, a novel analysis tool was developed for quantifying confocal micrographs of live/dead stained biofilms. The protocol was validated on different bacterial species, and the tool demonstrated a reliable measurement of biofilm growth and cell viability. Advantages of this tool include the low computational time to analyse images, ease of use, and transparency of the image processing methods employed.

Finally, a computational model of initial bacterial adhesion to a surface was developed, based on a cellular automaton. The parameters that affected this initial stage of biofilm formation were investigated. The balance between the rate of migration to the surface, division rate, and death rate of a bacterial species had a significant input on the cells adhering to the surface. If the balance of these parameters can be controlled *in vitro* and *in vivo*, then this could inform the development of strategies for preventing surface colonisation.

Ultimately, the work presented in this thesis will support the development of antimicrobial strategies and novel implant devices to prevent the occurrence of dental implant infection by providing improved methods of analysing the effect of such strategies *in vitro*.

## ACKNOWLEDGMENTS

I would firstly like to thank my wonderful supervisors, Dr Sarah Kuehne, Dr Sophie Cox, Dr Richard Shelton and Dr Sara Jabbari. I am truly grateful for all the support, encouragement and guidance you have given me throughout my PhD journey, without which I wouldn't be the scientist I am today. I would also like to thank Dr Rachel Sammons for your mentorship, which was invaluable to me in my development as a researcher.

A further thanks goes to the brilliant technicians at the School of Dentistry. In particular, I would like to thank Gay Smith, Helen Wright, Jianguo Liu and Lisa Shriane for your continued help and support in the lab. Much of my experimental work would not have been successful without your patience and willingness to teach.

I have had the pleasure of working with outstanding researchers across the University of Birmingham throughout my PhD, both within the School of Dentistry and the Healthcare Technologies Institute. A special thank you goes to Dr Nina Vyas for your work on the biofilm viability automated analysis tool; it was a great experience to collaborate with you and I truly appreciated your expertise and guidance, as well as your friendship. I am also very grateful to Dr Victor Villapun for your mentorship and guidance throughout the final year of my studies.

I have been fortunate to share an office at the School of Dentistry with many wonderful friends and colleagues. I couldn't have completed my research without your constant support and kindness, and numerous cups of tea. It was a pleasure to share my journey with you all.

Next, I would like to acknowledge the financial support I received from EPSRC as part

of the Physical Sciences for Health Doctoral Training Programme. I also thank Professor Michael Hannon and Professor Hamid Dehghani for welcoming me onto the course and your belief in my abilities. A huge thank you to my fellow coursemates Menisha, Jana, Tasha, Ben, Steven, Tom, Larry and Alex. You are all brilliant scientists and I am excited to see you achieve great things.

I wish to thank my incredible friends and housemates, past and present, who have been such a huge part of my PhD. I hugely appreciate your willingness to listen, words of advice, and the many moments of laughter that have helped me through the challenging days.

I cannot express enough how grateful I am to my family for their constant love and support. Mum, Dad, Lydia and Jack, thank you for encouraging me and reminding me that I can achieve anything I set my mind to. Finally, I want to thank the truly wonderful James Hughes. I feel incredibly lucky to have met you right at the start of my PhD journey, and couldn't have wished for anyone better to share this adventure with.

# Contents

# List of Figures

# List of Tables

# Acronyms

**AM** additively manufactured. 140, 149, 150

**bFGF** basic fibroblast growth factor. 11

**BHI** brain-heart infusion. 131, 132, 137, 138, 172–174

**$CaCl_2$** Calcium chloride. 56–61, 71, 73, 77–82, 96–98, 107–111, 113, 201, 202

**CFUs** colony-forming units. 124, 129, 132, 173, 174

**CLSM** confocal laser scanning microscopy. 124, 127, 128, 133, 134, 142, 152, 154, 155, 157–159, 204

**CPC** cetylpyridinium chloride. 139, 146

**CV** coefficient of variation. 144, 145

**DMEM** Dulbecco's Modified Eagle's Medium. 93, 94, 96, 99, 110

**DMSO** dimethyl sulfoxide. 96

**DPX** Distyrene Plasticizer Xylene. 52, 102

**ECM** extracellular matrix. 11, 15, 47, 48, 91, 202

**eDNA** extracellular DNA. 15

**EGF** epithelial growth factor. 11

**EPS** extracellular polymeric substance. 14, 125, 126, 144, 153, 156, 163

**FCS** fetal calf serum. 95, 96, 98

**FIB** focused ion beam. 127

**FPR** false positive rate. 136, 142

**FTIR** Fourier-Transform Infrared Spectroscopy. 61, 85, 88

**GFOGER** glycine-phenylalanine-hydroxyproline-glycine-glutamic acid-arginine. 48

**H & E** Haematoxylin and Eosin. 52, 62, 101, 114, 115

**HA** hydroxyapatite. 34

**HDF** Human dermal fibroblast. 105–108, 110, 111, 113, 115, 121, 202, 203

**HDFs** Human dermal fibroblasts. 94

**HEPES** 4-(2 hydroxyelthyl)-1 piperazineethanesulfonic-acid. 97

**HGFs** human gingival fibroblasts. 25, 26, 30, 35

**HGKs** human gingival keratinocytes. 30

**IMDM** Iscove's Modified Dulbecco's Medium. 56, 57, 93, 96–98, 110

**IMS** industrial methylated spirit. 93

**KGF** keratinocyte growth factor. 11

**LPS** lipopolysaccharides. 13

**MCR** mercury cadmium telluride. 61

**MES** 2-(N-morpholino)ethanesulfonic acid. 56, 96

**MMP** matrix metalloprotease. 23

**MMPs** matrix metalloproteases. 13, 23

**MRSA** methicillin-resistant *Staphylococcus aureus*. 37

**PBS** phosphate-buffered saline. 100, 139–141

**PCA** principal component analysis. 183

**PI** propidium iodide. 99, 100, 110, 127, 129, 132, 133, 141, 144, 158

**RGD** arginine-glycine-aspartic acid. 48

**RO** reverse osmosis. 56, 58, 93, 97, 101, 107, 110, 130

**ROC** receiver operating characteristic. 136, 142–144

**rpm** revolutions per minute. 95–97, 99, 131, 137, 138, 172–174

**SEM** scanning electron microscopy. 61, 82, 84, 126, 127

**t-SNE** t-distributed Stochastic Neighbour Embedding. 183

**TLRs** Toll-like receptors. 13

**TPR** true positive rate. 136, 142

**TSA** tryptone soya agar. 131, 172, 173

**VDC** vertical diffusion chamber. 36, 37

**VEGF** vascular endothelial growth factor. 11

# Chapter One

# Introduction

## 1.1 The race to the surface

Gristina [1] first introduced the concept of the "race to the surface" in 1987. This publication described the two main barriers to long-term use of implanted biomaterials in the human body to be: (a) the possibility of infection and (b) unsuccessful tissue integration [1]. The contest between host tissue cells and foreign bacteria for an implant surface is vitally important. If the battle is won by the host cells, then the surface becomes occupied and the body's natural defences can eliminate any bacteria still present [1]. However, if the bacteria are able to colonise the implant surface without intervention, then the subsequent infection can result in significant tissue damage and has the potential to lead to systemic illness [2].

In 2012, decades after Gristina first described the "race to the surface" [1], Busscher et al. [3] reviewed the current status on the use of biomaterials for implants and devices. The authors determined that, despite much research into the promotion of tissue integration and prevention of infection, bacteria still often "win" the race [3]. Medical and dental implants are highly susceptible to infection and if left untreated, these infections can be chronic, lead to the development or propagation of resistant bacterial strains, have debilitating effects on

patients, and ultimately be very costly to eliminate [3]. For researchers to continue developing novel biomaterials and antimicrobial therapies to tackle implant-related infections, it is essential that *in vitro* models are relevant to the environment they represent. In particular, the oral cavity presents unique challenges to the use of laboratory-based models. These include the presence of several hundred species of bacteria, soft and hard tissues and many external factors that have an impact on the environment, such as diet, oral hygiene and mechanical forces (for example shear flow from saliva) [4].

This introductory section will describe the challenges surrounding the use of implants in the field of dentistry, detail the biology and structure of the oral mucosa and its role in preventing infection, and evaluate the current oral tissue and biofilm models published in the literature. It will also discuss the formation of biofilms and their role in peri-implant disease. Furthermore, the use and benefits of computational (*in silico*) modelling of bacterial colonisation of surfaces will be introduced.

## 1.2 Dental implants

The ultimate goal in the use of dental implants is to restore a patient's oral environment to normal function, both in terms of performance and aesthetics [5–7]. Endosseous implants are embedded in the maxilla (upper jaw) or mandible (lower jaw) by placing them within a drilled space in the jawbone and attaching a permanent crown (Figure 1.1) [8]. Over recent decades, removable dentures and fixed bridges have become less acceptable among patients and there is a trend towards the use of endosseous implants [5, 9–11]. Whilst there are no current estimates of the number of endosseous implants placed in the UK annually, according to the latest UK Adult Dental Health Survey published in 2011, half a million adults have at least one dental implant [12]. This number has likely to have continued to increase over

the past decade, with similar trends reported globally [13–15].

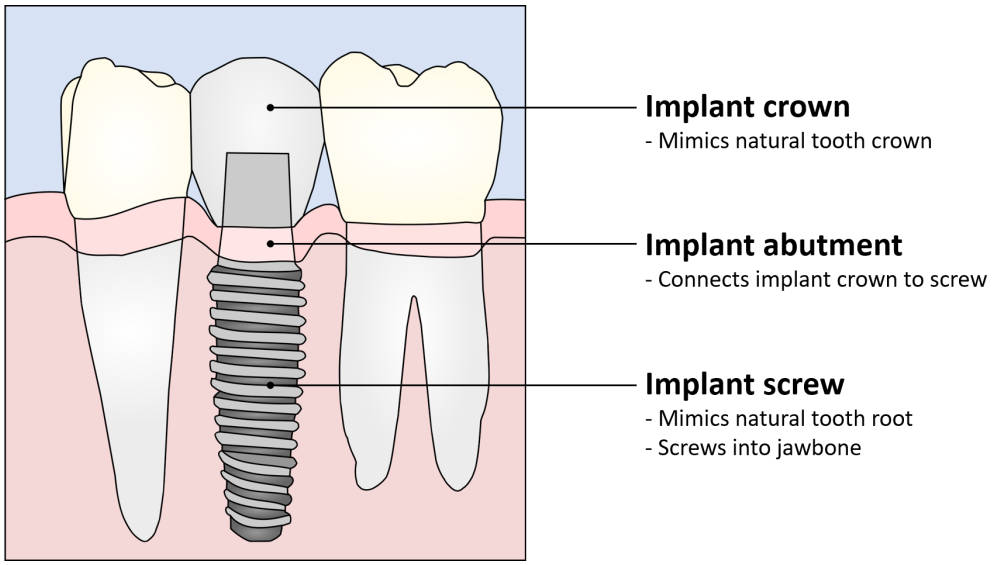


Figure 1.1: Illustration of a dental implant indicating the three key elements: the crown, used to simulate the natural tooth; the screw, which is embedded into the jawbone to anchor the implant and mimics the natural root of the tooth; and the abutment, which connects the screw to the crown and perforates through the soft tissue.

Commercially pure titanium (grade II or grade IV) or titanium alloy (Ti-6Al-4V) are the most common constituents of dental implants [7–9, 16]. The primary reason for the widespread use of titanium for dental applications is that it is widely accepted to be biocompatible with the jawbone and surrounding soft tissues, and furthermore is corrosion-resistant due to the formation of an oxide layer ($TiO_2$) over its surface [17]. In addition, titanium offers mechanical strength and resilience in line with that of human bone, when compared with alternative materials [18]. However, the introduction of new surgical techniques and narrower implants has resulted in the suggestion that commercially pure titanium does not have enough mechanical strength to support loading in all jaw sites [19].

### 1.2.1 Failure of dental implants

For dental implants, stated failure rates due to infection vary. Whilst most clinical studies report overall five-year success rates of 90-95%, there are limited long-term clinical studies on the lifetime of dental implants and it is challenging to determine an overall failure rate from the highly varied clinical data in the literature [20, 21]. Studies suggest that between 10 and 22% of patients will develop peri-implantitis within 10 years of implant placement [22, 23]. For younger recipients, and with an ageing population, dental implants may need to be replaced multiple times during a patient's lifetime [6, 7].

Implants can fail for several reasons. Primarily, these are: a lack of osseointegration during early healing, infection of the peri-implant tissues, and breakage [24]. Integration is a key element contributing to the success or failure of an implant, as the device needs to be united with the surrounding bone and soft tissues. There are many factors that affect peri-implant tissue healing including surgical technique and the host immune response, as well as design features and fit of implant [5, 7].

Osseointegration is defined as "a direct structural and functional connection between ordered, living bone, and the surface of the load-bearing implant" [25, 26]. It has been extensively studied in the human body and is well-characterised with predictable processes. It has been the focus of much dental implant research due to its essential role in ensuring an increased lifespan of the implant. Osseointegration of a dental implant into the jaw bone occurs through the following three stages:

- Proteins and ligands from the blood are adsorbed onto, and released from, the implant surface. This recruits osteogenic cells to the implant/tissue interface [27].
- In the second stage, the osteogenic cells at the implant surface differentiate and form *de novo* bone by secreting a matrix directly on the implant surface [27].

- The final stage, bone remodelling, is a much slower process. The bone surrounding the implant is remodelled through several cycles to achieve a more ordered structure and improved mechanical properties [27].

Despite its consideration as a biocompatible material, titanium implants can induce a "foreign body" response that can lead to implant rejection [28]. This foreign body response can be dependent on the surface properties of the implant or the presence of microbial agents. In this situation, after the initial interaction of blood with the implant surface, an immune response is triggered and consequently fibrous granulation tissue forms at the bone-implant interface [28]. Due to the lack of contact of the implant with the native bone, this is considered to be poor integration (Figure 1.2).

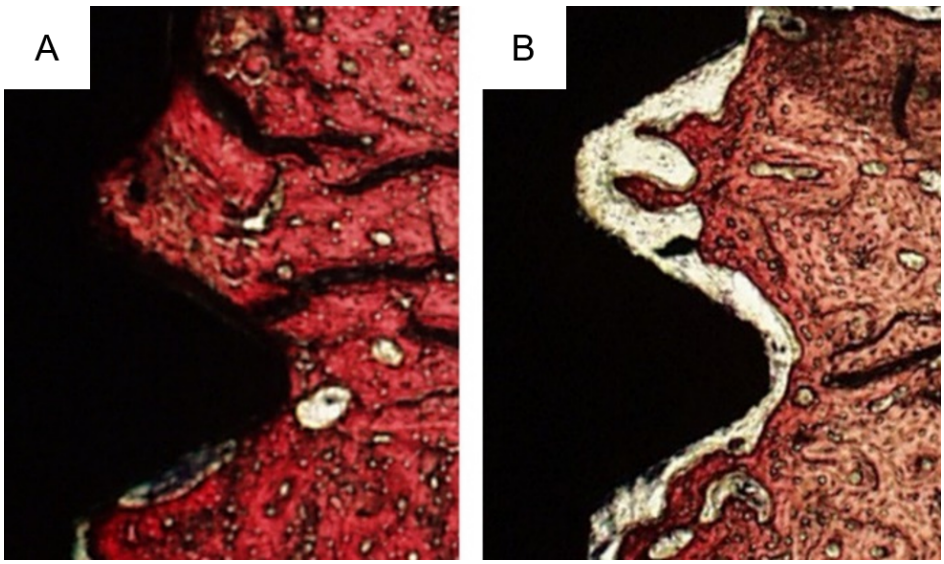


Figure 1.2: Image reproduced from Civantos et al. [28]. Histological images of rabbit tibia bone tissue harvested 8 weeks post screw implantation surgery. The titanium screw can be observed as black opaque, while bone is observed as red tissue. (A) Implant integrated with direct contact between host bone and implant surface. (B) Non-integrated implant with lack of direct bone-implant contact, with fibrous tissue in white present at the bone-implant interface.

In addition to osseointegration, the soft tissues present in the oral cavity also need

to integrate with the implant material. In recent years, soft-tissue healing has become a focus of scientific and clinical research due to its role in establishing a barrier between the oral environment and the bone-implant interface [29]. For example, greater width of the keratinised mucosa adjacent to a dental implant has been shown to be important in successful outcomes, whereby a width of less than 2 mm resulted in greater plaque accumulation and bleeding as well as soft-tissue recession over a five-year period [30]. A full discussion of the biology of the oral mucosa and its role in wound healing is carried out in Section 1.3.

In addition to preventing serious infection within the jawbone, the attachment between the peri-implant soft tissue and the material surface can significantly affect the aesthetics of the device [31]. It should be a priority for those developing implant materials to consider how the surface preparations, design and mechanics can influence the cells in the surrounding soft tissues as well as the bone.

Oral inflammatory diseases such as periodontitis and peri-implantitis are driven by the accumulation of plaque biofilms in the oral cavity [32]. Plaque biofilms can form on solid surfaces such as dental implants and cannot easily be washed away [32] (see Section 1.4.1). The human mouth contains a diverse range of microbial organisms that make up the oral microbiome [33]. However, pathogenic species are also present and if plaque is allowed to accumulate, the numbers of pathogens may increase, shifting the equilibrium from healthy to diseased (see Section 1.4.1). If untreated, this shift can result in the development of the destructive disease peri-implantitis. A 2013 systematic review by Atieh et al. [34] identified a prevalence of peri-implantitis in 18.8% of implants (based upon 6,283 implants in 1,497 patients).

The effects of peri-implantitis include bone loss and inflammation of the surrounding soft tissue and it can ultimately result in loss of the implant [35, 36]. The definition of peri-implantitis used in the scientific literature varies, making it difficult to compare studies

and gain an understanding of the key pathogens that drive the disease [22, 37]. Sanz et al. [38] define peri-implantitis as greater than 1 mm of bone loss after the first year of implant placement. Patients with a history of periodontal disease have a high prevalence of peri-implantitis, which has likely led to the association between the two diseases. However, differences have been identified between the progression rates of periodontal and peri-implant diseases [36]. It has been shown that the inflammation is more pronounced in peri-implantitis and the inflammatory process is more aggressive than in periodontitis [39].

In addition to the variation in aetiology, differences between the microbiota at the site of infection for peri-implantitis and periodontitis have been identified. While bacteria associated with periodontitis were found to be the dominant species in peri-implant infection (including *Treponema*, *Prevotella*, *Campylobacter* and *Eubacterium*), the levels of *Treponema*, *Campylobacter* and *Eubacterium* were significantly higher in both peri-implant health and disease than in periodontitis [40]. The same study identified high levels of *Streptococcus mutans* (*S. mutans*) in peri-implant, but not periodontal, communities. This is an interesting finding because *S. mutans* is strongly associated with dental caries. Furthermore, peri-implant associated communities have been shown to lack diversity, suggesting that peri-implantitis is a simpler infection than periodontitis [40]. However, the same study found that the species at the site of infection were not the same in all individuals, suggesting that the disease is microbially heterogeneous [40].

One of the key differences between peri-implantitis and periodontitis is the ease at which it can be diagnosed. Implants rarely present a source of pain or sensitivity due to the lack of nerves present (unlike the root of a natural tooth) [41]. The early warning signs of infection, including pain and sensitivity, are often missing in the progression of peri-implantitis and therefore early diagnosis is challenging.

Treatment of peri-implantitis is also considerably more challenging and invasive than

for periodontitis. The latter is easily managed with simple surgical and antibiotic therapies, as well as hygiene approaches such as regular cleaning. However, bacteria present on implant surfaces are much more challenging to remove due to the roughness of the material [42, 43]. Treatments for peri-implantitis typically incorporate mechanical debridement alongside antimicrobial agents. Studies that have investigated the effectiveness of this therapy have reported a reduction in the total bacterial counts and levels of periodontal pathogens in the first 3 months following treatment [44]. However, those with longer follow-up periods have observed a gradual return to baseline levels of the microbiota [44]. Furthermore, once an implant is considered failed, treatment is limited to removal surgery.

### 1.2.2 Evaluating implant materials

Novel coatings, surface modifications and materials are being developed to tackle the challenges of poor integration and implant infection. However, the choice of devices available in the clinic remains limited to titanium and ceramic-based materials. This may be due to the difficulties in taking a novel medical device from research laboratory to clinic – these include the large cost associated with this process and a lack of experience in, or facilities for, animal and clinical trials.

A considerable challenge to the evaluation of dental implants *in vitro* is the complex environment in the oral cavity. Many different tissue types and bacterial strains are present [33, 45], making experimental models difficult to develop. Novel materials for dental implants and antimicrobial approaches are continuously being developed, but these are difficult to translate into clinical practice. It is critical that we can test implants and biomaterials in physiologically relevant environments. Therefore, the development of a model that mimics the implant surface and surrounding bacteria and eukaryotic cells would be extremely valuable to the biomaterials field and support the progression of new implants towards clinical

use. Prior to discussing the current models available to study these interactions, an understanding of the biology of the oral mucosa is essential. The following section will describe the structure and function of the oral mucosa.

## 1.3 The oral mucosa

A mucous membrane consists of one or more layers of epithelial cells overlying a layer of loose connective tissue [46] and the function of most mucous membranes is to stop pathogens and dirt from entering the body [46]. The oral cavity is lined by a mucous membrane known as the oral mucosa, which has a function akin to that of skin: to act as a physical barrier to the outside environment [47]. The oral mucosa therefore has some similarities with skin in its structure. As with all mucous membranes, there are two layers to the oral mucosa, an epithelium and an underlying connective tissue termed the lamina propria (Figure 1.3). The surface layer of both skin and oral mucosa is made up of a stratified squamous epithelium [47]. These are flattened (squamous) cells arranged in layers (stratified). This structure provides a flexible covering to the underlying tissues and prevents infection from pathogens.

There are three classifications of oral mucosa: masticatory, lining, and specialised [47, 48]. The three tissue types display regional differences, particularly in the keratinization of the epithelium. The masticatory or gingival mucosa covers the gingivae and hard palate (roof of the mouth) and is an important tissue in relation to implant integration. The epithelium in the masticatory mucosa is keratinized (containing the protein keratin) and is bound tightly to the underlying bone by the lamina propria [48]. Firm attachment to the underlying connective tissue and bone is essential as the masticatory mucosa undergoes mechanical stresses during mastication. The lining and specialised mucosa are found on the floor of the mouth, the bottom surface of the tongue, and the soft palate [49]. These are non-

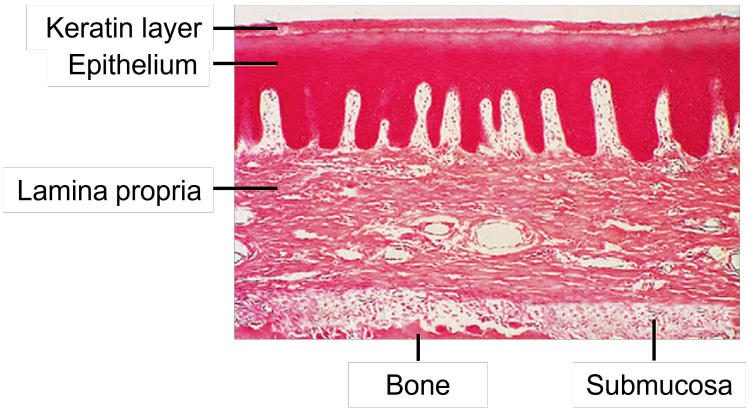


Figure 1.3: Histological staining of human masticatory mucosa demonstrating the different regions of the tissue including the stratified keratin layer and epithelium, where keratinocytes are present, and the laminar propria populated by fibroblasts. Figure adapted from Nanci [48].

keratinized, making them more elastic and flexible for speech [49]. Another key difference between the masticatory and other mucosae is the turnover time for cell division. Turnover is much faster in the lining mucosa (14 days) than the masticatory mucosa (24 days) [47].

### 1.3.1 Wound healing

The oral mucosa is of particular interest to those working with dental implants. This is because rapid attachment of the oral mucosa to the dental implant after placement is essential to prevent bacteria migrating into the jawbone and causing serious infection. The peri-implant mucosa plays a key role in the longevity and survival of a dental implant by creating a "seal". The peri-implant mucosa responds to plaque in a similar manner to healthy gingival mucosa that surrounds teeth [50]. When the integrity of this seal is disturbed by the inflammatory process, the underlying bone can be exposed to the oral bacterial environment and this can ultimately lead to peri-implantitis [50].

In general, healing in the mucosa occurs much faster than in skin and is significantly

less likely to scar [51, 52], although the exact reason for this is still under investigation. However, it has been suggested that the inflammatory reaction to wounding is resolved much faster in the oral mucosa than in the skin, with reduced numbers of macrophages, neutrophils, and T-cells detected [52, 53]. In addition, there are differences in gene and cytokine expression, including the production of vascular endothelial growth factor (VEGF), between the epithelial cells of oral mucosa and skin. The expression pattern in skin is more intense and much longer in duration than in oral mucosa [53].

Both skin and oral mucosa go through the same stages of wound healing: haemostasis, inflammation, proliferation, and remodelling [54, 55]. Haemostasis describes the process of clot formation and platelet aggregation. These platelets release growth factors which initiate the wound healing cascade through the activation of neutrophils, endothelial cells, and macrophages [54]. The clot provides an early extracellular matrix (ECM) to allow for cell migration to the wound site. Inflammation starts with the activation of neutrophil migration, and they phagocytose any bacteria present in the wound site. In the secondary inflammatory phase, monocytes are attracted to the wound and undergo a phenotypic change to become macrophages. These macrophages are fabricators of growth factors responsible for the production of ECM and the proliferation of smooth muscle and endothelial cells [54]. During the proliferation stage, keratinocytes at the wound edge proliferate and migrate – this occurs within a few hours of wounding to prevent infection. Several growth factors are responsible for keratinocyte proliferation and migration including keratinocyte growth factor (KGF), epithelial growth factor (EGF), and basic fibroblast growth factor (bFGF) [55].

Fibroblasts present in the laminar propria play several crucial roles in the healing process. They release the growth factors that promote keratinocyte proliferation and form the granulation tissue, the new connective tissue containing microvasculature formed as part of the healing process. They also reorganise the early ECM, and remodel the resulting scar [54, 55]. The final stage of wound healing, remodelling, occurs over a longer period

of time as the disorganised collagen is remodelled into a more ordered structure. Various hypotheses exist to explain the minimal scarring that occurs in the oral cavity: firstly, that the presence of bacteria stimulates rapid wound healing, secondly, the moist environment and growth factors present in the saliva encourage better healing, and finally, a non-fibrotic fibroblast phenotype that is distinct from skin fibroblasts is present [52, 56, 57]. This distinct phenotype has been described as "replicatively younger", giving them an increased ability to repopulate a wound space [58].

There have been a number of studies that focus on the wound healing process around dental implants [29, 50, 59–61]. The scarless wound healing in oral mucosa exhibits less extensive inflammation with smaller numbers of neutrophils and macrophages than are found in the healing process of a typical wound [62]. The process of forming a biological "seal" around a dental implant can be described in several stages:

- After the initial inflammation at the site of the implant placement, fibroblasts within the adjacent epithelium adsorb onto the implant surface [62, 63].
- These fibroblasts secrete proteins that direct the keratinocytes in the epithelium to orientate parallel to the implant surface [62].
- Finally, after approximately 4 weeks of healing, the collagen fibres are reorganised to become more ordered and the wound is considered healed [63]

### 1.3.2 Immune function

Aside from being a physical barrier to microbiota and playing a key role in preventing migration of bacteria to the dental implant, the oral mucosa has an important role in responding to pathogens. Recent evidence has shown that epithelial cells coordinate the local immune response to pathogenic species [64, 65]. The major receptors involved in pathogen recognition

are Toll-like receptors (TLRs) that can detect bacterial products such as lipopolysaccharides (LPS) and bacterial DNA [65, 66]. Activating these TLRs that are present in epithelial cells, results in a signalling pathway that leads to the recruitment of immune cells from the underlying tissues. There are several signalling pathways that can lead to an immune response when challenged by pathogenic bacteria [66]. As part of their response to pathogens, oral epithelial cells can synthesise a number of cytokines, adhesion molecules, growth factors, chemokines, and matrix metalloproteases (MMPs) [66]. Investigating the relationship between epithelial cells and pathogens in the presence of implant materials is important to discern the impact they have on the oral mucosa response to infection. Models that can incorporate multiple elements of the complex environment are useful to gain a better understanding of these integral processes that prevent peri-implant infection.

In summary, it is crucial to understand the structure and biology of the oral mucosa when developing *in vitro* models, as it plays an essential role in the healing around dental implants. A fast response to implant placement is important, as the keratinocytes proliferate and migrate to the implant surface to prevent microbial organisms reaching the underlying bone, thus reducing the risk of peri-implantitis and implant failure. Experimental models of the oral mucosa are extremely useful for better understanding cell response to implant surfaces and enabling the design of improved materials for soft tissue integration. However, as the mouth is a highly complex environment, the role of bacterial biofilms in implant failure is important to consider when designing and evaluating new implant materials and designs. The next section will discuss the biology of biofilms and their role in the oral cavity.

## 1.4 Biofilms

A biofilm is a population of bacterial cells adhered to a surface (and to each other), encapsulated within a secreted extracellular polymeric substance (EPS). They can be comprised of a single-species or multiple bacterial species. The key advantage to bacteria existing in a biofilm is that they act as an organised community, sharing resources for growth and survival. The formation of biofilms in some settings has advantages. For example, biofilms have been used for wastewater treatment [67], for protection of the marine ecosystem [68], and prevention of corrosion in industrial settings [69].

However, the formation of biofilms is detrimental in several industries, including food and healthcare, and can cause biofouling; the deterioration of materials such as iron, steel and concrete which results in large costs for the oil, gas and marine industries [69]. In the food industry, pathogenic biofilms can form in processing facilities, which can cause food spoilage and potentially lead to poor human health outcomes [70]. In a healthcare setting, biofilm formation on medical devices and implants including pacemakers, vascular grafts, catheters, prosthetic joints, sutures, and contact lenses poses a critical problem of infection in patients [71].

### 1.4.1 Oral biofilms

Oral biofilms are also known as plaque, and they accumulate on the teeth and on foreign surfaces such as dental implants. They can either form above the gingivae (supragingival plaque) or below the oral epithelium, between the tooth and the gingival crevice (subgingival plaque). Oral biofilm composition varies greatly between individuals and can be influenced by several factors including diet and oral hygiene.

Over 700 different bacteria species have been identified in the oral cavity [33]. The species vary significantly between different environments within the mouth. For example, the microbiota of the tongue differs from that present on the tooth or from the species in the periodontal pocket. Microbial community differences also occur between individuals, even in health. The complex equilibrium between resident species in the oral cavity is responsible for the maintenance of a healthy state (in symbiosis) or a state associated with disease (in dysbiosis) [33]. Typically, oral diseases such as periodontitis and peri-implantitis occur when there is an increase in pathogenic species, shifting from a symbiotic state to a dysbiotic state.

### 1.4.2 Biofilm attachment and development

The initial step in the formation of an oral biofilm is the adhesion of primary colonisers to a surface, including *Streptococcus* and *Actinomyces* species. This stage is considered reversible, as microbes may detach from the surface or remain adhered. Bacteria attach to the tooth surface via a thin film containing salivary proteins [72]. Following this initial attachment stage, the bacteria multiply and secrete ECM [73]. This is termed the growth phase, whereby bacteria grow and recruit other bacteria through auto-aggregation (attraction between the same species) and co-aggregation (attraction between different species). Initially, the formation of the ECM is dominated by extracellular DNA (eDNA). As the biofilm continues to mature, polysaccharides and structural proteins become the more dominant component of the ECM. Through the maturation stage, microcolonies begin to form, which can facilitate cell-cell communication [73]. In the final stage, termed the dispersal stage, some of the mature biofilm will break off into the environment and these planktonic cells are able to start a new cycle of biofilm formation. This process of biofilm formation is depicted in Figure 1.4.

The primary environment within which bacteria in the oral cavity exist is in biofilms. Therefore, it is essential to incorporate these complex communities into models of oral disease

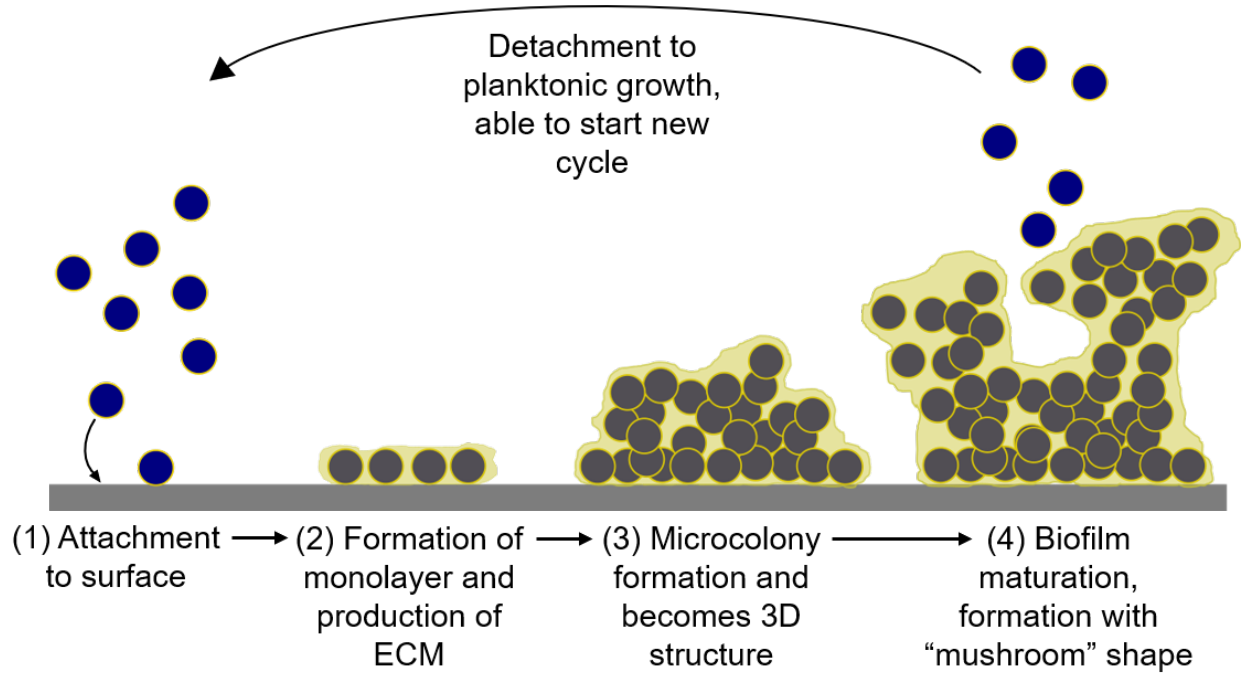


Figure 1.4: Graphical representation of biofilm formation showing the four key stages. (1) Attachment of bacteria to surface (this is reversible). (2) Formation of monolayer and secretion of extracellular matrix. (3) Biofilm growth and formation of microcolonies. (4) Maturation results in detachment of parts of the biofilm to form planktonic culture. Figure adapted from Vasudevan [73].

and the local implant environment. The next section will discuss *in vitro* models of the oral mucosa and how they have been utilised to understand the relationship between this vital tissue and the microflora present in the mouth.

## 1.5 A review of co-culture models to study the oral microenvironment

*This section is adapted from a review paper by Mountcastle et al. published in the Journal of Oral Microbiology (2020) [4].*

Co-cultures allow for the study of cell-cell interactions between different eukaryotic species or with bacteria. Such an approach has enabled researchers to closely mimic complex tissue structures. This review is focused on co-culture systems modelling the oral cavity, which have been used to evaluate this unique cellular environment and understand disease progression. Over time, these systems have developed significantly from simple 2D eukaryotic cultures and planktonic bacteria, to more complex 3D tissue engineered structures and biofilms. Careful selection and design of the co-culture, along with critical parameters such as seeding density and choice of analysis method, have resulted in several advances. This review provides a comparison of existing co-culture systems for the oral environment, with emphasis on progression of 3D models and the opportunity to harness techniques from other fields to improve current methods.

The oral cavity is a complex environment that contains many microbial species that thrive in the warm, moist conditions [74] (Figure 1.5A). Furthermore, different regions of the oral cavity are made up of several cell types and tissues, both soft (mucosa, connective tissue, smooth muscle) and hard (enamel, dentine, bone) [49, 75] (Figure 1.5B). Changes in the soft tissues can indicate disease, for example periodontitis and oral cancer, and reveal systemic conditions such as diabetes or vitamin deficiency [49]. Equally, the mineralised structures within the mouth may bear signs of disease, including dental caries, that might result in significant hard tissue loss or damage [76]. The composition of microbial species in the mouth can either cause or intensify many of these diseases [33], thus demonstrating the importance of balance within this complex multi-cellular environment.

The microorganisms present in the oral cavity attach to surfaces in communities called biofilms; highly regulated and organised interspecies habitats that provide defence against competitors and adapt to changes in the wider environment (see Section 1.4.1) [33]. These communities are essential for many metabolic, physiological, and immunological functions. They support food digestion, regulation of the host immune system, maintenance of mucosa

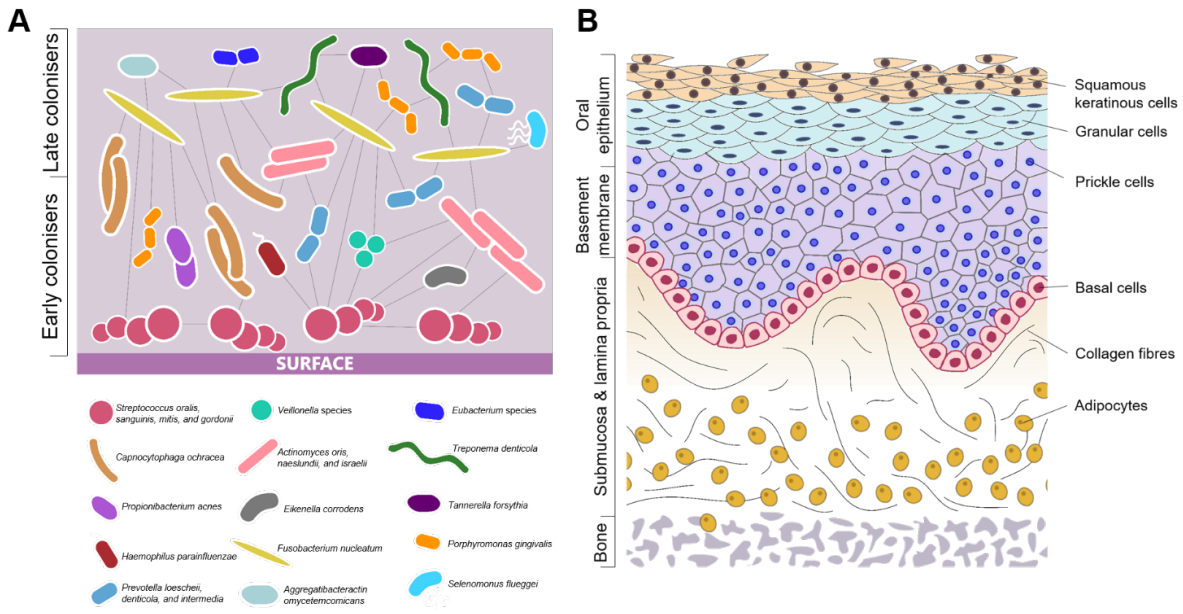


Figure 1.5: (A) Common bacterial species present in pathogenic oral biofilms and their communication between species (adapted from Parashar et al. [77]). (B) Cells and tissue types present in the oral mucosa, demonstrating complexity of 3D structure.

barrier function, detoxification of environmental chemicals, and prevent invasion of disease-promoting species [33]. However, a shift in the species present in the oral microbiome can unsettle the local environment, switching from a healthy to disease state [78]. Saliva also plays a key role in the oral cavity in maintaining homeostasis and defending from disease, as well as containing proteins, minerals, and antimicrobial enzymes that control biofilm formation and activity [79, 80]. Evidently, understanding the processes and interactions that occur in the oral cavity, in both healthy and disease states, as well as the shift between the two, is vital to furthering our knowledge of disease progression and the discovery of new treatments.

For both human and bacterial cells, utilising single species for *in vitro* modelling of the oral cavity does not fully represent the *in vivo* conditions (Figure 1.5). This presents a key question for researchers in this field regarding how best to study the oral cavity, both

for understanding disease pathogenesis and evaluating novel therapeutics. Challenges in studying this complex environment are not just limited to the presence of many cell types and bacterial species, but also the substantial variations in microbiota between individuals [81]. Mimicking these various degrees of complexity remains difficult and therefore *in vivo* studies remain the gold standard for observing processes in oral pathogenesis. However, clinical *in vivo* studies and animal models bring their own obstacles: they are expensive, labour intensive and can generate ethical concerns. In addition, human and animal oral microbiota may not be the same and therefore can be difficult to compare. As such, the use of co-culture models to mimic *in vivo* conditions has been recognised as a valuable approach to further our understanding of the relationship between eukaryotic and bacterial cells and is especially applicable to the oral cavity.

Co-culture techniques allow a variety of cell types to be cultivated together, enabling examination of cell-cell interactions [82]. These systems may refer to the culture of two or more eukaryotic cell types together, or eukaryotic and prokaryotic cells. The effectiveness of co-cultures is heavily determined by the choice of experimental set up. Cell-cell interactions in co-cultures are strongly influenced by the extracellular environment, which in turn is influenced by the employed protocol [83]. There are numerous factors that need to be optimised to ensure these systems are representative of the native oral cavity, such as the number of cell populations. Having more than two species can result in unstable systems due to multiple reaction pathways, which may be difficult to monitor, analyse and interpret [83].

Studying the relationship between the oral microbiome and eukaryotic cells is essential to understanding disease progression and evaluating the effect of new treatments. Many studies have published co-culture methodologies, but these techniques have not been directly compared, making it challenging to identify and optimise the most appropriate system for a research question. Hence, this review discusses the use of co-culture *in vitro* models to study

the oral environment, the progression of these models in complexity, and the disadvantages and benefits of using a range of published methods (Table 1.1). In addition, the lessons and approaches that can be adapted from other fields that regularly utilise co-cultures is considered with the aim of providing future insights for development.

### 1.5.1 2D cell culture

The simplest oral environment co-culture systems apply planktonic bacteria to a monolayer of confluent eukaryotic cells [84–87] (Figure 1.6A, Table 1.1). Compared with more complex approaches, these basic models have an advantage in that cellular response to bacteria can be attributed to specific interactions allowing for direct comparison between species, both bacterial and cellular. For example, the inflammatory response of epithelial cells to different bacterial species may be compared [85] or different eukaryotic cell lines may be challenged with the same oral pathogenic species, such as *Porphyromonas gingivalis* (*P. gingivalis*), a key contributor to the pathogenesis of periodontitis [88]. However, it is known that interactions between different bacteria can affect disease progression [89, 90] and therefore applying single species cannot elucidate more complex physiological interactions.

A number of innovative studies utilised 2D co-culture systems to study the adhesion to and invasion of epithelial cells by key oral pathogens. *Aggregatibacter actinomycetemcomitans* (*A. actinomycetemcomitans*, formerly *Actinobacillus actinomycetemcomitans*) is a bacterium associated with aggressive periodontitis. Mintz and Fives-Taylor [91, 92] applied *A. actinomycetemcomitans* to an oral cancer cell line under different conditions and highlighted that adhesion is affected by both host (saliva, serum) and culture (pH) conditions. Using a similar approach, Yilmaz et al. [93] cultured primary gingival epithelial cells and introduced *P. gingivalis* and its fimbriae-deficient mutant, demonstrating that *P. gingivalis* fimbriae promote adhesion to gingival epithelial cells through interaction with $\beta 1$ integrins.

In a later study, Yilmaz et al. [94] showed that *P. gingivalis* is capable of targeting specific epithelial cell pathways during invasion and can adapt to an intracellular environment. They suggested that disease may ensue from a disruption of the balance between the bacteria and host cells by factors that may trigger virulence or lead to host-immune-mediated tissue damage [94]. Studies like these are essential to determine key proteins and interactions involved in oral pathogenesis, which could potentially provide targets for future treatments.

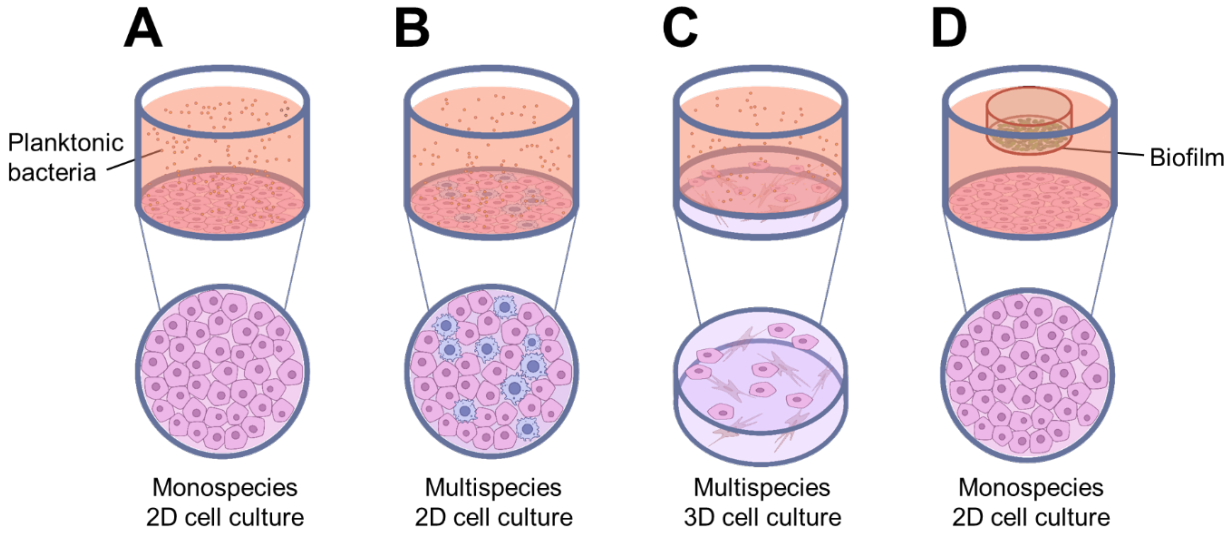


Figure 1.6: Common co-culture systems reported in the literature. (A) monospecies 2D cell culture with planktonic bacteria applied; (B) multispecies 2D cell culture with planktonic bacteria applied; (C) multispecies 3D cell culture, typically a collagen-based or decellularised matrix containing fibroblasts, with planktonic bacteria applied; and (D) monospecies 2D cell culture with biofilm applied, typically suspended from a well-insert.

In addition to looking at a specific bacterium, 2D co-culture systems can be effectively used to compare the response of host cells when challenged with different oral pathogens (Table 1.1). Han et al. [95] individually applied six key Gram-negative anaerobic bacteria associated with periodontal diseases to human gingival epithelial cells to compare their ability to adhere and invade, as well as measuring levels of interleukin-8 (a proinflammatory cytokine) secretion from the human cells. Their findings demonstrated that whilst all bac-

teria species were able to adhere to oral epithelial cells, only *Fusobacterium nucleatum* (*F. nucleatum*) was highly invasive, to levels comparable with *P. gingivalis* [95]. Not only can comparisons be made between different bacteria species using multiple 2D co-cultures, but the ability of different strains to adhere and invade oral epithelial cells can be investigated. The *Prevotella intermedia* (*P. intermedia*) group are made up of three strains (*P. intermedia*, *Prevotella nigrescens*, and *Prevotella pallens*) and are connected with oral disease pathogenesis. Gursoy et al. [96] showed that *P. intermedia* and *P. nigrescens* type strains can adhere to and invade epithelial cells, the capability of *P. intermedia* being highest. Another key publication in which strains were compared, was the work of Dabija-Wolter et al. [97] in which the authors examined the invasion of human gingival fibroblasts by three different *F. nucleatum* strains using a 2D co-culture system. In order to evaluate the amount of bacteria present inside the fibroblasts after infection, live bacteria were fluorescently stained prior to being introduced into the co-culture, and this allowed for visualisation using confocal laser scanning microscopy and quantification using flow cytometry. The studies described use a range of assays and analytical techniques to determine key interactions between host cells and pathogenic bacteria, showing the importance of simple 2D co-culture systems, as well as the influence of strain, cell type and culture conditions.

To elevate 2D co-cultures and gain further insight into *in vivo* interactions, multiple eukaryotic species can be cultured together (Figure 1.6B, Table 1.1). In two studies by Bodet et al. [98, 99], epithelial cells were cultured alongside macrophages to gain a better understanding of the interplay between these two cell types in the presence of *P. gingivalis*. Careful optimisation of the ratio between cell types is essential and consideration should be given to the analytical techniques applied. In these studies, Bodet et al. [98, 99] were unable to identify which cells had a greater role in IL-6 and IL-8 secretion. This highlights that more complex assays, such as flow cytometry, may be required to target each cell type. Recently, a three-cell co-culture was described whereby dendritic cells, gingival epithelial keratinocytes

and T-cells were cultured in a three-cell transwell co-culture plate, essentially allowing for three mono-layers to be cultured in the same well and therefore allowing interactions to be determined when challenged with *P. gingivalis* [100]. Different single- and co-cultures were prepared to compare the production of MMPs in response to the pathogen. Interestingly, the cellular reaction changed when T-cells were present with a reduction in MMP9 and a reduced immune response, which indicated that multiple cell types could influence MMP expression, providing further evidence of the complex cell-cell signalling occurring *in vivo*.

Not only can 2D co-cultures elucidate information on interactions between oral eukaryotic cells, they can also be used to evaluate microbial communication. Several authors have employed 2D co-cultures to study the effect of multiple oral bacterial species on the invasion of gingival epithelial cells by respiratory pathogens [84] and *P. gingivalis* [86]. Findings suggested that commensal oral species could modulate invasion. Providing careful consideration is given to the controls used, a 2D co-culture system with multiple bacterial species can determine very useful information on the pathogenesis of oral disease. From the *in vitro* study described [84], the authors suggest that increased presence of oral bacteria in the throat could prevent invasion of respiratory pathogens. However, it is important to recognise that these co-culture models are not physiologically representative, due to a lack of host immune system and the use of monolayer cell cultures. Therefore, extrapolating the results of such studies to *in vivo* conditions should be done with care.

Interactions of anaerobic species with human cells raise challenges in culturing these bacteria with oxygen-requiring epithelial cells. One of the limitations in the literature described is the culture of *P. gingivalis* in aerobic conditions. Bodet et al. [98, 99] and Saito et al. [86] did not report viability of *P. gingivalis* under the growth conditions applied when co-cultured with their respective oral mucosa model. The growth of *P. gingivalis* under oxygenated environments has been shown to affect its physiology and result in changes in expression of different proteins, including virulence factors [101]. Gursoy et al. [96] also

Table 1.1: Summary of several co-culture methodologies utilised within the literature.

| **Method** | **Summary of protocol** | **References** |
|---|---|---|
| 2D monospecies co-culture with planktonic bacteria | (1) Seed eukaryotic cells into well-plate.<br>(2) Culture until confluent monolayer formed, with media changes every 1-2 days.<br>(3) Prepare overnight culture of chosen bacteria.<br>(4) Centrifuge overnight culture and re-suspend bacteria in eukaryotic cell culture media to achieve desired concentration.<br>(5) Add media containing bacterial suspension to monolayer and perform assays at desired time points. | [84–86, 88, 102, 103] |
| 2D multispecies co-culture with planktonic bacteria | (1) Seed appropriate ratio of eukaryotic cells into well-plate.<br>(2) Culture until confluent, with media changes every 1-2 days.<br>(3) Prepare overnight culture of chosen bacteria.<br>(4) Centrifuge overnight culture and re-suspend bacteria in eukaryotic cell culture media to achieve desired concentration.<br>(5) Add media containing bacterial suspension to monolayer and perform assays at desired time points. | [98, 99] |
| 2D co-culture with biofilm | (1) Seed eukaryotic cells into well-plate.<br>(2) Culture until confluent, with media changes every 1-2 days.<br>(3) Prepare overnight culture of chosen bacteria.<br>(4) To form biofilm, seed overnight planktonic culture onto coverslips placed in the bottom of a well-plate. Change media every 1-2 days.<br>(5) At chosen time point, once biofilm has formed, remove broth and attach coverslip to base of transwell insert.<br>(6) Place insert into cell-culture plate and perform assays at desired time points. | [104–109] |

| | | |
|---|---|---|
| 3D tissue-engineered co-culture with planktonic bacteria | (1) Mix fibroblasts with collagen gel and pipette into transwell inserts. Set gel in incubator at 37°C for 4 hr. Culture for 4-7 days until gel has contracted.<br>(2) Seed epithelial cells onto surface of gel. Seed monolayer of epithelial cells into separate well-plate to monitor confluence. Culture cells until confluent monolayer formed (2-3 days).<br>(3) Raise model to air-liquid interface and culture for 7-10 days to allow stratified epithelium to form.<br>(4) Prepare overnight culture of chosen bacteria.<br>(5) Re-suspend bacteria in eukaryotic cell culture media to achieve desired concentration. Add media containing bacterial suspension to 3D cell-culture. Perform assays at desired time points. | [104, 110–113] |

highlighted the tolerance of *P. intermedia* strains to oxygen exposure as a limitation of their co-culture study. The test conditions applied were aerobic, and the type strain had been handled in laboratory conditions for longer than the clinical isolates. Consequently, increased tolerance to oxygen exposure of the type strain may have explained their findings of increased adhesion. It is vital to assess and report the effect of the aerobic growth conditions used on anaerobic species for the duration of the experiment.

Simple 2D co-cultures prove useful for testing responses to a dental material, for example implants or resins. Human gingival fibroblasts can be cultured directly onto the surfaces of these materials, with planktonic oral species added subsequently to investigate their effect. Using this method, oral bacteria have been shown to modulate toxicity of dental resins on human gingival fibroblasts (HGFs) [102]. It is also possible to adapt these 2D co-cultures to enable high throughput studies to be performed in 96-well plates. For example

a study by Giulio et al. [103] reported the effect of dental resin monomers on HGFs in the presence of *Streptococcus mitis* (*S. mitis*) and demonstrated there was no reduction in bacterial adhesion to the eukaryotic cells. Simple 2D cultures also allow for the interaction between cells and dental resin materials (e.g. HEMA) to be studied in the presence of oral microbes, an important interaction to understand in the context of the oral environment [114].

A key factor to consider when using a co-culture system containing eukaryotic cells is their origin. A range of cell types have been used in the studies described, including primary human gingival epithelial cells [85, 93–95] and fibroblasts [102, 103], immortalised human gingival cell lines [87], oral carcinoma cell lines [84, 86, 91, 92, 95], and skin keratinocyte cell lines [96, 98, 99]. Some studies did not take the source of their human cells into account when discussing their findings. However, oral keratinocytes and fibroblasts show distinct characteristics to those derived from the skin [53, 57]. In addition, whilst cell lines are a convenient choice for these *in vitro* systems as they are highly proliferative and easier to culture, they often have phenotypic, morphological and genetic differences to their primary tissue origin. Primary cells on the other hand, maintain many of the markers and functions seen *in vivo* and are therefore useful for elucidating responses from human cells when challenged with oral pathogenic bacteria.

The publications described have demonstrated that a simple 2D co-culture model ensures that subsequent assays and analyses are easier to perform and less complex analytical techniques can be used. They also allow for specific interactions to be identified, which is important when investigating disease progression and potentially identifying new therapies for oral pathogenesis. However, there are challenges associated with using simpler models. In particular, neglecting the effects of the host immune system and not representing the 3D structure of *in vivo* tissues often means these models lack certain signals that are present in the body (Table 1.2).

Table 1.2: Advantages and disadvantages of co-culture methodologies.

| **Method** | **Advantages** | **Disadvantages** |
|---|---|---|
| 2D monospecies co-culture with planktonic bacteria | (1) Can use simple assays to investigate<br>(2) Can attribute direct cellular responses from interactions with bacteria<br>(3) Reproducible with reduced batch-to-batch variation<br>(4) Supports homogenous growth<br>(5) All cells have equal access to nutrients. | (1) Not representative of *in vivo* tissue structure<br>(2) Does not account for immune cells<br>(3) Does not account for many cues found *in vivo*, including mechanical signalling<br>(4) Cannot monitor interaction between cell types, in particular the immune system<br>(5) Does not represent the complex bacterial biofilms present in the oral cavity. |
| 2D multispecies co-culture with planktonic bacteria | (1) Can monitor the interaction between cell types<br>(2) Reproducible with reduced batch-to-batch variation<br>(3) Supports homogenous cell growth<br>(4) All cells have equal access to nutrients. | (1) May require optimisation due to different nutrient requirements<br>(2) Not representative of *in vivo* tissue structure<br>(3) Traditional assays cannot determine between cell species<br>(4) Does not account for many cues found *in vivo*, including mechanical signalling<br>(5) Does not represent the complex bacterial biofilms present in the oral cavity. |

| | | |
|---|---|---|
| 2D co-culture with biofilm | (1) Can monitor the interaction between cell types<br>(2) Reproducible with reduced batch-to-batch variation<br>(3) Supports homogenous cell growth<br>(4) All cells have equal access to nutrients<br>(5) More clinically relevant, as biofilms show increased antibiotic resistance compared to planktonic cultures. | (1) Bacteria can overrun eukaryotic cells if co-culture system is not carefully designed. |
| 3D tissue-engineered co-culture with planktonic bacteria | (1) More representative of *in vivo* environment<br>(2) Can study cell-cell signalling<br>(3) Two mucosa models already established in literature: collagen-based hydrogel and decellularised matrix. | (1) Can be challenging to achieve cell numbers required for multiple models<br>(2) Require specifically enriched media<br>(3) Significant optimisation may be required<br>(4) More resource-intensive than other co-culture systems<br>(5) More difficult to produce replicates<br>(6) Models may not be fully representative of native tissue structure<br>(7) Does not represent the complex bacterial biofilms present in the oral cavity. |

### 1.5.2 3D cell culture

As we have gained an understanding of the importance of cues from the surrounding environment, such as mechanical and biological signalling between cell types [115–117], there has been a move to mimic the structure of the tissue in which the eukaryotic cells are located (Figure 1.6C). *Candida albicans* (*C. albicans*) is a commensal yeast that can shift to become pathogenic in immunosuppressed individuals and is therefore an important oral pathogen. A number of 3D *in vitro* culture systems have been developed to mimic the oral mucosa in order to study the interaction between epithelial cells and *C. albicans* [110, 111]. The 3D models commonly utilised in these investigations comprise a fibroblast-containing collagen gel with oral keratinocytes cultured on the surface at the air-liquid interface. An alternative to the collagen model is the use of decellularised matrix as a 3D scaffold. Interestingly, Yadev et al. [118] demonstrated that a 3D tissue engineered oral mucosa model of human keratinocytes and a fibroblast-containing matrix displayed more similar immunohistological and proliferation characteristics to normal mucosa when compared with a 2D oral cell line. In this study, full-thickness oral mucosa models were prepared from decellularised human matrix and compared with collagen-based 3D mucosa models purchased from SkinEthic Laboratories (Nice, France) and MatTek Corporation (Ashland, MA).

Surprisingly, there are relatively few 3D oral mucosa co-culture studies that have been applied to model bacteria relevant to oral disease. Of those that have, Pinnock et al. [112] reported significant differences in the response of oral mucosa models to *P. gingivalis*, compared with monolayer cultures of epithelial cells. This study described their use of a collagen-fibroblast gel with surface epithelial cells cultured at the air-liquid interface, with the application of *P. gingivalis* in planktonic culture. Subsequently, it was shown that utilising 3D co-culture systems was important in order to fully discern cellular responses to infection and confirmed that the interaction between cell types played an important role.

Another key study that supported the significance of 3D co-cultures in the field of oral pathogenesis investigated the bacterial species *F. nucleatum*, which is known to form a bridge between early and late colonisers in the formation of dental plaque (a common oral biofilm) [119]. Gursoy et al. [104] used a collagen-based 3D mucosa model and applied planktonic cultures of *F. nucleatum* to determine the bacteria's ability to attach to and invade epithelial cells. Like Pinnock et al. [112], they also highlighted the difference in response between the 3D co-culture and a simple monolayer of epithelial cells. Given the strong evidence of an interplay between epithelial cells and fibroblasts in response to infection, there is a clear need for future studies to consider the application of 3D mucosa models to studies of oral disease pathogenesis [104, 112]. Furthermore, it is worth highlighting that both Pinnock et al. [112] and Gursoy et al. [104] reported that the viability of the anaerobic species they utilised (*P. gingivalis* and *F. nucleatum* respectively) was not reduced under aerobic growth conditions for the duration of their infection co-culture model. It is essential to examine the oxygen tolerance for anaerobic species when applying them to oxygen-requiring epithelium models to ensure physiology is not affected. One of the challenges with developing 3D cultures is that primary cells have relatively short lifespans, as they lose their *in vivo* phenotype after a few passages, and therefore may not offer sufficient cell numbers to use in multiple 3D co-cultures [113]. Furthermore, enriched media specific to each cell type are often required; without this, primary cells can display an altered phenotype and metabolic function [120]. To combat these drawbacks, immortalised cell lines of human gingival keratinocytes (HGKs) and HGFs have been established. Promisingly, Bao et al. [113] have demonstrated that immortalised HGKs still formed a stratified epithelial layer and both HGKs and HGFs displayed cell-specific markers similar to those found in human gingival tissues. The need for reproducibility makes the use of cell lines desirable, although it must be noted that there is a pay-off between reproducibility and physiological relevance, with Yadev et al. highlighting that the commercially available epithelial cell line TR146 does not form a fully differentiated epithelium [118].

As with 2D co-culture systems, the origin of the human eukaryotic cells in a 3D mucosa model is an important aspect to consider when analysing the cellular response to bacteria. A range of cell sources were utilised in the co-culture studies described. These included primary cells from gingival biopsies [112, 118], immortalised gingival keratinocyte and fibroblast cell lines [104, 113], oral carcinoma cell lines [111, 118], human skin epithelial cell lines [104, 110], and 3T3 cells (a mouse embryonic fibroblast cell line) [110]. Not only do these cells exhibit different phenotypes and morphologies, but moreover, the choice of fibroblast origin can influence the characteristics of the keratinocytes in a 3D model. Merne and Syrjänen [121] highlighted the importance of standardising the matrix, both in terms of extracellular matrix components and in the source of fibroblasts used. Where possible, human eukaryotic cells should be utilised since they are the most physiologically relevant with regards to the *in vivo* tissue of interest.

An additional factor that needs to be taken into account regarding the application of oral pathogens in 2D and 3D co-cultures is the strain of bacteria utilised. Many of the studies cited throughout this review do not detail the origin of the bacteria used. However, it has been previously shown that there is a difference in keratinocyte response between clinical and type strains of *A. actinomycetemcomitans* [122]. Therefore, it is important to appreciate that strains of the same bacterial species may have varying characteristics. It is advisable, where possible, to use clinical strains as well as type strains to conduct co-culture studies in order to compare them with their standards.

The choice to use a 3D culture needs to be a carefully considered decision, as there is currently no universal system available and therefore significant optimisation may be required [123]. Moreover, 2D cell culture approaches can still provide useful information to enhance our understanding of *in vivo* processes. As well as being easier to reproduce and less resource-intensive, 2D cell cultures support homogenous growth and equal access to nutrients for all cells present, whilst cells embedded in a 3D system may not have access

to sufficient nutrients [123]. Despite the challenges that come with 3D systems, the studies cited demonstrate that 3D co-cultures are highly valuable, as monolayer culture systems do not fully represent the high complexity of the oral cavity (Table 1.2). A review of 3D oral mucosa models by Moharamzadeh et al. [124] described the different approaches that have been taken and the advantages and limitations of each, as well as the range of applications for these systems. As protocols and analysis methods continue to improve, these 3D techniques will become more accessible within the oral field.

It should be noted that the tissue models described thus far have not considered the influence of the mechanical properties of the 3D environment. It has emerged in the last decade that scaffold stiffness can significantly influence and control cell function and behaviour [115, 116, 125]. Therefore, when designing scaffolds for tissue engineering applications, it is necessary to match the mechanical properties of the native tissue. There are a few studies that have attempted to characterise the native oral mucosa's mechanical behaviour [126–130]. However, despite these various mechanical properties of the native tissue reported in the literature, the *in vitro* models of the oral mucosa previously described have not referred to these in the development of their model. Research areas with similar methodologies for 3D tissue models have begun explore this area, most notably the skin (see Section 1.5.4). This is a potential opportunity to enhance and develop the current models that exist and will be explored further in this research.

### 1.5.3 Biofilms

The studies described thus far have utilised bacteria in the form of planktonic cultures, applied within nutrient media to the 2D and 3D cell cultures. Often only one or two bacterial species are considered in these studies, compared to the 700 species that have been detected in the oral cavity [131]. Bacteria in the mouth mostly exist in the form

of polymicrobial biofilms (see Section 1.4.1), which are particularly relevant when looking at plaque-related pathogenesis [33]. Furthermore, species growing in biofilms have been shown to have higher resistance to antibiotics when compared with planktonic bacteria [132]. This highlights that applying biofilm models in co-culture studies is particularly relevant to mimicking the oral cavity, both for studying disease progression and evaluating antimicrobial approaches. Millhouse et al. [105] showed there is interplay between a complex biofilm and oral epithelial cells, determined through changes in pro-inflammatory mediators. Other studies have similarly revealed pro-inflammatory responses of epithelial cells after challenge with biofilms [106, 107]. These investigations demonstrated that specific interactions occur between bacteria in a biofilm, as well as with the host cells, yet these interactions are not present in a planktonic culture. Therefore, it may be concluded that the application of biofilms in co-culture studies with oral eukaryotic cells are essential to unearth the complexity of these microenvironments.

Biofilm models are useful to evaluate anti-inflammatory and antimicrobial properties of treatments and compounds. Traditionally, the efficacy of novel antimicrobial compounds are assessed on pathogens in planktonic and biofilm states and subsequently these compounds are applied to oral eukaryotic cells to identify any cytotoxic (or beneficial) effects. This approach is very common in *P. gingivalis* research, as this pathogen is known to induce a response in several oral cell types including epithelial cells, osteoblasts, and fibroblasts [133]. Hence, many studies have an interest in the oral cellular response to novel antimicrobial compounds, as well as the effect on *P. gingivalis* itself [134–136]. However, an area this approach does not address is the interaction between the pathogen and oral eukaryotic cells in the presence of the antimicrobial under investigation. *P. intermedia* is another potential periodontal pathogen associated with the shift from health to disease in a biofilm and has been shown to increase the immune response at the site of infection [137]. Fteita et al. [87] demonstrated that the chemically synthesised quorum-sensing (QS) molecule butyl-

dihydroxy-2, 3-pentanedione, an analogue of autoinducer-2 which is commonly produced by many Gram-positive and Gram-negative species, was able to reduce cytokine expression of a human gingival keratinocyte cell line and simultaneously inhibit biofilm growth of *P. intermedia*. Without observing the entire system in one *in vitro* study, this synergistic effect may have been missed. To further support the importance of evaluating biofilms and oral cells in co-culture, a study by Ramage et al. [138] applied both single- and multi-species biofilms to an oral epithelial cell line (OKF6/TERT2) and the results implied the immune function changes with varying biofilm composition. They reported the dependence of the immune response on the type of bacterial challenge, further highlighting the complexity of the oral cavity and the need to investigate several different interactions to understand disease pathogenesis and identify novel therapeutic targets.

A challenge with using biofilms in a co-culture is the highly different growth rates between the bacteria and eukaryotic cells [139]. High numbers of bacteria in cell culture can cause rapid nutrient depletion and changes in pH, subsequently hindering the growth of eukaryotic cells [140]. Biofilms contain larger numbers of bacteria compared with planktonic cultures, where the concentration of bacteria can be easily adjusted through dilutions. Hence it can be useful to adopt a methodology whereby the biofilm does not come directly into contact with the eukaryotic cells, or where flow is present to reduce the bacteria numbers in the co-culture system (Figure 1.6D). Different approaches have been taken to achieve this. Guggenheim et al. [108] and Thurnheer et al. [109] grew a multispecies biofilm on a hydroxyapatite (HA) disc and placed this upside-down on a ring support that was layered onto a gingival epithelial cell monolayer culture. In contrast, Millhouse et al. [105] and Ramage et al. [138] attached the coverslip on which the biofilm was grown to the base of a transwell culture insert, which was placed within the well-plate. Hence, the biofilm was suspended approximately 0.5 cm above the monolayer culture and did not directly come into contact with the oral epithelial cells in the bottom of the well (Table 1.2). An alternative

approach to introducing bacteria is to use a flow chamber. These have been used in some studies to evaluate biofilm formation on implant surfaces [141, 142]. To grow biofilms in flow chambers the hydrodynamic conditions must be carefully controlled, ideally akin to saliva flow in the mouth [143]. A review of different biofilm flow methodologies has been described elsewhere [143, 144]. Relevant to this review, a recent study utilised a flow chamber to compare adhesion of bacteria versus HGFs on titanium surfaces and determined that the smoothest surface best supported fibroblast adhesion and reduced biofilm formation [142]. These findings highlight that dynamic culture systems remain a promising avenue for further exploration. This is of particular relevance to those studying in the oral cavity since it enables the system to mimic saliva flow, thus creating an environment more closely aligned to *in vivo* conditions.

Due to the complexity of analysing both 3D tissue models and biofilms, very few studies have attempted to combine the two in a single system. The most simple reported method, published by Gursoy et al. [104], applied biofilms of *F. nucleatum* grown on coverslips directly onto epithelial cells grown on fibroblast-containing collagen matrices. By comparing the application of planktonic species with biofilms, they were able to determine differences between the ways bacteria behaved in these different states, with biofilm bacteria causing significantly greater epithelial cell death than when applied in planktonic form. This study also demonstrated that cells from biofilms of *F. nucleatum* were able to invade the collagen matrix of the mucosal model, highlighting the benefits of choosing a complex system to model the *in vivo* environment. However, the biofilm was directly in contact with the mucosal model and hence this may have increased the magnitude of the effects observed. A more complex approach to modelling the interaction between oral biofilms and oral tissues is to utilise a perfusion bioreactor system [145, 146]. Bao et al. [146] were the first to use one of these systems to study periodontal infections and later also used it to characterise the global proteome regulations present in the host-biofilm model [146]. One of the benefits

of using a perfusion bioreactor is that immune cells such as monocytes can be incorporated to generate an environment that is potentially more physiologically relevant. However, the cost of a bioreactor system can be a significant barrier to using this technique. Overall, the research described provides clear evidence that understanding the interactions occurring within an oral biofilm will enhance our understanding of the pathogenesis of oral disease, and novel approaches for introducing biofilms to host cells are key to achieving this.

### 1.5.4 Perspectives from other fields

#### Gut microbiology

The human intestines exhibit a multifaceted microbiota, with an abundance of host-microbe, microbe-microbe and environmental interactions [147]. This complexity creates many similar challenges to researchers working in the oral field. Links between the gut microbiome and obesity, diabetes, liver disease, cancer, and neurodegenerative diseases [148, 149] have now been established, which has driven considerable growth in this research area. Similar approaches to the co-culture models described herein have been utilised in this field, including monolayer/planktonic cultures [150–153] and 3D/planktonic cultures [154, 155]. Reported methods to generate an *in vitro* environment that better represents the *in vivo* surroundings of the digestive tract include bioreactors [152], 3D organoid cultures [156, 157], and organ-on-a-chip systems [158], all of which are described in detail by a review published in 2017 [151]. As with certain anaerobic bacteria in the oral field, interactions of anaerobic gut species with the intestinal mucosa are less-frequently studied due to challenges in culturing anaerobes with the oxygen-requiring epithelium. Anonye et al. [159] reported for the first time the use of a dual environment vertical diffusion chamber (VDC) to study the effect of *Clostridioides difficile* (*C. difficile*) on a 3D gut epithelium model. The use of a VDC allowed for monitoring this interaction over a longer time frame and the study reported that

*C. difficile* adhered more effectively to epithelial cells grown on the surface of the 3D model than on single epithelial monolayers. A VDC could similarly be employed in the field of oral microbiology to better study the effect of anaerobic pathogens such as *P. gingivalis* and *F. nucleatum*, key species identified in the progression of periodontitis.

### Skin microflora

The skin is inhabited by a multitude of microorganisms, with many factors including genetics, environmental characteristics, and host demographics having an influence on the composition of the microflora and consequently on the shift from health to disease [160]. There are a number of 3D skin models established, including some that are available to purchase, which have a fully differentiated epithelium [161]. These models have typically been used in toxicity studies and drug testing applications [162], however due to the similarities in structure between skin and oral mucosa, lessons can be taken from some of the advanced approaches to 3D dermal models. For example, El Ghalbzouri et al. [163] demonstrated that collagen secretion by human fibroblasts provided a long-term functional human dermal matrix, and that this could be cultured for nearly three times as long as traditionally used rat-tail collagen matrices. This methodology could be beneficial in the oral field, as the short timespan that primary gingival fibroblasts can be cultured is a limiting factor for longer-term studies of periodontal disease. A similar technique frequently applied in the dermal field is to seed keratinocytes onto decellularised matrix. Anderson et al. [164] were interested in the formation of a biofilm phenotype of MRSA, to mimic a natural infection. They used decellularised porcine vaginal mucosa to generate a stratified, squamous epithelium, an advantage of which is that it is inexpensive and easily reproducible. The same study compared planktonic application of *Staphylococcus aureus* (*S. aureus*) with the formation of a biofilm directly on the skin model and demonstrated the importance of closely mimicking natural biofilm infections. In summary, 3D skin models are becoming increasingly useful

in the study of the human dermal microbiota. Some of the novel advances made in this area, in particular the production of 3D extracellular matrix from human fibroblasts, could be translated to the oral mucosa to improve the reproducibility and accessibility of current techniques.

### 1.5.5 Summary

Significant progress has been made towards the development of physiologically relevant models of the oral environment, from simple 2D co-cultures to more complex 3D tissue constructs and from the application of planktonic bacteria to multispecies biofilms. These advances have led to a greater increase in our understanding of the interactions taking place in the oral cavity, and thus deepening our knowledge of how periodontal diseases progress. However, current *in vitro* models have limitations, either due to their simplicity or complexity. Whilst able to identify specific interactions between cell types, simple 2D cultures cannot be used to determine the more complex cell-cell interactions that occur in the oral cavity, for example between bacterial species and with the host immune system. On the other hand, due to the analytical complexity or equipment costs, very few studies have successfully introduced biofilms to a 3D organotypic mucosa model. Selecting a co-culture system with an appropriate degree of physiological relevance to answer the research question is essential. As a growing number of studies utilise more complex models, many analytical techniques and 3D mucosa models are being optimised. Utilising knowledge from multiple disciplines, including biology, engineering and mathematics, is likely to become important in furthering the field due to the multifaceted nature of co-culture systems. Additionally, *in silico* models of interactions in the oral cavity may become of increasing significance for simulating more complex environments, though *in vitro* and *in vivo* data will still be required to make computational approaches reliable. Adapting and applying techniques from other fields facing

similar challenges can enhance the methodologies currently available in the study of the oral cavity. Systems that combine these approaches will ensure advancement in the field. As such, this will enhance our understanding of disease progression and enable the evaluation of the effects of new antimicrobial compounds and novel therapies.

## 1.6 *In silico* modelling of cell adhesion to surfaces

As outlined thus far, there are several challenges with *in vitro* models of biological environments. Typically, the more complex the laboratory model, the harder it is to analyse and achieve reproducible results [4]. Other key elements that cannot be easily considered with *in vitro* representations include environmental factors, host factors, and other biotic signals [165]. These become particularly noticeable in the case of the oral cavity, where several soft and hard tissues are present and interact with many hundreds of bacterial species in the form of biofilms, often along with other non-biological materials such as implants.

Computational models are a promising solution to meet these challenges. They allow for examination of biological behaviour on different scales, test hypotheses and predict behaviour, and can sometimes lead to new experimental approaches [166]. Furthermore, a key advantage of using a mathematical model is that it can characterise complex data in terms of few parameters.

This thesis seeks to improve methods for examining the "race to the surface" [1] between bacteria and tissue cells in the oral cavity. There are many ways in which *in silica* approaches can be used to explore this concept, including models of wound healing [167] or the interaction between an implant material and the surrounding tissue [168]. However, for the purposes of supporting the aims of this research, a model that can help to understand the behaviour of bacteria in the presence of different surfaces is a promising tool.

### 1.6.1 Computational biofilm models

Biofilm models are an excellent means to aid in our understanding of the basic principles determining biofilm formation. Computational biofilm models can consider different elements of biofilm formation, for example the fast processes affecting solutes within the biofilm (reaction and transport by diffusion or convection) and the slower processes affecting bacterial mass (growth and division, transport within the biofilm, detachment or erosion at the biofilm surface, and attachment to the surface) [169]. Three key approaches have been taken to modelling microbial biofilm formation – population-based modelling (also known as continuum modelling), individual-based modelling, and cellular automata [169–171]. There are also hybrid models that adopt combinations of these approaches.

Biofilm models have traditionally represented biomass as a continuum, based on population-averaged behaviour [172]. These models treat the biofilm as a continuum with certain properties, for example as a viscous fluid or gel and model the dynamics of biofilm growth by using differential equations [173, 174]. For this reason, an advantage of continuum models is that they produce quantitative results that can be compared with data measured in real systems. However, locally constrained environments within the biofilm may cause individual or localised behaviours to vary significantly from population-averaged behaviour [172, 175]. In multi-species biofilms, these local variations in environment can cause localised dominance or co-localisation of specific species [173]. These types of local observations are not adequately described or predicted by population-averaged models.

The need to account for and understand the cell-level and micro-scale differences within a biofilm and also to establish how individual processes, interactions, and variability affect the macroscopic structure of biofilms, has led to the development of individual-based models. In an individual-based biofilm model, each bacterium or "agent" is modelled explicitly, with the higher-level population behaviour emerging from their lower-level interactions

[169]. In these models, biofilm growth is assumed to be a stochastic process [174]. These models can represent the structural heterogeneity of biofilms, however, there are some challenges to modelling biofilms using an individual-based approach. These include incorporating the production and effects of the extracellular polymeric substance (EPS) and modelling movement of bacteria to, from and within the biofilm [172]. Furthermore, they introduce elements of randomness due to their stochastic nature and so several runs of the model (in the same state) are required before any conclusions can be drawn [174] and this is computationally expensive.

The final approach to computational biofilm modelling is cellular automata. These are discrete models that condense the physical process of biofilm formation into a series of simple rules, which are consequently fairly easy to compute. For this research, a cellular automata approach was chosen for several reasons:

- The rules of a cellular automaton can be constructed around the parameters of interest, which has an advantage when it is being used to support the development of *in vitro* systems.
- It is simple for a non-mathematician to understand the rules that the model is based around, and so can be utilised by those working in the dental field.
- A cellular automaton is mechanistic, and so it is simple to run several simulations in parallel to investigate the effect of the parameters used in the model.

### 1.6.2 Cellular automata

Cellular automata were originally developed for the Game of Life, created by John Horton Conway. They have been used for a variety of applications across many fields including

biology, physics, ecology, geography, and sociology [176, 177]. Specific uses include modelling bacterial growth and urban planning. The reason for their widespread use is their ability to create complex behaviour from simple rules [178].

A cellular automaton is a collection of cells on a grid that evolves through discrete time steps according to a set of rules. Usually this grid is formed of squares in a 2D system, or cubes in a 3D system. The size of the grid determines the space constraints of the model. A cellular automaton operates in an algorithmic manner as follows: (1) an initial "state" is set for all grid points, (2) the simulation cycles through each pre-established rule/event with an assigned probability, and (3) the "state" of each grid point is updated according to result of the rule/event.

Modelling biofilm growth has been previously performed using a cellular automata approach [179–184]. In these models, each space or cell on the grid has a state associated with it, for example a live or dead bacterium, or a bacterium of a certain species. The state of a cell at the next iteration of the model is determined by earlier states and the rules of the system.

As previously mentioned, cellular automata have advantages in their simplicity. The rules can be constructed around the area of interest, which for this thesis is the early colonisation of dental implant materials. Furthermore, a discrete approach is useful for capturing local variations in the biofilm structure. For example, the impact of surface modifications on initial cell adhesion can be observed in a cellular automaton by adjusting the rules regarding the state of a grid space. This could be an interesting avenue to explore when modelling bacterial adhesion to different surfaces. However, one drawback of these types of models is that the rules are arbitrarily formulated, which can lead to aesthetically driven outputs [174, 185]. Validation is an essential part of computational modelling, and this thesis presents a great opportunity to utilise the results of *in vitro* experiments to enhance the computational

model. This validation and fitting process should ensure the parameters and rules used in the cellular automaton described in this thesis are grounded in *in vitro* observations.

In summary, modelling biofilm growth using a computational approach has many advantages, and it can support the development of *in vitro* systems by providing an understanding of the fundamental processes of biofilm formation. Cellular automata have many advantages; a key one for this research is their simplicity to enable researchers from non-mathematical disciplines to apply them to their work. *In silico* models are also "cheap", in that many thousands of scenarios can be simulated that could not all be examined in a laboratory environment and these simulations can guide *in vitro* experiments. Furthermore, a cellular automaton is an excellent way to model the initial stages of biofilm formation, which is relevant to the concept of the "race to the surface". Surface adhesion is the first stage in biofilm formation and preventing or inhibiting it is key to tackling infection.

## 1.7 Conclusion

Throughout this introductory chapter, several themes have been explored that all play a role in the "race to the surface", the competition between bacteria and eukaryotic cells for colonisation of an implant device. This concept bears great relevance to the oral cavity, whereby several tissue types and many hundreds of species of bacteria can interact with a dental implant. In discussing models of the oral microenvironment, several gaps have been identified:

- There is a lack of mechanical considerations in 3D hydrogel models of the oral mucosa.
- Often, there is a simplification of oral tissue models to contain only 2D cells and planktonic bacteria. Furthermore, almost no studies have applied biofilms to 3D oral mucosa

models due to the challenge in the subsequent analysis of these complex systems.

- No studies that have evaluated implant materials have applied both biofilm and 3D cultures in one *in vitro* system to identify how the material interacts with both these key elements of the implant environment.

## 1.8 Research Aim and Objectives

The aim of this thesis is to address the identified gaps in modelling of the oral microenvironment through the development of a 3D hydrogel tissue model with improved mechanical properties. The interactions of this model with implant materials and biofilms will be explored. Within this work, an interdisciplinary approach is essential, combining elements of materials science, cell culture, microbiology and mathematical modelling. To achieve this aim, this thesis has the following objectives:

1. Tackle the lack of mechanical data on native oral mucosa and compare 3D hydrogel models with this data to select an appropriate gel system. Characterise the chosen hydrogel system in terms of gelling properties, chemical composition and its ability to support cell growth and proliferation.

2. Develop a method to analyse confocal micrographs of live/dead stained biofilms, for the purpose of analysing biofilm growth on dental implant surfaces.

3. Devise a computational model based on cellular automata for evaluating cell adhesion to implant surfaces.

4. Use the computational model combined with experimental data to understand the fundamental parameters that affect cell adhesion to implant surfaces. Comment on how we can use this knowledge to inform our approach to implant design.

5. Develop an *in vitro* system that includes an implant material, biofilm, and 3D oral mucosa model that can be used to examine the "race to the surface".

# Chapter Two

# Physical and mechanical characterisation of porcine oral mucosa and a hydrogel scaffold

This chapter addresses the first objective described for this research: "Tackle the lack of mechanical data on native oral mucosa and compare 3D hydrogel models with this data to select an appropriate gel system, characterise the chosen hydrogel system in terms of gelling properties and chemical composition". The physical and mechanical properties of porcine gingival mucosa were determined to provide target properties for the development of the tissue model. For the native tissue, the mechanical properties measured included stress relaxation and elastic (storage) modulus. Specimen thickness was quantified and histological staining was conducted to determine tissue characteristics. The choice of alginate and collagen as scaffold materials for the *in vitro* tissue model was explored. The mechanical and physical characteristics of acellular hydrogel models were compared with the properties of the native tissue to identify a concentration range for biological studies (Chapter 3).

## 2.1 Introduction

The mechanical properties of hydrogel scaffolds for 3D cultures are known to play a key role in cell behaviour [186–188]. In particular, the mechanical properties of the extracellular matrix (ECM) have been shown to impact a range of cell behaviours including growth, differentiation, adhesion, and signal transduction [187]. As these differences in cell behaviour have been identified in recent years, more studies have tried to mimic the mechanical forces cells experience *in vivo* within 3D cell cultures to improve *in vitro* models of different tissues [189, 190].

The oral mucosa experiences a range of external forces in the mouth, especially during mastication. These include elastic deformation (tension and compression) and shear forces from saliva flow [191]. Mucosal thickness, location and type have all been identified as factors that affect the biomechanical properties of the tissue [126]. Given the importance of mechanical forces on cellular response and the presence of several external forces on the oral mucosa, the mechanical properties of the scaffold should be considered when developing an *in vitro* 3D tissue model of the oral mucosa. Therefore, the primary aim of this work was to characterise the mechanical properties of porcine oral mucosa under compression and use these properties to develop a scaffold that closely aligns mechanically to the native tissue.

Scaffold models of 3D tissues are defined as cells grown in the presence of a support, which is often hydrogel-based [188]. Hydrogels are 3D cross-linked networks of water-soluble polymers [192]. These materials can be made up of natural or synthetic polymers, or a combination of both. Natural polymers that have been used as hydrogel scaffolds for 3D cell culture include collagen, elastin, fibrin, silk, alginate and chitosan [193]. The key advantage to using these natural polymers is that they typically display good biocompatibility and are bioactive. Furthermore, natural hydrogels can promote natural cellular functions and seldom elicit an inflammatory response [188, 193]. Factors to consider when selecting a hydrogel

for an application include its cost and availability, its rate of degradation, the method of cross-linking, and mechanical properties such as elasticity and stiffness [194].

Collagen type I (Figure 2.1) is the most commonly used natural polymer in 3D oral mucosa models, as it is the primary component of gingival ECM. Collagen-based models of the oral mucosa have been previously developed and published [195–197]. They have been used to study cellular response to various challenges, including host-pathogen interactions [197]. Studies using collagen as the scaffold material have demonstrated that a stratified epithelium can be achieved with a variety of epithelial cell types and growth conditions [195–197]. A key advantage of collagen-based hydrogels is that collagen molecules can self aggregate at 37°C, making gel formation simple. Furthermore, collagen contains native binding motifs which allow for cell attachment. These motifs are integrin-binding sites and include the glycine-phenylalanine-hydroxyproline-glycine-glutamic acid-arginine (GFOGER) sequence and the arginine-glycine-aspartic acid (RGD) sequence [198]. To take advantage of these benefits, collagen was chosen as the basis for the oral mucosa model developed in the present work.

Despite their many advantages, however, collagen hydrogels are considered to have poor mechanical properties due to the high water content (typically over 90%) [188, 200]. For example, collagen I is susceptible to physical contraction when fibroblasts adhere and exert forces on the polymer [201]. There are ways to enhance its mechanical properties; this can be done by increasing the density of the collagen, chemically modifying the polymer chain, or blending collagen with a secondary polymer that has improved mechanical properties. In order to keep the method simple and easily reproducible, the latter option was chosen for this work.

Alginate is a linear polysaccharide and the polymer chain carries a net negative charge. This negative charge allows for solutions of alginate to be covalently cross-linked (Figure

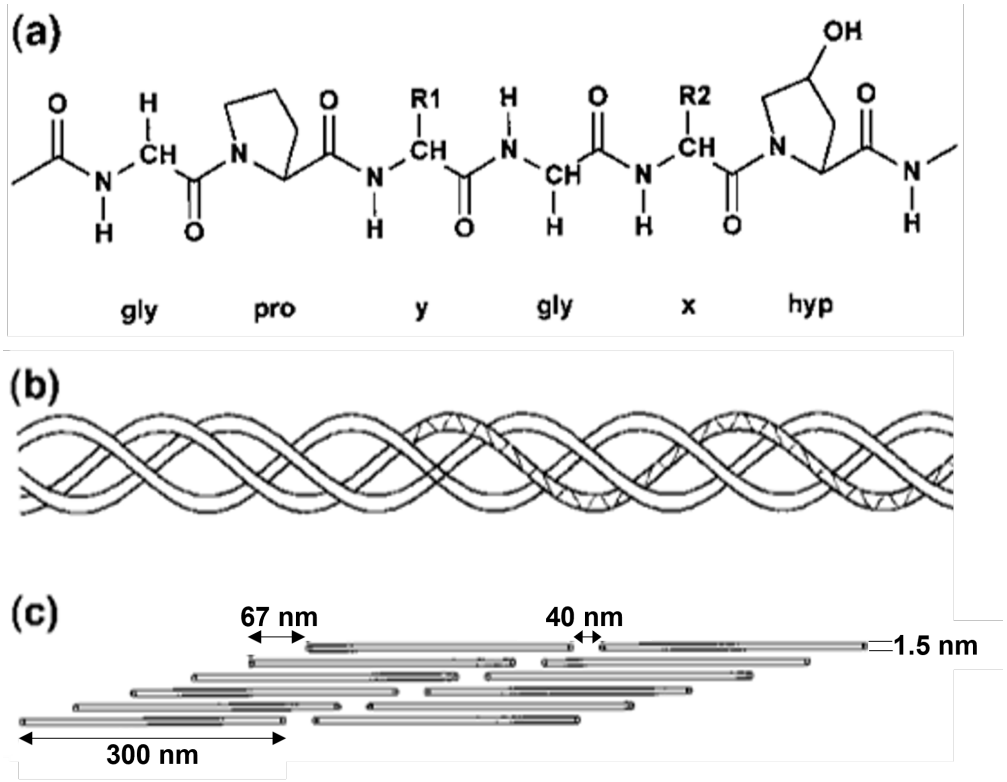


Figure 2.1: Figure showing the chemical structure of collagen and the structure of collagen fibrils. (a) Primary amino acid sequence, (b) Secondary left handed helix and tertiary right handed triple-helix structure, and (c) staggered quarternary structure. Collagen self-aggregates to form a hydrogel at 37 °C, and this occurs due to its underlying structure. A collagen polymer chain contains repeating proline-hydroxyproline-glycine sequences, as shown in (a). These sequences allow the polymer to form a continuous fibrillar structure through hydrogen bonding and electrostatic interactions with amino acids on neighbouring protein strands [198]. Figure adapted from Friess [199].

2.2) [202, 203]. Gelation occurs rapidly and can be initiated under physiological conditions, which ensures cell viability is not impacted by the process [203, 204]. The mechanical properties of alginate hydrogels can be easily tuned by varying either the polymer or cross-linker concentration [203]. However, a lack of cell adhesion motifs on the polysaccharide chain means alginate has to either be chemically modified or blended with cell-adhesive materials to ensure cells can adhere to the scaffold [203]. Due to the ease of tuning the mechanical properties, alginate was chosen to blend with collagen for the oral mucosa model

in the present work. Collagen and alginate blended hydrogels have previously been used to reproduce connective [205], renal [206], ocular [207], and brain tissues [203]. However, they have not yet been used in combination for *in vitro* oral tissue models.

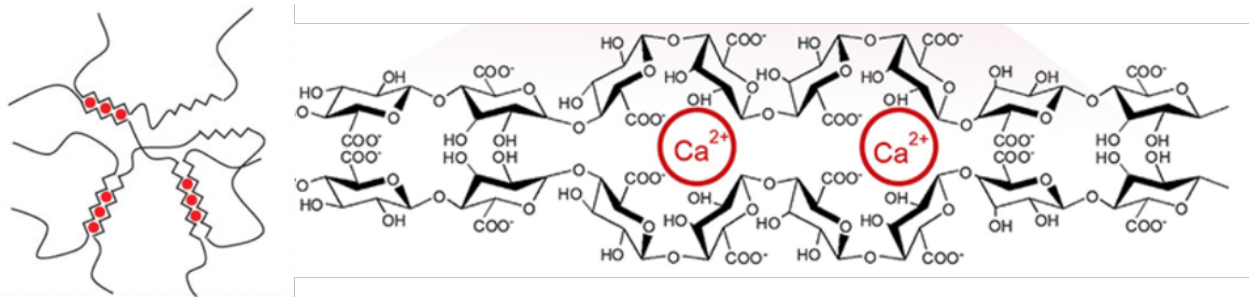


Figure 2.2: Figure showing the chemical structure of alginate, demonstrating the covalent cross-linking of polymer chains in the presence of calcium ions. Reproduced from Bahram et al. [208] and Sun et al. [209]

There are several advantages to using a collagen and alginate blended hydrogel for an *in vitro* oral mucosa model. Firstly, it is relatively inexpensive to produce, which will enable it to be accessible to more researchers. Secondly, it is mechanically tuneable through the alginate component, and therefore the mechanical properties can be aligned with the native tissue. Finally, this hydrogel is simple to prepare given no chemical modifications of either the alginate or collagen are required. In this chapter, the mechanical and physical properties of blended alginate-collagen hydrogels were explored and compared with the properties of porcine oral mucosa to determine whether this approach was advantageous for the development of representative *in vitro* tissue models of the oral mucosa. Porcine oral mucosa was chosen as a model tissue as it resembles that of human oral mucosa more closely than any other animal in terms of structure and composition [210].

## 2.2 Materials and Methods

All chemicals were from Sigma Aldrich (Dorset, UK) unless otherwise specified.

### 2.2.1 Characterisation of native tissue

#### Preparation of porcine mucosa specimens

Fresh porcine tissue from 3-month old female pigs was delivered within 24-hours of slaughter (Medical Meat Supplies, Rochdale, UK). The tissue was washed with a saline solution (15% w/v saline) prior to transportation, in order to preserve the tissue and reduce risk of degradation from bacterial contamination. Discs of oral mucosa, 6 mm diameter, were obtained from the gingival mucosa region of porcine maxilla (upper jaw) and mandible (lower jaw) from four animals (n = 4) using a biopsy punch and scalpel. Discs were taken as close to the teeth as possible to standardise the samples. Additionally, the region from which each sample was collected was recorded (Figure 2.3A). Any remaining connective tissue on the sample was removed using surgical scissors to achieve a flat disc (Figure 2.3B). Sections of porcine mucosa directly adjacent to the disc were also taken for histological staining. A total of 81 samples were collected (See Appendix 1). Mucosa specimens were collected the same day as delivery of the tissue and placed in PBS prior to further testing.

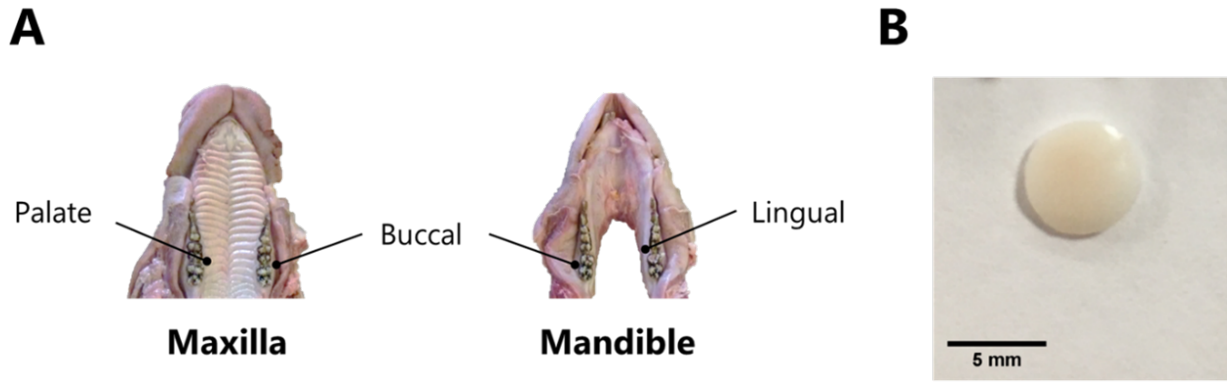


Figure 2.3: (A) Schematic demonstrating the location of collected porcine specimens. (B) Representative image of a single specimen prior to mechanical testing.

**Histological staining of porcine mucosa**

Porcine mucosa sections were trimmed to a maximum size of 4 mm x 2.5 mm x 2.5 mm and placed into a histology cassette. Formalin fixation and paraffin-embedding was performed on the mucosa tissue according to a standard protocol [211, 212] whereby the cassettes containing the tissue sections were placed into 10% formalin for 48 hours at room temperature. To paraffin-embed the tissue, samples were first placed in increasing concentrations of ethanol at room temperature (70% x2, 80%, 95%, and 100% x3) for 1 hour at each concentration to dehydrate the tissue. They were subsequently placed in xylene for a minimum of 1.5 hours at room temperature. Finally, the samples were placed in paraffin wax at 60°C for 1 hour, and this step was repeated three times.

After paraffin embedding, 10 $\mu$m sections were cut from samples using a Leica rotary microtome (RM2035, Leica Biosystems, Milton Keynes, UK) and mounted onto glass slides.Haematoxylin and Eosin (H & E) staining was performed on the fixed and sectioned porcine oral mucosa samples according to a standard protocol [213]. Samples were de-waxed in xylene for 5 minutes with agitation, then re-hydrated by placing in decreasing concentrations of ethanol (100% x2, 95%, 70%, and 50%) for 1 minute under agitation at each concentration. Samples were then washed well under running water for a minimum of 2 minutes. Slides were immersed in Gill's III Haematoxylin for 5 minutes. Samples were rinsed in tap water, differentiated with 0.3% acetic acid for 30 seconds, and treated with 0.3% hydrochloric acid in 70% ethanol for 30 seconds. Following this, samples were washed in tap water, treated with Scott's tap water substitute for 2 minutes and washed again. Eosin stain was applied for 1-2 minutes before the final washing step was performed. Sections were dehydrated by treating in 100% ethanol for 1 minute and then with xylene for 1 minute (x2). Finally, the sections were mounted under a glass coverslip using Distyrene Plasticizer Xylene (DPX). Fixed and stained sections were imaged using a light microscope (Zeiss Primotech,

Zeiss, Germany).

### Mucosal thickness measurements

The diameter and thickness of each porcine oral mucosa disc was measured using a digital Vernier caliper. The measurement was taken three times, rotating the sample each time, and an average was calculated. These measurements were also used in the calculation of the elastic and relaxation moduli (Section 2.2.1).

### Mechanical characterisation of porcine tissue

Mechanical tests were designed to mimic *in vivo* forces. Stress relaxation tests were performed on porcine oral mucosa specimens. Each specimen was loaded until compression equivalent to 10, 20, or 30% strain was reached, using an ElectroForce 5500 test instrument equipped with a 250 g load cell (TA Instruments, New Castle, USA) (Figure 2.4). This strain value was maintained for a total of 360 seconds. The accompanying instrument software (WinTest 7.1) recorded the load (N) and displacement (mm) values for the duration of the experiment. From these values, the storage modulus (E'), a measure of a materials elasticity, was calculated at 300 seconds after peak stress was measured. This property is known as the relaxation modulus and provides information about the stress relaxation behaviour of a material. The peak strain value of 30% was selected based on literature that reported the mechanical forces experienced by the oral mucosa *in vivo* [127]. Table 2.1 details the porcine mucosa samples used to analyse the relaxation modulus of the tissue.

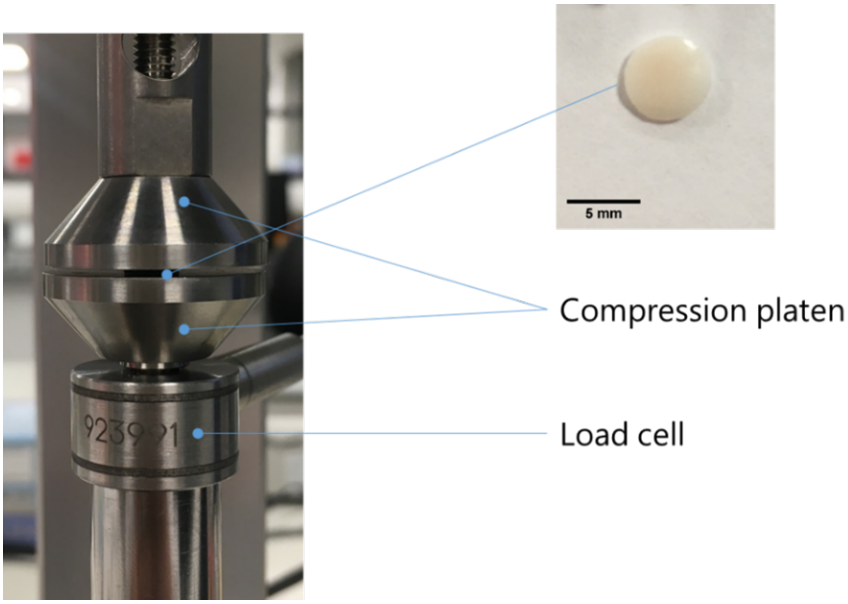


Figure 2.4: Schematic of mechanical tester (ElectroForce 5500) with loaded sample, demonstrating the load cell and compression platen.

A second mechanical property determined was the elastic modulus of the specimen after 9 loading cycles on the ElectroForce 5500, which provides information about a material's stiffness. Specimens were compressed from 0-30% strain at a rate of 0.1 mm/s. Following this, the compressive strain was removed at the same rate and this loading-unloading cycle was repeated a total of 9 times consecutively (Figure 2.5). The elastic modulus was determined by calculating the gradient of the stress-strain curve in the linear region of the 9th loading cycle. Repeated loading cycles were required due to the viscoelastic nature of the tissue. The reason for determining the elastic modulus at the 9th cycle was because it was the point at which the material had stress relaxed and reached a steady-state, and therefore ensured comparability between samples and with the hydrogel model. Table 2.2 details the porcine mucosa samples used to analyse the elastic modulus of the tissue.

Table 2.1: Sample information for porcine mucosa specimens used to calculate relaxation modulus.

| Jaw | Location | Number of Samples |
|---|---|---|
| Mandible | Lingual | 23 |
| | Total | 23 |

Table 2.2: Sample information for porcine mucosa specimens used to calculate elastic modulus.

| Jaw | Location | Number of Samples |
|---|---|---|
| Mandible | Lingual | 9 |
| Mandible | Buccal | 17 |
| Maxilla | Buccal | 17 |
| Maxilla | Palatal | 11 |
| | Total | 54 |

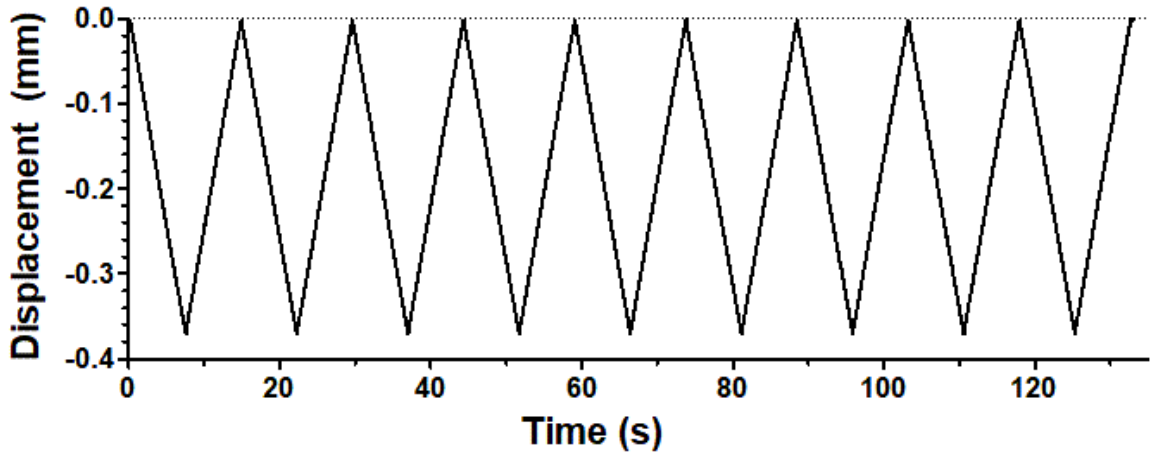


Figure 2.5: Representative loading-unloading profile applied to each sample for a total of 9 cycles using an ElectroForce 5500 mechanical tester. The displacement and load measurements recorded by the instrument during the final loading cycle were used to calculate the elastic modulus of the sample. For all samples, the displacement measurement was calculated to achieve a loading profile of 0% to 30% strain.

### 2.2.2 Preparation of acellular hydrogels

All acellular hydrogels were prepared in 24 mm diameter transwell inserts in 6-well plates (Corning Costar Transwell plates, polycarbonate membrane, 0.4 $\mu$m pore size).

#### Alginate only hydrogels

Alginate solutions of 20 mg/mL, 30 mg/mL and 40 mg/mL were prepared by adding sodium alginate to 100 mL 2-(N-morpholino)ethanesulfonic acid (MES) buffer (0.1 M, pH 6.5). The alginate was left to dissolve at 25°C overnight on a magnetic stirrer (100 rpm). The stock solutions were autoclaved and stored at 4°C for up to four weeks. Calcium chloride ($CaCl_2$) solutions of 75, 100, and 150 mM concentration were prepared by adding $CaCl_2$ to reverse osmosis (RO) water, autoclaved, and stored at 25°C. To make the hydrogels, for each stock solution the alginate was diluted to a 1:1 ratio with Iscove's Modified Dulbecco's Medium (IMDM) to achieve final concentrations of 10, 15, and 20 mg/mL. To characterise the acellular model, hydrogels were also made using 30 and 40 mg/mL stock solutions with no dilution. 2 mL of each alginate solution was added to the inside of a transwell insert. A piece of sterile filter paper was soaked in 1 mL of $CaCl_2$ and placed on top of each insert. 3 mL of $CaCl_2$ was also added to the outside of each insert. The plates were incubated at 37°C for 20 minutes and then washed both inside and out with sterile RO water to remove any remaining $CaCl_2$ solution and prevent further cross-linking.

#### Collagen only hydrogels

Rat tail collagen type I was purchased at two concentrations, 3 mg/mL and 11 mg/mL (Corning, Flintshire, UK) and stored at 4°C prior to use. All solutions were kept on ice until ready for gelation. The 11 mg/mL solution was diluted to 5 mg/mL with IMDM. Following

this, 2 mL of each collagen solution (3 mg/mL and 5 mg/mL) was added to the inside of a transwell insert and incubated at 37°C for a minimum of 4 hours.

### Blended hydrogels

Alginate stock solutions of 20, 30 and 40 mg/mL were mixed in a 1:1 ratio with IMDM, while kept on ice, to produce solutions of 10, 15, and 20 mg/mL. Collagen stock solutions were kept on ice and diluted down to concentrations of 3 mg/mL and 5 mg/mL using IMDM. Alginate and collagen stock solutions were gently mixed in a chilled Falcon tube at a 1:1 ratio (Figure 2.6). Following this, 2 mL of the composite solution was pipetted into a transwell insert and the plate was incubated at 37°C for a minimum of 4 hours to allow the collagen to self aggregate and form fibrils.

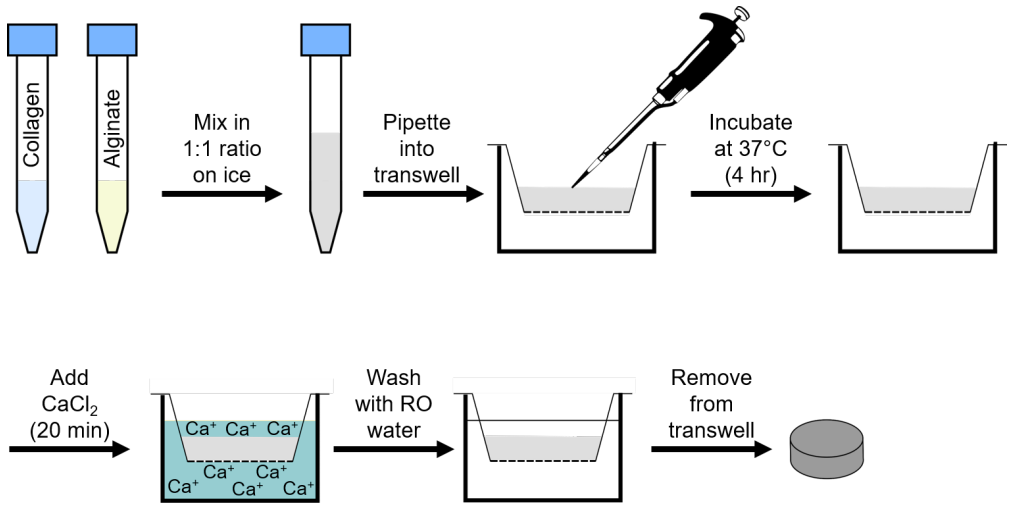


Figure 2.6: Schematic illustration showing the protocol for formation of acellular composite gels.

After collagen gelation, a piece of sterile filter paper was soaked in 1 mL of $CaCl_2$ and placed on top of each insert. 3 mL of $CaCl_2$ was also added to the outside of each insert. The plates were incubated at 37°C for 20 minutes in order for the alginate to form a gel. Finally, the samples were washed both inside and outside the transwell insert with sterile

RO water to remove any remaining $CaCl_2$ solution.

### 2.2.3 Mechanical characterisation of acellular hydrogels

For mechanical characterisation, only alginate and blended alginate-collagen hydrogels could be analysed under compression due to the low mechanical strength of the collagen samples. Alginate and blended hydrogel samples were kept in RO water at room temperature prior to testing to ensure they did not dehydrate. All hydrogels were tested the same day as they were prepared.

#### Elastic and relaxation moduli

Hydrogel discs from alginate and blended samples were removed from the transwell plate using a 6 mm biopsy punch and stored in a clean 6-well plate in 2 mL of RO water. Samples underwent compression using an ElectroForce 5500 test instrument equipped with a 250 g load cell (TA Instruments, New Castle, USA). Tests were carried out as described previously. Briefly, to determine the relaxation modulus, samples were placed under a compressive load equivalent to 30% strain for 360 seconds. The storage modulus, also called the elastic modulus (E'), a measure of a materials elasticity, was calculated at 300 seconds after peak stress was measured, and this is known as the relaxation modulus.

To determine the hydrogel stiffness, the elastic modulus (E') of each hydrogel specimen was calculated after 9 loading cycles on the ElectroForce 5500. Specimens were compressed from 0-30% strain at a rate of 0.1 mm/s. Following this, the compressive strain was removed at the same rate. This loading-unloading cycle was repeated a total of 9 times consecutively (Figure 2.5). The elastic modulus was determined by calculating the gradient of the stress-strain curve in the linear region of the 9th loading cycle. The gradient was calculated by

performing linear regression on the stress-strain curve and reducing the length of the curve on a point-by-point basis, until the linear regression achieved an $R^2$ value of 0.98.

### Rheology

For collagen gels, rheology was performed to determine the frequency-dependent elastic shear modulus (G'). Rheology was chosen due to the collagen concentrations tested being very weak, and therefore unable to maintain gelation under compression. Mechanical analysis was performed using a HR-1 Discovery Hybrid rheometer (TA Instruments, New Castle, USA). A 300 $\mu$L sample of each collagen solution was dispensed on the preheated (37°C) rheometer plate prior to gelation. The test geometry (20 mm diameter 2.004° cone plate) was lowered to a gap height of 1000 $\mu$m. The collagen was allowed to gel for 45 minutes before data was collected. Frequency sweeps from 0.01 to 1 Hz were conducted on each collagen gel (1 mg/ml, 2 mg/ml and 3 mg/ml concentration).

To demonstrate that rapid gelation could be achieved at physiological conditions for alginate hydrogels, a time sweep of storage (G') and loss (G") moduli of 10 mg/mL alginate solution was performed using a Kinexus rheometer with rSpace software version 1.75 (Malvern Instruments, Malvern, UK). For this, 2 mL of 10 mg/mL alginate was placed onto the preheated (37°C) plate geometry (20 mm diameter serrated parallel plate). The test geometry was lowered to a working gap of 1000 $\mu$m and the time sweep started. After 2 minutes, 8 mL of 100 mM $CaCl_2$ was added in a bath surrounding the plates (Figure 2.7) and the time sweep was continued for a further 8 minutes to monitor the gelation process. The time sweep was performed at 0.5% strain and a frequency of 1 Hz. Rheology was also used to determine the effect of cross-linker and polymer concentration on the mechanical properties of alginate hydrogels. Following gelation, a frequency sweep from 0.01 to 10 Hz was performed. A range of alginate concentrations (10 mg/mL, 15 mg/mL and 20 mg/mL)

and $CaCl_2$ concentrations (75 mM, 100 mM, and 150 mM) were investigated.

Figure 2.7: Image demonstrating rheometer set up used to perform alginate time and frequency sweeps. Serrated parallel plates (20 mm diameter) were utilised with a gap height of 1 mm and a weighing boat was used to create a bath for adding the $CaCl_2$ cross-linking solution.

Rheology was also used to examine the gelling process of the blended alginate-collagen system. For this, 2 mL of stock solution, at a concentration of 1.5 mg/mL collagen and 10 mg/mL alginate, was placed onto a preheated (37°C) plate (20 mm diameter serrated parallel plate). The test geometry was lowered to a working gap of 1000 $\mu$m and a time sweep was run for 3000 seconds at 0.5% strain with a frequency of 1 Hz. After 2400 seconds (40 minutes), 8 mL of 150 mM $CaCl_2$ was added to the outside of the plates, as described previously (Figure 2.7).

Finally, the effect of adding $CaCl_2$ on the gelation of two different collagen brands was characterised using rheometry. For this, the Corning collagen used previously was compared with 3 mg/mL rat tail collagen type I from Gibco (Thermo Fisher Scientific). As before, 2 mL of each collagen brand was placed onto a preheated (37°C) plate (20 mm diameter serrated parallel plate). The test geometry was lowered to a working gap of 1000 $\mu$m and a

time sweep was run for 3000 seconds at 0.5% strain with a frequency of 1 Hz. After 2400 seconds (40 minutes), 8 mL of 250 mM $CaCl_2$ was added to the outside of the plates, as described previously (Figure 2.7).

### 2.2.4 Physical characterisation of acellular hydrogels

#### Scanning Electron Microscopy

SEM provides high-resolution (1-20 nm) information on the surface structure of hydrogels, including details such as fibril thickness and porosity. Acellular collagen, alginate, and blended hydrogels were prepared according to the method described previously in Section 2.2.2. The hydrogels were frozen at -80°C for 48 hours before being placed under vacuum for 3 days. Samples were gold sputter coated (Emitech K55OX) prior to imaging using scanning electron microscopy (SEM). SEM was performed on a Zeiss EVO MA10 (Carl Zeiss Ltd, Cambridge, UK).

#### Fourier-Transform Infrared Spectroscopy

Fourier-Transform Infrared Spectroscopy (FTIR) is an analytical technique used to identify organic and polymeric materials. It works by measuring the absorption of different wavelengths of infrared radiation. FTIR was used to analyse the chemical composition of the alginate and collagen hydrogels. Acellular collagen, alginate, and blended hydrogels were prepared according to the method described previously in Section 2.2.2. The hydrogels were frozen at -80°C for 48 hours before being placed under vacuum for 3 days. Samples were then ground into a fine powder using a pestle and mortar. Traditional FTIR wavelengths (4,000 – 500 wavenumber) were scanned using a mercury cadmium telluride (MCR) detector. Data was collected on a Nicolet 6700 (Thermo Fisher).

### 2.2.5 Statistical analysis

All statistical analyses were conducted in GraphPad Prism (v. 5.03). A Mann-Whitney t-test was used to determine statistical significance for porcine mucosa thickness for upper and lower jaw, and storage and relaxation moduli for the upper and lower jaw. A Kruskal-Wallis test (one-way ANOVA) was used to determine statistical significance for porcine mucosa thickness by tissue region, storage and relaxation moduli of porcine mucosa by tissue region, and to compare storage moduli for alginate concentrations. A post-analysis Dunn's multiple comparison test was used to compare pairs. For all analyses, $p<0.05$ was considered statistically significant.

## 2.3 Results and Discussion

First, the physical features and mechanical properties of porcine oral mucosa were determined as a basis for determining the characteristics of the native tissue. Secondly, the mechanical properties of acellular hydrogels were compared with the properties of porcine mucosa to identify which concentrations align most closely with native tissue. Finally, the acellular hydrogels were physically characterised to determine the gelling behaviour and confirm the chemical structure of the polymers.

### 2.3.1 Histological staining of porcine oral mucosa

H & E is a widely used histological stain that can demonstrate general tissue architecture. Cell nuclei appear as blue-black, cell cytoplasm as varying shades of pink, and collagen fibres appear light pink [213]. Figure 2.8 highlights some key features of porcine gingival oral mucosa. The stratified epithelium, comprised of the keratin layer and granular layer,

is evidenced through the presence of elongated keratinocytes at the surface, with the nuclei no longer present at the topmost layer. There are also disordered collagen fibres displayed in the connective tissue, otherwise known as the lamina propria, compared with the more ordered, layered fibres at the surface. Histologically, porcine oral mucosa has been found to display many similarities to human oral mucosa [214] and therefore is a good basis for studying the structure of the epithelium. For example, porcine oral mucosa is the most similar to human in certain characteristics such as keratinisation, thickness and rete ridges (the epithelial extensions that project into the underlying connective tissue), as well as both tissue types having a glycogen-rich content in the upper epithelium and a similar vascular network [215]. Due to these common features, porcine tissue is a good tissue to compare with the hydrogel models, both in terms of mechanical properties and physical characteristics.

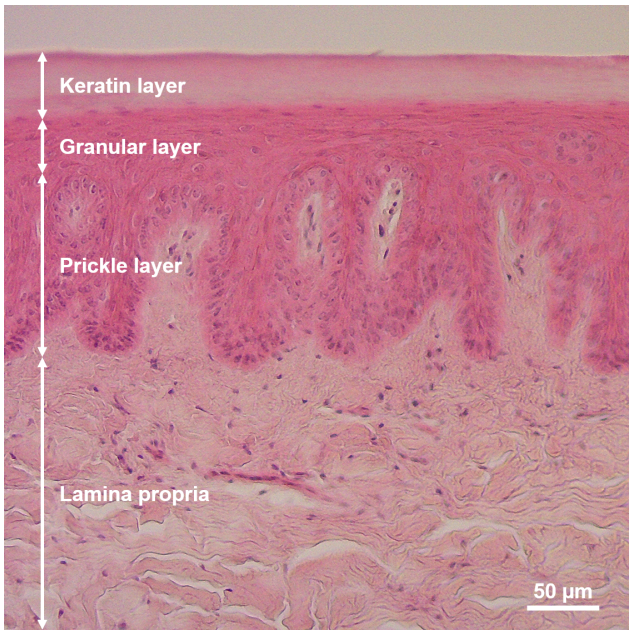


Figure 2.8: Representative image of H & E stained porcine oral mucosa imaged on a Zeiss light microscope, 20x magnification. Image is of gingival oral mucosa from the buccal region of the mandible, taken from adjacent tissue to that sectioned for mechanical testing. One tissue sample from each location (Appendix 1) was sectioned and stained, and three images of each sample were taken. The key features of the native tissue are labelled and marked.

### 2.3.2 Porcine mucosa thickness

Mucosa thickness can vary over a wide range, from 0.30 mm on the attached buccal mucosa of the mandible (lower jaw) to 6.7 mm in the maxillary tuberosity region (adjacent to the molars in the upper jaw) [126]. Therefore, thickness measurements of the samples used for mechanical testing were compared. For sections taken from the maxilla and mandible, a significant difference ($p = 0.0004$) was identified (Figure 2.9). The mean thickness of the porcine oral mucosa sections for tissue from the mandible and maxilla was found to be 1.43 $\pm$ 0.295 mm and 1.70 $\pm$ 0.398 mm respectively.

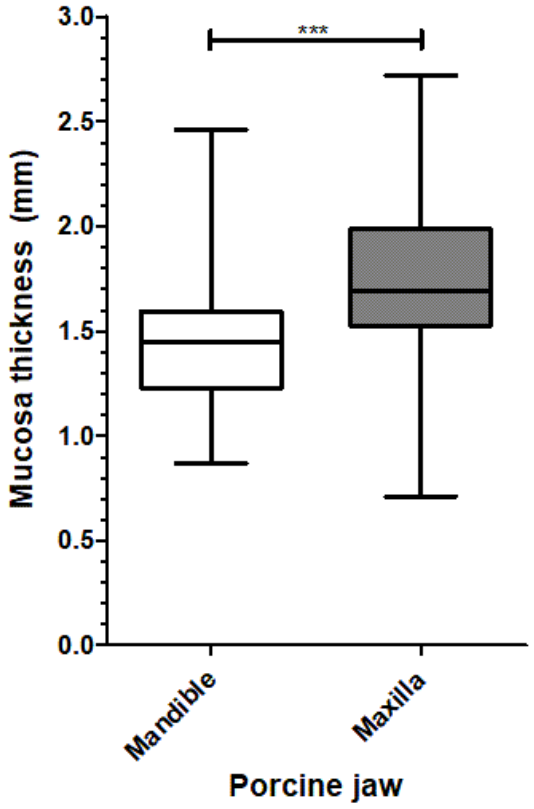


Figure 2.9: Thickness of porcine gingival mucosa for upper and lower jaw. Graph shows mean, 25th and 75th percentile (box), and maximum and minimum values (whiskers), n = 48 for mandible and n = 32 for maxilla. Statistical significance represents a p value of 0.0004.

Thickness measurements were also compared between gingival tissue locations on each jaw. A significant difference was identified in the thickness of mucosa in the three regions ($p = 0.0015$) (Figure 2.10). The mean thickness of porcine oral mucosa for lingual, palatal, and buccal tissue was found to be $1.413 \pm 0.360$ mm, $1.901 \pm 0.407$ mm, and $1.521$ mm $\pm$ 0.280 mm respectively. Using a post-comparison test, no significant difference was identified between the tissue sections taken from the lingual and buccal regions. Significant differences were identified between the palatal and buccal tissues ($p < 0.05$) and the palatal and lingual tissues ($p < 0.001$). It should be noted that a higher number of samples from the maxilla came from the palatal region, and hence this may have explained the reason for the difference identified in sample thickness between the maxilla and mandible (Figure 2.9). For all samples, the tissue thickness was found within the expected range for porcine oral mucosa [126]. Specifically, Goktas et al. [127] reported the mean tissue thickness of porcine attached lingual mucosa and attached buccal mucosa to be $1.31 \pm 0.26$ mm and $1.60 \pm 0.20$ mm respectively. This is in line with the reported mean tissue thickness for the lingual and palatal regions in this study (1.41 mm and 1.52 mm respectively).

### 2.3.3 Porcine mucosa storage modulus

The same study by Goktas et al. [127] demonstrated differences in the relaxation modulus based on the region of the oral cavity the specimen was taken from. Similar studies have suggested that the mechanical properties of the tissue vary depending on the location of the oral mucosa within the mouth [126, 128, 129]. In order to see whether location had an influence on the mechanical properties of the tissue in this study, the elastic modulus of porcine gingival mucosa was compared by location. The elastic modulus is a measurement of a materials ability to resist deformation when a stress is applied, and is also known as a material's stiffness. The mean storage moduli for mandibular and maxillary tissues under

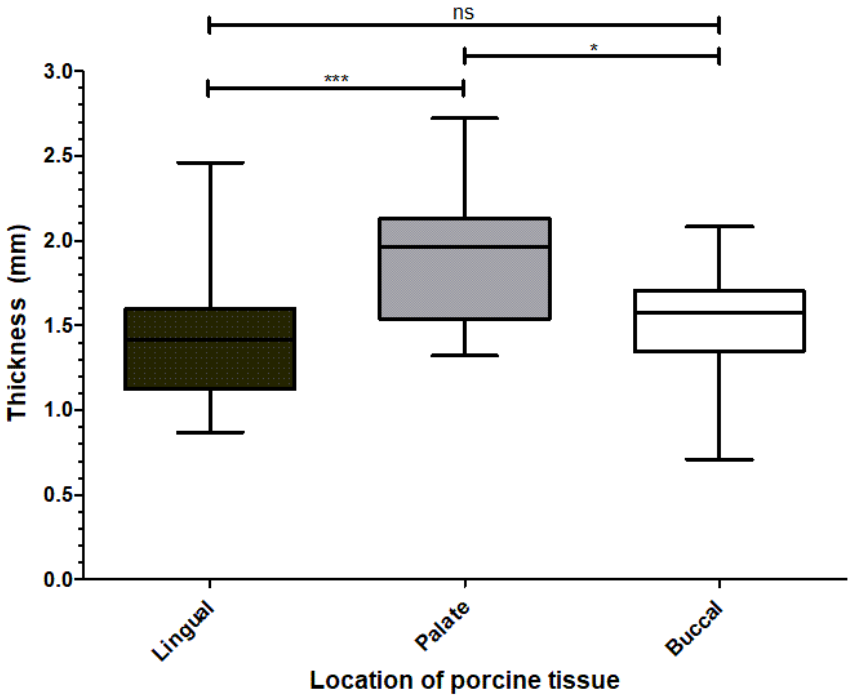


Figure 2.10: Thickness of porcine gingival mucosa for various locations taken from both mandible and maxilla. Graph shows mean, 25th and 75th percentile (box), and maximum and minimum values (whiskers), n = 28 for lingual, n = 12 for palatal, and n = 40 for buccal.

30% maximum strain were determined to be 24.42 ± 18.08 Pa and 19.46 Pa ± 10.00 Pa respectively (Figure 2.11). For lingual, palatal and buccal tissues, the storage moduli were found to be 13.29 ± 6.18 Pa, 22.47 ± 11.84 Pa, and 23.58 ± 16.06 Pa respectively (Figure 2.12).

No significant differences were determined between the elastic modulus (E') of porcine oral mucosa when separated by region. This finding was likely due to the methods used to standardise the oral mucosa sections in the present work. For this study, all mucosa sections were taken from the region directly adjacent to the tooth (the attached gingiva), as this is the part of the oral mucosa that forms a seal around a dental implant, and hence is relevant for the model being developed. However, Goktas et al. [127] took tissue from a range of locations moving further away from the tooth (Figure 2.13). They identified no significant

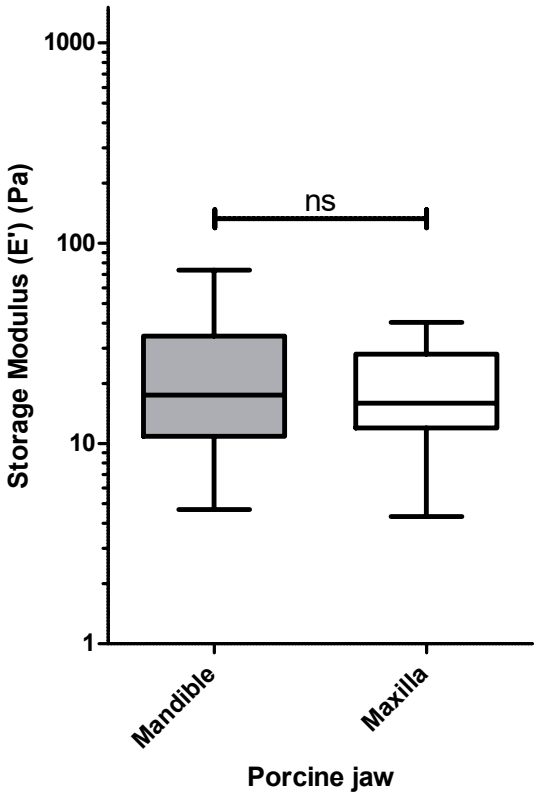


Figure 2.11: Storage modulus (E') at 30% strain of porcine gingival mucosa for upper and lower jaw. Graph shows mean, 25th and 75th percentile (box), and maximum and minimum values (whiskers), n = 25 for mandible and n = 28 for maxilla.

differences between the behaviour of the lingual attached gingiva and the buccal attached gingiva in response to compression of 10% strain. This was thought to be because there are anatomic similarities between the lingual and buccal aspects of the attached gingiva [127]. Therefore, the differences in mechanical properties they identified are explained by the range of samples they tested, compared with only the attached gingiva utilised in the present study.

Very few studies have investigated the biomechanical properties of native oral mucosa, making it challenging to identify comparable values in the literature. Applied stress and strain values, tissue location and storage conditions are all known to influence the material's elastic modulus. For example, Goktas et al. [127] dissected the mucosal tissue from

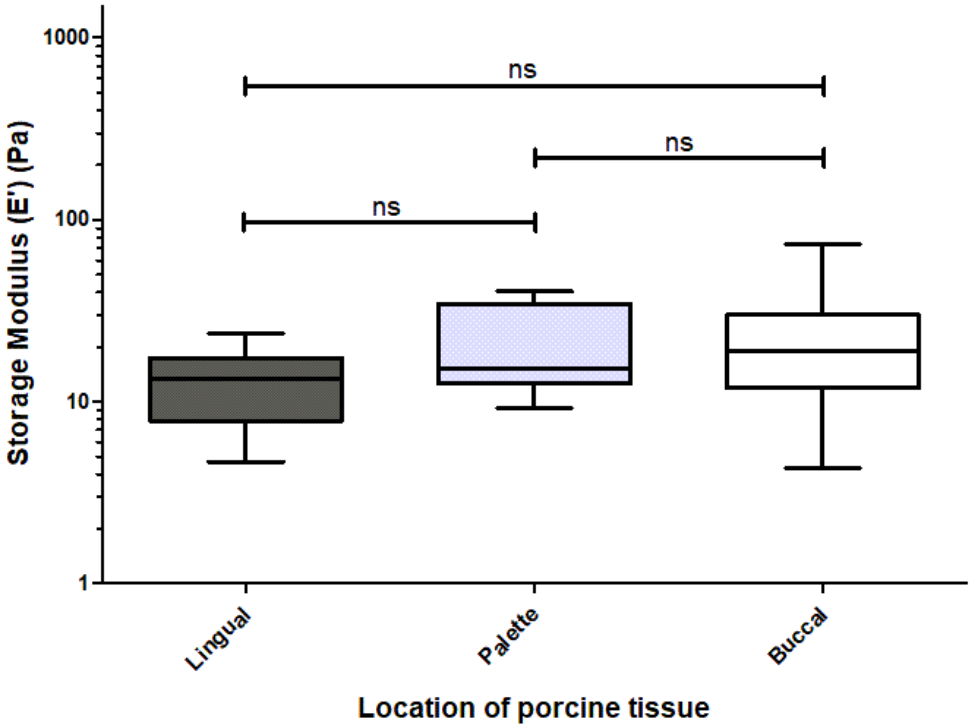


Figure 2.12: Storage modulus (E') at 30% strain of porcine gingival mucosa for various locations. Graph shows mean, 25th and 75th percentile (box), and maximum and minimum values (whiskers), n = 8 for lingual, n = 11 for palatal, and n = 34 for buccal.

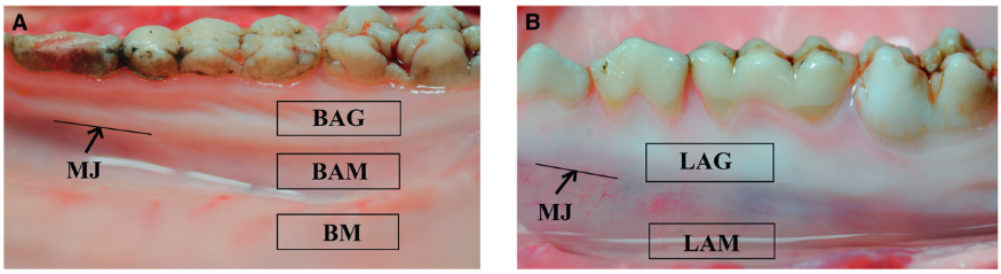


Figure 2.13: Figure reproduced from Goktas et al. [127]. Images show the porcine oral soft tissues extracted from the buccal (A) and lingual (B) aspects of porcine lower jaws for the published study.

epithelium to bone, including the periosteum. However, in the present study, connective tissue was removed in order to focus on the specific properties of the epithelium. This may explain why the mean storage modulus identified for gingival epithelium ranging from 13.29

Pa to 24.42 Pa in the present work (Figures 2.11 and 2.12) was significantly lower than the reported storage modulus of 0.86 MPa for the buccal attached gingiva by Goktas et al. [127]. This suggested that the supporting connective tissue played a vital role in resisting the compressive forces generated in the oral cavity. In the present work, the mechanical properties of the epithelium alone were used to select the composition of the hydrogel scaffold. However for future development of the model, it could be important to consider the connective tissue. For example if the 3D mucosa model was being used to investigate the effect of compressive forces on the encapsulated cells, the difference in mechanical properties due to the presence of the connective tissue *in vivo* would be an interesting factor to assess.

### 2.3.4 Porcine mucosa relaxation modulus

The relaxation modulus provides information on a material's stress relaxation behaviour. Porcine tissue is known to display a non-linear viscoelastic tissue response, whereby the stress within the tissue decays with time until an equilibrium value is reached [127, 216]. Furthermore, the applied compressive strain is known to impact on the reported mechanical properties of a material. Therefore, to investigate both the relaxation behaviour of the tissue, and the effect of peak strain on the mechanical properties, the relaxation modulus ($E_R$) was determined for porcine oral mucosa at peak strain values of 10, 20, and 30%.

The mean relaxation modulus for porcine mucosa at 10, 20 and 30% strain was found to be 7.75 ± 4.98 Pa, 19.95 ± 14.95 Pa, and 59.99 ± 87.39 Pa respectively (Figure 2.14), with a significant difference identified using a 1-way ANOVA ($p = 0.0124$). Using a post-comparison test, a significant difference was specifically identified between the relaxation moduli measured at 10% peak strain and 30% peak strain ($p < 0.01$).

Figure 2.14 supported the understanding that the peak strain affects the mechanical

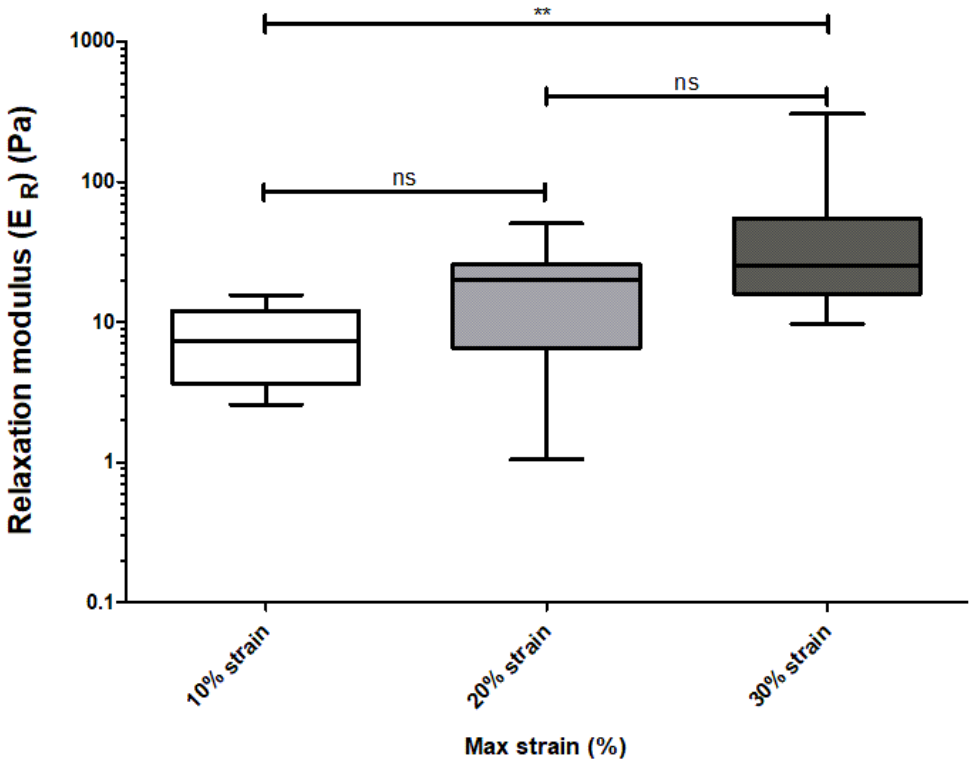


Figure 2.14: Relaxation modulus ($E_R$) at 10, 20, and 30% strain of porcine gingival mucosa. Graph shows mean, 25th and 75th percentile (box), and maximum and minimum values (whiskers), n = 5 for 10% strain, n = 10 for 20% strain, and n = 11 for 30% strain. Statistical significance shown from a post-comparison test where ** indicates a p value of $<0.01$.

properties of a material. Specifically, as expected, an increase in the peak strain applied to the sample resulted in an increase in the stiffness of the porcine mucosa after the tissue had relaxed to equilibrium.

### 2.3.5 The effect of alginate concentration on the mechanical properties of hydrogels

The elastic modulus of alginate hydrogels depends on the number density of physical cross-links between polymer chains, as well as the length and stiffness of the chains [217]. Therefore,

the modulus of the gel can be tuned by varying the concentration of alginate and calcium ions. To investigate the effect of alginate concentration on the mechanical properties of the hydrogel model, firstly alginate-only hydrogels were examined. The storage modulus (E') was calculated for alginate concentrations of 10 to 40 mg/mL at 30% peak strain (Figure 2.15). The storage modulus for alginate hydrogels increased with increasing concentration up to 30 mg/mL. The mean values for storage modulus for each concentration of alginate were found to be 191 ± 113 Pa for 10 mg/mL, 289 ± 89.9 Pa for 15 mg/mL, 660 ± 159 Pa for 20 mg/mL, 814 ± 250 Pa for 30 mg/mL, and 569 ± 401 Pa for 40 mg/mL. This supported the understanding that the mechanical properties of the composite hydrogel model could be tuned by adjusting the concentration of the alginate component, which was important for the development of the oral tissue model being generated in the present work. It is useful to understand how alginate concentration can be tuned to achieve the desired mechanical properties that emulate the native tissue, as this element of the composite system will provide the mechanical strength of the mucosa model.

Several studies have looked at the mechanical properties of alginate hydrogels [202, 217–220]. There are many factors that affect the measured elastic modulus of alginate, including alginate source, polymer concentration, cross-linker type, cross-linker concentration, gelation time, and compressive load applied. This makes it challenging to directly compare results with other published works. In the present study, alginate storage modulus was calculated to range between 101 Pa to 814 Pa for concentrations between 10 and 40 mg/mL, cross-linked with 150 mM $CaCl_2$ for 20 minutes, tested under compression at a strain of 30%. In comparison, other literature has reported storage moduli ranging from 17.1 kPa for 15 mg/mL alginate cross-linked with 50 mM $CaCl_2$ solution [218], to 160 kPa for 20 mg/mL alginate cross-linked with 72 mM calcium carbonate [220]. These are an order of magnitude higher than the values reported in the current study, however, since information on gelation time and compressive strain applied are not available, it is likely that these parameters are

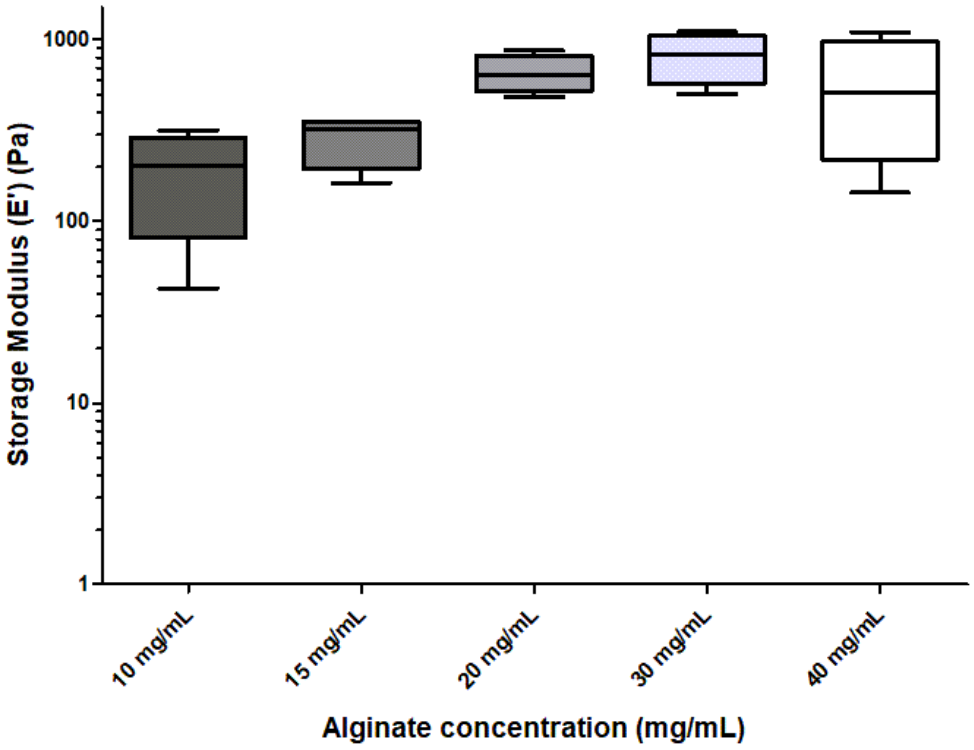


Figure 2.15: Storage modulus (E') at 30% strain for different concentrations of alginate hydrogel (n = 4). Graph shows mean, 25th and 75th percentile (box), and maximum and minimum values (whiskers).

the reason for the differences.

One noticeable feature presented in Figure 2.15 is the decrease in mean storage modulus for 40 mg/mL samples, compared with 30 mg/mL samples. Alginate hydrogels formed with slower rates of gelation tend to exhibit greater structural homogeneity and therefore a higher elastic modulus than those gelled rapidly [202]. Furthermore, previous works have shown that the rate of gelation decreases with increasing polymer concentration since the alginate is more viscous and this hinders the polymer chains rearrangement to form effective cross-links [202]. This study determined a gelation time of less than 20 minutes for alginate gels at a concentration of 15 mg/mL, but over 100 minutes for alginate gels at a concentration of 30 mg/mL [202] and therefore explains the observation that at 40 mg/mL, the mean

elastic modulus was found to be lower than that of the 30 mg/mL hydrogels. In the method used for the present work, gelation is rapid due to using $CaCl_2$ as a cross-linker and the fact that $CaCl_2$ is highly soluble. Furthermore, gelation occurred for only 20 minutes before the $CaCl_2$ solution was removed and the samples washed. The reason for choosing rapid gelation is to ensure that this process does not affect cell viability once cells are encapsulated in the gel. From this data, it is suggested that using lower alginate concentrations in the model will ensure that lower gelation times are required to form effective cross-links.

### 2.3.6 Mechanical properties of blended alginate-collage hydrogels

Next, the mechanical properties of blended alginate-collagen hydrogels were investigated. As the collagen-only gels were too weak to be tested under compression, it was expected that the collagen concentration would not influence the mechanical properties of the composite gel as significantly as the alginate concentration. Furthermore, due to its poor mechanical properties, the addition of collagen to the hydrogel was expected to reduce the measured stiffness of the gel for two reasons. Firstly, the presence of the collagen reduced the concentration of alginate and secondly, the collagen may have reduced the number of cross-links that can be formed within the gel.

As expected, the addition of collagen significantly reduced the storage modulus of the hydrogels compared with alginate alone (Figure 2.16). Mean storage moduli were determined to be 16.18 Pa for 1.5 mg/mL collagen and 5 mg/mL alginate, 13.40 Pa for 1.5 mg/mL collagen and 7.5 mg/mL alginate, 27.76 Pa for 1.5 mg/mL collagen and 10 mg/mL alginate, 15.28 Pa for 2.5 mg/mL collagen and 5 mg/mL alginate, 13.83 for 2.5 mg/mL collagen and 7.5 mg/mL alginate, and 27.16 Pa for 2.5 mg/mL collagen and 10 mg/mL alginate. A significant difference was identified using a 1-way ANOVA ($p = 0.0317$). However, using a post-comparison test, no significant differences were identified between pairs of conditions.

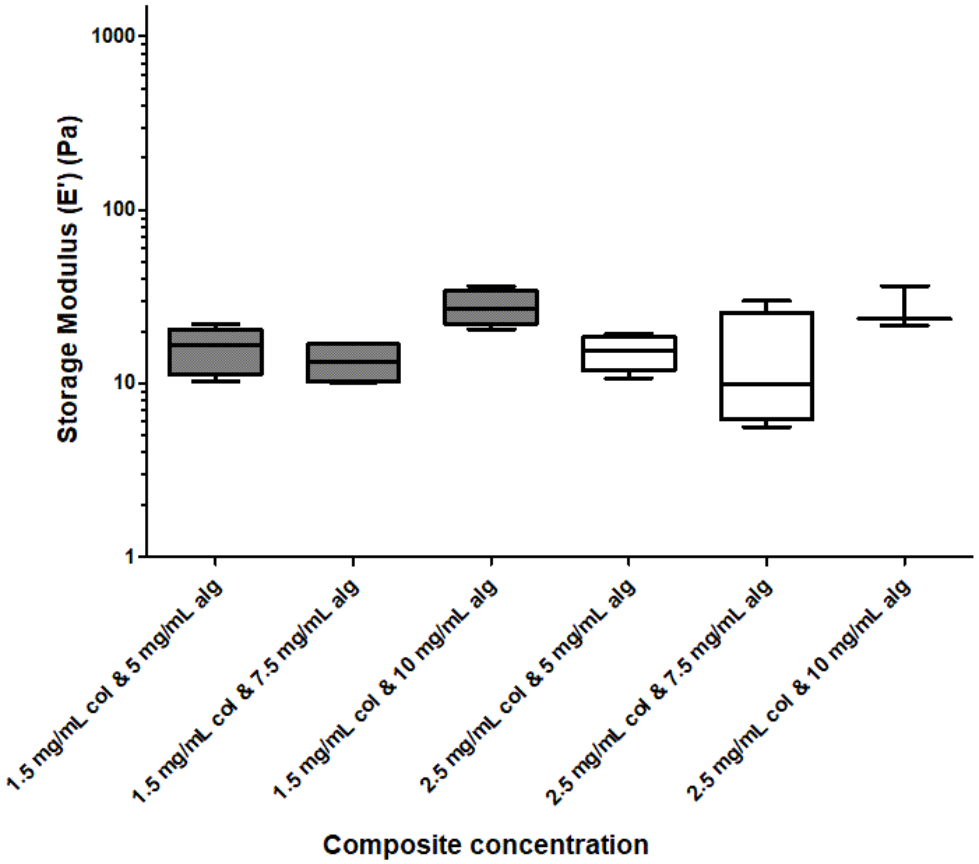


Figure 2.16: Storage modulus (E') at 30% strain for different concentrations of composite hydrogel (n = 4 for all conditions except 2.5 mg/mL collagen and 10 mg/mL alginate where n = 3). Graph shows mean, 25th and 75th percentile (box), and maximum and minimum values (whiskers).

Figure 2.16 shows that there is little difference between the mean storage moduli of blended hydrogels with alginate concentrations of 5 and 7.5 mg/mL. However, the blended hydrogels containing 10 mg/mL alginate were shown to have a higher storage modulus by approximately 10 Pa. It was noted that some concentrations had a larger range than others, most notably the blended hydrogel 2.5 mg/mL collagen with 7.5 mg/mL alginate. This could be due to the effects of the high water content of the hydrogels, as the presence of water on the surface of the gel can cause surface tension to influence the forces measured by the instrument, especially at the low loads applied in this study (less than 250 g).

As with alginate-only scaffolds, comparing the results from this study with literature values is challenging due to the effect of several different parameters on the measured compressive modulus. Determining a value for the stiffness of a hydrogel scaffold should be defined in terms of the type of deformation (e.g. compression, tension, or shear forces) and technique used [200]. In addition, collagen and alginate are non-linear viscoelastic materials, and therefore differences in time-span or strain used can influence the measured compressive modulus [200]. Since no studies have been published that look specifically at the elastic modulus of alginate-collagen blended hydrogels under compression, it is not possible to compare the current measurements with already published values. However, these measurements will be essential in determining an appropriate collagen-alginate concentration that aligns with the elastic modulus of porcine mucosa.

### 2.3.7 Comparison of hydrogel and porcine storage modulus

The relaxation moduli and elastic moduli of alginate and composite gel systems were compared with the average for porcine tissue at 30% peak strain. Figure 2.17 shows the elastic modulus of six composite gel systems and four alginate concentrations with the elastic modulus of porcine oral mucosa. A statistically significant difference was determined using a 1-way ANOVA ($p = < 0.0001$). The mean stiffness of porcine mucosa for all samples tested was determined to be 21.80 Pa. This aligns well with the stiffness values calculated for the blended scaffolds, which ranged from 13.40 Pa to 27.76 Pa. However, pure alginate hydrogels were deemed to be too stiff for the purpose of mimicking the native tissue properties, as the stiffness values measured ranged from 191.4 Pa to 814.5 Pa, an order of magnitude higher than porcine gingival mucosa.

Based on the data in Figure 2.17, blended alginate-collagen hydrogels were an ideal choice for mimicking the native tissue mechanical properties. Within the concentration

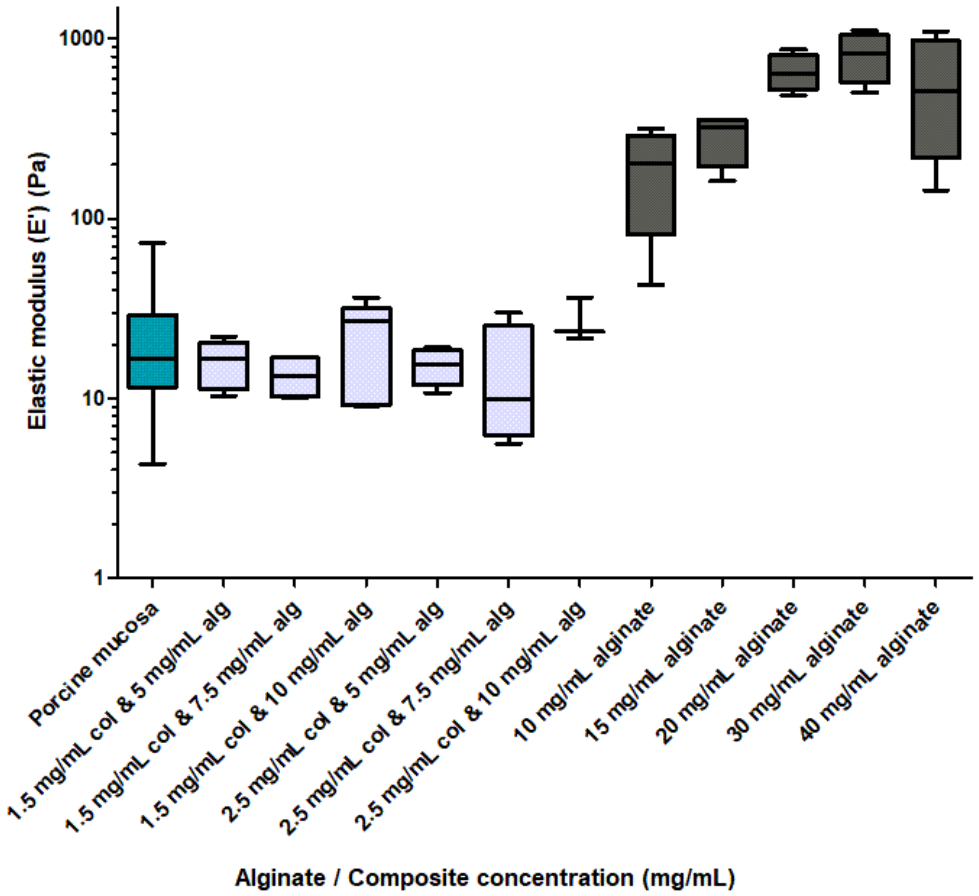


Figure 2.17: Comparison of storage modulus (E') at 30% strain for porcine and hydrogel (n = 53 for porcine mucosa, n = 4 for all hydrogel conditions except 2.5 mg/mL collagen and 10 mg/mL alginate where n = 3). Graph shows mean, 25th and 75th percentile (box), and maximum and minimum values (whiskers).

ranges studied, it appeared there was very little difference between the mean values for porcine mucosa and blended hydrogels with an alginate concentration of less than 7.5 mg/mL. Therefore, the chosen blended concentrations taken forward for biological characterisation were 2.5 mg/mL collagen and 5 mg/mL alginate, and 2.5 mg/mL collagen and 10 mg/mL alginate.

### 2.3.8 Rheology

Rheology is commonly employed to investigate the mechanical characteristics of alginate and collagen-based hydrogel scaffolds [203, 217, 221, 222]. In particular, rheology is a useful technique for understanding the alginate gelation process. To do this, a 20 minute time sweep of 10 mg/mL alginate-only stock solution was performed on a rheometer with serrated parallel plate geometry (Figure 2.18). $CaCl_2$ (100 mM) was added to the outside of the plate geometry after 120 seconds (2 minutes) and an immediate increase in both shear storage (G') and shear loss (G") moduli was observed, providing evidence of a rapid gelation process. Rapid gelation is useful as it minimises the length of time the cells will be in the presence of the cross-linking solution, which should maintain cell viability. Calcium ions are considered to be important in cell culture because they are involved in a wide range of cell functions. A high calcium concentration is believed to instigate cell apoptosis and therefore minimising the concentration and duration of the presence of calcium ions was preferred [223].

As evidenced in Figure 2.18, after approximately 480 seconds (8 minutes), the rate of increase of storage and loss moduli decreased, suggesting there was minimal further gelation occurring. Therefore, a gelation time of 20 minutes used in the production of the composite hydrogel mucosa model was felt to be sufficient to ensure a homogenous gel was formed.

Rheology was further used to examine the effect of the concentration of alginate stock solution and cross-linking solution on the mechanical properties under shear oscillation (Figure 2.19). The results aligned well with a published study by Zhou et al. (2019) [222], which determined the complex shear modulus (G*) of a 20 mg/mL alginate hydrogel to range from 400 Pa to 1000 Pa [222]. Changing the concentration of cross-linking solution appeared to have minimal impact on the complex shear modulus of alginate hydrogels, although it was notable that the 150 mM $CaCl_2$ solution did result in higher complex moduli than the 75

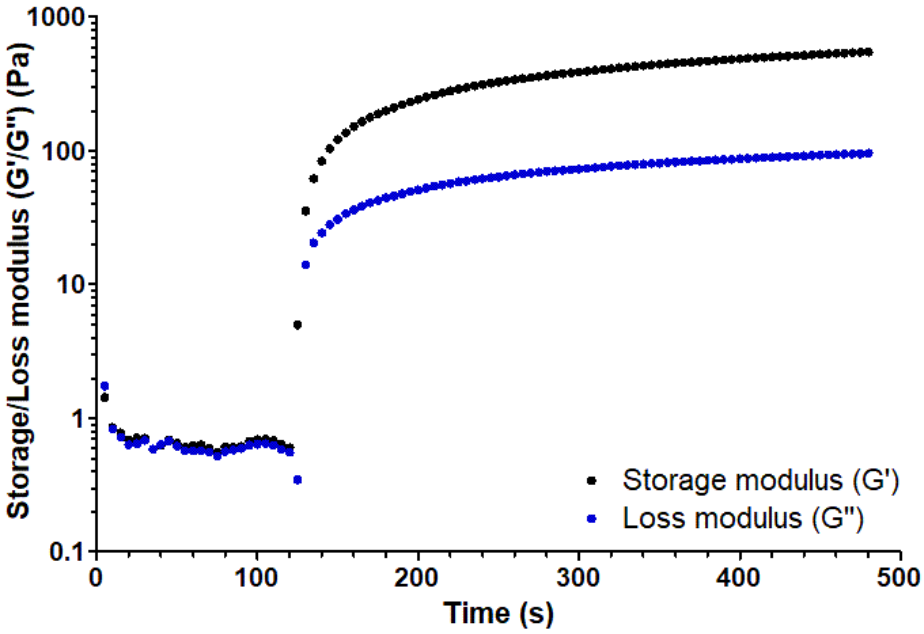


Figure 2.18: Time sweep of storage (G') and loss (G") moduli of 10 mg/mL alginate gel with 8 mL of 100 mM $CaCl_2$ added after 2 minutes. Performed on a Kinexus rheometer at 0.5% strain, at a frequency of 1 Hz, using serrated parallel plate geometry with a 1 mm working gap.

mM solution. However, the concentration of the alginate appeared to have greater impact on the mechanical properties of the hydrogel than the concentration of $CaCl_2$, with increasing concentration of alginate resulting in an increase in shear modulus (Figure 2.19). The results provided further evidence that the concentration of alginate could be used effectively to control mechanical behaviour of the hydrogel scaffold.

Within the blended hydrogel tissue model, the presence of collagen was designed to provide motifs for cell adhesion and ensure that cells receive biological cues to support their growth and proliferation. Formation of collagen fibrils was desired for this, and therefore during preparation of the tissue model, the collagen was allowed to gel for a minimum of 4 hours prior to cross-linking the alginate with $CaCl_2$, although collagen gelation is known to typically occur within 1 hour.

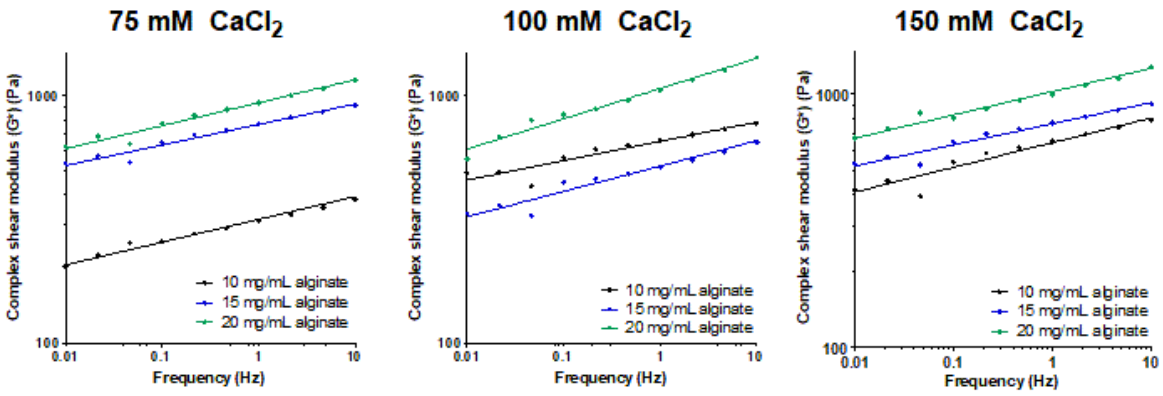


Figure 2.19: Frequency sweep of complex shear modulus (G*) of alginate hydrogels at a range of concentrations (10, 15 and 20 mg/mL), cross-linked with difference concentrations of CaCl2 (75, 100, and 150 mM). Graphs show data points plus non-linear regression line (n = 1).

As the collagen hydrogels were too weak to examine under compressive load, rheology was utilised to assess the effect of collagen concentration on its mechanical properties (Figure 2.20). An increase in collagen concentration resulted in a small increase in shear modulus at frequencies over 0.1 rad $s^{-1}$. However, as demonstrated in the compressive testing of composite hydrogels, the difference in mechanical properties for collagen was very small compared to the alginate component, and therefore the mechanical properties were primarily controlled by alginate concentration.

Once the mechanical behaviour of both alginate and collagen had been analysed separately, the blended alginate-collagen system was examined. In Figure 2.21A, a slow increase in the shear storage and loss moduli for collagen over the first 40 minutes was observed, as the collagen self-aggregated and formed fibrils. However, the addition of $CaCl_2$ at 40 minutes significantly reduced the storage and loss moduli for the collagen hydrogel, disrupting gel formation and demonstrating very weak gellation and poor mechanical strength. In contrast, at 40 minutes, the addition of $CaCl_2$ caused rapid gelation of the alginate (Figure 2.21A). When both materials were blended and the same gelation method applied, the

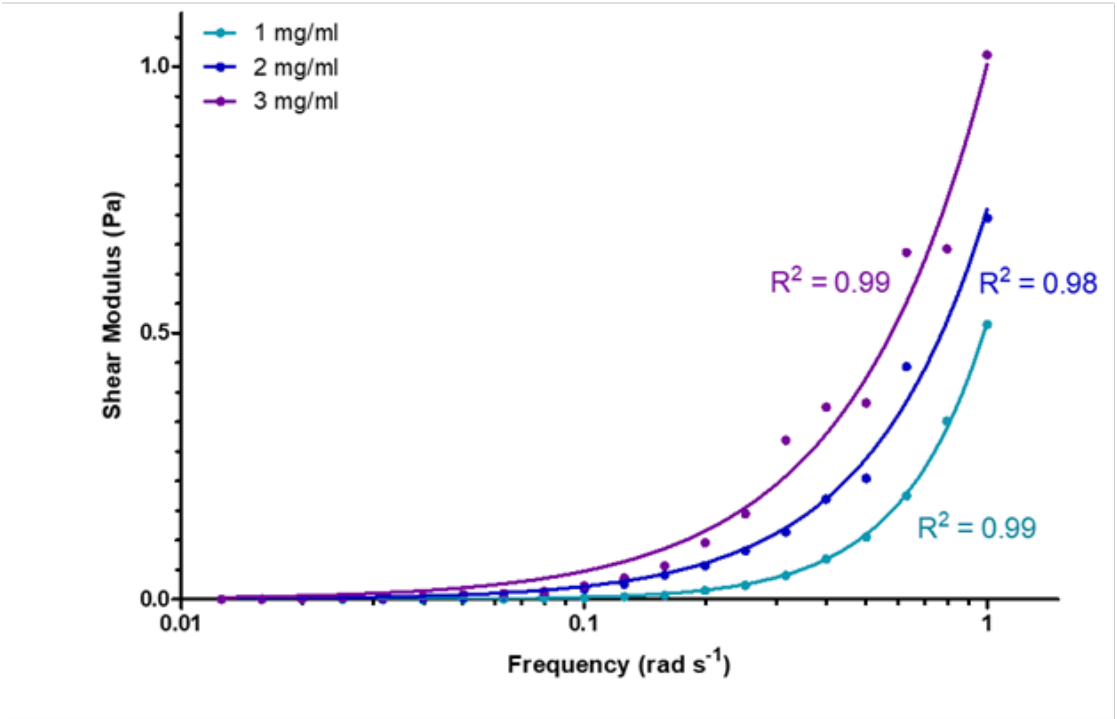


Figure 2.20: Frequency sweep on collagen hydrogels of 1, 2, and 3 mg/mL concentration performed after 1 hour of heating at 37°C on a Kinexus rheometer at 0.5% strain with a 1 mm working gap (n=1). Graph shows data points and non-linear regression line.

gelation mechanisms of both collagen and alginate were observed (Figure 2.21B). A gradual, slow increase in stiffness as the collagen self-aggregated was observed, between 0 and 2500 seconds, followed by a sharp increase in stiffness once the $CaCl_2$ was added at 2500 seconds. However, it was notable that the stiffness of the collagen in the blended hydrogel over the first 40 minutes of gelation was much lower than for collagen alone, suggesting that the presence of alginate inhibits collagen self-aggregation.

The gelation behaviour demonstrated in Figure 2.21 was supported with similar findings by Moxon et al. [203]. However, in this published study, the increase in storage modulus for collagen alone was reported to increase from 1 Pa to 476 Pa over the 40 minute time period. This was a much greater increase than the results of the present study, which saw

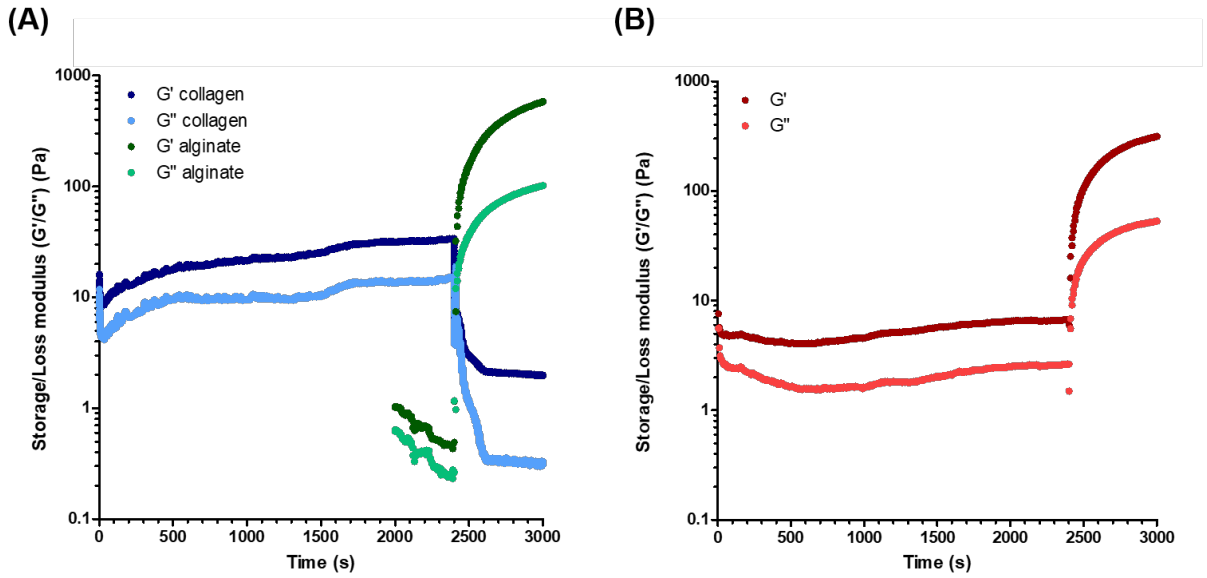


Figure 2.21: 1 hour time sweep of shear storage (G') and loss (G") moduli for (A) pure collagen and alginate hydrogels at concentrations of 1.5 mL for collagen and 10 mg/mL alginate (n = 1), and (B) a blended alginate-collagen hydrogel at a concentration of 1.5 mg/mL collagen and 10 mg/mL alginate (n = 1). Calcium chloride solution (150 mM) was added after 40 minutes (2500 seconds) to cross-link the alginate component.

an increase in storage modulus from 4 Pa to 30 Pa. It was noted that a difference between the collagen used in the present study, and that used by Moxon et al. [203] was the brand from which the rat tail collagen type I was purchased. To investigate if this had an impact on the mechanical properties of the hydrogel, two different collagen sources were compared (Figure 2.22).

In Figure 2.22, both brands showed a similarly low increase in storage and loss moduli over the first 40 minutes of the time-sweep, with Gibco displaying higher stiffness than Corning overall. Similarly, both the Corning and Gibco collagen displayed a rapid and significant drop in G' and G" when the $CaCl_2$ solution was added. Most notably, at this point, the stiffness of the Gibco collagen remained stable, while the Corning collagen displayed scattered data points. This suggested that Corning collagen was affected by the addition of

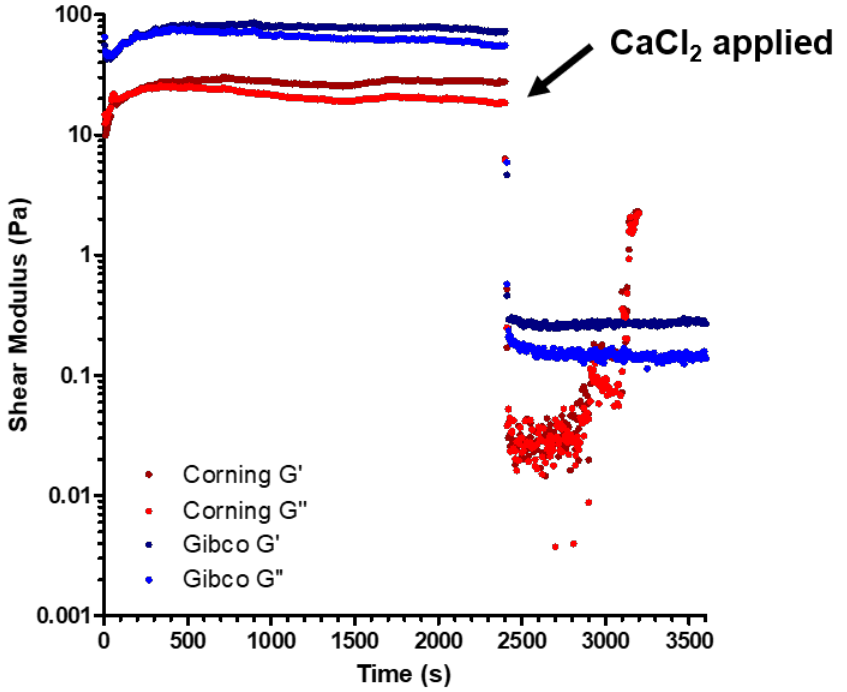


Figure 2.22: A 1 hour time sweep of shear storage (G') and loss (G') moduli for two different brands of rat tail collagen type I (n = 1). Corning collagen was purchased at a concentration of 3.57 mg/mL and Gibco collagen was purchased at a concentration of 3 mg/mL. Calcium chloride solution (150 mM) was added after 40 minutes.

the $CaCl_2$ solution, and this may have impacted the formation of collagen fibrils. Further investigation was deemed necessary to ensure that the Corning collagen still formed fibrils and provided cell-attachment motifs for cell-binding.

### 2.3.9 Scanning Electron Microscopy

SEM utilises a focused beam of high-energy electrons to generate a signal at the surface of specimens, and provides high-resolution (50 to 100 nm) information on the microstructures and surface composition of a sample. This technique was used to visualise acellular hydrogels

in order to identify the presence of collagen fibrils in the blended alginate-collagen gels.

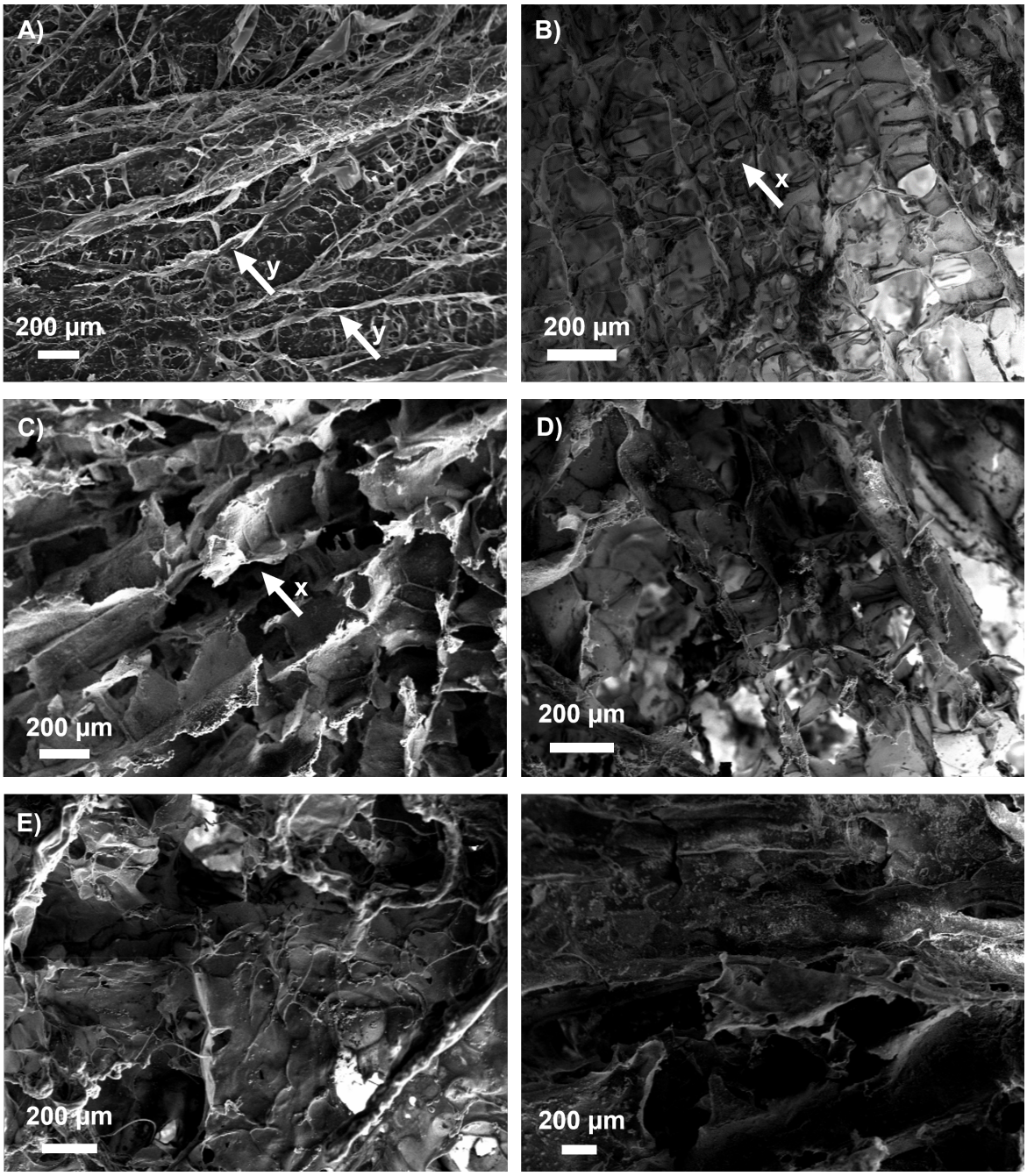


Figure 2.23: SEM micrographs of control and blended hydrogels. (A) 3 mg/mL collagen. (B) 5 mg/mL alginate. (C) 10 mg/mL alginate. (D) 1.5 mg/mL collagen + 5 mg/mL alginate. (E) 1.5 mg/mL collagen + 7.5 mg/mL alginate. (F) 1.5 mg/mL collagen + 10 mg/mL alginate. Arrows point to (x) fin-like, porous structures of alginate hydrogels and (y) collagen fibrils.

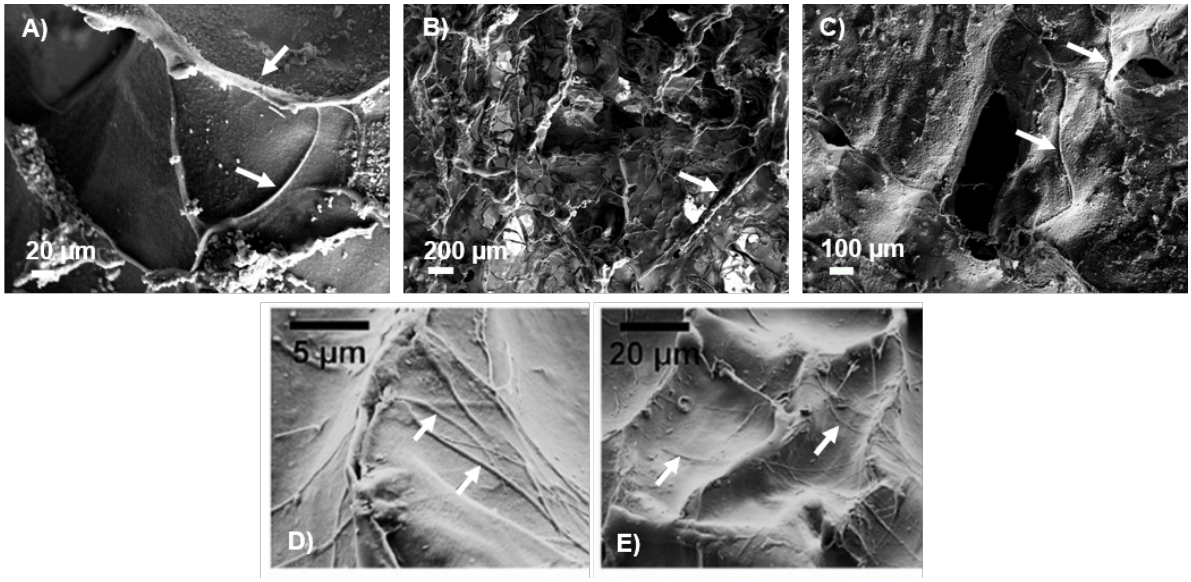


Figure 2.24: SEM micrographs of blended hydrogels. (A) 1.5 mg/mL collagen + 5 mg/mL alginate. (B) 1.5 mg/mL collagen + 7.5 mg/mL alginate. (C) 1.5 mg/mL collagen + 10 mg/mL alginate. (D,E) Figure reproduced from Baniasadi and Minary-Jolanden (2015) [221]. Arrows indicate suggested presence of collagen fibrils.

Figure 2.23 shows the surface structure of alginate and collagen hydrogels. A key feature of the alginate hydrogels were the fin-like, porous structures and for collagen, fibrils were evident in the images. Figure 2.23 showed representative samples of the blended alginate-collagen hydrogels. From the images, the change in the surface structure of the alginate was evident. The ordered fin-like structure became more disordered with larger pores due to the presence of the collagen. However, it should be noted that a critical step in hydrogel characterisation by SEM is the required sample preparation using drying or freezing of the material. [224]. This made it difficult to measure features such as pore size, as the hydrogels were not in their swelled state.

Collagen fibrils were identified at all three composite concentrations imaged (Figure 2.24). These resembled SEM images of composite alginate-collagen hydrogels published by Baniasadi and Minary-Jolanden [221] (Figure 2.24 D and E), and suggested that collagen

fibrils were able to form in the presence of alginate at all concentrations. This finding, combined with the rheological data previously presented, suggested that collagen fibrils were able to form in the blended hydrogel system, which is vital for ensuring encapsulated cells are able to adhere.

### 2.3.10 Fourier-Transform Infrared Spectroscopy

FTIR is a technique used to measure the absorption or emission of electromagnetic waves in the infrared region from a sample. Radiation in this region is absorbed by interatomic bonds in compounds at varying frequencies and intensities. FTIR collects absorption information from samples and this data can be correlated with atomic bonds within the compound [225]. This technique is considered one of the most powerful for chemical analysis due to its speed, sensitivity, and versatility [225]. Figure 2.25 shows the absorbance spectra for a range of concentrations of alginate and collagen hydrogels (Table 2.3). Increasing the concentration of the gel caused an increase in absorbance, as expected. The alginate peaks were found to be more intense than for collagen, likely due to the higher alginate concentrations used. Identified peaks are marked on the spectra, the most important of which are discussed further below.

The peak at 3312 $cm^{-1}$ (Figure 2.25A) represents the stretching of the O-H bonds present throughout alginate polymer chains, as evidenced by the presence of a smooth, broad peak in the region of 3000-3600 $cm^{-1}$. The appearance of a peak at this wavenumber may also be due to the presence of some remaining water molecules after the freeze-drying process. A similar peak at 3305 $cm^{-1}$ was identified in the collagen-only spectra (Figure 2.25B), this is also due to the presence of O-H bond stretching. The peaks identified at 2976 $cm^{-1}$ and 2934 $cm^{-1}$ (Figure 2.25A and B respectively), correspond to -$CH_2$ stretching. As the concentration of the alginate gels analysed were higher than that of the collagen gels, the

Table 2.3: Control hydrogel concentrations examined by FTIR

| **Alginate (mg/mL)** | **Collagen (mg/mL)** |
|---|---|
| 5 | 0 |
| 7·5 | 0 |
| 10 | 0 |
| 20 | 0 |
| 30 | 0 |
| 40 | 0 |
| 0 | 2.5 |
| 0 | 3 |
| 0 | 5 |

Table 2.4: Blended hydrogel concentrations examined by FTIR

| **Alginate (mg/mL)** | **Collagen (mg/mL)** |
|---|---|
| 5 | 1.5 |
| 7·5 | 1.5 |
| 10 | 1.5 |
| 5 | 2.5 |
| 7·5 | 2.5 |
| 10 | 2.5 |

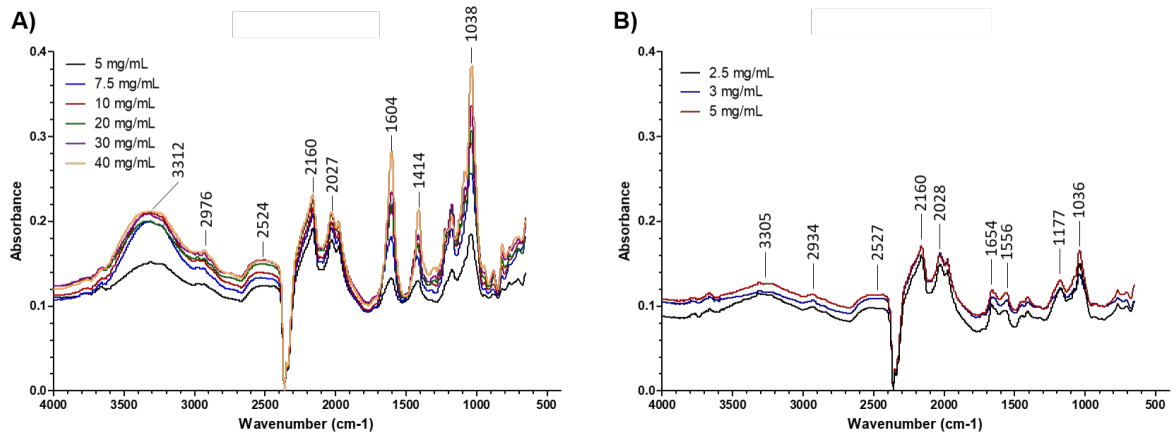


Figure 2.25: FTIR spectra of (A) alginate and (B) collagen hydrogels at a range of concentrations. Hydrogels were freeze-dried prior to analysis.

absorbance was higher for the alginate spectra (Figure 2.25A).

For alginate (Figure 2.25A), peaks at 1604 $cm^{-1}$ and 1414 $cm^{-1}$ are attributed to asymmetric and symmetric stretching vibrations, respectively, of carboxylate salt groups (COONa) [226, 227]. Additionally, several vibrations in the range 1100–1000 $cm^{-1}$ are assigned to the glycoside bonds in the polysaccharide (C-O-C stretching) [226].

For the collagen spectrum (Figure 2.25B), absorption bands at 1654 and 1556 represent amides I and II respectively [228]. The amide I band results from the stretching vibration of the peptide carbonyl group (–C=O) [229]). Both the collagen and alginate spectra align with those previously reported in the literature, with bands showing up in expected regions [226–229].

Spectra were also collected for blended collagen-alginate hydrogels at different concentrations (Figure 2.26, Table 2.4). The peaks identified in these two studies align strongly with the alginate control spectrum, due to the concentration of alginate being much higher than that of collagen in the composite system and therefore dominating the spectra. This

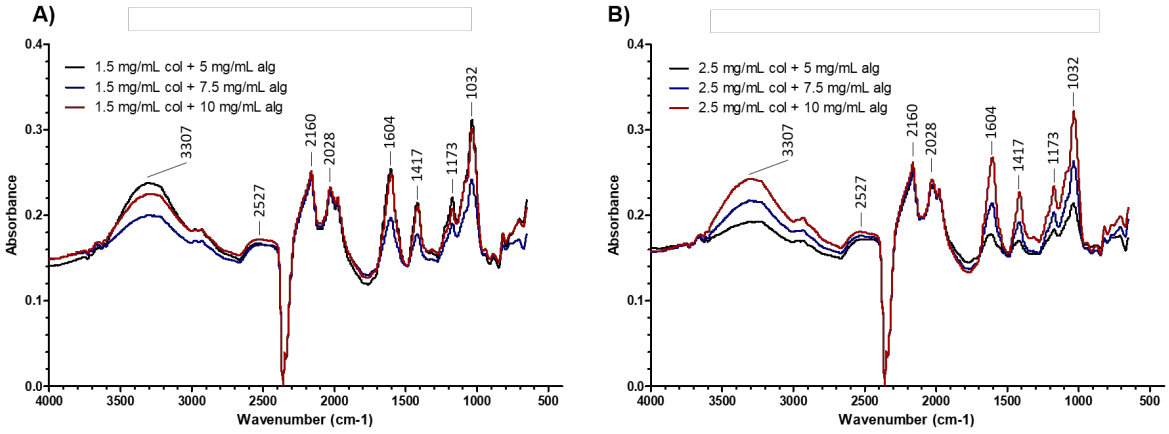


Figure 2.26: FTIR spectra of blended alginate-collagen hydrogels at a range of concentrations. A) Collagen concentration of 1.5 mg/mL and B) collagen concentration of 2.5 mg/mL. Hydrogels were freeze-dried prior to analysis.

makes it challenging to confirm the presence of collagen in the blended hydrogel system using FTIR. However, previous analysis using SEM and rheology has demonstrated the presence of collagen in the blended hydrogels. Finally, it should be noted that the peaks at 2160 $cm^{-1}$ and 2028 $cm^{-1}$ that show up in all spectra (Figures 2.25 and 2.26) are attributed to the presence of carbon dioxide, which is reported to produce peaks in the region of 900–2300 $cm^{-1}$ [230, 231]. This is likely appearing due to contamination of the sample upon loading into the FTIR instrument.

## 2.4 Summary

In this chapter, porcine oral mucosa has been histologically examined, and the mechanical properties of the tissue under compression have been determined. Further to this, the mechanical properties of alginate and collagen hydrogel systems were measured and compared with the porcine tissue. Through these experiments, the mechanical properties of the com-

posite hydrogel system were found to align with the mechanical properties of porcine tissue. The chosen blended concentrations taken forward for biological characterisation were 2.5 mg/mL collagen and 5 mg/mL alginate, and 2.5 mg/mL collagen and 10 mg/mL alginate. As well as generating mechanical data for the model, the hydrogels have been physically characterised using rheology, scanning electron microscopy, and Fourier-transform infrared spectroscopy in order to understand the gelling characteristics of the model. Therefore, this chapter has demonstrated that the first objective of this research has been met, through selection of an appropriate gel system and characterisation of gelling properties and chemical composition. The latter part of this objective, determining the selected scaffold's ability to support cell growth and proliferation, will be examined in Chapter 3. In this next chapter, the effect of the chosen hydrogel system on fibroblasts and epithelial cells was determined.

### 2.4.1 Conclusion

Blended collagen and alginate solutions are a suitable choice of hydrogel scaffold for *in vitro* oral mucosa models when considering their mechanical properties under compression, which align well with those of porcine oral mucosa. Mucosa models in the literature have not previously considered the mechanical properties of the native tissue in their development, which is a unique aspect to the model developed in this research.

# Chapter Three

# Biology of oral mucosa model

Thus far, the mechanical properties of porcine oral mucosa under compression have been determined. By comparing the mechanical strength of the native tissue with those of alginate and collagen hydrogel systems, concentrations of the blended hydrogel scaffold were selected to be 2.5 mg/mL collagen and 5 mg/mL alginate, and 2.5 mg/mL collagen and 10 mg/mL alginate (concluded from Chapter 2). In this next chapter, the latter part of the first objective will be addressed: "Characterise the chosen hydrogel system in terms of its ability to support cell growth and proliferation." Primary fibroblasts and an epithelial cell line were characterised in 2D. Subsequently, the effect of the chosen blended hydrogel concentrations on the encapsulated and epithelial cells was examined using live/dead staining and cell counting assays. Finally, studies were conducted using histological staining to determine whether a stratified epithelium could be achieved, and the results of this work are presented here.

## 3.1 Introduction

There are two commonly used approaches to generate a 3D oral mucosa model that have been described in the literature, the first of which is the use of decellularised matrix [118]. The main goal of this approach is to remove the cells from a tissue sample and preserve the extracellular matrix (ECM) components such as collagen, glycosaminoglycans, laminin, and growth factors [232]. Various decellularising agents can be used, for example alkaline compounds, acids, alcohols, detergents, and enzymes [232, 233]. A key advantage of this method is that the tissue model contains functional vasculature and as a result, decellularised matrix scaffolds can improve cellular functions compared with cells seeded onto hydrogels [232, 233]. However, there are still several challenges associated with using these types of models, including variations caused by different decellularisation methods, insufficient preservation of vasculature and ECM composition, inhomogeneous recellularisation within the scaffold, and diffusion limitations for thicker tissue sections [234]. A second and more common approach is to use a polymer scaffold to create a 3D culture *in vitro*. For this, fibroblasts are typically encapsulated within a substrate and oral keratinocytes are seeded on the surface to generate a stratified epithelium. The most commonly used scaffold material is type I collagen due to its ease of extraction and manipulation, reproducibility, and high growth of epithelial cells on its surface [235].

A range of fibroblast types have been used in 3D oral mucosa models prepared using a scaffold, including both primary cells and cell lines. Normal oral keratinocytes derived from human tissue are the most commonly reported cells used in 3D oral mucosa models [195]. Cell lines have also been used, the most frequently reported of which are 3T3s (mouse embryo fibroblast cell line) [236–238]. Using primary fibroblasts derived from human tissue has its disadvantages, as the cells typically have a finite lifespan and limited expansion capacity, which can make it especially challenging to obtain the number of cells required

for 3D culture [4]. However, primary cells have normal cell morphology and maintain many of the important markers and functions seen *in vivo*, which make them ideal for studying disease, infection, and wound healing around dental implants. In the present study, primary dermal fibroblasts were used to develop the protocols for a blended alginate-collagen oral mucosa model. Whilst these cells differ slightly from oral fibroblasts in terms of phenotype [239, 240], they also display many important similarities. Since human dermal fibroblasts were easier to obtain and considerably cheaper than oral fibroblasts, for the preliminary development of this model, dermal fibroblasts were deemed a useful way to ensure fibroblast attachment and proliferation was possible with the proposed scaffold.

For the keratinocytes that form the epithelium, again, there are a range of primary cells and cell lines that have been utilised in the literature for studying the response of the oral epithelium to various challenges [235, 241]. Some of the most commonly used epithelial cell lines for 3D mucosa models include TR146 (oral squamous cell carcinoma cell line) [110, 242–244], OKF6/TERT-2 (normal oral epithelial cell line, immortalised by forced expression of telomerase) [195, 236, 245], and HaCaT (immortalised keratinocyte cell line) [104, 235, 244, 246]. Whilst cell lines often display differences both genetically and phenotypically from their tissue origin and show altered morphology, the advantages of using an epithelial cell line are that they are highly proliferative and easier to culture than their primary counterparts. For this reason, the cell line H400 (oral squamous cell carcinoma cell line) was chosen to seed on the surface of the model and form the epithelium. H400s have been used by many researchers within the institution and have been previously shown to form a stratified epithelium on collagen scaffolds [247]. The stratified epithelium is an important feature to replicate in the present *in vitro* model because the epithelium has a barrier function and is essential in preventing infection. One future application of the *in vitro* hydrogel model would be to utilise it in the investigation of interactions between oral biofilms, the epithelium, and dental implant materials. Therefore, aligning the model

with the physical features of the native tissue, including the stratified epithelium, is highly desired.

Cell culture conditions such as growth medium, supplements, cell seeding density, submerged versus air-lift set-up, cell type and origin, mono – or multi-species culture, 2D or 3D culture, and choice of scaffold for 3D culture, distinctly influence the properties of an *in vitro* model of the oral mucosa [241]. Features of the oral mucosa that need to be replicated in an *in vitro* model include a stratified epithelium and encapsulated fibroblasts within the scaffold. These aspects are examined in this chapter, and the results of the chosen culture conditions for the oral mucosa model developed in the present work are described.

## 3.2 Materials and Methods

All chemicals were from Sigma Aldrich (Dorset, UK) unless otherwise specified.

### 3.2.1 Cell culture

All tissue culture experiments were conducted in a Type II laminar air flow hood (Guardian MSC T1200, Monmouth Scientific Ltd, Somerset, UK). Sterilisation of flow hoods was conducted using 5% ChemGene, reverse osmosis (RO) water, and 70% industrial methylated spirit (IMS). Additional equipment was sterilised by autoclaving at 121°C, 100kPa, for 1 hour (MLS-3781L, Sanyo, Japan) or by using a 0.22 $\mu$M filter (Millipore, US). All cells were incubated at 37°C in an atmosphere of 5% $CO_2$ and 95% humidity.

All cell culture media was made up 500 mL at a time, stored at 4°C and used for up to one month. The composition of supplemented Dulbecco's Modified Eagle's Medium (DMEM) and Iscove's Modified Dulbecco's Medium (IMDM) are outlined in Tables 3.1 and

Table 3.1: DMEM supplemented media components for 500 mL media

| **Component** | **Volume** | **Final concentration** |
|---|---|---|
| DMEM | 395 mL | 79% |
| FCS | 50 mL | 10% |
| Pen/Strep | 5 mL | 1% |

Table 3.2: IMDM supplemented media components for 500 mL media

| **Component** | **Volume** | **Final concentration** |
|---|---|---|
| IMDM | 395 mL | 79% |
| FCS | 50 mL | 10% |
| Pen/Strep | 5 mL | 1% |

3.2 respectively.

### Passaging, counting and storage of cells

The H400 cell line is an immortalised keratinocyte cell line established from a human squamous cell carcinoma of the alveolar process. H400 keratinocytes were obtained from frozen stocks at the institution and were cultured in supplemented DMEM (Table 3.1). Human dermal fibroblasts (HDFs) were purchased from ATCC (strain number CCD-1135Sk, ATCC, CRL-2691) and were cultured in supplemented IMDM (Table 3.2). Growth media was changed every 2-3 days.

When cells reached approximately 80% confluence, based upon microscopic observation at 10X magnification (Zeiss Axiocam erc 5s, Carl Zeiss Microscopy Ltd, Cambridge, UK), they were transferred into a new T75 $cm^2$ cell culture flask (Nunc$^{TM}$, Thermo Fisher

Scientific, Loughborough, UK) with lower cell numbers to enable cell proliferation to continue. For this, the cell culture medium was removed and cells washed with 10 mL of non-supplemented media to remove any remaining serum proteins from fetal calf serum (FCS) in the residual cell culture medium. Cells were incubated at 37°C with 4 mL 0.25% w/v trypsin-EDTA for 10 minutes or until all cells had detached. The trypsin-EDTA was neutralised using 4 mL supplemented cell culture medium containing 10% FCS. Following this, cells were transferred to a 15 mL Falcon tube and centrifuged at 800 revolutions per minute (rpm) for 4 minutes using a bench top centrifuge (Durafuge 100, Precision, Expotech, USA). The supernatant was then aspirated and discarded in bleach, and the cellular pellet was re-suspended in the desired volume of cell culture medium. Cell counts were performed on cell suspensions prior to seeding. The cell suspension was added in a 5:1 ratio with 0.4% trypan blue. Using trypan blue allowed for differentiation between live and dead cells under the microscope, whereby dead cells appeared blue. This is because trypan blue enters cells with compromised membranes and, upon entry into the cell, binds to intracellular proteins. Cell counts were performed using an improved Neubauer haemocytometer (Sigma-Aldrich, UK) and a light microscope at 10X magnification (Zeiss Axiocam erc 5s, Carl Zeiss Microscopy Ltd, Cambridge, UK). At least three 1 $mm^2$ squares were counted and their average taken. Cell number was calculated as follows:

$$\begin{aligned} viable\ cell\ yield\ (cells/mL) = & \frac{viable\ cell\ count}{quadrants\ counted} \times\ dilution\ factor \\ & \times\ haemocytometer\ factor\ (10,000) \\ & \times\ current\ volume\ (mL) \end{aligned} \tag{3.1}$$

e.g average cell count of 100 with no dilution = 1 million cells per mL

**Freezing cells for cryopreservation**

For cryopreservation, cells were treated as for passaging. However, rather than re-suspending the pellet in cell culture media, cells were re-suspended into cryopreservation media (70% IMDM or DMEM, 25% FCS, and 5% dimethyl sulfoxide (DMSO) (v/v)). The pellet was re-suspended to give a concentration of 1 million cells per mL of cryopreservation medium. Following this, 1 mL of the cell suspension was pipetted into each cryovial and cryovials were placed in a -80°C freezer overnight, before being transferred to a liquid nitrogen dewar at -196°C.

**Thawing cells**

Cryovials were removed from liquid nitrogen using appropriate safety precautions and the cells were quickly thawed (2-3 minutes) in a 37°C water bath. Once thawed, the cell solution was diluted in cell culture medium and centrifuged for 5 minutes at 1000 rpm at room temperature. The supernatant was discarded and the cellular pellet re-suspended in the appropriate cell culture medium, and transferred to a T75 culture flask (Nunc, Thermofisher Scientific).

### 3.2.2 Preparation of stock solutions

Stock solutions of alginate and collagen were prepared as described previously in Chapter 2, Section 2.2.2. Briefly, alginate stock solutions of 20, 30, and 40 mg/mL were prepared by adding sodium alginate to 100 mL 2-(N-morpholino)ethanesulfonic acid (MES) buffer (0.1 M, pH 6.5). Alginate was left to dissolve overnight at room temperature (25°C) on a magnetic stirrer at 100 rpm. Solutions were autoclaved at 120°C prior to use in tissue culture. To prepare the cross-linking solutions, calcium chloride $CaCl_2$ was added to 100

mL reverse osmosis (RO) water at a concentration of 150 mM. Following this, 1 mL of 4-(2 hydroxyelthyl)-1 piperazineethanesulfonic-acid (HEPES) buffer was added to each $CaCl_2$ solution. All $CaCl_2$ solutions were autoclaved at 120°C prior to use in tissue culture. Alginate stock solutions were stored at 4°C and $CaCl_2$ solutions were stored at room temperature (25°C).

To make the collagen stock solutions, 3.5 mg/mL and 10 mg/mL rat tail collagen I (Corning) were diluted on ice to concentrations of 3 and 5 mg/mL respectively with IMDM supplemented with 10% FBS. Solutions were kept at 4°C to prevent early gelation.

### 3.2.3 Formation of blended collagen-alginate tissue model

To make up the composite hydrogel, alginate and collagen stock solutions were mixed in a 1:1 ratio on ice (Figure 3.1A). Human dermal fibroblasts were added to the solution at a concentration of 4.5 x $10^5$ cells per well. To achieve this, trypsin was added to the confluent fibroblast cultures for 10 minutes to detach cells from the culture flasks. Cells were centrifuged at 900 rpm for 4 minutes, and the supernatant was removed. The cell pellets were re suspended in 1 mL IMDM media and cells counted using a haemocytometer. The solutions were diluted accordingly to achieve a concentration of 2.7 x $10^6$ cells/mL. Finally, 0.5 mL of cell solution for every gel to be produced was added to the stock alginate-collagen solution and gently inverted to mix (Figure 3.1B). The fibroblast-containing solution was pipetted into each well of a 6-well transwell culture plate (1 mL per well) and incubated at 37°C for 4 hours to allow the collagen to gel (Figure 3.1C).

Once the collagen had gelled to ensure collagen fibrils had formed, 2 mL of 150 mM $CaCl_2$ solution was added to the outside of each transwell insert (Figure 3.1D). The transwell plate was incubated at 37°C for a further 20 minutes to allow the alginate to gel. Following

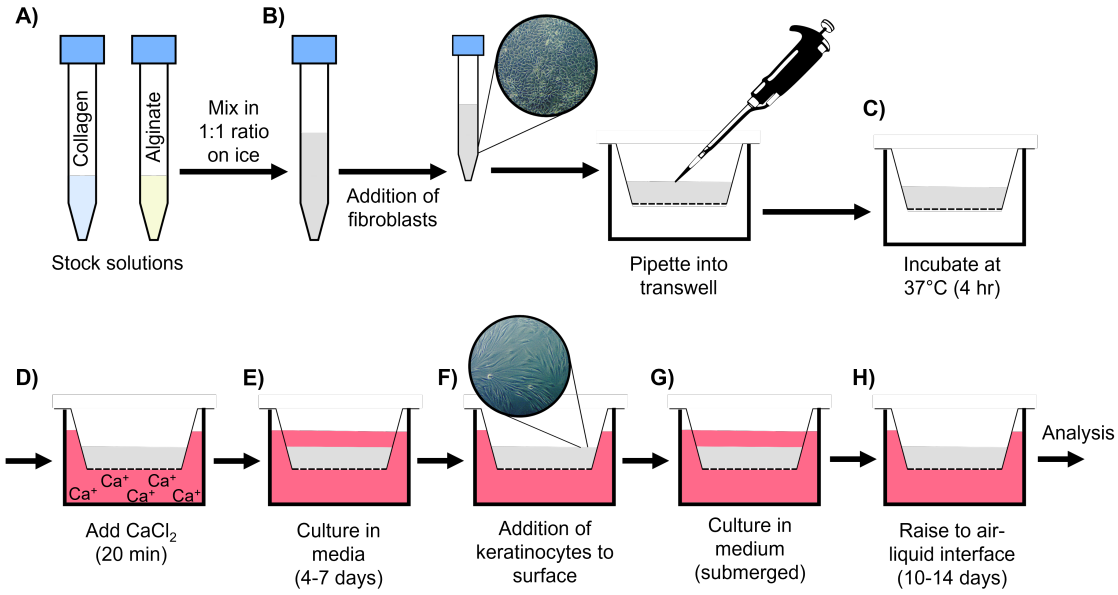


Figure 3.1: Schematic showing method for producing blended hydrogel model containing human dermal fibroblasts and with addition of epithelial cells to surface. (A) Alginate stock solutions of 20, 30, and 40 mg/mL and collagen solutions of 3 and 5 mg/mL were mixed in a 1:1 ratio on ice. (B) For gels with cells encapsulated, primary human dermal fibroblasts were added at a concentration of 4.5 x $10^5$ cells/well and pipetted into 6-well transwell culture plates (12 mm internal diameter). (C) The gels were incubated at 37°C for 4 hours. (D) 2 mL of 150 mM calcium chloride solution was added to the outside of insert and the gels were incubated for a further 20 minutes. (E) The gels were cultured submersed in IMDM supplemented with 10% FBS for 4-7 days until gels had contracted. (F) A human keratinocyte cell line (H400) was added to the surface of the gels at a concentration of 1 x $10^6$ cells/well. (G) Gels were cultured submersed in DMEM medium for 2-3 days to allow the keratinocytes to form a monolayer on the surface of the gel. (H) The media inside the transwell insert was removed to create an air-liquid interface at the surface of the hydrogel. The oral mucosa models were cultured for 10-14 days to allow the epithelium to stratify, before being removed for analysis.

removal of the $CaCl_2$ solution, the outside of the gels was washed with IMDM media. The gel was cultured in IMDM supplemented with 10% FCS for 4-7 days, with media changes every 2-3 days, until the gel had slightly contracted, indicating fibroblast adherence (Figure 3.1E).

To form the epithelial layer, H400s were detached from the base of their culture flask using trypsin. After 5 minutes (or until visible cell detachment), cells were centrifuged at 1000 rpm for 4 minutes, and the supernatant was removed. H400s were resuspended in 1 mL of supplemented culture medium. Using a haemocytometer, the number of cells per mL were determined. The solution was diluted to a concentration of 2 x $10^7$ cells/mL and 50 µL was pipetted onto the surface of each gel (Figure 3.1F). The plate was incubated for 1 hour to allow cell attachment and then 1 mL of supplemented DMEM was added above the surface of the gel. Gels were cultured submersed in DMEM medium for 2-3 days to allow the keratinocytes to form a monolayer on the surface (Figure 3.1G). Finally, the media inside the transwell insert was removed to create an air-liquid interface at the surface of the hydrogel. The oral mucosa models were cultured for 10-14 days to allow the epithelium to stratify, changing the medium every 2-3 days (Figure 3.1H). Hydrogels were removed from the transwell using a scalpel to cut around the edge of the membrane. Figure 3.2 shows a blended hydrogel removed for subsequent analysis using live/dead staining and confocal microscopy.

### 3.2.4 Confocal microscopy

Once the 3D blended hydrogel model had been cultured to completion, the media was removed from the transwell. The gels were washed several times with PBS to remove any remaining media components and stop any residual esterase activity. The gels were then stained using a Cellstain double staining kit containing Calcein-AM and propidium iodide (PI) solutions (Sigma-Aldrich). Calcein-AM stains only viable cells and the calcein generated from the solution by esterase in a viable cell emits a strong green fluorescence. However, PI cannot pass through a viable cell membrane. It reaches a cell nucleus through disordered areas of dead cell membrane and intercalates with the DNA double helix of the cell to emit

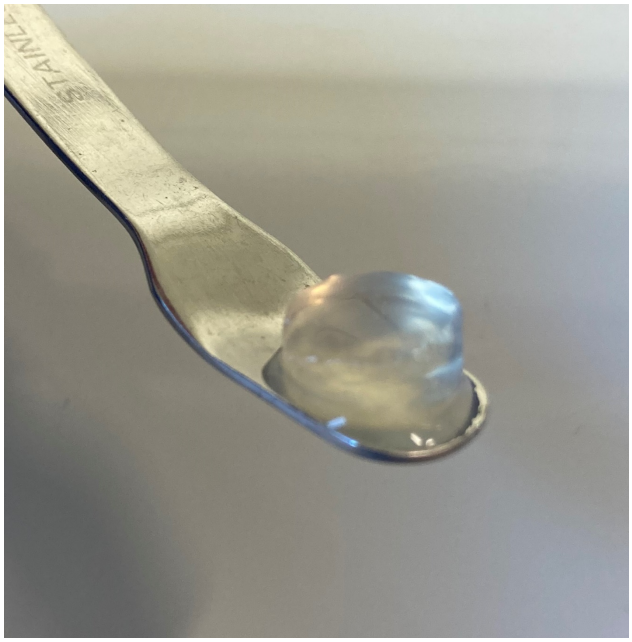

Figure 3.2: Image of a blended hydrogel model removed from a transwell plate before analysis using either confocal microscopy or fixation, sectioning and histological staining.

red fluorescence. The staining kit was stored at -20°C. Prior to making up the staining solution, the stains were removed from storage and allowed to reach room temperature.

To prepare the staining solution, 10 $\mu$L of Calcein-AM solution and 5 $\mu$L of PI solution were added to 5 mL of phosphate-buffered saline (PBS). After removing the hydrogels from the transwell insert using a scalpel, they were placed in a clean 6-well plate. Following this, 2 mL of the prepared staining solution was added to each well and the gels were incubated for 30 minutes at 37°C, to allow the staining solution to penetrate the gel. The stain was removed and the gels were placed in a 24-well black culture plate (Nunc, Thermofisher Scientific). These plates have a thinner base so are preferable for confocal imaging. Confocal imaging of the samples was performed using a confocal laser scanning microscope (Zeiss, Cambridge, UK), using a 5X lens (EC Plan - Neofluar 5X/0.16 Ph1 M27). 2D images and z-stacks were taken of each sample, with a gap of 10 $\mu$m between each slice of a z-stack.

### 3.2.5 Histology

To prepare the tissue model for histological staining, the hydrogels were placed (within their transwell) in 4% formal saline made up of 100 mL of 40% formaldehyde, 9 g of sodium chloride, and 900 mL of RO water. Samples were left at room temperature in the formal saline overnight to fix the samples. Following this, each sample was removed from the transwell by cutting the transwell membrane using a scalpel. Next, the fixed hydrogels were dehydrated using increasing concentrations of ethanol: concentrations were added for 10 minutes each as follows, 10, 20, 30, 40, 50, 60, 70, 80 and 90%. The hydrogels were then placed in 100% ethanol three times for 10 minutes each before drying off thoroughly and submerging in xylene for 10 minutes, twice. The hydrogels were dried off once again, carefully put into labelled histology cassettes, then embedded in paraffin wax overnight.

Glass slides were subbed with poly-L-lysine. To do this, a drop of 0.1% (w/v) poly-L-lysine solution was added to each glass slide and a thin layer spread across the surface. Slides were left to dry at room temperature for 30-40 minutes, and then baked in the oven at 56°C for 1 hour. Subbing glass slides helped the extracellular matrix adhere to the slide better when preparing for staining.

After paraffin embedding, samples were sectioned to 10 $\mu$m thick using a Leica Rotary Microtome (RM2035, Leica Biosystems, Milton Keynes, UK) and mounted onto the subbed glass slides. Haematoxylin and Eosin (H & E) staining was performed on the fixed and sectioned hydrogel samples according to a standard protocol. Samples were de-waxed in xylene for 5 minutes under agitation, then re-hydrated by placing in decreasing concentrations of ethanol (100% x2, 95%, 70%, and 50%) for 1 minute under agitation at each concentration. Samples were then washed well under running water for a minimum of 2 minutes. Gill's III Haematoxylin was applied for 5 minutes, then samples were rinsed in tap water and differentiated with 0.3% acetic acid for 30 seconds and treated with 0.3%

hydrochloric acid in 70% ethanol for 30 seconds. Following this, samples were washed in tap water, treated with Scott's Tap Water Substitute for 2 minutes and washed again. Eosin stain was applied for 1-2 minutes before the final washing step was performed. Sections were dehydrated by treating in 100% ethanol for 1 minute and then treated with xylene for 1 minute (x2). Finally, the sections were mounted under a glass coverslip using Distyrene Plasticizer Xylene (DPX) ready for visualisation under a light microscope. The slides were imaged using a Zeiss Primotech light microscope using either a 5X objective (Zeiss Epiplan 442020-9902, 5X/0.13) or a 20X objective (Zeiss Epiplan 442020-9902, 20X/0.4).

## 3.3 Results and Discussion

### 3.3.1 Epithelial cell characterisation

The oral epithelial cell line H400 was selected for use in the 3D tissue model. First, the characteristics of normal 2D H400 growth were investigated. Light microscopy was used to assess the morphology and growth characteristics of H400 cells. Cells were cultured according to the methods detailed in Section 3.2.1. For this experiment, H400s were seeded at a density of 4 x $10^4$ cells per well in a 6-well plate, in triplicate. Cells were imaged and counted at 1, 2, 3, 6, 7 and 10 days.

Figure 3.3 shows light microscopy images of H400 cells grown over a 10-day period. Key features of the growth characteristics of this cell line can be seen in the images, including a regular cobblestone appearance, outward growth from cell islands, tight cell-cell junctions, and a cuboidal shape once confluence was reached.

Light microscopy in conjunction with a trypan blue assay was used to count the number of live H400s over 10-days, along with determining cell viability, according to the

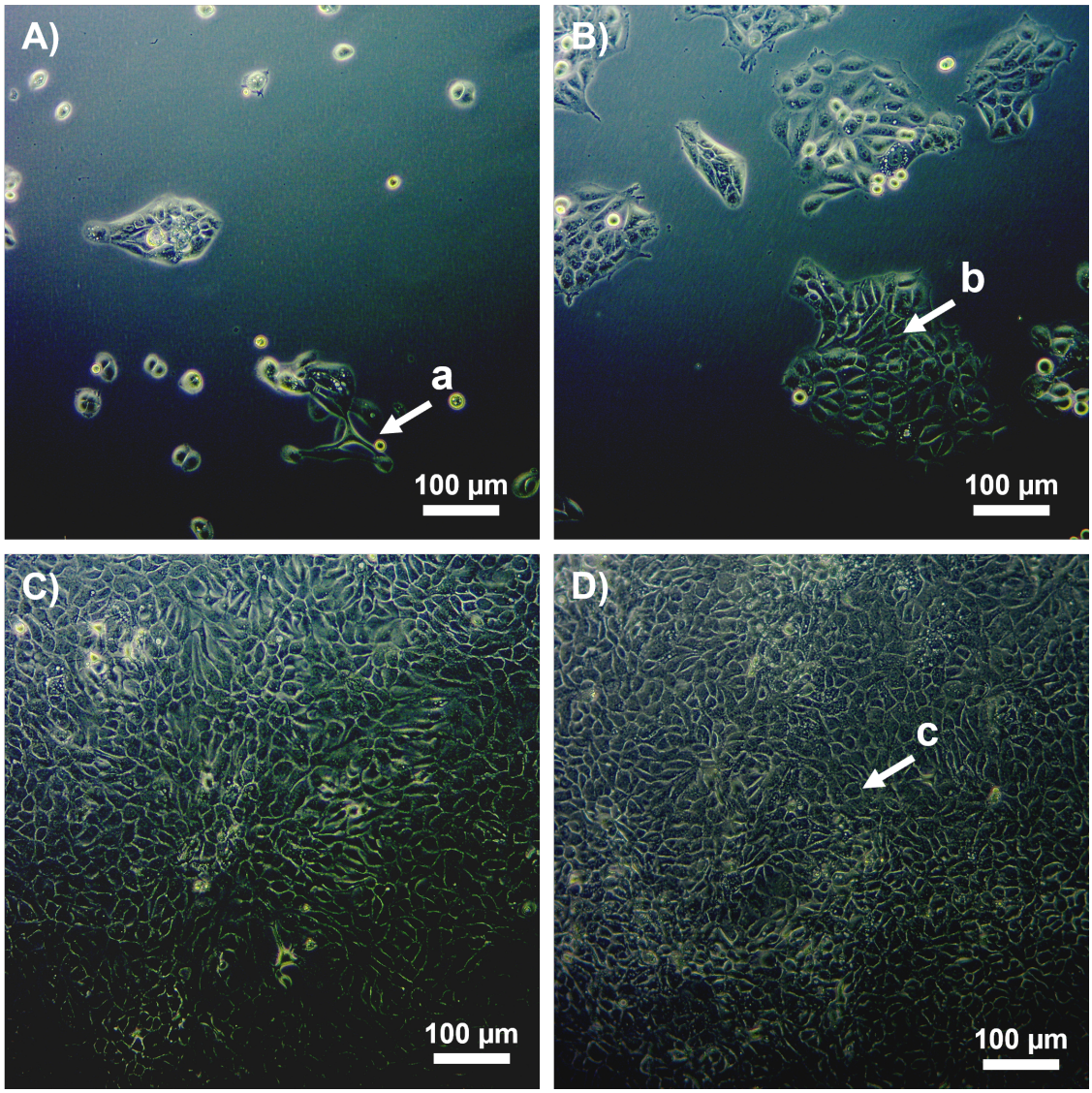


Figure 3.3: Light microscopy images illustrating H400 cell growth from 1 to 10 days post-seeding (10X magnification). (A) 1-day post seeding, (B) 3-days post-seeding, (C) 6-days post-seeding, and (D) 10-days post-seeding. This figure is representative of the typical pattern of H400 cell growth, including features such as (a) outward growth from cell islands, (b) tight cell-cell junctions, (c) a cuboidal shape once confluence was reached, and formation of a confluent monolayer. Cells became compressed and appeared smaller once they achieved confluence at Day 6.

methods described in Section 3.2.1. Figure 3.4 demonstrates exponential growth of H400 cells and a viability of greater than 80% was achieved throughout the duration of the ex-

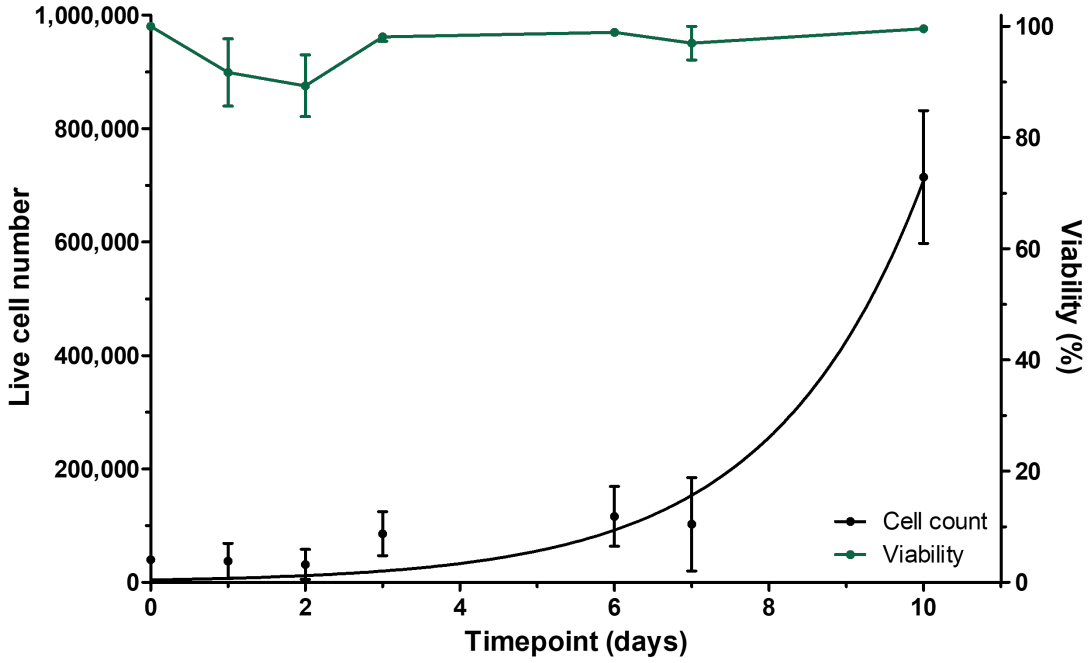


Figure 3.4: Live cell count and viability of H400 cells using a haemocytometer showing an exponential pattern of growth (n = 3, mean and SD shown). An exponential growth curve was applied to the live cell count, $R^2 = 0.9273$.

periment. It should be noted that the trypan blue method may underestimate the number of cells in a well as not all cells are detached from the surface of the 6-well plate.

Figure 3.3 confirmed that H400 cells had an epithelial appearance, and Figure 3.4 demonstrated consistent and reliable growth under the conditions applied. The growth characteristics and time for cells to reach confluence were used to determine the methods and duration of future experiments in 3D culture. In the hydrogel model, fibroblasts were cultured for 4-7 days prior to seeding epithelial cells on the surface of the scaffold. Epithelial cells were then cultured for 10-14 days post-seeding (as described in Section 3.2.3) It should be noted that H400 cells are a cancer-derived cell line and findings cannot necessarily be extrapolated to predict the behaviour of primary cells. However, they do offer advantages such as reproducibility and ease of growth.

### 3.3.2 Fibroblast cell characteristics

For this model, a HDF primary cell source was chosen. Oral and dermal fibroblasts display many similar characteristics, however oral fibroblasts were much more expensive to obtain. As this work comprised of the preliminary development of the 3D tissue model, it was decided that dermal fibroblasts would suffice in order to determine growth and behaviour when encapsulated in the hydrogel model. In this section, the characteristics of normal 2D dermal fibroblast growth are presented and discussed.

Light microscopy was used to assess the morphology and growth characteristics of HDFs. Cells were cultured according to the methods detailed in Section 3.2.1. For this experiment, HDFs were seeded at a density of 1 x $10^4$ cells per well in a 6-well plate, in triplicate. Cells were imaged and counted at 1, 2, 3, 4, 7, 8, 11 and 14 days. HDFs were grown for a period of 14 days (compared with 10 days for H400s) due to the length of time they were cultured within the 3D tissue model, which was a minimum of 14 days. Figure 3.5 shows light microscopy images of HDFs grown over a 14-day period.

Light microscopy in conjunction with a trypan blue assay was used to count the number of live HDFs over 14 days, along with determining cell viability, according to the methods described in Section 3.2.1. Figure 3.6 demonstrated exponential growth of HDFs and a viability of greater than 80% was achieved throughout the duration of the experiment. Key features of the growth characteristics of these cells can be seen in the images in Figure 3.5, including a flat, elongated spindle-shape and branched cytoplasm. As with the previous results for H400s, it should be noted that the trypan blue method may underestimate the number of cells in a well as not all cells are detached from the surface of the 6-well plate.

In summary, light microscopy and cell viability studies showed consistent and repeatable growth of HDFs, which is essential for producing the hydrogel models. It is important

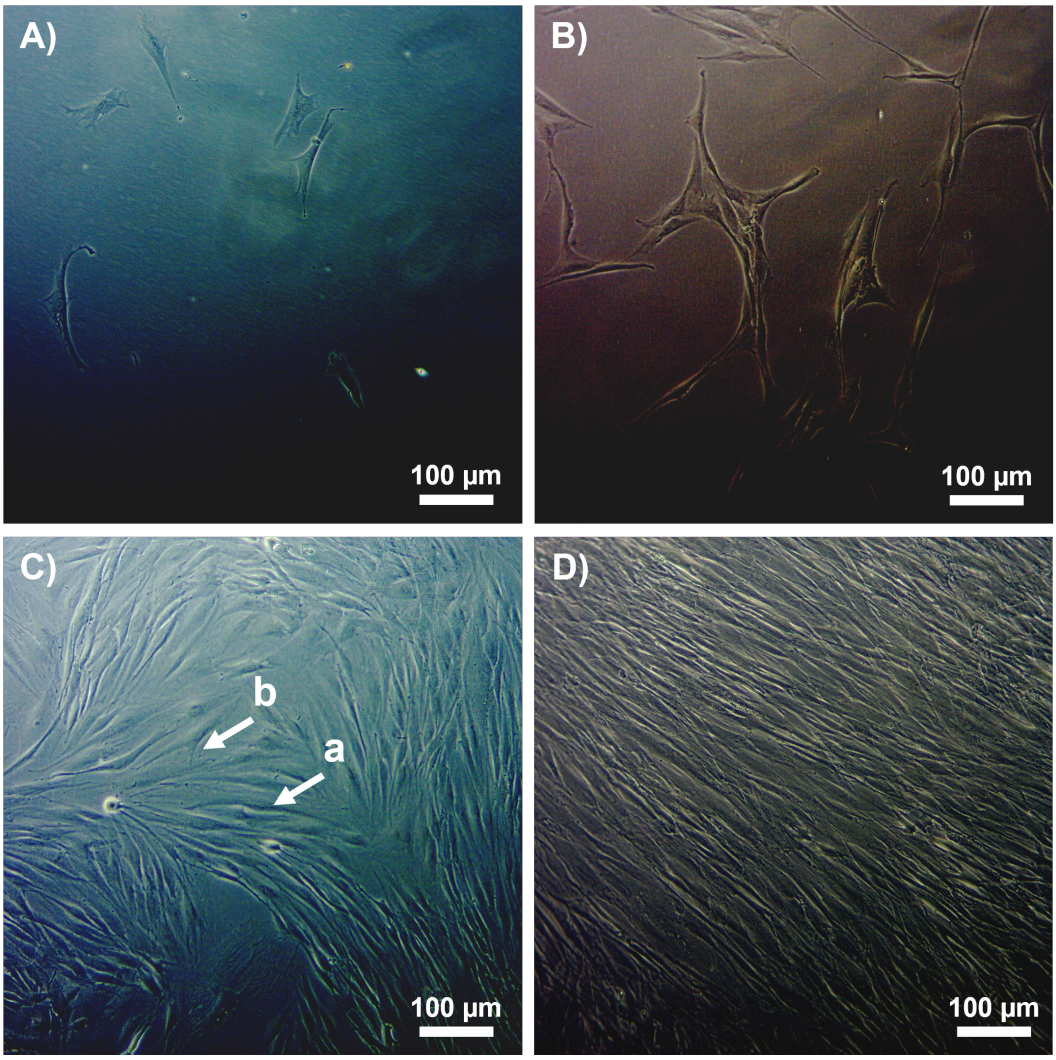


Figure 3.5: Light microscopy images illustrating HDF cell growth from 1 to 14 days post-seeding (10X magnification). (A) 1-day post-seeding, (B) 4-days post-seeding, (C) 7-days post-seeding, and (D) 14-days post-seeding. This figure is representative of the typical pattern of HDF cell growth, including features such as (a) a flat, elongated spindle-shape and (b) branched cytoplasm.

to note that the number of HDF cells produced over 10 days ($1.25 \times 10^5$) was an order of magnitude lower than the number of epithelial cells produced over the same time period ($7 \times 10^6$). Producing the required number of HDFs to create multiple 3D tissue models is challenging, particularly when using primary cells. However, the growth characteristics of both cell lines were felt to be adequate to take forward to 3D culture studies.

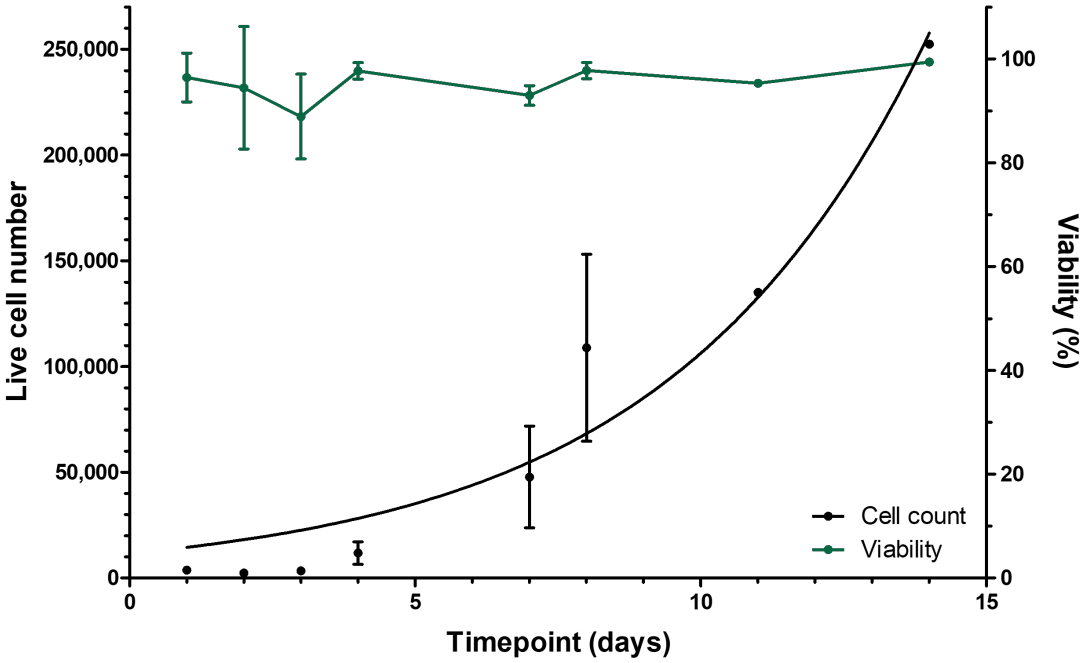


Figure 3.6: Live cell count and viability of HDFs using a haemocytometer showing an exponential pattern of growth (n = 3, mean and SD shown). An exponential growth curve was applied to the live cell count, $R^2$ = 0.9515.

### 3.3.3 Fibroblast growth with calcium chloride applied

The HDFs used in the 3D tissue model were subjected to the application of $CaCl_2$ in the protocol. In this process, the HDFs were mixed with the alginate-collagen solution, pipetted into wells, and incubated for 4 hours at 37°C, 5% $CO_2$ to allow the collagen to form fibrils. Finally, 150 mM $CaCl_2$ was added to the wells to cross-link the alginate component. To determine whether the addition of $CaCl_2$ at this concentration affects the growth of HDFs, cells were cultured as detailed in Section 3.2.1, whereby HDFs were seeded at a density of 1 x $10^4$ cells per well in a 6-well plate, in triplicate. Cells were counted and viability was determined at 1, 2, 3, 4, 7, 8, 11 and 14 days. At Day 2, 3 mL of 150 mM $CaCl_2$ was added to each well for 20 minutes, before being removed and the cells washed with sterile RO water

to remove any remaining $CaCl_2$. A growth curve was plotted and is shown in Figure 3.7.

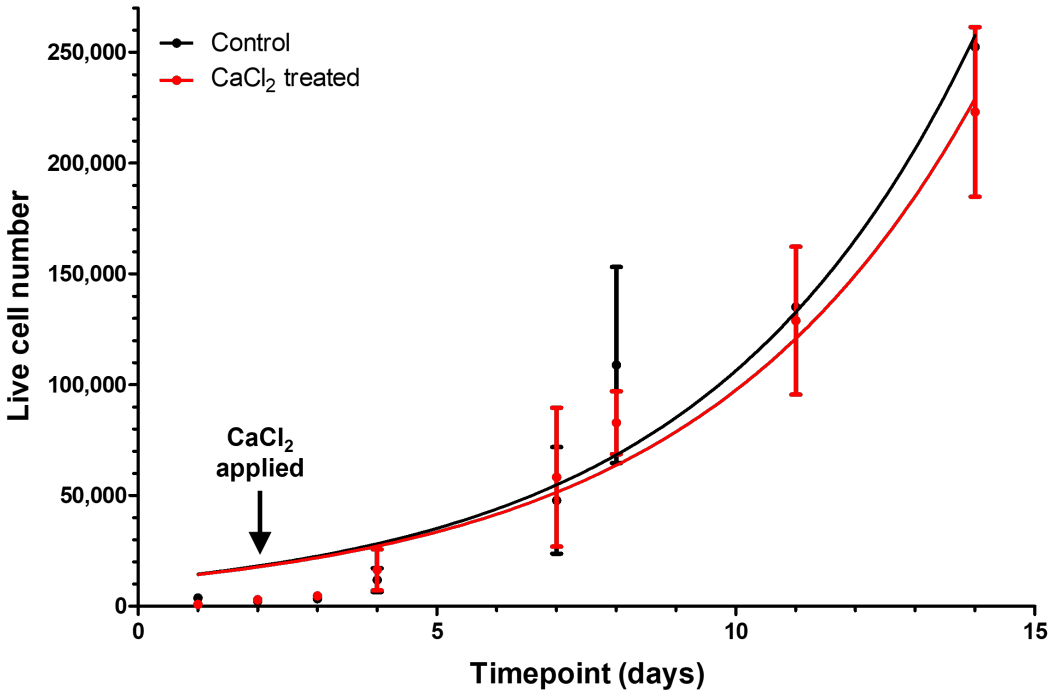


Figure 3.7: Live cell count of human dermal fibroblasts (HDFs) treated with 150 mM calcium chloride at Day 2. Both control and treated conditions demonstrated an exponential pattern of growth (n = 3, mean and SD shown). An exponential growth curve was applied to the live cell count, $R^2 = 0.9515$ for control and $R^2 = 0.9694$ for treated. The figure shows that there was a small decrease in the number of viable cells obtained when calcium chloride was applied to the HDF culture, although this was not deemed to be significant.

Figure 3.7 demonstrates that the application of 150 mM $CaCl_2$ did not significantly affect the number of live cells or the growth characteristics of HDFs. After approximately 100 hours, the exponential growth of cells treated with $CaCl_2$ slowed slightly, in comparison to the control, resulting in a mean live cell count of $2.2 \times 10^5$ for the treated HDFs, compared to a live cell count of $2.5 \times 10^5$ for the control. Whilst this provides evidence that the addition of $CaCl_2$ did not heavily impact HDF growth, viability was also calculated at each time point to confirm that the addition of $CaCl_2$ did not reduce the number of viable cells

produced. Figure 3.8 demonstrates there was little difference in the viability of the control compared with the $CaCl_2$ treated cells. For both conditions, viability remained above 80% throughout the 14-day period, and at the final time point, viability was almost 100% for both conditions. These results, in conjunction with Figure 3.7, showed that the addition of $CaCl_2$ for 20 minutes, as part of the formation of the alginate-collagen composite hydrogel model, caused a slight reduction in cell number. However, this small reduction was deemed acceptable for the 3D tissue culture experiments. Following this study, the morphology and viability of fibroblasts embedded within an alginate-collagen blended hydrogel was examined, and this is discussed in the next section.

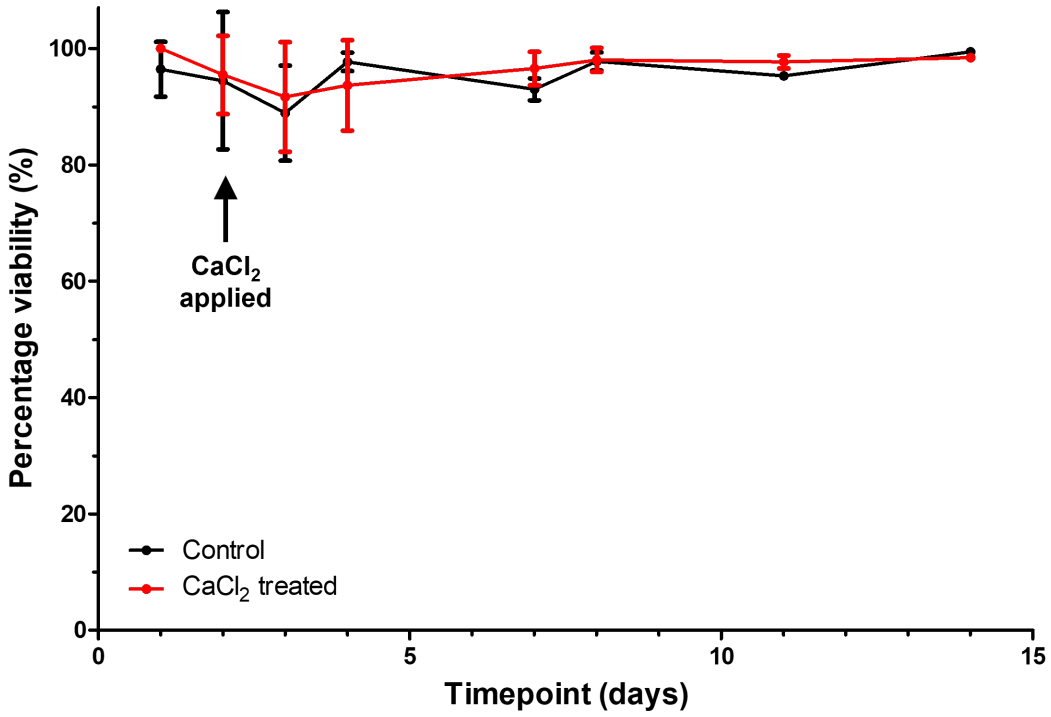


Figure 3.8: Viability of HDFs treated with 150 mM calcium chloride at Day 2. Both control and treated conditions show viability of above 80% at all time points (n = 3, mean and SD shown).

### 3.3.4 Confocal imaging of fibroblasts embedded within blended hydrogels

The blended alginate-collagen hydrogel system was produced using a similar method to that described in Chapter 2, but with the addition of HDFs and H400s. The full method is detailed in Section 3.2.3, but is briefly described here. Collagen and alginate stock solutions were mixed in a 1:1 ratio. At this point, a suspension of human dermal fibroblasts were added at a concentration of 4.5 x $10^5$ cells per well. The solutions were gently mixed and then 1 mL of the blended solution was pipetted into each transwell of a 6-well plate. Plates were incubated at 37°C for 4 hours to allow the collagen to gel. Following this, 3 mL of 150 mM $CaCl_2$ was added to the outside of the transwell plate to gel the alginate component. The $CaCl_2$ was removed after 20 minutes and RO water was used to wash the outside of the transwell. Finally, IMDM media was added to both the outside and inside of the transwell to allow the fibroblasts to adhere and proliferate inside the gel. After 4-7 days of culture, H400s were seeded on the surface of the hydrogels at a concentration of 2 x $10^7$ cells/mL (50 $\mu$L added to each gel). The hydrogels were incubated for 2 hours to allow for the epithelial cells to adhere to the surface. The gels were cultured submersed in DMEM medium for 2-3 days. Finally, the media inside the transwell insert was removed to create an air-liquid interface at the surface of the hydrogel. The oral mucosa models were cultured for 10-14 days to allow the epithelium to stratify. The models were stained using Calcein-AM and PI (live/dead) and imaged using confocal microscopy.

Figure 3.9 shows images of primary HDFs embedded within two concentrations of alginate and collagen blended hydrogel. No dead cells were identified within the model, as evidenced by the lack of red cells in the images. This suggests that primary fibroblasts remained viable in the blended hydrogel model at both high (10 mg/mL) and low (5 mg/mL) alginate concentrations. A key difference noted between the two different alginate concen-

trations in the blended system was the morphology of the fibroblasts. Figures 3.9A and B are of fibroblasts embedded within a blended hydrogel of 2.5 mg/mL collagen and 5 mg/mL alginate. At this lower alginate concentration, the HDFs displayed a morphology similar to that of the cells in 2D culture, with an elongated shape. However, Figures 3.9C and D show HDFs had a rounded morphology in a blended hydrogel of 2.5 mg/mL collagen and 10 mg/mL alginate. This suggests that the higher alginate concentration restricted the morphology of the cells. Figure 3.10A is a representative image of HDFs grown in 2D culture and stained and imaged using the same protocol as for the 3D models presented in 3.9. The morphology of the fibroblasts in 2D was as expected, and showed a flat, elongated spindle-shape similar to that seen in the light microscopy images of 2D culture presented in Figure 3·5·

Confocal imaging of fibroblasts embedded within alginate hydrogels has been previously reported [207, 248]. Hunt et al. [248] demonstrated that mouse NIH 3T3 fibroblasts remained viable in alginate hydrogels for up to 150 days. Live/dead stained fibroblasts in the study were shown to have a rounded morphology when encapsulated in 20 mg/mL alginate cross-linked with 100 mM $CaCl_2$, supporting the findings of the present work which found HDFs to have a rounded morphology at the higher alginate concentration used (10 mg/mL). Furthermore, live/dead staining of fibroblasts has also been reported in collagen-only hydrogels. Hamilton et al. [249] published confocal images of lung fibroblasts embedded in 2 mg/mL collagen I gels. High viability was reported as live fibroblasts were seen throughout the scaffold and the cells had taken on a mature spindle-like morphology after 1 week of culture, suggesting that fibroblasts adopt a typical elongated morphology when embedded within a collagen hydrogel. This is likely due to the adhesion motifs that collagen fibrils display, unlike unmodified alginate polymer chains which do not enable cells to adhere.

Cells *in vivo* interact with their surrounding microenvironment and their morphology is affected by the different mechanical and biochemical cues they encounter. Several studies

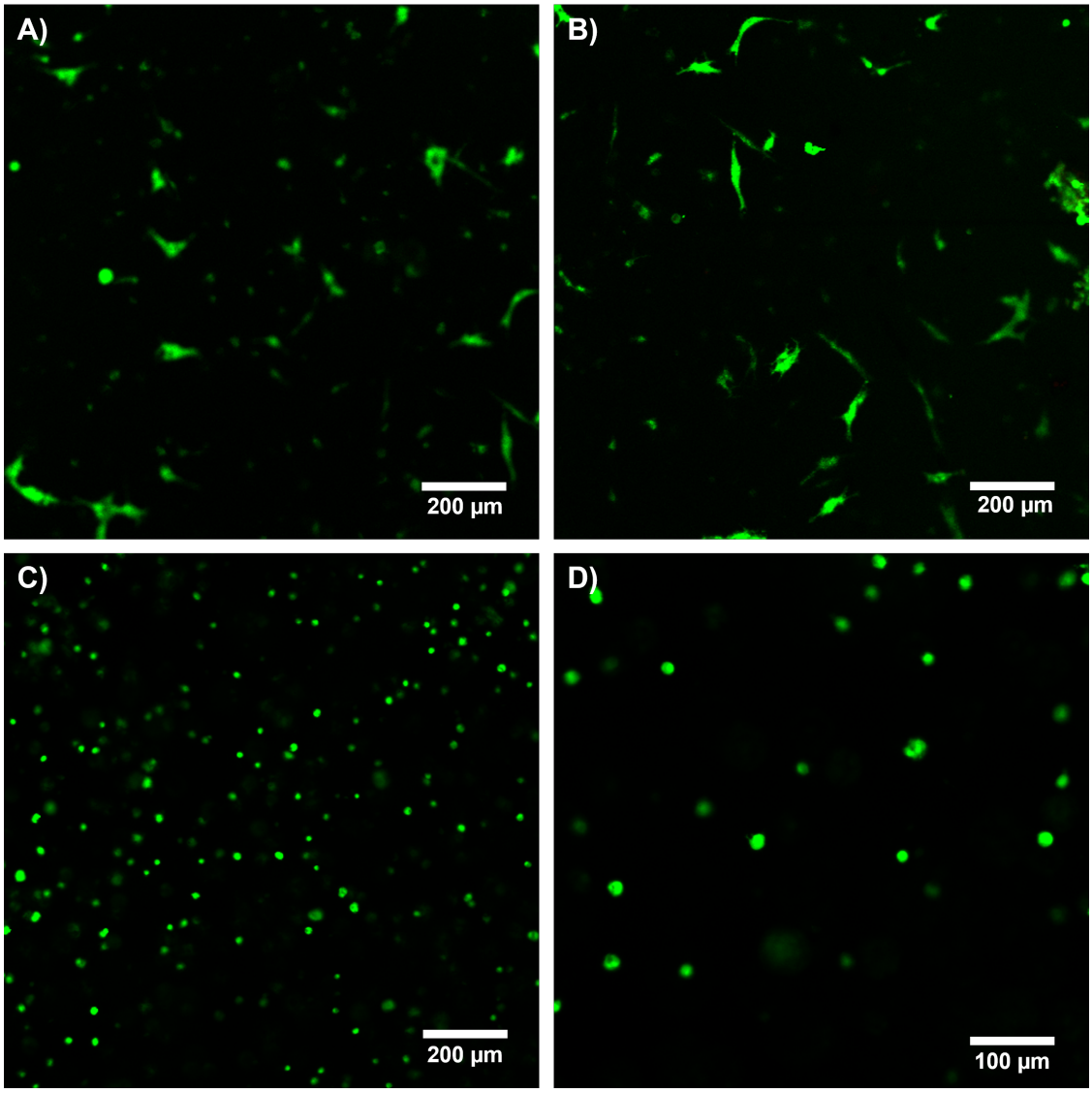


Figure 3.9: Representative images of live-dead stained human dermal fibroblasts (HDFs) embedded within collagen-alginate hydrogels at concentrations of (A and B) 2.5 mg/mL collagen and 5 mg/mL alginate, and (C and D) 2.5 mg/mL collagen and 10 mg/mL alginate. At the lower concentration of alginate, fibroblasts show typical spindle shape. At the higher concentration of alginate, fibroblasts remain rounded.

have reported that cell shape plays an important role in regulating the growth, migration and differentiation of cells [250, 251]. It is therefore important for *in vitro* models to replicate the biomechanical cues that cells receive in the body. In a recent paper, Liu et al. [207] encapsulated NIH 3T3 fibroblasts in collagen–alginate hybrid hydrogels. The paper reported

two different hydrogel systems: fibroblasts were encapsulated in 3 mg/mL collagen and then the gel was stiffened with 15 mg/mL alginate and 120 mM $CaCl_2$ on (1) Day 0 or (2) Day 2 of the culture. They reported high viability of cells after 6 days in culture in the hybrid hydrogels [207], supporting the finding of the present work that alginate-collagen blended hydrogels produced high cell viability. The study also found that the spreading state of the fibroblasts (i.e. displaying an elongated or rounded morphology) had a significant impact on their responses to mechanical and biochemical stimuli. A key factor that may have influenced the cell morphology of the HDFs in the present work was the storage modulus of the hydrogel matrix. As reported in Chapter 2, the storage modulus is a measure of stiffness. For hydrogels at a concentration of 2.5 mg/mL collagen and 5 mg/mL alginate, the mean storage modulus was measured to be 15.28 Pa, and for 2.5 mg/mL collagen and 10 mg/mL alginate, the storage modulus was 27.16 Pa, almost double that of the lower alginate concentration. An important future study to continue this work would be to investigate cellular response for HDFs encapsulated within a range of alginate concentrations for collagen-alginate blended hydrogels, in order to determine how the matrix stiffness affects cell behaviour.

Following the evaluation of fibroblast morphology within the blended alginate-collagen hydrogels, the presence of a layer of epithelial cells (H400s) was searched for. Figure 3.11 shows regions on the surface of the hydrogels where cells were found to heavily overlap. This could be a region of epithelial cells, however the morphology differs from the control image of H400s cultured in 2D (Figure 3.10B). H400s typically show a regular cobblestone appearance, outward growth from cell islands, and tight cell-cell junctions, which were not evidenced in the regions identified in Figure 3.10B. H400s are a cancer-derived cell line, which could lead to the cells migrating into the hydrogel rather than remaining on the surface and forming a stratified epithelium. In order to clearly identify the epithelial cells in the model, cell-specific staining is required, and this would be a future study to continue this work. For example, keratinocytes could be stained for E-cadherin or cytokeratins to differentiate them

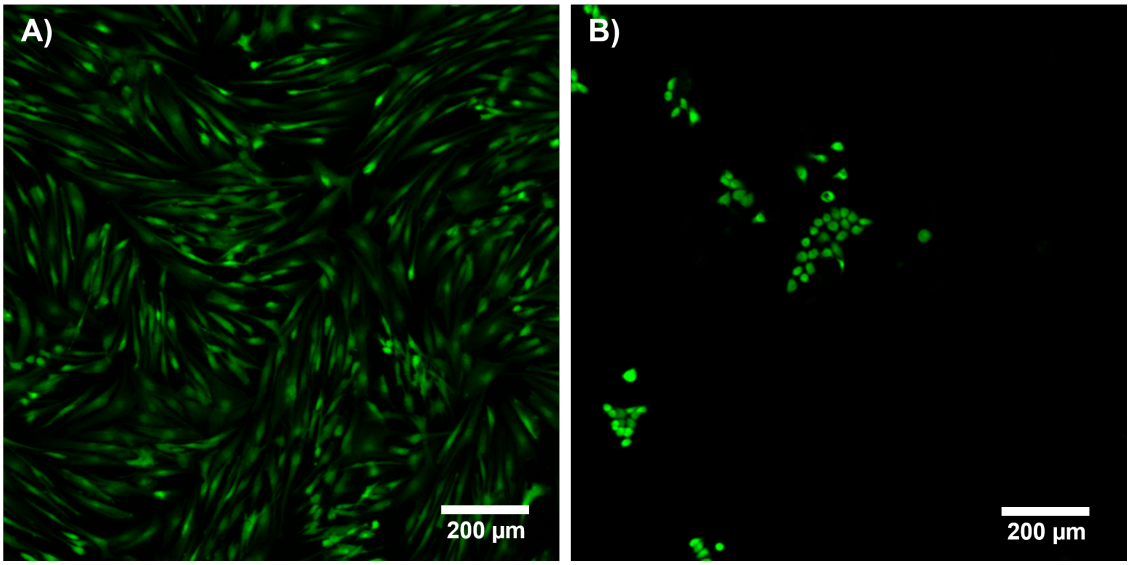


Figure 3.10: Representative images of live-dead stained 2D cultures of (A) human dermal fibroblasts (HDFs) after 6 days in culture, and (B) epithelial cells (H400s) after 4 days in culture, for comparison to cells grown in 3D culture. HDFs demonstrated typical elongated shape and H400s showed a cobblestone appearance as expected.

from fibroblasts in the co-culture system. Further future experiments also should include culturing H400s on the surface of cell-free blended hydrogels with subsequent live/dead staining to investigate whether the cells are migrating into the scaffold or remaining on the surface, and using different cell sources to identify the best cell type to form a stratified epithelium using the alginate-collagen scaffold.

### 3.3.5 Histological staining of 3D hydrogel models

In order to investigate whether a stratified epithelium was formed in the blended-hydrogel model, the gels were fixed, embedded in paraffin wax, sectioned, and stained with H & E. Figure 3.12 shows representative images of the stained sections. The presence of fibroblasts encapsulated within the hydrogels was identified in all samples, and were shown as dark purple circles (Figure 3.12). The stained sections further confirmed, following confocal imaging,

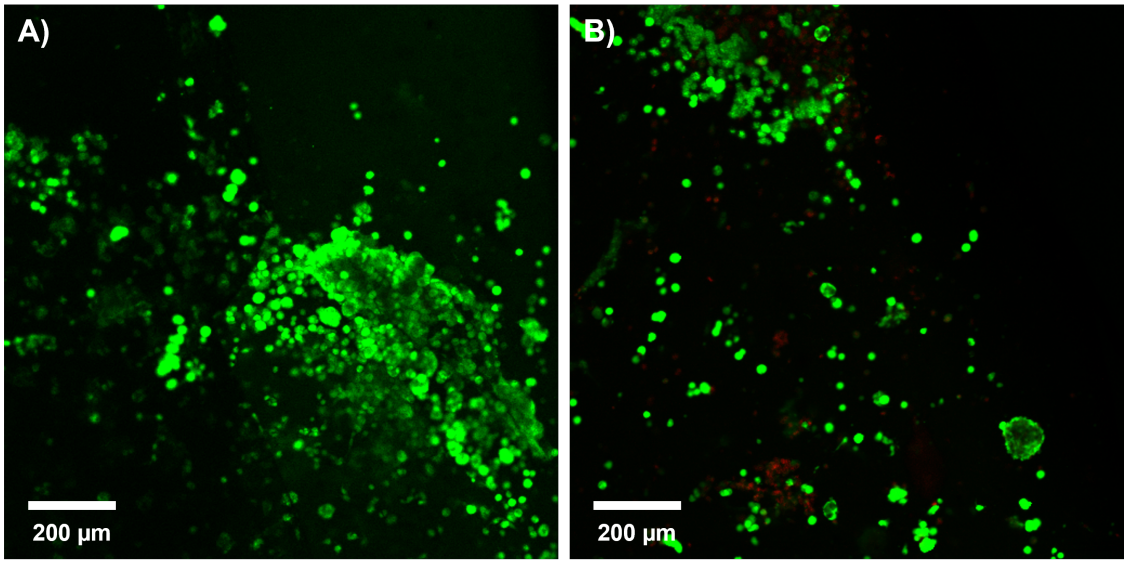


Figure 3.11: Representative images of a live-dead stained human epithelial cell line (H400s) on the surface of collagen-alginate hydrogels at a concentration of 2.5 mg/mL collagen + 5 mg/mL alginate (human dermal fibroblasts were encapsulated within the gels). The surface of the gel is in the x-y plane. Images show regions of overlapping cells suggesting the presence of an epithelial cell layer on the surface of the gels, although it should be noted that cell-specific staining was not used.

that a good distribution of fibroblast cells throughout the tissue was achieved and that this was reproducible across different experiments. This finding, combined with the high viability of the primary dermal fibroblasts, demonstrated that alginate-collagen blended scaffolds can successfully support the growth of primary HDFs at various concentrations.

A further observation of the H & E-stained tissue sections in Figure 3.12 was the presence of gaps or unstained regions within the tissue where there appeared to be no scaffold or cells. Collagen is known for not adhering to slides during preparation of sections on slides, and this may have been compounded by the blending of two different hydrogels in the present model. Two different approaches were taken to try and improve the adherence of the sections to the slides: (1) by subbing the slides with poly-L-lysine and (2) by using positively charged microscope slides. Both methods improved the adherence of the sections to the slides, although still resulted in regions of the section appearing 'missing' when examined under

the microscope (as seen in Figure 3.12, despite the use of subbed slides for these images). Additional optimisation of the fixation and sectioning method used would be beneficial to improve the quality of the histological images. For example, other methods such as flash-freezing and cryo-sectioning could be explored, as the dehydration process for fixation of these models was challenging given the high water content of the hydrogel model.

Despite culturing at the air-liquid interface for 10-14 days, the presence of H400s on the surface of the hydrogels could not be easily identified from the histological staining (Figure 3.12). Further optimisation of the seeding density and culture conditions are also required to achieve the formation of a stratified, mature epithelium in the current model. Previous work completed within the department found that the thickness of oral epithelium in *in vitro* models using H400s, as well as the degree of stratification, was significantly greater in decellularised dermis scaffolds, compared with collagen gels [252, 253]. Whilst the same study successfully produced a stratified epithelium on collagen scaffolds using H400s, they reported that the keratinocytes did not appear to grow as efficiently (never more than 2-3 cell layers thick) on collagen than on decellularised matrix scaffolds [252, 253]. This may explain the lack of visible epithelium on the present model given that additional optimisation of the culture conditions was required and the presence of alginate with a lack of adhesion motifs may have hindered the formation of the mature epithelium.

Whilst studies have shown that decellularised matrix is typically a very effective scaffold for producing 3D oral mucosa models, one of the challenges with using such a scaffold is its reproducibility. Collecting tissue samples from different sources and regions of the oral cavity often results in variation in the thickness and behaviour of the scaffold. Using a hydrogel-based scaffold like the one in the present study has the advantage of reproducibility, which is important when improving our fundamental understanding of the interactions occurring between different cells and the microflora in the oral cavity, as well as when testing new implant materials or antimicrobial approaches.

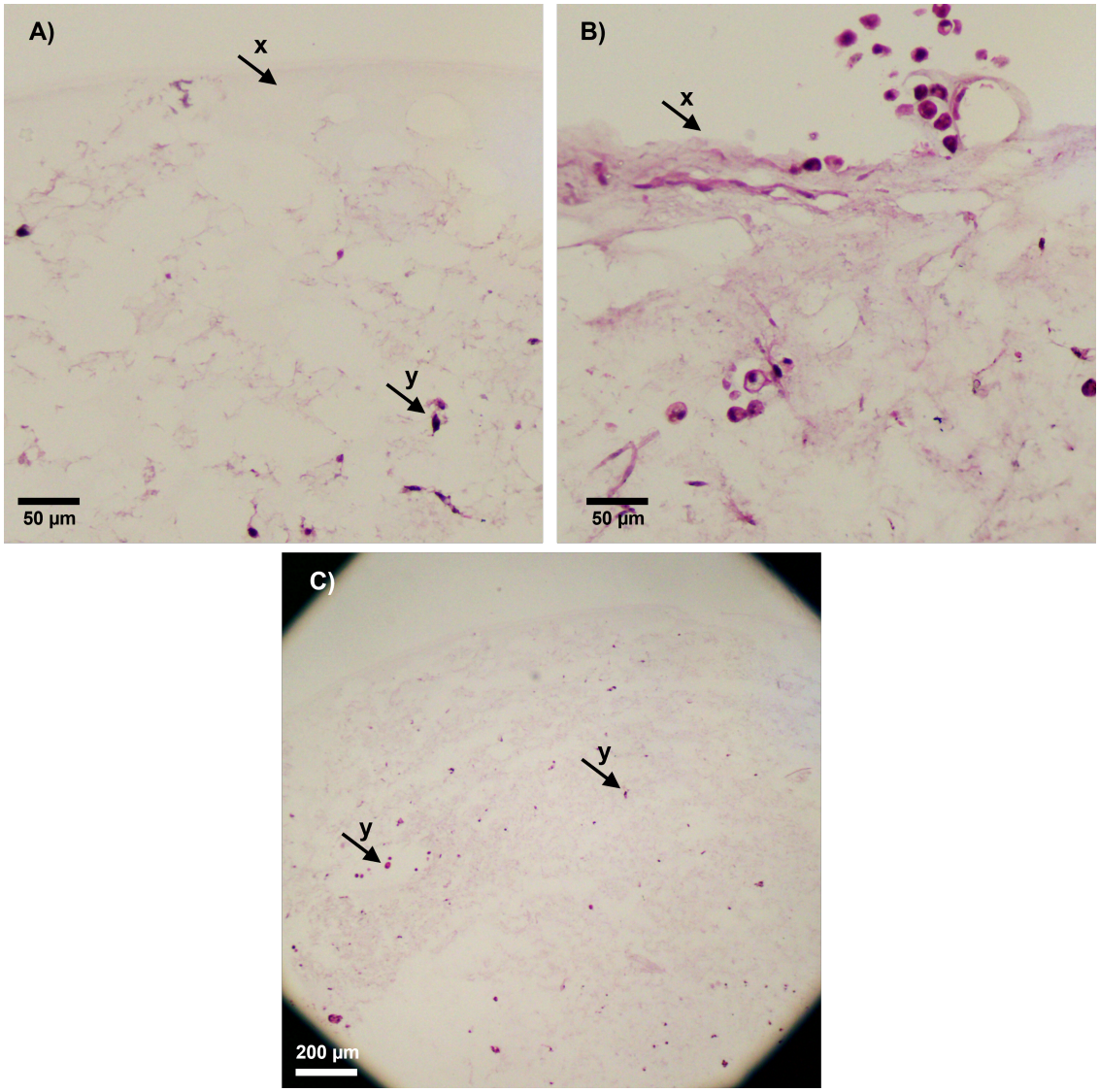


Figure 3.12: Representative images of 5 $\mu$m thick sections of fixed blended hydrogels stained with Haematoxylin and Eosin (H & E). All images of hydrogels at a concentration of 2.5 mg/mL collagen and 10 mg/mL alginate. (A) and (B) taken at 20X magnification and (C) taken at 5X magnification. Arrows show (x) the surface of the hydrogels and (y) HDFs embedded within the gel.

Other models of tissue-engineered oral mucosa have been previously described in the literature [104, 112, 118]. These models typically utilise either a fibroblast-containing collagen gel with oral keratinocytes cultured on the surface at the air-liquid interface, or a decellularised matrix to produce a 3D model of the oral mucosa. One of the challenges with

developing 3D cultures is that primary cells have relatively short lifespans, as they lose their *in vivo* phenotype after a few passages, and therefore may not offer sufficient cell numbers to use in multiple 3D co-cultures [113]. Furthermore, enriched media specific to each cell type are often required; without this, primary cells can display an altered phenotype and metabolic function [120]. The need for reproducibility makes the use of cell lines desirable, although it must be noted that there is a pay-off between reproducibility and physiological relevance, with Yadev et al. [118] highlighting that the commercially available epithelial cell line TR146 does not form a fully differentiated epithelium.

Focusing on the use of the H400 cell line in the present work, the data presented in this chapter raises questions as to whether this was an appropriate choice. Several research groups have reported the use of epithelial cell lines in the development of 3D oral mucosa models. These include the immortalised human oral mucosa line OKF6/TERT-2 [110], the immortalised human keratinocyte cell line HaCaT [104] and other cancer cell lines such as TR146 cells (derived from a squamous cell carcinoma of the buccal mucosa) used in SkinEthic Human Oral Epithelium models [111, 118]. All these studies successfully identified the presence of a stratified epithelium in their culture, further suggesting that the use of a cell line can successfully generate a 3D oral mucosa model with a mature epithelium, and therefore the initial choice to use the H400 line was reasonable. The key advantage for using such a cell line is that they are relatively easy to culture and do not require the use of a feeder layer unlike many primary keratinocyte culture systems. However, cell lines exhibit different phenotypes and morphologies to primary cells. The cells used in the present study, whilst selected for the preliminary studies described in this chapter, are not clinically relevant. Where possible, primary human cells should be utilised since they are the most physiologically relevant with regards to the *in vivo* tissue of interest. Future continuation of this work should investigate the use of different cell lines and primary cell sources to produce a mature epithelium in the blended hydrogel model.

The purpose of generating a 3D *in vitro* model that is aligned with the matrix stiffness of the native oral mucosa is to investigate whether this matrix stiffness has an effect on the cells' ability to form a junction with a dental implant material. The ultimate goal of this work is to combine a biofilm model, with a 3D oral mucosa model and implant material to study the interaction between the epithelium, bacteria, and material surface. A further disadvantage of using H400s in the present model is the potential for studying the production of inflammatory cytokines in response to challenging the 3D tissue with a biofilm. The cytokine of choice is interleukin 8 (IL-8), a marker of an immune response. However, within the department, H400s have been found to produce high levels of IL-8 even when grown under optimal conditions, and there is no difference in IL-8 production between control conditions and the challenge conditions. Therefore for studies such as this to be conducted in the future, there is a need to choose a different cytokine to study the model's response to biofilms, carefully accounting for negative controls, or to use a different epithelial cell line as previously suggested.

As well as reporting on the design and development of such models, the field has been employing these approaches to study different oral interventions and diseases. 3D engineered human oral mucosa models have been used *in vitro* to investigate oral diseases such as bacterial and fungal infection [104, 112], as a model of drug delivery and diagnostics [254]) and to evaluate the biocompatibility of dental materials [124]. Of great relevance to the present work is the use of such *in vitro* models to investigate the interactions between bacteria and the oral epithelium. Pinnock et al. [112] reported significant differences in the response of oral mucosa models to *Porphyromonas gingivalis* (*P. gingivalis*), compared with monolayer cultures of epithelial cells. This study described their use of a collagen-fibroblast gel with surface epithelial cells cultured at the air-liquid interface, with the application of *P. gingivalis* in planktonic culture. Subsequently, it was shown that utilising 3D co-culture systems was important in order to fully discern cellular responses to infection and confirmed

that the interaction between cell types played an important role. Another key study that supported the significance of 3D co-cultures in the field of oral pathogenesis investigated the bacterial species *Fusobacterium nucleatum* (*F. nucleatum*), which is known to form a bridge between early and late colonisers in the formation of dental plaque (a common oral biofilm) [119]. Gursoy et al. [104] used a collagen-based 3D mucosa model and applied planktonic cultures of *F. nucleatum* to determine the bacteria's ability to attach to and invade epithelial cells. Like Pinnock et al. [112], they also highlighted the difference in response between the 3D co-culture and a simple monolayer of epithelial cells. Given the strong evidence of an interplay between epithelial cells and fibroblasts in response to infection, there is a clear need for future studies to consider the application of 3D mucosa models to studies of oral disease pathogenesis. It should be noted that both these studies utilised planktonic cultures in their investigations.

Due to the complexity of analysing both 3D tissue models and biofilms, very few studies have attempted to combine the two in a single system. The simplest reported method, published by Gursoy *et al.* [104], applied biofilms of *F. nucleatum* grown on coverslips directly onto epithelial cells grown on fibroblast-containing collagen matrices. By comparing the application of planktonic species with biofilms, they were able to determine differences between the ways bacteria behaved in these different states, with biofilm bacteria causing significantly greater epithelial cell death than when applied in planktonic form. This study also demonstrated that cells from biofilms of *F. nucleatum* were able to invade the collagen matrix of the mucosal model, highlighting the benefits of choosing a complex 3D system to model the interaction between biofilms and the oral epithelium. However, the biofilm was directly in contact with the mucosal model and hence this may have increased the magnitude of the effects observed. *In vivo*, plaque biofilms form on the adjacent tooth or implant surface, rather than directly on the epithelium. Furthermore, oral biofilms experience flow forces from saliva, which are not replicated in *in vitro* models cultured in traditional wells. As previously

discussed, the future direction of the research presented in this thesis is to combine 3D tissue engineered oral mucosa models with dental implant materials and oral biofilms, which is a very challenging system to optimise, reproduce, and most importantly analyse. However, the benefits of using an *in vitro* system that is a good representation of the *in vivo* environment are clear from the studies discussed in this section.

## 3.4 Summary

In this chapter, the viability and morphology of the cells within the blended hydrogel tissue models were examined. Collagen-alginate hydrogels were shown to support cell growth, with high cell viability displayed from live-dead staining at all concentrations investigated. Initial experiments to investigate the presence of an epithelial layer did not provide any evidence that one had formed in the model. Further optimisation of the model is required to produce a mature epithelium, although as previous studies have demonstrated that a stratified epithelium can be obtained with H400s, this approach was still considered to be appropriate in the development of the 3D *in vitro* system. In summary, the remainder of research objective 1, to characterise the chosen hydrogel system in terms of its ability to support cell growth and proliferation, was completed, with the chosen scaffold materials and concentrations shown to support both HDF and H400 growth.

### 3.4.1 Conclusion

Matrix stiffness was found to influence fibroblast morphology, as HDFs encapsulated within higher alginate concentrations displayed a rounded morphology whilst in lower alginate concentrations, they demonstrated a typical elongated shape. Further studies are required to elucidate whether a stratified epithelium can be formed on collagen-alginate hydrogel scaf-

folds and these are described in Chapter 7.

Alongside reliable and physiologically relevant 3D *in vitro* oral mucosa models, novel approaches to introducing biofilms to host cells in 3D environments are key to understanding the complex interactions in the oral cavity between the host cells and tissues, the oral microflora, and of dental implants. The rest of this thesis will focus on the challenge of analysing biofilm growth on implant materials in such a complex system, with the ultimate goal of bringing the engineered mucosa, biofilm and dental materials into one *in vitro* model system.

# Chapter Four

# Evaluating bacterial growth on implant surfaces

*This chapter is adapted from a paper by Mountcastle and Vyas et al. published in npj Biofilms and Microbiomes (2021) [255].*

A key component of developing an *in vitro* system that can assess the interaction of a 3D tissue model, a dental implant material, and a biofilm, is the ability to evaluate biofilm growth on the implant material in a complex experimental system. This chapter addresses the second research objective of this thesis, to develop a method to analyse confocal micrographs of live/dead stained biofilms, for the purpose of analysing biofilm growth on dental implant surfaces. Methods of determining biofilm viability are discussed, and a new image analysis tool for calculating biofilm viability from confocal images was developed. The novel automated tool has several advantages that make it useful not just for the specific application described, but more broadly in the development of novel antimicrobial approaches. The tool is written in open-source software, is easy to use, transparent in function, and is modifiable for those with expertise in image analysis. However, it should be noted that there are limitations to using a method based on confocal micrographs. The full advantages and

disadvantages of the developed method are discussed in this chapter.

## 4.1 Introduction

A complex *in vitro* model containing eukaryotic cells, bacteria, and a dental implant material is challenging to investigate. Alongside traditional assays to analyse cellular response, a method is also needed to determine bacterial and eukaryotic cell attachment to the implant surface and to understand biofilm formation. Quantifying biofilm formation on surfaces is challenging because traditional microbiological methods, such as totalling colony-forming units (CFUs), often rely on manual counting. These are laborious, resource intensive techniques that are susceptible to human error. Furthermore, samples are irreversibly altered as the biofilm needs to be removed before CFUs can be, and it is difficult to recover all the bacteria from a surface in order to undertake this approach and can introduce an additional source of error. An alternative approach to these traditional methods is the use of confocal laser scanning microscopy (CLSM). CLSM is a high-resolution technique that allows 3D visualisation of biofilm architecture. In combination with a live/dead stain, it can be used to quantify biofilm viability on both transparent and opaque surfaces, such as dental implants.

Figure 4.1 provides a summary of four commonly used methods for biofilm quantification on surfaces and the challenges and limitations associated with each. Traditionally in microbiology, viability quantification is performed through serial dilution of a culture to count the number of CFUs on agar plates to give an estimation of the number of live bacteria in a culture [256]. A CFU-plating method can be used to quantify a reduction in biofilm viability, for example, during efficacy analysis of an antimicrobial agent [257, 258]. However, despite its common use, CFU-plating cannot quantify the dead cells present in a biofilm and thus reduces the amount of information available for analysis. An additional problem with

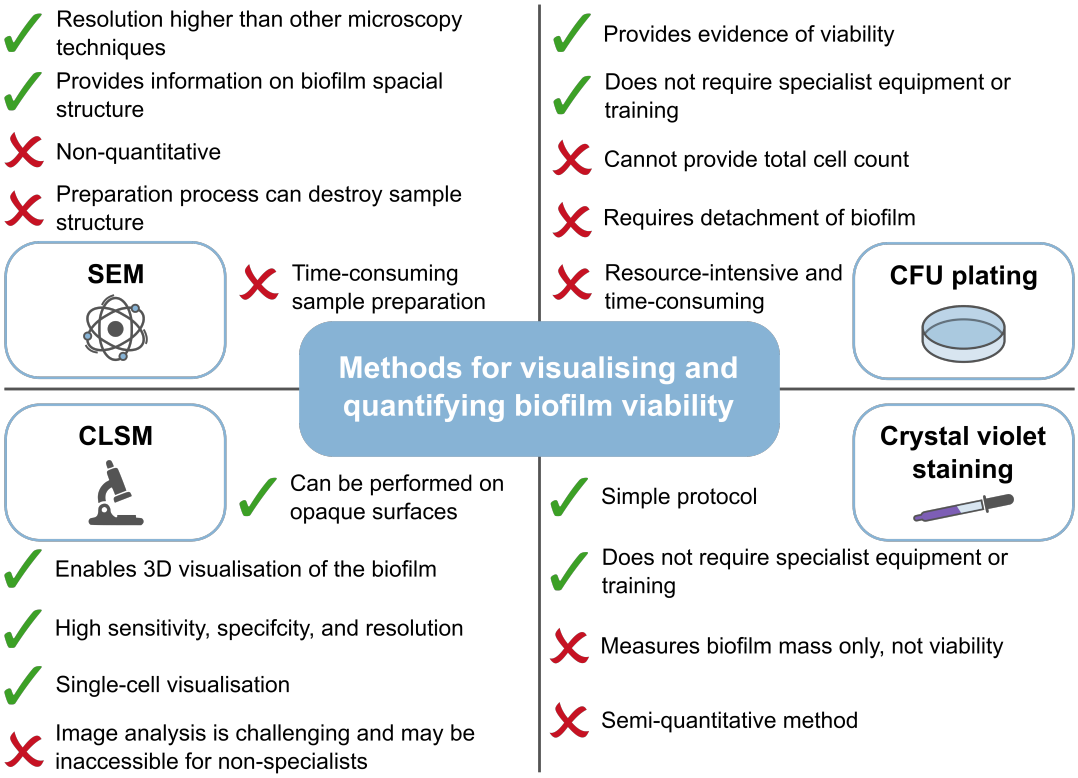


Figure 4.1: Summary of the benefits and challenges of four commonly used methods to visualise and characterise biofilm viability. Scanning electron microscopy (SEM) has higher resolution than light microscopy techniques and can provide information on biofilm spatial structure. However, it is challenging to obtain quantitative data and the sample preparation process can destroy the sample structure. Colony-forming unit (CFU) plating provides reliable evidence of viability and does not require expensive or specialist equipment. However, it cannot elucidate information on total cell number and requires physical or chemical detachment of the biofilm. Crystal violet staining does not require specialist equipment or training, however it only measures biofilm mass and not viability and is considered a semi-quantitative method. Confocal laser scanning microscopy (CLSM) can be performed on opaque surfaces and can enable 3D visualisation of a biofilm. It has high sensitivity, specificity and resolution and can achieve single-cell visualisation.

using this technique is that it requires detachment of the biofilm from the intended surface using physical or chemical methods. This can affect the viability of the cells and therefore the resulting conclusions drawn. Furthermore, CFU-plating does not provide information about biofilm architecture. Understanding 3D structure is important because extracellular

polymeric substance (EPS) contributes to antimicrobial resistance properties of biofilms by impeding transport of antibiotics [259]. In the future, the models developed in this research could be used to assess antimicrobial strategies to improve dental implant success rates, including evaluating materials that have novel coatings or surface modifications. Disruption of biofilm architecture to expose cells and increase the efficacy of antimicrobial drugs is a potential approach to tackle device-related infections, and therefore is an important aspect to analyse [260]. A second commonly utilised microbiological method to evaluate bacterial colonisation is crystal violet stain along with spectrophotometry [261–264]. Whilst this method is simple to perform, crystal violet staining only determines mass and not biofilm viability, as it stains both live and dead cells alongside the extracellular matrix [265]. In addition, concerns have been raised regarding its sensitivity and specificity, as it is only a semi-quantitative method [266]. Whilst these traditional methods have applications and advantages, a move towards more direct quantitative analyses of biofilms that reduce operator variability seems desirable.

Neither CFU-plating nor crystal violet staining allow for detailed visualisation of biofilm architecture. In contrast, direct imaging of biofilms using microscopy techniques provides information on structural characteristics, which can in turn determine whether an intervention has been successful in preventing biofilm formation or disrupting an established biofilm. To view a biofilm at the cellular level, scanning electron microscopy (SEM) is frequently employed [267–270]. SEM utilises a focused beam of high-energy electrons to generate a signal at the surface of specimens. It provides high-resolution (50 to 100 nm) information on cell morphology, spatial structure, and the presence of EPS. The key disadvantage of SEM, however, is that the vacuum required to prevent beam scattering requires bacterial cells to be chemically processed and dehydrated in a time-consuming process that can destroy the biofilm structure [271]. In addition, SEM can only provide information on biofilm structure and biofilms cannot be labelled to determine other important information

such as viability. Quantifying SEM micrographs is also challenging, especially given that only surface information is available due to its lack of vertical resolution. For this reason, high sample numbers may be required to produce statistically significant data, which in turn is very time-consuming and potentially costly.

CLSM selectively excites fluorescence signals from different planes within a sample, acquiring images point by point with localised laser excitation at specific wavelengths. CLSM is a useful technique as it enables 3D visualisation of biofilm structure by excluding signals from adjacent planes. This represents an advantage of CLSM compared with SEM, as confocal imaging has a vertical resolution of 10 to 50 $\mu$m, whereas SEM can typically only provide surface information, unless a focused ion beam (FIB) is available. A second benefit of CLSM compared with SEM is the versatility offered by fluorescent stains added to a sample, allowing further information to be obtained; for example, the presence of extracellular DNA, exopolysaccharides, and biofilm viability. CLSM with viability staining provides high sensitivity, specificity and resolution. Of the fluorescent stain protocols available, live/dead staining is a conventional method of evaluating biofilm formation in microbiology for a wide variety of applications including oral, bone, and gut microbes [265, 272–276]. A live/dead stain provides a fluorescence assay of bacterial viability, based on membrane integrity. Most commonly, SYTO 9 acts as the green fluorescent nucleic acid stain, labelling bacteria with intact cell membranes, and propidium iodide (PI) forms the red-fluorescent nucleic acid stain, penetrating only bacteria with damaged membranes [277]. Examples of the application of CLSM and fluorescent staining to biofilms include examining *Pseudomonas aeruginosa* (*P. aeruginosa*) biofilm formation on antibiotic-loaded bone cement [275], observing the effect of antimicrobial therapy on biofilm formation in endotracheal tubes [274], and screening cinchona alkaloids for anti-biofilm activity against *Staphylococcus aureus* (*S. aureus*) [278]. Overall, CLSM is a useful method to analyse the effect of biofilm formation on dental implant materials within the model developed in this thesis.

Despite the varied and wide-ranging use of CLSM and live/dead staining to investigate biofilm formation, there is little consensus regarding evaluation of the resulting micrographs. Specifically, there is no consistent method applied for quantifying live/dead bacteria from the confocal images reported in the literature. Some groups use CLSM to simply visualise the biofilm and qualitatively interpret the images, or conduct manual segmentation using a global threshold or delineating the cells in the images manually [268, 272, 279]. Simple segmentation methods such as these are time consuming and may result in inconsistencies due to user subjectivity. Other studies do not report in full the segmentation algorithm or validate its accuracy [267, 275, 280, 281]. One useful way of validating accuracy is to perform a sensitivity and specificity analysis that determines whether an algorithm can successfully detect a pixel that corresponds with bacteria and a pixel that corresponds with background, respectively [282]. While more robust segmentation protocols have been reported, these are not always accessible or reproducible if the method lacks detail and may be particularly challenging to implement for non-experts. Many studies use bespoke software such as Imaris [280], COMSTAT [283], PHLIP [284], and most recently BiofilmQ [285]. These can make CLSM micrograph analysis easier to navigate through a user-interface. Some are built on open-source software (for example, COMSTAT is available as an extension to ImageJ), while others are written in subscription-based languages, such as MATLAB [285]. Whilst the algorithms used in some bespoke software are made available, an understanding of the settings in each package and how these impact on the data is required. These settings should be reported for a study to be repeatable. Furthermore, it is necessary to report any image pre-processing as this will affect comparability across literature.

In addition to navigating the range of segmentation methods and software available, the commonly used stain for bacterial biofilm viability, the FilmTracer LIVE/DEAD Biofilm Viability Kit (Invitrogen, USA) [277], can generate erroneous data if images are not analysed correctly. Depending on the contrast of the red and green channel images, bacteria which

are dead can appear yellow in images (due to red and green being superimposed on each other) [286, 287]. A further challenge with the FilmTracer LIVE/DEAD Bacterial and Biofilm Viability Kits is that PI can stain extracellular DNA that is present in biofilms [288]. Therefore, qualitative observation of live/dead stained biofilms could lead to misleading conclusions since the contrast of each channel is manually adjusted by the user. If automated image analysis is used to analyse the red and green channels separately this would give more objective quantitation with no possibility of the two channels being superimposed. Although numerous studies have published new image analysis techniques for biofilms [289–293], many microbiological studies that use image processing still do not report the exact methods used, including the type of threshold applied. Such information is critical to determining accuracy of the study and ensuring reproducibility. Ultimately this leads to the conclusion that the current suite of image processing tools available for biofilm analysis is difficult to access and cumbersome for non-specialists with no significant programming experience. This highlights a need for an open-source image analysis tool designed specifically to assess biofilms which balances accessibility, transparency, and accuracy.

In order to utilise an automated image analysis approach to study biofilms formed on the surface of dental implant materials, the work in this chapter aimed to develop a robust but easy to use automated image analysis technique to quantify biofilm formation from confocal micrographs, which accounted for the errors identified with SYTO 9 and PI stains. A new image analysis method is proposed that incorporates image pre-processing and automated thresholding, using the open-access software Fiji (ImageJ, U.S. National Institutes of Health, Bethesda, Maryland, USA). No prior studies have directly compared confocal micrograph image analysis with counting CFUs and therefore this was undertaken in the present work. Alongside method comparison, sensitivity and specificity of the automated image analysis was carried out to evaluate its accuracy. Further validation of the method was conducted on Gram-positive and Gram-negative species of different cell morphologies:

*P. aeruginosa*, *Lactobacillus casei* (*L. casei*), *Streptococcus sanguinis* (*S. sanguinis*), and a multi-species biofilm consisting of *Fusobacterium nucleatum* (*F. nucleatum*), *Actinomyces naeslundii* (*A. naeslundii*), *Streptococcus gordonii* (*S. gordonii*) and *Porphyromonas gingivalis* (*P. gingivalis*). This novel analysis method will prove useful by ensuring reproducibility across studies, by offering a faster analysis approach than traditional microbiological methods enabling higher sample numbers, and finally by reducing human error compared with CFU-counting or manual image segmentation.

## 4.2 Materials and Methods

All chemicals were from Sigma Aldrich (Dorset, UK) unless otherwise specified. A full list of bacteria species utilised in this work can be found in Appendix B

### 4.2.1 Artificial saliva preparation

Artificial saliva was prepared by adding the following sequentially to 1 L of reverse osmosis (RO) water, stirring throughout [294]

- 0.25 g/L sodium chloride (NaCl)
- 0.2 g/L potassium chloride (KCl)
- 0.2 g/L calcium chloride ($CaCl_2$)
- 2 g/L yeast extract
- 1 g/L lab lemco powder
- 2.5 g/L hog gastric mucin (Type III, partially purified)

- 5 g/L protease peptone

The solution was stirred for 1 hour at room temperature (25°C), then autoclaved to sterilise. After autoclaving, 1.25 mL of 40% (w/v) sterile-filtered urea was added (0.22 $\mu$m filter). The artificial saliva was wrapped in foil to exclude light and prevent protein degradation. Artificial saliva was stored at 4°C and used no later than one week after preparation.

### 4.2.2 *Streptococcus sanguinis* biofilm growth

Frozen stock of *S. sanguinis* (ATCC 10556) was streaked onto a tryptone soya agar (TSA) plate and incubated at 37°C, 5% $CO_2$ for 48 hours. Using the colonies grown on the agar plate, an overnight culture of *S. sanguinis* was prepared in 5 mL brain-heart infusion (BHI) broth and incubated at 37°C overnight, agitating at 100 revolutions per minute (rpm) for the duration. A serial dilution in BHI broth containing 1% sucrose (w/v) was performed with the overnight culture, from $10^9$ (an optical density of approximately 0.5) to $10^3$ cells/mL. Individual Thermanox coverslips (Nunc, Thermo Fisher Scientific) were placed in the bottom of each well in 24-well culture plates (Nunc, Thermo Fisher Scientific). Prior to adding the planktonic culture, 1 mL of artificial saliva was added to each well containing a cover slip and left for 15 minutes before being removed; this was to aid initial adhesion of the bacteria. Subsequently, *S. sanguinis* monospecies biofilms were prepared by adding 1 mL of the $10^3$ dilution to each well containing a coverslip. The plates containing the biofilms were incubated for up to 7 days at 37°C, 5% $CO_2$, shaking at 100 rpm, with a change in BHI broth every 24 hours, to ensure a well-established biofilm had developed.

### 4.2.3 Cell counting

Any remaining BHI broth from the *S. sanguinis* biofilms was removed from each well and each coverslip with biofilm was placed in 5 mL of fresh BHI broth in a universal tube. The bacteria were removed from the coverslip by sonication in an ultrasonic cleaner (In-Ceram, Vitasonic) for 10 minutes at 50-60 Hz, followed by agitation using a vortex mixer for 5 minutes. A serial dilution was performed using the Miles and Misra method to count the number of CFUs [256]. This enabled an estimation of the number of live cells found in the biofilm. To quantify the total number of cells in each biofilm, 10 $\mu$L of the lowest dilution from the serial dilution was transferred to a improved Neubauer haemocytometer (Hawksley, UK) and the number of bacteria were counted in each of the corner squares.

### 4.2.4 Fluorescent staining

For live-dead staining of all biofilms, any remaining broth was removed from each well and coverslips were transferred to a fresh 24-well plate. A working solution of fluorescent stains was prepared by adding 3 $\mu$L of SYTO 9 stain and 3 $\mu$L of PI stain (FilmTracer LIVE/DEAD Biofilm Viability Kit, Invitrogen, USA) to 1 mL of filter-sterilised water in a foil-covered container. Subsequently, 200 $\mu$L of staining solution was added onto each biofilm sample, gently so as not to disturb the biofilm. Samples were incubated for 30 minutes at room temperature, protected from light, before being rinsed with 200 $\mu$L filter-sterilised water. Each coverslip was then placed face up onto a clean, dry microscope slide and a drop of mounting medium added (ProLong Gold Antifade, ThermoFisher Scientific, Massachusetts, USA). A 22 mm diameter glass coverslip was used to fix the sample in place [295]. Samples were stored protected from light at room temperature (25°C).

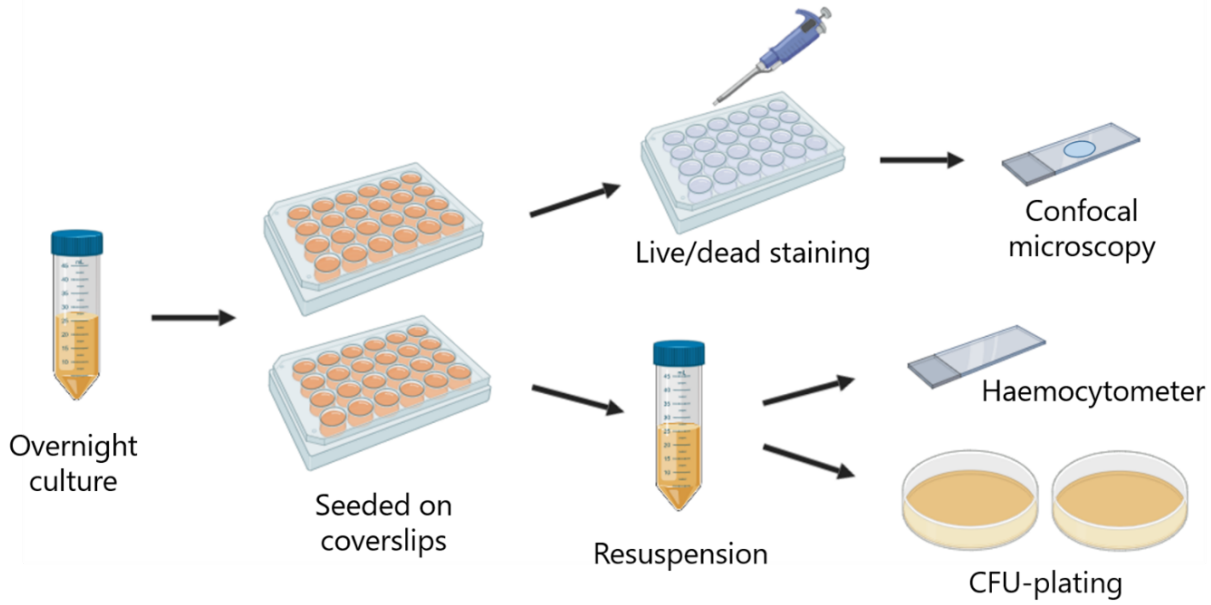


Figure 4.2: An overnight culture of *S. sanguinis*, an early coloniser in oral biofilms, was diluted down to approximately $10^3$ cells/mL and seeded on coverslips in a 24-well plate. At each time point (1, 2, 5 & 7 days), one plate was sacrificed and stained using a fluorescent live/dead stain, and imaged using confocal microscopy. Subsequent image analysis was used to determine the live/dead ratio at each time point. The biofilms on the remaining plate were re-suspended in fresh media using sonication and vortexing to remove them from the coverslip. The total number of live cells was established using CFU-plating. Total bacteria (live and dead) were counted using a haemocytometer. The percentage viability calculated from each of the two methods was then compared at each time point. Figure prepared using BioRender.

### 4.2.5 Confocal laser scanning microscopy

Once fixed and stained, biofilms were imaged with CLSM (LSM 700, Zeiss, Germany) using a x40 oil immersion objective (Zeiss Objective EC Plan-Neofluar 40X/1.30 Oil DIC M27, FWD=0.21 mm). The two stains were first imaged separately to control for any cross bleed between channels. The excitation/emission was 488 nm/<550 nm for SYTO 9 and 555 nm/>550 nm for PI. Five random locations were scanned on each biofilm sample, resulting in 25 total images for each experimental condition. Three z-stacks were taken for each condition to calculate the biofilm thickness and for 3D visualisation and analysis. Z-stacks

were taken at 1 $\mu$m increments from the surface (the first plane in which bacteria were identified).

### 4.2.6 Image analysis

The percentage of viable and dead bacteria in each image was determined from the CLSM images. The percentage of viable bacterial was evaluated by calculating the number of pixels corresponding with the total bacteria in the image (green + red), then calculating the number of pixels corresponding with the dead (red) bacteria in the image, and finally subtracting to find the number of pixels corresponding with live bacteria. The live bacteria were quantified as a percentage of the total bacteria in each image. The image analysis method was carried out using Fiji (ImageJ, U. S. National Institutes of Health, Bethesda, Maryland, USA) (Figure 4.3). This was chosen due to it being open-source software and therefore freely available. A copy of the macro code is available at https://github.com/sophie-mountcastle/Biofilm-Viability-Checker. It should be noted that this macro calculates viability based on the assumption that the image contains a single-species biofilm and therefore the areas of red and green bacteria are proportional to the number of red and green bacteria respectively. It is still possible to use this macro to analyse multi-species biofilms, although the output should be considered as percentage of live cell area, rather than viability. The workflow operated as follows:

1. First, the green and red channels were separated.
2. A series of erosion, reconstruction, and dilation steps were performed on each channel using a disk structuring element of size 3.
3. An additional step was applied to the red channel to compensate for the staining of extracellular DNA that can result in underestimation of the number of live cells [288].

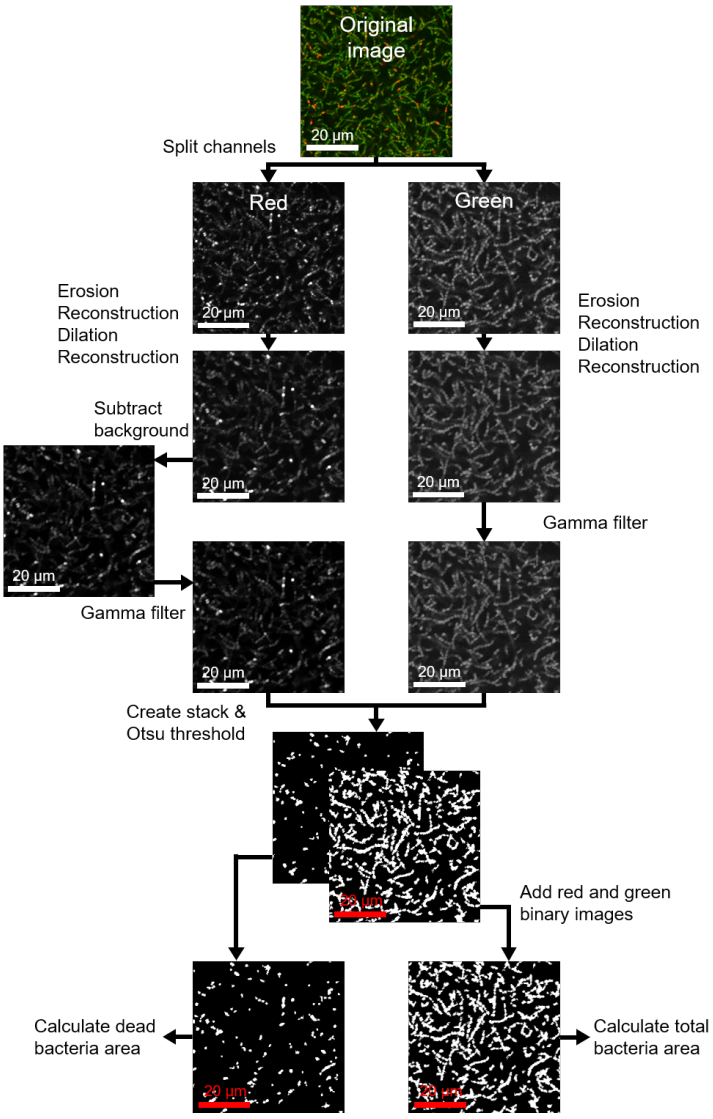


Figure 4.3: Image analysis steps used to calculate bacterial viability from a confocal image. In brief, the image channels were separated and a series of pre-processing steps were performed to improve image brightness and contrast. The images were segmented using Otsu's threshold. The number of white pixels in the red channel determined the area of dead bacteria. The binary images were combined and the total number of white pixels determined the total bacteria area. Finally, these values were used to calculate the percentage of viable cells. Images taken from a representative *S. sanguinis* 48-hour biofilm (20 $\mu$m scale bar).

The 'Subtract Background' command was applied to the red channel. This was based on a 'rolling ball' algorithm and removed smooth continuous backgrounds from images [296].

4. A non-linear histogram adjustment was applied to both channels using the Gamma command to correct for uneven fluorescence intensities. This allowed faint bacteria to become brighter, while the bright bacteria remained at the same intensity. The gamma value was set at 1.5.

5. The resulting images were placed into a stack and segmented using Otsu's threshold, with the threshold value selected based on the histogram from both images [291].

6. The number of white pixels in the red channel was recorded from the segmented images to determine the area of dead bacteria.

7. The binary images were combined, and the total number of white pixels was recorded to determine the area of all bacteria.

8. Finally, the total area of bacteria and area of red bacteria were used to determine the percentage of viable cells. The area of all pixels can also be utilised to determine the percentage coverage of the image, which can be a useful alternative to measuring biofilm mass.

### 4.2.7 Sensitivity and specificity analysis

A receiver operating characteristic (ROC) curve is a performance measurement for classification problems [297]. It defines how well a model is capable of distinguishing between classes; in the current study it defined how accurate the automated process was at determining when a pixel was green or when a pixel was red. The true positive rate (TPR) or sensitivity was plotted on the y-axis and '1 – specificity' (false positive rate (FPR)) was plotted on the x-axis [297]. To determine the 'ground truth', small sections of confocal micrographs of *S. sanguinis* biofilms were selected (three sections per image, for a total of eight images) and manually segmented in Fiji (by manually delineating all bacteria in each image) (ImageJ,

U.S. National Institutes of Health, Bethesda, Maryland, USA). The eight images included two images from each time point (1, 2, 5 and 7-day biofilms). The automated image analysis script was run on the 24 image sections and the resulting segmentation was compared with the 'ground truth' segmentation results using equations 4.1 to 4.3:

$$\text{TPR or Sensitivity} = \frac{\text{Number of true positive pixels}}{\text{Number of true positive pixels} + \text{Number of false negative pixels}} \tag{4.1}$$

$$\text{Specificity} = \frac{\text{Number of true negative pixels}}{\text{Number of true negative pixels} + \text{Number of false positive pixels}} \tag{4.2}$$

$$\begin{aligned} \text{FPR} &= 1 - \text{Specificity} \\ &= \frac{\text{Number of false positive pixels}}{\text{Number of true positive pixels} + \text{Number of false positive pixels}} \end{aligned} \tag{4.3}$$

All calculations were made in MATLAB (R2018a, MathWorks Inc., USA).

### 4.2.8 Validation of image analysis tool on single- and multi-species biofilms

#### *Pseudomonas aeruginosa* biofilm growth

A frozen stock of *P. aeruginosa* (PA01-N) was streaked on BHI agar at 37°C, 5% $CO_2$. Overnight cultures were grown by inoculating 5 mL of BHI broth with 3 colonies of *P. aeruginosa* and incubating at 37°C, continuously shaking at 100 rpm for 18 hours. The overnight culture was diluted using BHI broth to an optical density of 0.01 (at 600 nm), of

which, 1 mL was placed in a well of a 24-well plate containing a coverslip (13 mm diameter, Thermo Scientific Nunc Thermanox) and this was performed in triplicate. The plate was then incubated for 3 hours at 37°C, shaking at 80 rpm to allow cells to adhere to the coverslip. The culture was removed from the wells and replaced with 1 mL of BHI broth, which was incubated for 24 hours at 37°C, shaking at 80 rpm. The fluorescent staining protocol was conducted as described previously in Section 4.2.4.

### *Lactobacillus casei* (*L. casei*) biofilm growth

For the *L. casei* (NCTC 16341) biofilms, frozen stock of *L. casei* was streaked onto a De Man, Rogosa and Sharpe (MRS) agar plate and incubated at 37°C, 5% $CO_2$ for 48 hours. Using the colonies grown on the agar plate, an overnight culture of *L. casei* was prepared in 10 mL MRS broth and incubated at 37°C overnight, agitating at 100 rpm for the duration. A serial dilution in MRS broth was performed with the overnight culture, from $10^9$ to $10^3$ cells/mL. Individual Thermanox coverslips (Nunc, Thermo Fisher Scientific) were placed in the bottom of each well in 24-well culture plates (Nunc, Thermo Fisher Scientific). 1 mL of the $10^3$ dilution was added to each well containing a coverslip. The plates containing the biofilms were incubated for 7 days at 37°C, 5% $CO_2$, shaking at 100 rpm, with a change in MRS broth every 48 hours. The fluorescent staining protocol was conducted as described previously in Section 4.2.4.

### Multi-species *F. nucleatum ssp. polymorphum* biofilm growth

The multi-species biofilm consisted of the strains *F. nucleatum* (ATCC 10953), *A. naeslundii* (DSM 17233), *S. gordonii* (NCTC 7865), and *P. gingivalis* (W83). Overnight cultures of *F. nucleatum* were prepared in Schaedler anaerobic broth and grown anaerobically at 37°C. *A. naeslundii*, *P. gingivalis*, and *S. gordonii* cultures were prepared in BHI broth. Bacteria

were grown anaerobically (Whitley anaerobic workstation, Don Whitley Scientific Ltd, UK) at 37°C, except *S. gordonii*, which was grown at 37°C in 5% $CO_2$. The overnight cultures were diluted with phosphate-buffered saline (PBS) (0.01 M) to an optical density of 0.5 for *S. gordonii* and 0.2 for all other species (at 600 nm). To form the biofilms, 500 $\mu$L of *A. naeslundii* and *S. gordonii* were pipetted into a well of a 24-well plate onto a coverslip (13 mm diameter, Thermo Scientific Nunc Thermanox), and incubated with 500 $\mu$L of artificial saliva for 24 hours at 37°C. The planktonic culture was then replaced with 500 $\mu$L of *F. nucleatum* and 500 $\mu$L of artificial saliva and cultured for a further 24 hours. Finally, the planktonic culture was replaced with 500 $\mu$L of *P. gingivalis* and 1.5 mL of artificial saliva. Biofilms were incubated at 37°C until 5 days old. The fluorescent staining protocol was conducted as described previously.

### 4.2.9 Validation of protocol on all-dead biofilms

Five 2-day old biofilms of *S. sanguinis* (grown as detailed previously in Section 4.2.2) were treated with the antimicrobial cetylpyridinium chloride (CPC) (0.05% w/v) to act as a negative control for cell viability to test the image analysis protocols. 1 mL of 0.05% (w/v) CPC was added to biofilms for 5 minutes before fluorescent staining. As well as image analysis, a serial dilution and plating was performed to confirm the viability of the antibiotic-treated biofilm. CPC treatment reduced the mean number of cells from 19 million CFU/mL to 1800 CFU/mL. Hence, the images generated using the confocal could be assumed to be 99.99% dead for the purpose of validating the image analysis protocol.

### 4.2.10 Biofilm formation on additively manufactured materials

In order to examine the robustness of the developed approach, and to ensure the tool has broad applications, it was applied to biofilms grown on an additively manufactured (AM) material. Grade 5 titanium is a titanium alloy composed of 90% titanium, 6% aluminium and 4% vanadium (Ti-6Al-4V). Ti-6Al-4V is a common choice of material for medical and dental implants and AM is growing as a manufacturing method, since it offers customisation possibilities that are being taken advantage of for dental applications.

#### Base material manufacturing

Ti-6Al-4V 10x10x3 mm discs with an array of sloping angles (20, 30, 45, 60 and 90 °) were fabricated with a laser powder bed fusion AM system (RenAM 500M, Renishaw PLC, United Kingdom). Changing the sloping angle resulted in surfaces of varying roughness, which challenged the analysis method by offering a range of 3D surfaces. A powder layer thickness of 30 $\mu$m, laser power of 200 W, a point distance of 55 $\mu$m, exposure time of 50 $\mu$s, a hatch distance of 0.105 mm and a spot size of 70-75 $\mu$m were selected [298].

#### Bacterial colonisation assays

Bacterial colonisation on additively manufactured sample surfaces was studied by culturing *Staphylococcus epidermidis* (*S. epidermidis*) (ATCC 12228) biofilms. Samples were degreased with acetone, disinfected by autoclaving, immersed in pure ethanol for 5 minutes and dried whilst exposed to UV light. An overnight culture of *S. epidermidis* grown at 37°C, 5% $CO_2$ was diluted in sterile Mueller Hinton broth to a density of $10^3$ CFU/mL and 1 mL was inoculated onto a 24-well plate containing the samples. After 24 hours, all samples were moved to a new 24-well plate, washed gently three times with 10 mM PBS and fixed with

2.5% (v/v) glutaraldehyde in PBS for 1 hour [298].

**Bacterial imaging**

One sample for each sloping angle was washed gently three times with 10 mM PBS. Samples were stained with 200 $\mu$L of SYTO 9 and PI solution (FilmTracer LIVE/DEAD Biofilm Viability Kit, Invitrogen, USA) and incubated for 30 minutes. Imaging was carried out using a Zeiss LSM 710 confocal microscope (Carl Zeiss GmbH, Germany) at x10 magnification [298].

### 4.2.11 Statistical analysis

All statistical analyses were conducted in GraphPad Prism (v. 5.03). For the additively manufactured material study, a Kruskal-Wallis test (one-way ANOVA) was used to determine any significant differences between the bacterial colonisation on the different sloping angles. For all analyses, $p<0.05$ was considered statistically significant.

## 4.3 Results and Discussion

This study focused on meeting objective 2 (Section 1.8): to develop a method to analyse confocal micrographs of live/dead stained biofilms, for the ultimate purpose of analysing biofilm growth on dental implant surfaces. The method was designed to be simple and accessible to a range of researchers that work on the development of antimicrobial strategies related to biofilms, including microbiologists and materials scientists. Therefore, the analysis protocol was written in the open-source software ImageJ and the method required no preliminary image preparation or modification. The ImageJ macro is outlined in Figure 4.3. The algorithm

was effective and accurate on a range of biofilms, including different bacterial morphologies, such as cocci (*S. sanguinis*) and rod-shaped (*L. casei*) bacteria, and different biofilm ages (from 24 hours up to 7 days), as presented in the following section. A full workflow was provided alongside a series of validation methods in this study and furthermore includes application of the code to translational case studies, which is an advantage compared with other literature that include analysis of CLSM micrographs of biofilms.

### 4.3.1 Validation of image analysis protocol

To assess the reliability and accuracy of the automated protocol developed (Figure 4.3), a series of analyses were performed. This included sensitivity and specificity analysis (Figure 4.4), a comparison with traditional microbiological techniques (Figure 4.5), and the application of the protocol to a variety of bacterial species with varying morphologies (Figure 4.6).

The sensitivity and specificity of the image analysis method was determined using an ROC analysis (Figure 4.4). An ROC curve is a plot of sensitivity (TPR) versus 1 – specificity (FPR). The greater the algorithm's ability to correctly identify pixels in an image, the closer the curve sits to the upper left-hand corner of the graph [299]. An ROC curve lying on the diagonal reflects a performance that is no better than identifying pixels by chance. The ROC analysis in the present study demonstrated that the specificity for both red and green channels was high, with means of 99.9% and 81.7% respectively. However, the sensitivity of the automated image analysis method in the red channel varied, ranging from 6.1% to 100.0%.

The sensitivity and specificity analysis compared the automated results with manual segmentation of the images. This manual segmentation represented a 'ground truth' state,

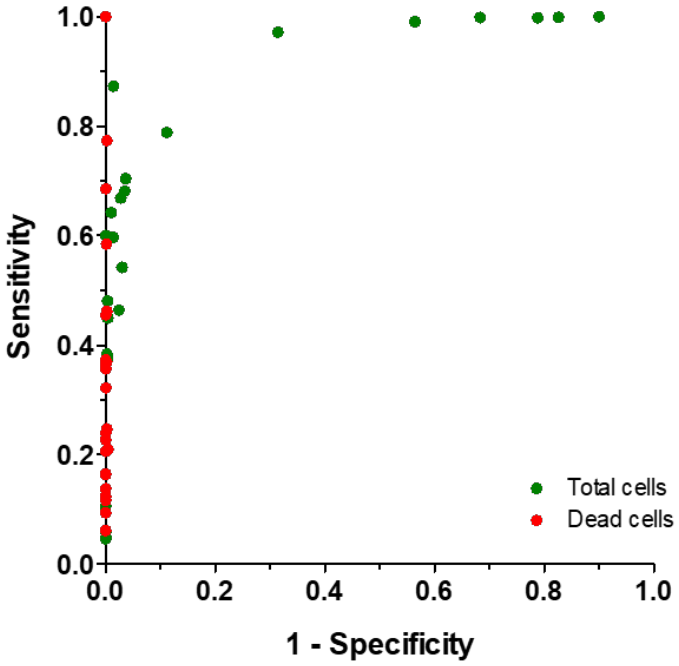


Figure 4.4: ROC curve demonstrating sensitivity and specificity of the image analysis protocol. Green points represent sensitivity and specificity of the green channel (total cells) and red points represent sensitivity and specificity of the red channel (dead cells). The greater the algorithm's ability to correctly identify pixels in an image, the closer the curve sits to the upper left-hand corner of the graph. The ROC analysis demonstrated that the specificity for both red and green channels was high. However, the sensitivity of the automated image analysis method in the red channel varied considerably.

although it should be noted that the manual segmentation was conducted on the original images with no pre-processing and therefore background fluorescence and extracellular matrix staining had not been accounted for. The ROC study showed good sensitivity and specificity for the green channel (total bacteria), 60.3% and 81.7% respectively, and very good specificity of 99.9% for the red channel (dead bacteria), although the sensitivity for the red channel had a wider range (Figure 4.4). This was likely to arise from the additional steps implemented to remove background noise in the red channel necessary to prevent the analysis from including red areas that were not bacteria. Reduced sensitivity in the red

channel was needed due to the challenge of extracellular matrix staining that occurred and therefore the potential to underestimate the percentage of live cells [286–288]. Furthermore, the ROC curve was calculated by comparing the resulting binary images after running the automated analysis with manually segmented sections of images (determined by manually delineating all bacteria) that underwent no pre-processing. During manual segmentation it was likely that low-level background fluorescence combined with the red PI stain marking EPS, resulted in the 'ground truth' images used to calculate the ROC curve including pixels that were not bacteria. This also contributed to the lower sensitivity of the automated analysis in the red channel.

Figure 4.5 shows the resulting quantification of *S. sanguinis* biofilm over time using the automated image analysis method developed in this work and CFU-plating combined with counting using a haemocytometer. Both methods demonstrated viability decreased with biofilm age, however, the rate at which this occurred varied significantly between the two methods. It should be noted that the traditional methods induced greater errors than the image analysis tool, with a CV ranging from 17.0% to 78.1%, compared with 4.24% to 11.5% for image analysis, and this was likely due to the manual nature of the method. Manual analysis of CFU plating and cell counts using a haemocytometer typically resulted in wider errors due to the subjectivity of the user defining what was considered a cell, as well as from volume and dilution errors.

Very few prior studies have directly compared image analysis with traditional quantification methods. As an example of those that have, Larimer et al. [293] compared the cell coverage determined by image analysis with cell coverage determined by measuring the optical density of the biofilm. In the current study cell viability determined using image analysis was compared with that determined using CFU-plating and cell counting, which helped to build confidence in the presented approach. Figure 4.5 demonstrates that the overall trend in live cell percentage varied between the image analysis and manual counting methods.

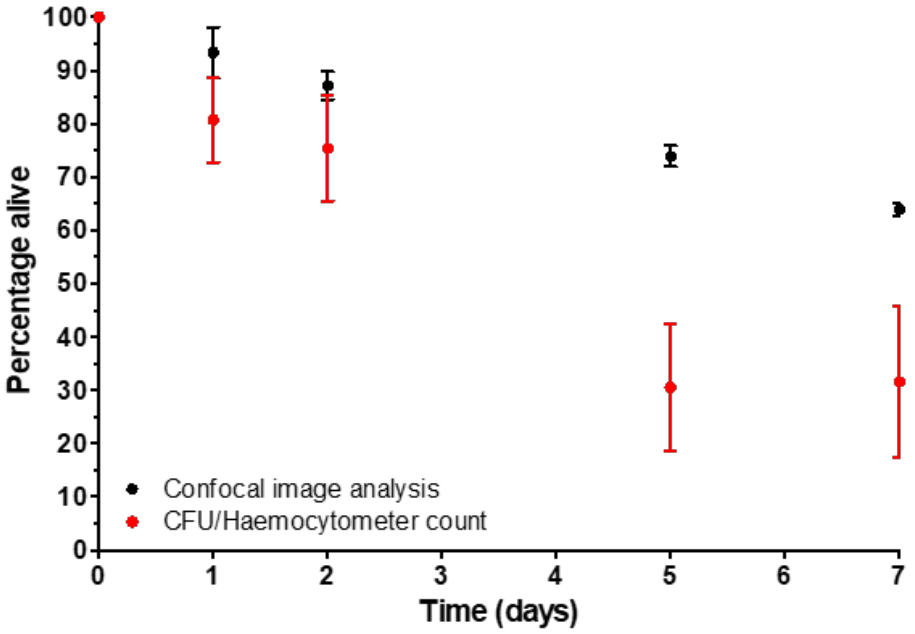


Figure 4.5: Comparison of image analysis and biological methods. Figure shows mean ± standard deviation (for image analysis, five confocal images were analysed of each of five biological replicates, N=5, and for biological methods, three biological replicates were analysed, N=3). To obtain the percentage viability using biological methods, live cells were counted using a serial dilution and CFU-plating. Total cell count was obtained using a haemocytometer.

Using traditional techniques such as CFU-plating and counting cells using a haemocytometer resulted in larger errors as the age of the biofilm increased, rising from a CV of 17.0% at 24 hours to a CV of 78.1% at 7 days. It also led to a lower percentage of live cells at later time points compared with the automated image analysis data; for example, the mean percentage alive at 7 days calculated by image analysis was 63.9%, whereas from traditional techniques it was determined to be only 31.6%. This could have been due to the increased number of cells present in the larger, older biofilms, making counting the cells manually less accurate. Figure 4.5 suggests that automated image analysis was likely to be more accurate and therefore a better method to identify statistically significant variations between biofilm growth conditions when researching antimicrobial approaches. Other benefits of the image

analysis method presented are detailed in Table 4.1.

To confirm that the developed analysis could be performed on biofilms of species with different morphologies, the ImageJ macro was applied to 24-hour *P. aeruginosa* and 7-day *L. casei* biofilms, and to further challenge it, a 5-day multi-species biofilm consisting of *F. nucleatum*, *A. naeslundii*, *S. gordonii* and *P. gingivalis* (Figure 4.6). *L. casei* and *P. aeruginosa* were selected for rod-shaped cell morphologies, to contrast with the cocci-shaped *S. sanguinis*. The protocol was applied to a multi-species biofilm containing a range of morphologies to ensure it could accurately determine biofilm viability and coverage in more challenging and complex images. Figure 4.6 shows that the analysis protocol successfully identified live and dead bacteria of different morphologies. Through qualitative observation of the outline of stained bacteria (Figure 4.6), this was evidenced by very few bacteria being incorrectly identified as background by the automated segmentation method.

It is important to ensure that any image analysis method can cope with a wide range of conditions. In the development of antimicrobial techniques and novel implant surface coatings, it is expected that conditions which include non-viable cells in biofilms will be analysed. To ensure that the protocol dealt with such conditions, the macro was applied to *S. sanguinis* biofilms treated with the antimicrobial CPC at bactericidal levels (Figure 4.7). The macro consistently identified 0% alive (n = 6) for all biofilms treated with CPC which confirmed it was reliable across a range of biofilm viabilities.

A limitation of studies that implement CLSM micrograph analysis is that many do not report in full the chosen segmentation algorithm or validate its accuracy, which makes reproducibility, reliability and comparability difficult to assess [267, 275, 280, 281, 300, 301]. It is vital that the validity of an image segmentation algorithm is demonstrated across different species, on 'extreme' cases such as all-dead biofilms, and by comparing with separate techniques. In this study a series of validation steps were carried out to demonstrate that

Table 4.1: Summary of advantages and disadvantages of image analysis and CFU-plating combined with counting cells in a haemocytometer to quantify biofilm formation.

| **Method** | **Approach** | **Advantages** | **Disadvantages** |
|---|---|---|---|
| Fiji Macro (ImageJ) | (1) Correct for uneven fluorescent intensities.<br>(2) Remove noise.<br>(3) Segment bacteria from background using Otsu threshold.<br>(4) Record number of pixels for total bacteria.<br>(5) Apply same process for red channel to determine dead bacteria count.<br>(6) Calculate viability. | (1) Uses open-source software.<br>(2) Can run macro on multiple images at once.<br>(3) Time taken to run image analysis on 25 CLSM micrographs is <10 minutes.<br>(4) Removes user error. | (1) Workflow may need altering to observe mammalian cells or for alternative staining protocols. |
| Biological Methods | (1) Determine number of live cells from CFU-plating.<br>(2) Determine total cell number using haemocytometer.<br>(3) Calculate viability. | (1) No specific software required.<br>(2) Actual cell number determined rather than being inferred from pixel number. | (1) Time consuming.<br>(2) Resource-intensive.<br>(3) Susceptible to human error.<br>(4) Challenging for larger, increased density biofilms as further dilution required to analyse. |

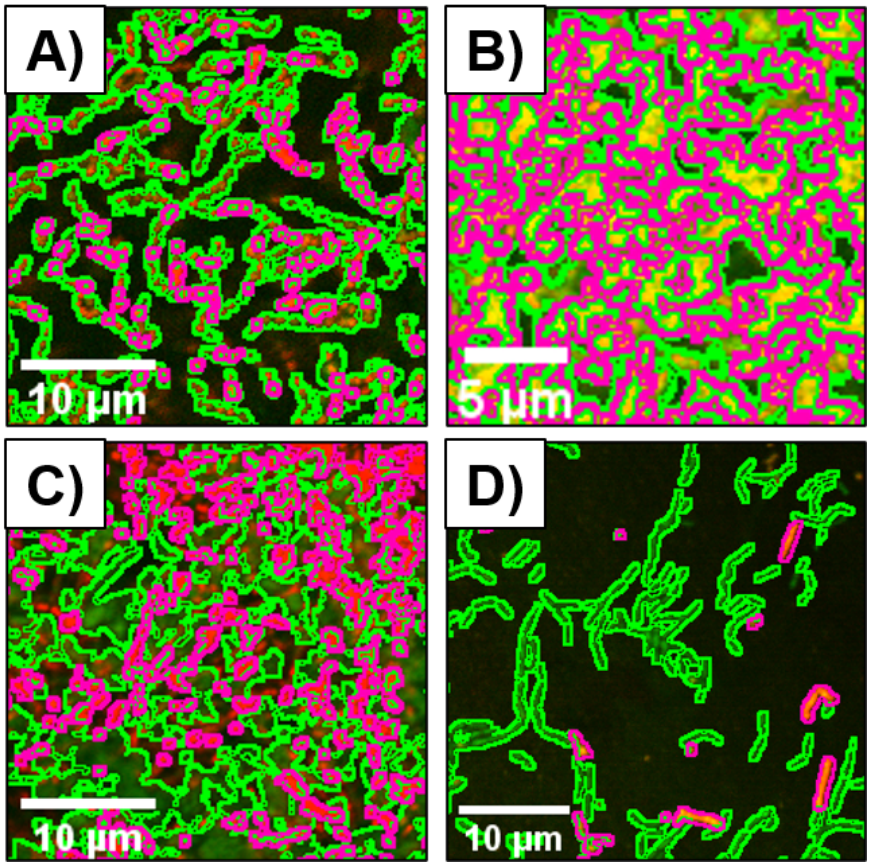


Figure 4.6: Sample images of a variety of single-species biofilms demonstrating results of automated image analysis. The green outline indicates the total bacteria area, and the magenta outline indicates the dead bacteria area. (A) *S. sanguinis* (10 $\mu$m scale bar), (B) *P. aeruginosa* (5 $\mu$m scale bar), (C) multi-species biofilm consisting of *F. nucleatum*, *A. naeslundii*, *S. gordonii* and *P. gingivalis* (10 $\mu$m scale bar), (D) *L. casei* (10 $\mu$m scale bar). The images demonstrate that the workflow is successful at identifying bacteria from background.

the protocol was effective and accurate.

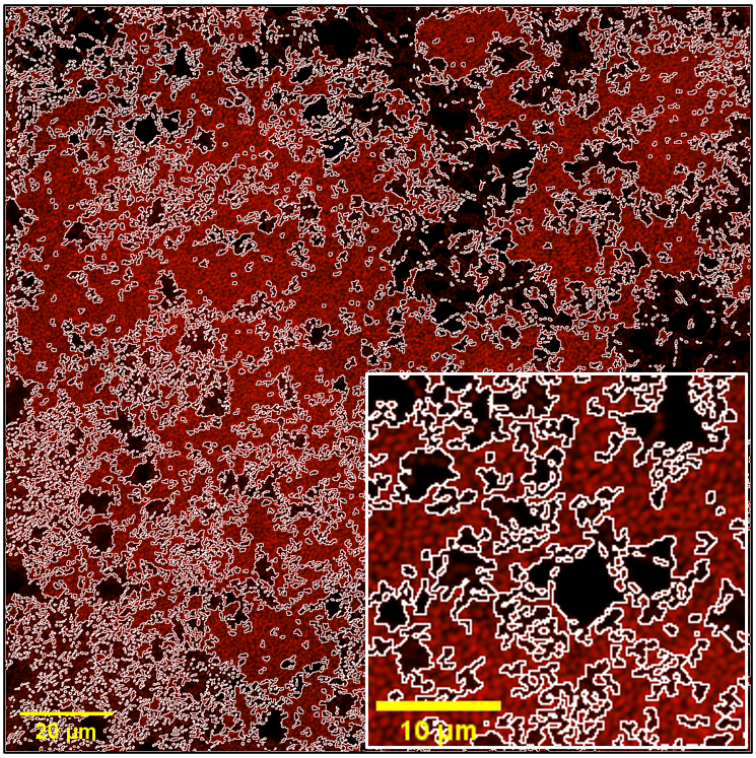


Figure 4.7: Representative micrograph of an *S. sanguinis* biofilm treated with 5% CPC to demonstrate the ability of the macro to handle extreme conditions (Full image 20 $\mu$m scale bar, small image 10 $\mu$m scale bar). The magenta line shows the result of the segmentation of the red channel. The resulting output from the macro is 0% percentage viability.

### 4.3.2 Translation of image analysis method to research applications

The aim of the present research was to develop an accurate image analysis protocol that will aid in the development of implant devices. Current reported image analysis methods for CLSM images of biofilms do not often demonstrate their application to a range of translational research. In the present work, the protocol was applied to two key areas that can benefit from automated CLSM micrograph analysis. First, biofilms of *Staphylococcus epidermidis* (*S. epidermidis*) were grown on AM Ti-6Al-4V discs to understand the effect of manufacturing protocols on the viability of a frequently detected pathogen in implant infec-

tions [298, 302]. Second, to demonstrate the information that can be obtained regarding the 3D architecture of biofilms, the automated protocol was applied to z-stacks taken from 1 day and 7-day old *S. sanguinis* biofilms, which are described below.

An area of research where preventing infection is paramount is implants and medical devices. Infection of implants can result in costly restorative surgeries and can also increase the failure rate of subsequent implant placement [3]. A specific example comes in the form of AM or bespoke implantable devices. These technologies are capable of producing personalised complex geometries while introducing features to enhance osseointegration (a structural and functional connection with the natural bone), reduce stress shielding, and incorporate therapeutically loaded materials [303–305]. Nevertheless, clinical cases requiring such devices are commonly associated with complex interventions, typically arising from traumatic injuries, which may significantly raise infection rates by up to 23-40% for personalised cranioplasties [306, 307]. Thus, much research is being conducted to reduce the occurrences of biofilm-related implant infections. One strategy to limit colonisation and proliferation of bacterial species results from careful selection of surface finish for AM materials to ensure the implant allows for osseointegration but prevents biofilm formation [298]. Villapún et al. [298] demonstrated that *in situ* roughness control can be achieved through changing the orientation at which an implant is manufactured, with maximum mammalian cell adhesion and minimum *S. epidermidis* growth for printing angles between 20 to 30 degrees to the normal plane .

To showcase the applicability of the current approach in the development of novel medical devices, two properties of *S. epidermidis* biofilms on AM titanium implants manufactured with different orientations (20 to 90 degrees from the normal plane) were investigated, namely cell viability and coverage (Figure 4.8). Orientation of AM samples significantly modified the resulting average roughness from 8 $\mu$m up to 18 $\mu$m, for 20 and 90 degrees respectively, as shown in previous works [298]. Nevertheless, the number of live

bacteria expressed as a percentage of total bacteria showed no significant difference (p=0.07) between surfaces (Figure 4.8A). In contrast, when percentage coverage was analysed (as it relates to biomass), it was demonstrated that increasing the sloping angle resulted in a significant increase in percentage coverage of the biofilm (p=0.02) (Figure 4.8B). The difference between viability and coverage indicated that albeit an increase in biomass developed on the surface of the samples, the percentage of living cells was not dependent on surface modification. This could have been the result of the selected alloy lacking any antimicrobial effect [308], coupled with the larger surface area and shear force protection offered by the peaks and valleys present in the rougher samples, leading to more favourable growth conditions [309, 310].

The percentage of live cells showed no significant changes with sloping angle modification; however, it was determined that an increase in sloping angle resulted in a rise in biomass for angles higher than 30 degrees (Figure 4.8). This indicated that the growth of *S. epidermidis* biofilm was constrained, however there was no potential antimicrobial effect enacted from the metallic surface. The rise in biomass concurred with crystal violet and confocal image results reported by Villapún et al. [298], while the lack of contact killing was expected from a bacteriostatic alloy such as Ti-6Al-4V. Crystal violet staining can complicate the analysis of biofilm formation and potentially introduce artefacts during the recovery of the dye [311]. In contrast, confocal imaging is a more versatile method that can quantify biofilm viability and biomass accurately. The current automated method allows for subjectivity to be removed when interpreting CLSM micrographs and can generate additional information regarding cell viability when compared with crystal violet staining methods. Whilst viability did not change with sloping angle (which linked to surface roughness) in this experiment, viability is a key parameter to obtain in future studies of this nature, where surface functionalisation may induce a bactericidal response that would not be picked up from crystal violet staining alone.

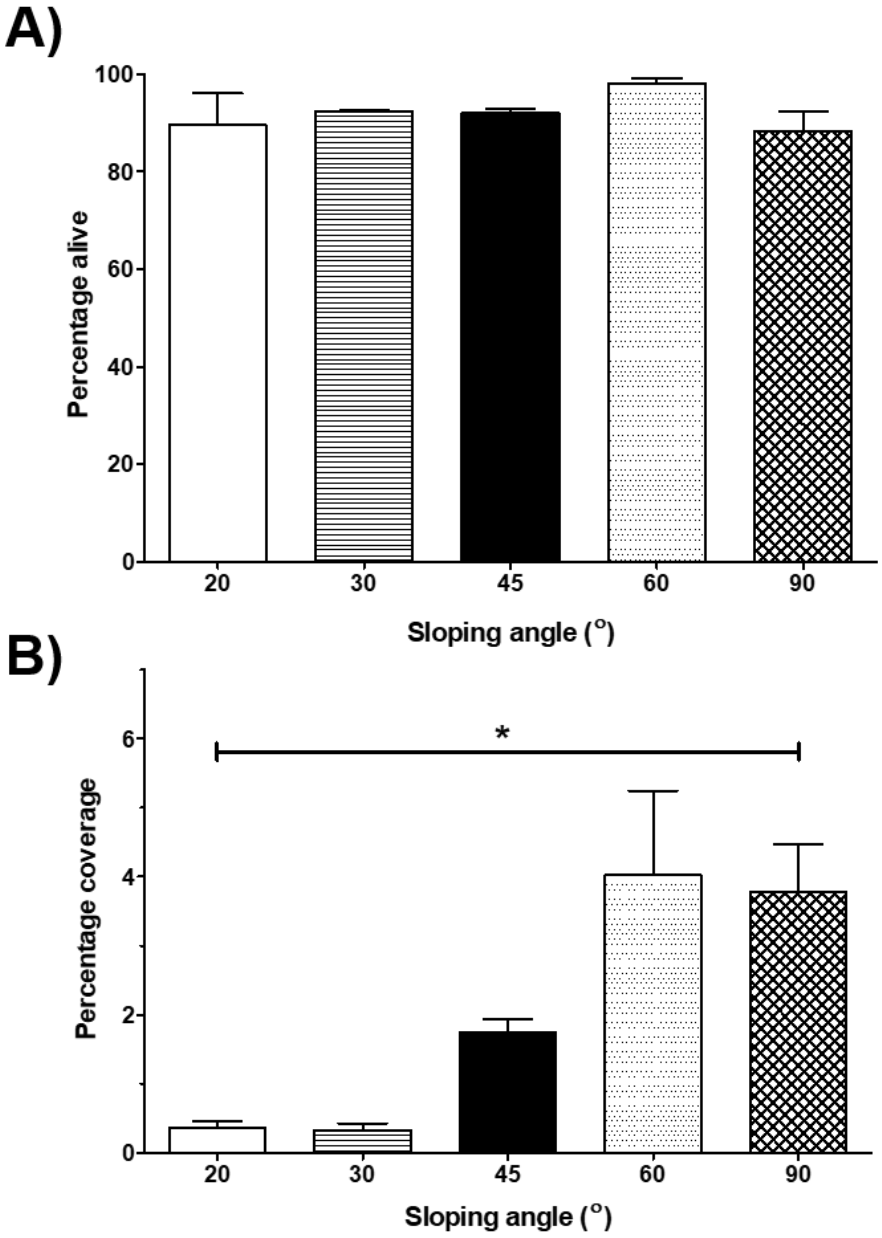


Figure 4.8: Analysis of *S. epidermidis* biofilms grown on additively manufactured coupons at different sloping angles: (A) Percentage alive and (B) Percentage coverage.

Finally, the translation of the presented method has a further application investigated in this research. One of the advantages of CLSM imaging is that it can generate an understanding of the 3D structure of a biofilm using z-stacks. Not only can this provide

information about biofilm thickness and biomass, but the application of the image analysis protocol can elucidate information about biofilm composition throughout. In addition, the total number of pixels that correspond with bacteria (live or dead) can also be used to calculate biomass as 'percentage coverage', i.e. the number of stained pixels as a percentage of total pixels in the image. This was carried out for an *S. sanguinis* biofilm cultured for 1 and 7 days on a Thermanox coverslip (Figure 4.9). For the 24-hour biofilm, viability remained consistent throughout, ranging between 82.9% and 99.18%. However, the coverage increased in the centre of the biofilm, peaking at 69.0% at 41 $\mu$m from the coverslip, and decreased towards the surface, ending at 19.24% at 58 $\mu$m from the coverslip. In contrast, viability varied significantly across the 7-day biofilm. Low viability was observed in the centre, with values lower than 50% for distances between 23 $\mu$m to 46 $\mu$m from the coverslip surface. In contrast, high viability was detected at the coverslip interface (99%) and on the biofilm surface (100%). The reduction in viability in the centre of the biofilm may be due to nutrients being limited and unable to reach those species in the centre or could be caused by an oxygen gradient throughout the biofilm. Percentage coverage, which relates to biomass, also decreased in the centre of the older biofilm, dropping below 45% between 10 $\mu$m and 52 $\mu$m from the coverslip, which may have been linked to the fact that viability had decreased significantly.

For the younger biofilm, the percentage of live cells remained consistent and above 80% throughout its depth. However, in comparison the viability of the 7-day old biofilm was reduced significantly in the centre and increased towards the surface. The reduced coverage identified in the centre of the 7-day biofilm compared with the 24-hour biofilm could be explained due to biofilm age. More mature biofilms that have increased EPS compared with early-stage biofilms may prevent the live/dead stain diffusing through to the centre and this may explain the reduced coverage at the centre of the biofilms. Gaining an insight into the 3D structure of a biofilm, combined with information on viability, can enhance the

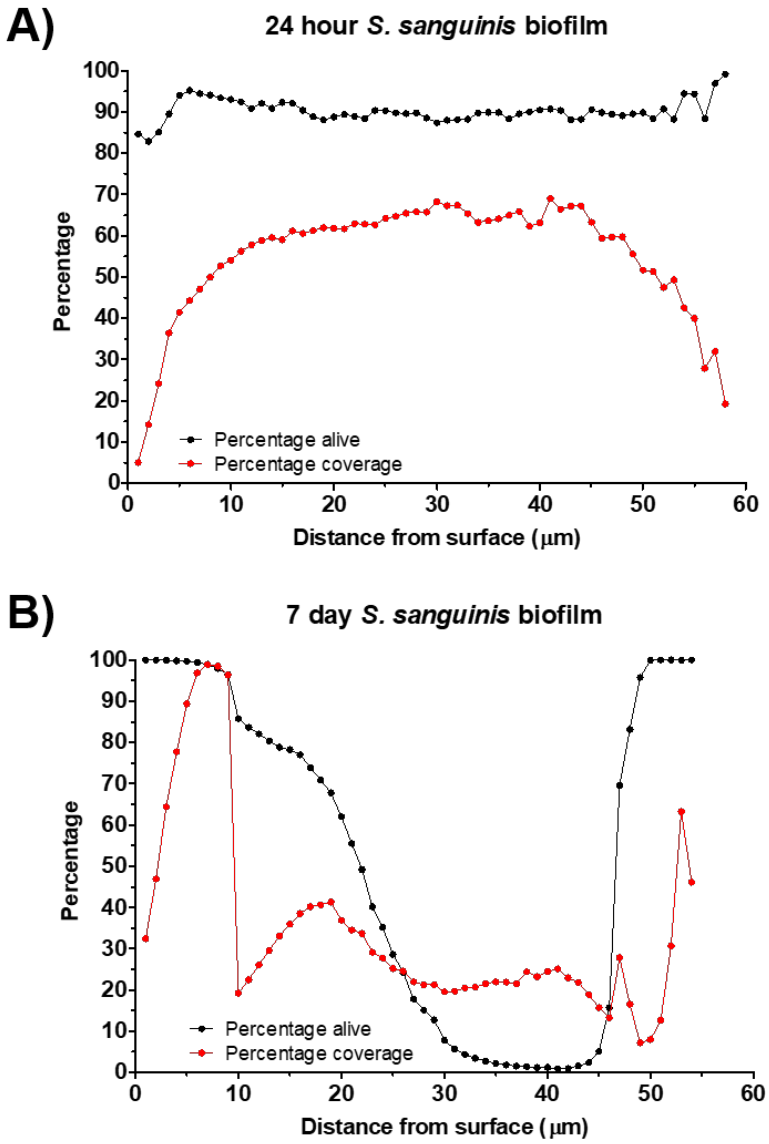


Figure 4.9: Biofilm coverage and viability with increasing distance from coverslip for (A) a 24-hour biofilm of *S. sanguinis* and (B) a 7-day biofilm of *S. sanguinis*. Z-stacks were taken at 1 $\mu$m increments from the surface (the first plane in which bacteria were identified), and hence the distance from the surface is equivalent to the biofilm thickness.

understanding of the effect of antimicrobial compounds and materials. CLSM is an optimal tool for this as it has a large vertical range that can image a biofilm of up to 60 $\mu$m thickness, and fluorescence staining can provide information on viability. Applying the automated

method described in this study to biofilms grown on modified surfaces could provide further information on how the modification is affecting the biofilm structure throughout. Gaining an understanding of biofilm composition is especially important when studying implant-related infections. This method could be applied to biofilms formed on modified implant surfaces to quantify antimicrobial effects. The advantage of the proposed segmentation method is that multiple images can be analysed very quickly and consistently, as well as ensuring each image within a single z-stack is treated the same, increasing comparability across samples.

Over the past two decades, many researchers have attempted to tackle the problem of automated analysis of biofilm micrographs, including developing commercial and free software tools [283–285]. Two approaches can be taken to automated quantification of biofilm images: (1) detect and count discrete objects or cells, or (2) make assumptions regarding the manner in which the properties of the entire image relate to the biofilm characteristics. The choice of which approach to use depends on the size of the cells, the quality and resolution of the image, and the thickness or density of the biofilm. In this study, the latter approach was taken, and the area of green or stain was assumed to be proportional to the number of live and dead cells respectively. Hence, the number of pixels stained red and green were used to quantify the number of viable (live) cells as a percentage of total cells. The reason for selecting this method was driven by the small cell size and frequent overlapping of bacteria in biofilm images, even in high-resolution CLSM micrographs. Furthermore, detecting discrete cells can be challenging if each have different morphologies. Therefore, making assumptions about the relationship between pixel count and bacteria viability ensured that the automated approach was accurate and applicable to a range of cell morphologies. The total number of pixels that correspond with bacteria (live or dead) can also be used to calculate biomass as 'percentage coverage', i.e. the number of stained pixels as a percentage of total pixels in the image.

A number of studies that utilise CLSM to analyse biofilm formation simply visualise

the biofilm and report qualitative results, or conduct manual segmentation of the micrographs [268, 272, 279]. The challenge with these approaches makes comparison with other literature difficult due to the subjective data. Neither of these methods take into consideration any non-specific staining or extracellular matrix staining that may occur when using the FilmTracer LIVE/DEAD Biofilm Viability Kit [288]. Furthermore, segmentation methods that involve manually selecting the cells in an image are time consuming and may result in inconsistent segmentation. To address these challenges, the image analysis protocol presented in this study demonstrated consistent and repeatable results. This was evidenced by a small standard deviation with a CV between 4.24% and 11.5% in the large biofilm study with over 100 images of 20 biofilms (Figure 4.1).

Some of the more frequently used software packages developed specifically for biofilm analysis, such as COMSTAT and BiofilmQ, have an easy to use graphical user interface that is popular. However, one main drawback of both of these packages is that there are no options to apply filters and morphological operators as with those used in the current study [283, 285], which allow for accurate detection of the bacteria in the image whilst neglecting EPS and non-specific staining, commonly found in biofilms. In addition, these software packages rely on the user deciding if pre-processing of the images is necessary, deciding which operators to apply and implementing any pre-processing, which is difficult for those with no prior knowledge of image analysis. In the present work, morphological operators and filters were included in the automated protocol to remove background fluorescence and account for potential staining of the extracellular matrix or extracellular DNA, particularly in the red channel. Furthermore, ImageJ is open-source and familiar to many researchers. Presenting the full macro created in this study enables users to adjust the gamma values, structuring element size, and add or remove steps in the image pre-processing according to their data.

Numerous studies have been published that develop new image analysis methods

for biofilm micrographs, however, many present several hurdles before being suitable to be applied by non-specialists. For example, they are often created in proprietary software such as MATLAB [289–291] or in programming languages such as C++ [292], which make them difficult to use for researchers with little or no programming experience. In some studies, the chosen image segmentation technique was applied to low resolution images where individual bacteria were not visible [293]. In the present research, high resolution (x40 magnification, numerical aperture 1.30) images were used to ensure the segmentations were accurate. Some published studies that use open-source software have not included the code to allow for easy replication by other scientists wishing to use their method. One of the key strengths of this work is that a copy of the code, instructions on how to implement it and an overview of the image analysis protocol are all provided to ensure reproducibility (see Figure 4.3). This allows users to understand the code and easily modify it to fit the data being analysed. For example, if a different staining protocol is used, the pre-processing steps can be removed or adjusted so as not to account for the issues identified with the FilmTracer LIVE/DEAD Biofilm Viability Kit. A further strength of the protocol presented is that it has low computational time, with 25 micrographs analysed in less than 10 minutes (Table 4.1). This allows for an increased number of samples to be analysed and can ultimately improve the robustness of studies investigating antimicrobial techniques to reduce implant-related infection.

There are, however, several limitations to using a method based on CLSM micrographs. Firstly, it is not possible to evaluate the entire biofilm at once; in this study imaging was performed at x40 magnification to obtain high resolution images of individual bacteria in the biofilm. Averaging data from across the biofilm sample and increasing the number of repeats can limit the impact of this. In this work, 5 images were taken across 5 samples for each biofilm condition (Figure 4.5). As the analysis protocol in ImageJ can process many images quickly, increasing the number of samples to account for the limited range of the con-

focal images was straightforward. Linked to this, a second limitation of the work presented its application to poorer quality micrographs. For example, if a sample is not completely flat when imaged using the CLSM, an area of the image may be over or under exposed and this can affect the resulting analysis. It is advisable to take appropriate steps to ensure optimal imaging of the samples. These include ensuring the fluorescent dye has sufficient signal to avoid noise caused by increasing the contrast artificially, ensuring the sample stays horizontal during sample preparation and imaging using a high numerical aperture/magnification to obtain high resolution images. Individual bacteria should be visible in the micrographs being analysed and it is recommended that a minimum magnification of x40 be used to implement the described method. It should also be noted that the results of the analysis will be more subjective if the user selects the location on the biofilm for the image to be taken. User subjectivity can be reduced significantly by taking a high number of images at random locations across the biofilm; a minimum of five per sample is recommended. A final challenge where this workflow demonstrated limitations was that the macro had been tailored specifically for bacterial biofilms and for fluorescent images that were stained with the FilmTracer LIVE/DEAD Biofilm Viability Kit. For this reason, the additional steps taken to reduce the error caused by PI would affect the results if a different fluorescent stain is used by over-reporting viability. Whilst there is potential for the macro to be applied to other confocal images, the workflow may need altering to examine larger mammalian cells or alternative staining protocols. However, this should be possible for users with some image analysis experience, as each step of the macro has been described within the code. Despite the limitations of the proposed approach, it is important to reiterate that CLSM and automated micrograph analysis can prove very useful for researchers working on novel medical and dental devices.

## 4.4 Summary

In summary, this work presents an image analysis protocol for quantifying CLSM micrographs of live/dead stained biofilms. The protocol was validated by comparing with other methods and on different bacterial species, and its use as an adjunct to traditional microbiology techniques was demonstrated, for example to support results from semi-quantitative methods such as crystal violet staining. Therefore, objective 2 of this research to develop a method to analyse confocal micrographs of live/dead stained biofilms for the purpose of analysing biofilm growth on dental implant surfaces, is considered complete. As shown in the present chapter, this approach is a reliable measurement of biofilm growth and cell viability assessment, critical for the development and analysis of novel antimicrobial strategies. This has been demonstrated on Ti-6Al-4V as an example implant material and has proven the tool is effective for such applications.

### 4.4.1 Conclusion

Confocal microscopy is a useful tool to generate high resolution images of live-dead stained biofilms, however quantifying the number of viable cells from these images is challenging. The tool described in this chapter demonstrates that automated tools can be developed that enable researchers to generate quantifiable data from confocal micrographs, such as percentage viability. Whilst developed for the purpose of analysing biofilm formation in the model developed throughout this research project, the method can also be translated to antimicrobial drug and surface modification testing in many different industries and research fields. The key advantages of this protocol are that it is written in open-source software, is easy to use, transparent in function and is modifiable, unlike other available software. This makes it a useful tool for those with different research backgrounds to enable quantitative analysis

of biofilm viability to be performed. Ultimately, this work will support the development of much needed approaches to prevent and treat costly infections.

# Chapter Five

# *In silico* modelling of cell adhesion to surfaces

Computational models can prove a useful tool to examine biological behaviour on different scales and predict behaviour. As this research seeks to improve methods for examining the "race to the surface" between bacteria and tissue cells in the oral cavity, a model that can help to understand the behaviour of bacteria in the presence of different surfaces is a promising tool. Objectives 3 and 4 of this research were to devise a computational model based on cellular automata for evaluating cell adhesion to implant surfaces and use the computational model combined with experimental data to understand the fundamental parameters that affect cell adhesion. This chapter addresses these objectives through the development of a cellular automaton that models the initial stages of surface adhesion of bacteria. The effect of the input parameters on cell number were explored, and the model was fit to *in vitro* experimental data to determine its ability to capture experimental observations.

## 5.1 Introduction

Dental implant infection is not uncommon in patients who undergo implant surgery, with studies suggesting that between 10 and 22% of patients develop peri-implantitis within 10 years of implant placement [22, 23]. Plaque biofilms can form on solid surfaces such as dental implants, and cannot easily be washed away [32]. The human mouth contains a diverse range of microbial organisms that make up the oral microbiome [33]. However, pathogenic species are also present, and if plaque is allowed to accumulate, the numbers of pathogens may increase, shifting the equilibrium from healthy to diseased. The two key barriers to successful implant placement are a lack of osseointegration and the implant becoming infected through colonisation of bacteria on the surface [24]. If untreated, this implant infection can result in the development of the inflammatory disease peri-implantitis. Many groups are developing novel materials and coatings for dental implants to try and reduce bacterial surface colonisation and improve the integration of the implant with the surrounding tissues. However, one of the many challenges with analysing these novel designs is assessing the interactions that occur between the host tissue, the implant, and the oral microbiome. Whilst this research thus far has sought to establish techniques for examining different aspects of these interactions, including a 3D *in vitro* tissue model and a tool for calculating biofilm viability using confocal microscopy, all *in vitro* methods have limitations.

In this chapter, a computational model of bacterial surface adhesion is described. Modelling biofilm growth using a computational approach has many advantages, and it can support the development of *in vitro* systems by providing an understanding of the fundamental processes of biofilm formation, which can subsequently be tested *in vitro*. In addition to fundamental understanding, computational models also offer the possibility to include elements that are more challenging to introduce *in vitro*, such as an immune response.

### 5.1.1 Computational models of biofilm formation

Some of the early computational models of biofilms represented biomass as a continuum, based on population-averaged behaviour [172]. These models treat the biofilm as a continuum with certain properties, for example as a viscous fluid or gel, and model the dynamics of biofilm growth by using differential equations [173, 174]. However, such models often struggle to capture or predict the local environments in the biofilm influenced by the presence of multiple species. This subsequently led to the development of "agent-based" or "individual" biofilm models where each bacterium is modelled explicitly, with the higher-level population behaviour emerging from their lower-level interactions [169]. In agent-based models, biofilm growth is assumed to be a stochastic process [174]. These types of models are useful for studying complex systems such as biofilms, in which individual heterogeneity and spatial interactions are important. However, incorporating the production and effects of the extracellular polymeric substance (EPS) and modelling movement of bacteria to, from, and within the biofilm is very challenging [172]. Furthermore, they introduce elements of randomness due to their stochastic nature and so several runs of the model (in the same state) are required before any conclusions can be drawn [174], and this can be computationally very expensive.

One type of agent-based model that can overcome the computational expense of individual-based models is a cellular automaton. Cellular automata are discrete models that condense the physical process of biofilm formation into a series of simple rules, which are consequently fairly easy to compute. They have been used for a variety of applications across many fields including biology, physics, ecology, geography, and sociology [176, 177]. Specifically within biological systems, cellular automata have been used to model the immune system, tumour growth, and angiogenesis [312]. The reason for their widespread use is their ability to create complex behaviour from simple rules [178].

A cellular automaton is a collection of cells on a grid that evolves through discrete time steps according to a set of rules. In these models, each space or cell on the grid has a state associated with it, for example a live or dead bacterium, or a bacterium of a certain species. The state of a cell at the next iteration of the model is determined by earlier states and the rules of the system. The computational model used in this study was based on a cellular automaton, which has many advantages. Firstly, cellular automata are typically more simple in design than other types of models such as those based on nonlinear partial differential equations [174]. This creates more potential for researchers from non-mathematical disciplines to apply the model to their data, and in the case of the present model, offers the potential to be utilised by those working in the dental and oral biology fields. Secondly, cellular automata are experimentally cheap to implement compared with *in vitro* or *in vivo* experiments, allowing the user to simulate many thousands of different scenarios that could never all be investigated in the lab. This offers the potential for the computational model to guide and inform *in vitro* experimental work. Thirdly, a cellular automaton is mechanistic, and so it is simpler to run several simulations in parallel to investigate the effect of the parameters used in the model. Finally, the rules of a cellular automaton can be constructed around the interpretable parameters of interest, which has an advantage when it is being used to support the development of *in vitro* systems. Therefore, a cellular automaton is an excellent way to model the initial stages of biofilm formation, which is relevant to the concept of the "race to the surface" previously described in Chapter 1. Surface adhesion is the first stage in biofilm formation and preventing or inhibiting it is key to tackling infection. The results of the simulations from this model have the potential to inform our approach to dental implant design.

This model focused on the initial colonisation of the implant surface and sought to understand the effect of certain parameters that influence bacterial adhesion. This work lays the foundations for more detailed models in the future that incorporate the presence of

mammalian cells, and a move towards a cellular automaton that can capture the 3D nature of biofilm formation, looking at the medium to long-term biofilm growth, rather than simply the initial surface colonisation captured in the present model.

## 5.2 Materials and Methods

### 5.2.1 Model formulation

The cellular automaton was built using MATLAB (Version R2017b) and is based on a study by van Gestel and Nowak [184] that aimed to model the evolution of cell differentiation in the context of surface colonisation, and is developed from code written by Paul Roberts (University of Birmingham). In this thesis, the code was expanded to include the ability to track dead cells. Furthermore, this model had not previously been used to fit to experimental data and hence, in this work, the model was tested to determine whether or not it is suitable for fitting to *in vitro* data. See Appendices C and D for a transcript of the model code with and without dead cell counts, respectively. The model in the present work had the following components, each of which are described in detail below.

1. The *environment* within which the agents exist.
2. The *agents* of the model, consisting of different bacteria species.
3. The *rules* that govern the dynamics of the system, representing the interactions of the individual bacteria with each other and the surface.
4. The *timescales* upon which the rules are executed.

**The environment**

The spatial environment of the cellular automaton represented the oral microenvironment in which the dental implant exists. The model environment had two components – a surface and a liquid compartment.

In order to represent the surface of a dental implant material, upon which a biofilm forms, this model contained a 2D surface marked by a hexagonal grid. The size of the grid could be adjusted within the model by attributing the number of grid spaces, G, along each axis. For example, a grid size of G = 10 resulted in a grid of 100 spaces, with each space able to bind 1 agent. Therefore, the width of each grid space roughly represented the diameter of a single bacterium, approximately 10 $\mu$m for *Streptococcus sanguinis* (*S. sanguinis*), a commensal species used in the experimental work in Chapter 4.

The liquid above the surface was where all the bacteria existed at the start of each simulation, i.e. initially the bacteria formed a fully planktonic culture. This liquid compartment did not have a dictated spacial size but was assumed to be a 3D environment directly above the grid surface. The liquid was assigned a carrying capacity (K), which was the maximum number of bacterial cells that could exist in the compartment before it became saturated and could not hold any more cells. Figure 5.1 depicts the spatial environment of the model showing the liquid compartment and grid surface.

**The agents**

This model represented a two-species model, containing two different types of bacteria: 'sticky' and 'non-sticky'. The difference between these two agents was the rules by which they could migrate to the grid surface from the liquid compartment. The sticky cells were able to migrate to any point randomly chosen on the grid, representing an early coloniser in

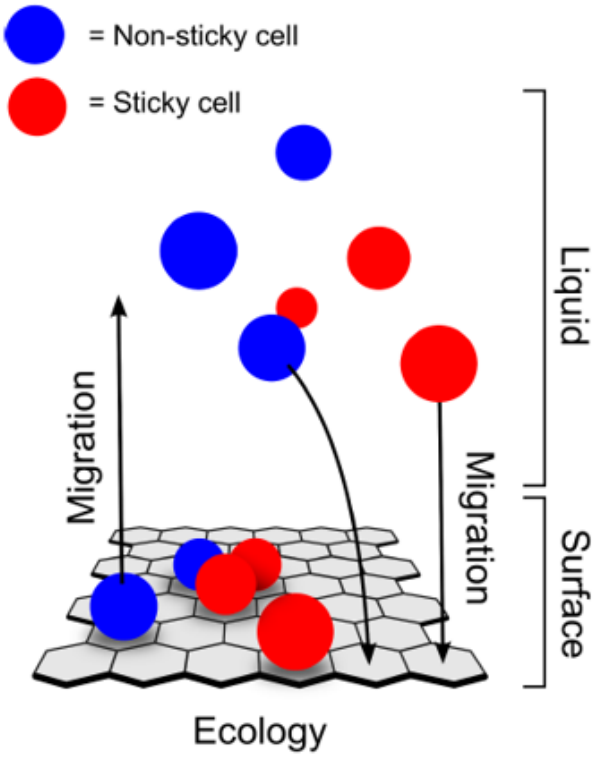


Figure 5.1: Depiction of computational model of bacterial adhesion to an implant surface (adapted from van Gestel and Nowak [184]). The model contained a 2D surface marked by a hexagonal grid, and a liquid above the surface from which cells could migrate to occupy a space on the grid. This model has been adapted to represent a two-species system with 'sticky cells' and 'non-sticky cells'. Sticky cells were able to migrate to any point randomly chosen on the grid. However, non-sticky cells were only able to migrate to the surface when a neighbouring grid space was occupied by a sticky cell.

biofilm formation. However, non-sticky cells were only able to migrate to the surface when a neighbouring grid space was occupied by a sticky cell. This simulated the process of biofilm adherence from a single species followed by later colonisation of a different species [313], essentially modelling cooperative biofilm formation. This is relevant in instances whereby a commensal species adheres and subsequently recruits a pathogenic species, as is the process for the formation of biofilms that cause oral disease. Figure 5.1 demonstrates the movement of sticky and non-sticky cells in the model.

**The rules**

As described in the previous section, the first rules of the model dictated where and when a bacteria cell could bind to the surface, depending on the species (sticky or non-sticky). A single iteration of the model operated as follows:

1. A bacteria cell was chosen at random.
2. One of three actions was chosen at random: divide, migrate, or die.
3. The action occurred based on the assigned probability of that event (see below).
4. The model performed (or did not perform) the action, updated the cell counts and moved on to the next iteration of the simulation.

The model uses probabilities to determine whether an action occurred or not upon each iteration. These parameters are input ahead of each simulation and consist of division probability (for each species), migration probability (to the surface), and death probability (see Table 5.1). The starting cell populations ware also input – this is the number of cells of each species, sticky or non-sticky, that start in the liquid compartment at iteration $i = 0$. The carrying capacity is input (as described in the previous section), as well as the size of the grid (see Table 5.1). With regard to unbinding from the surface, the model did not account for this as an action, and therefore sticky cells remained bound to the surface once this action had occurred. However, if a non-sticky cell was found to be bound to a grid space with no surrounding sticky cells, the non-sticky cell was released from the surface back into the liquid compartment.

The outputs from the model included total cell counts for each species in each location (surface-bound and 'free' cells in the liquid) In later developments of the code, the cell counts

were also separated by whether a cell was alive or dead. Multiple simulations were run (with a minimum of 100 simulations for each set of parameters) and an average was taken. The number of live cells as a percentage of total cell number was calculated at each iteration of the code, for comparison with experimental data.

#### Time

Time was discrete in this model. Thus, a simulation consisted of finite time-steps or iterations ($i$). The state of the system at time-step $i + 1$ was computed by applying a series of rules to the system at time-step $i$. In order to determine the length of time each iteration represents, the model was fitted to experimental data and therefore each iteration depended on the length of time the *in vitro* experiment lasted.

### 5.2.2 Model interrogation and parameter exploration

Firstly, the model was interrogated by counting the live cells at different parameter inputs to compare the outputs and understand the cell count over a simulation ($i = 0$ to $i = 400{,}000$). The parameters used for each of these simulations are shown in Table 5.2. This range of parameters were chosen to best study their individual effects on the cell counts for each cell type. For all simulations, a carrying capacity of 5,000 cells was set for the liquid: the maximum number of cells that can be present in the liquid at any one time. If the liquid was at capacity, no free cells were able to divide – this represented the stationary phase of a planktonic growth curve [314]. For each simulation, a starting population of 200 cells of each species was selected.

Once the behaviour of the model was established, the next objective was to clearly understand the effect of four key input parameters on the number of cells of each type (sticky

Table 5.1: Description of parameters used in the computational model. Typical values are given but a range were explored throughout, see for example Table 5.2.

| **Parameter** | **Symbol** | **Description** | **Typical value** |
|---|---|---|---|
| *Sticky cell division probability* | R | A value between 0 and 1 that marks the probability of a sticky cell dividing. | 0.75 |
| *Non-sticky cell division probability* | D | A value between 0 and 1 that marks the probability of a non-sticky cell dividing. | 0.5 |
| *Cell migration probability* | P_m | A value between 0 and 1 that marks the probability of any cell migrating from the liquid to the surface. | 0.2 |
| *Cell death probability* | P_d | A value between 0 and 1 that marks the probability of any cell dying. | 0.1 |
| *Carrying capacity* | K | The maximum number of cells that can exist in the liquid compartment. A cell cannot divide if the liquid has reached the carrying capacity. | 5000 |
| *Grid size* | G | The length of one side of the grid (e.g G = 10 would produce a 10x10 grid of 100 hexagonal grid spaces). | 100 |
| *Starting population of sticky cells* | Free sticky cells init | The initial number of sticky cells present in the liquid compartment at i = 0 (before the simulation starts). | 100 |
| *Starting population of non-sticky cells* | Free non-sticky cells init | The initial number of non-sticky cells present in the liquid compartment at i = 0 (before the simulation starts). | 100 |

Table 5.2: Parameters investigated to look at cell counts over the course of a simulation and the effect of different parameters. (P_m = migration probability, P_d = death probability, R = sticky cell division probability, D = non-sticky cell division probability.)

| **Simulation feature** | **P_m** | **P_d** | **R** | **D** |
|---|---|---|---|---|
| Baseline | 0.1 | 0.1 | 1.0 | 1.0 |
| High migration probability | 0.75 | 0.1 | 1.0 | 1.0 |
| High death probability | 0.1 | 0.75 | 1.0 | 1.0 |
| High sticky cell division probability | 0.1 | 0.1 | 1.0 | 0.1 |
| High non-sticky cell division probability | 0.1 | 0.1 | 0.1 | 1.0 |
| Low division probability | 0.1 | 0.1 | 0.1 | 0.1 |

and non-sticky) adhered to the surface and in the liquid compartment (Table 5.3). To do this, two of the four input parameters listed in Table 5.3 were fixed at either low (0.2), medium (0.5) or high (0.8) probabilities, and the other two input parameters were varied between 0.2 and 0.8 in increments of 0.1. The reason that very high and very low parameters were excluded from the input parameters was for two reasons. Firstly, it was expected that the extreme probabilities would not be representative of the *in vivo* environment. Secondly, often these extreme parameters resulted in a cell count of 0, or the maximum number of cells (on the surface or in the liquid). When trying to understand the effect of the input parameters on the outputs using heatmaps or data reduction techniques, a large number of 0 or maximum values in the results would skew the analysis.

Heat maps were generated for different combinations of two input parameters on the effect of a single output. Probability parameters not being investigated were fixed at three values: low (0.2), medium (0.5), and high (0.8). This resulted in a total of 72 heat maps that were used to assess the effect of input parameters on each output. The other parameters were fixed at K = 5,000 (carrying capacity), G = 100 (grid size), $i$=400,000, and the starting

Table 5.3: Parameters investigated for exploration of the input probabilities on cell number.

| **Input parameters** | **Outputs** |
|---|---|
| Division probability of non-sticky cell (D) | Number of sticky cells in the liquid |
| Division probability of sticky cell (R) | Number of non-sticky cells in the liquid |
| Migration probability (P_m) | Number of sticky cells on the surface |
| Death probability (P_d) | Number of non-sticky cells on the surface |

populations of both sticky and non-sticky cells both were fixed at 200. The MATLAB script used to generate the heat maps is reproduced in Appendix E. These simulations did not record the number of dead cells in order to reduce the computational time and the total number of heat maps generated for analysis.

### 5.2.3 Model fitting

Once an initial understanding of the effect of different parameters had been achieved, the next step was to identify the parameters that were relevant to *in vitro* experimental data by fitting the model results to *in vitro* growth curves. In order to do this, single-species bacterial growth curves for planktonic cultures and biofilm cultures were obtained.

#### Planktonic growth curves

*S. sanguinis* growth curves were generated in a 24-well plate (Nunc, Thermo Fisher Scientific). Frozen *S. sanguinis* stock was streaked onto three separate tryptone soya agar (TSA) plates (to ensure 3 biological replicates) and incubated at 37°C, 5% $CO_2$ for 48 hours. Following this, three overnight cultures were set up in 5 mL brain-heart infusion (BHI) broth, one from each agar plate, at 37°C, 5% $CO_2$, shaking at 100 revolutions per minute (rpm).

The three cultures were diluted down to an optical density of 0.05 at 600 nm. A liquid culture containing 10 mL of diluted stock was prepared and incubated at 37°C, 5% $CO_2$, shaking at 100 rpm for the duration of the experiment. At 0, 1.5, 3, 4, 5, 6, 7, 8, and 24 hours, 200 $\mu$L of the liquid culture was placed in the top well of a 96-well plate, and a serial dilution was performed. The dilution was plated onto BHI agar plates and the colony-forming units (CFUs) counted after 24 hours incubation, according to the Miles and Misra method [256]. To generate a growth curve using absorbance, 1 mL of diluted liquid culture (n = 3) was pipetted into 3 wells of a 24-well plate, to provide 3 technical replicates. The absorbance was measured at 600 nm every 30 minutes for 24 hours, using a Tecan Spark microplate reader (Tecan Group Ltd, Switzerland). The plate was kept at 37°C, with orbital shaking at 3 mm for 10 seconds prior to readings. Absorbance readings were taken at 600 nm, using 25 flashes and 100 ms settle time. Between readings, samples were shaken with orbital shaking at 3 mm for 800 seconds.

**Biofilm growth curves**

Frozen stock of *S. sanguinis* was streaked onto a TSA plate and incubated at 37°C, 5% $CO_2$ for 48 hours. Using the colonies grown on the agar plate, an overnight culture of *S. sanguinis* was prepared in 5 mLBHI broth and incubated at 37°C overnight, agitating at 100 rpm for the duration. A serial dilution in BHI broth containing 1% sucrose (w/v) was performed with the overnight culture, from $10^9$ (an optical density of approximately 0.5) to $10^3$ cells/mL. Individual Thermanox coverslips (Nunc, Thermo Fisher Scientific) were placed in the bottom of each well in 24-well culture plates (Nunc, Thermo Fisher Scientific). Prior to adding the planktonic culture, 1 mL of artificial saliva was added to each well containing a cover slip and left for 15 minutes before being removed; this was to aid initial adhesion of the bacteria. Subsequently, *S. sanguinis* monospecies biofilms were prepared by adding 1 mL of the $10^3$ dilution to each well containing a coverslip. The plates containing the biofilms

were incubated for up to 7 days at 37°C, 5% $CO_2$, shaking at 100 rpm, with a change in BHI broth every 24 hours, to ensure a well established biofilm had developed.

Any remaining BHI broth from the *S. sanguinis* biofilms was removed from each well and each coverslip with biofilm was placed in 5 mL of fresh BHI broth in a universal tube. The bacteria were removed from the coverslip by sonication in an ultrasonic cleaner (In-Ceram, Vitasonic) for 10 minutes at 50-60 Hz, followed by agitation using a vortex mixer for 5 minutes. A serial dilution was performed using the Miles and Misra method to count the number of CFUs [256]. This enabled an estimation of the number of live cells found in the biofilm.

### Model fitting

Model fitting was carried out in MATLAB where the fitting function *fminsearch* was used. The model fitting script can be found in Appendix F. The *fminsearch* function searches for the minimum of an unconstrained multi-variable function using a derivative-free method. An additional short function that calculated the value of the function to be minimised was added; in the present work this was the norm of the difference between the experimentally determined number of cells at a given iteration and the number of cells calculated by the cellular automaton at the same iteration.

Several assumptions were made to enable fitting. Firstly, one bacteria cell could bind to one space on the model grid. As one cell of *S. sanguinis* was approximately 1 $\mu$m in diameter, the model grid was therefore assumed to be 100 $\mu m^2$ (0.0001 $mm^2$) in area. As the *in vitro* experimental data was calculated from coverslips of 13 mm diameter (132.73 $mm^2$), the total cell counts from the biofilm growth curve were scaled accordingly. All model fitting was run for 40,000 iterations ($i = 40{,}000$), and it was assumed that the total number of iterations equated to the duration of the *in vitro* experiment. Once the parameters had

been identified, 50 further simulations were run using these parameters to generate the model result and this was compared to the experimental data. Model fitting approaches were carried out on both the grid surface using biofilm growth curve data, and the liquid compartment using planktonic growth curve data.

## 5.3 Results and Discussion

### 5.3.1 Model interrogation and parameter exploration

#### Initial simulations

Figures 5.2 and 5.3 show the results of the first simulations run using the model to understand the cell count over the course of the total iterations, and to gain an initial understanding of the behaviour of the model. See Table 5.2 in the Methods section for details of the parameters chosen for this initial study. From the baseline parameters chosen (Figure 5.2A and B), it was evident that the liquid reached full carrying capacity fairly quickly, at around the 25,000$^{\text{th}}$ iteration, and remained at full capacity for the duration of the simulation. It is worth noting that the population of free (liquid) cells was dominated by the non-sticky cell-type at the earlier timescale, but by the end of the simulation, the liquid was dominated by sticky-cells. The surface was dominated by sticky cells throughout, as expected, as non-sticky cells could only migrate to the surface if a sticky cell was present in an adjacent grid location.

A high migration probability (Figure 5.2C and D) resulted in a slightly longer time to reach peak carrying capacity within the liquid, at around the 40,000$^{\text{th}}$ iteration. The ratio of sticky to non-sticky cells present on the surface also decreased compared to the baseline parameters. This could be due to the probability of migration being higher, hence

the probability of a non-sticky cell migrating to a grid space next to a sticky cell was also higher.

Cell numbers significantly decreased both in the liquid and on the surface when a high death probability was introduced, as anticipated. The liquid still reached maximum carrying capacity, though at a significantly later point in the simulation, at around the 100,000$^{\text{th}}$ iteration. This suggested that cells were able to continue proliferating and occupying surface space despite the high death probability. Therefore, the balance between the various event probabilities (death, migration and division) must play a role in determining the final cell number, as a high death probability alone did not result in a low number of cells in the liquid and on the surface. This is further investigated in the next section.

Changing the division probabilities for each cell type produced interesting results. Whilst the total cell numbers on the surface changed very little from the baseline parameters when a high sticky cell division probability was introduced (Figure 5.3A and B, compared with Figure 5.2A and B), the population was entirely made up of sticky cells. There are mechanisms by which bacterial species in biofilms inhibit the growth other species, for example through matrix inhibition and quorum sensing [315]. Whilst the present model does not explicitly account for these aspects of biofilm formation, the behaviour observed from the model outputs did reflect that of competitive biofilm formation. However, where the non-sticky cells had a significantly higher proliferation probability, there was almost no surface migration at all (Figure 5.3C and D).

Finally, selecting very low division probabilities for both cell types resulted in a cell count of zero in the liquid and on the surface (Figure 5.3E and F). This scenario is unlikely to occur in a real-world surface adhesion scenario and therefore was not considered further in the analysis of the model.

In summary, the initial investigation into the cellular automaton demonstrated it

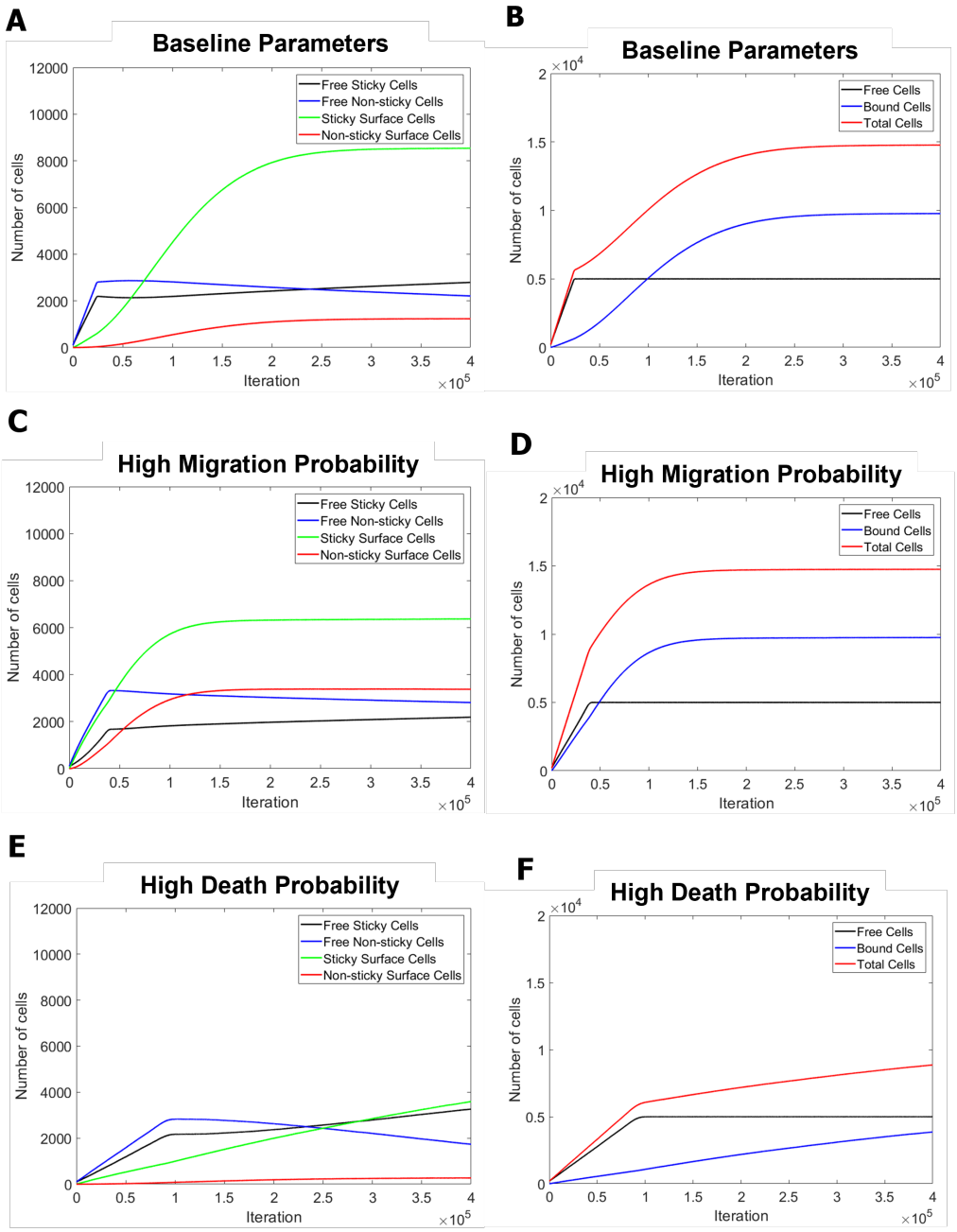


Figure 5.2: Cell number plotted against iteration for each set of parameters investigated (see Table 5.2. (A), (C) and (E) show cell count separated into individual cell species (sticky and non-sticky). (B), (D) and (E) show total cells counts on the surface and in the liquid. Free cells are present in the liquid. Bound or surface cells are adhered to the surface.

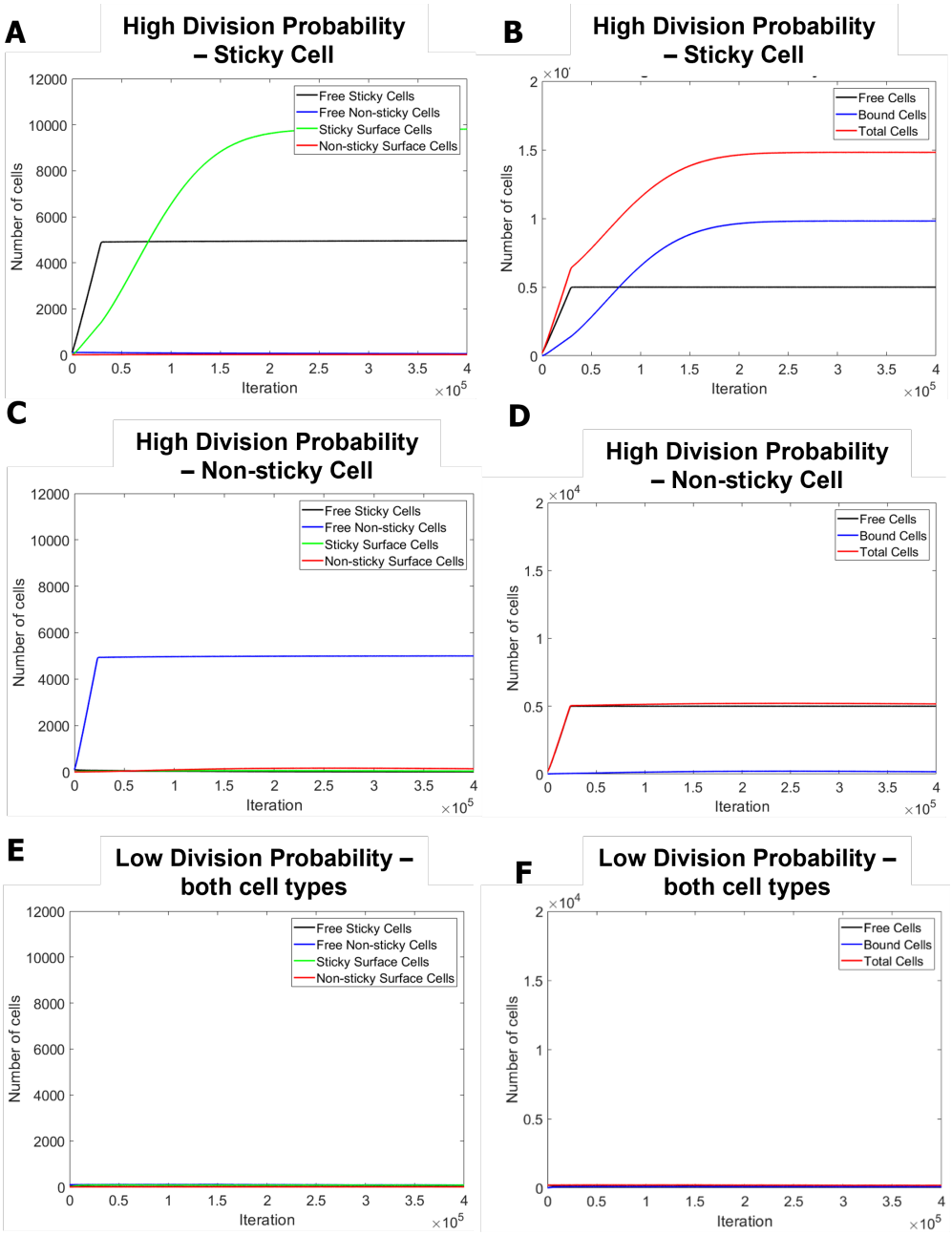


Figure 5.3: Cell number plotted against iteration for each set of parameters investigated (see Table 5.2. (A), (C) and (E) show cell count separated into individual cell species (sticky and non-sticky). (B), (D) and (E) show total cells counts on the surface and in the liquid. Free cells are present in the liquid. Bound or surface cells are adhered to the surface.

captured a range of scenarios that could inform *in vitro* and *in vivo* observations of surface adhesion of bacteria. The model was designed to represent a two-species system whereby cooperative biofilm formation occurs, through the use of sticky and non-sticky cell types. One limitation of these preliminary studies was that a single simulation was analysed. Cellular automata can produce a range of results with the same input parameters due to their discrete and rule-based nature. However, this was sufficient for early analysis to glean foundational insight into the relationship between the model parameters and the outputs. In further studies in this chapter, the mean output value of 100 simulations was used for analysis. Furthermore, whilst studying the simulation results of arbitrary parameters such as those used in this section can provide some indication of the effect of different parameters on cell number, it was identified that a more methodological approach would allow for parameters to be contextualised to *in vitro* and *in vivo* scenarios.

**Effect of input probabilities on cell number**

Once an initial understanding of the model behaviour was established, the next step was to more thoroughly identify the impact of each of the input event probabilities (death, migration and division) on the number of cells of each species on the surface and in the liquid compartment. To do this, a series of heat maps was generated. These analyses aimed to link the parameters in the cellular automaton to their clinical relevance in preventing bacterial surface adhesion to dental implants. In total, 72 heat maps were generated. In this section, the results of most interest are presented. See Appendices G and H for all heat maps generated in this analysis.

Firstly, the effect of different parameters on the number of sticky cells adhered to the surface was examined. Figure 5.4 shows the surface sticky cells as a result of a range of division probabilities for sticky (R) and non-sticky (D) cells. The other input variables,

death probability (P_d) and migration probability (P_d), were fixed at low (0.2), medium (0.5), and high (0.8) values. For all three simulations, an increasing division probability of the non-sticky cell reduced the number of sticky cells on the surface.

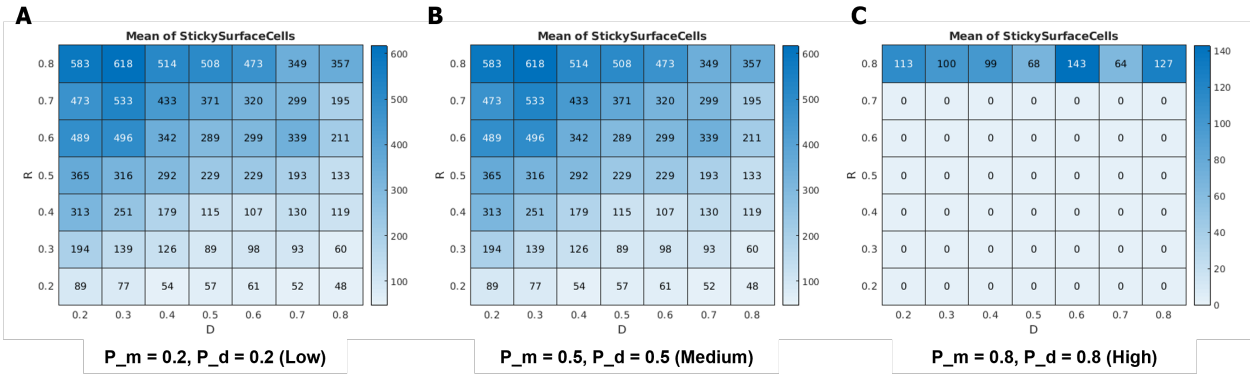


Figure 5.4: Number of sticky cells on the surface at $i$ = 400,000 for a range of values of R (sticky cell division probability) and D (non-sticky cell division probability). The migration probability (P_m) and death probability (P_d) were fixed at (A) 0.2, (B) 0.5, and (C) 0.8.

No clear relationships were identified between the number of sticky cells adhered to the surface and the input parameters migration probability (P_m) and non-sticky cell division probability (D). At low division probabilities (R = 0.2 and D = 0.2), a death probability of 0.3 or greater was high enough to prevent any sticky cells adhering to the surface at $i$ = 400,000 (Figure 5.5A). Similarly, when R = 0.5 and D = 0.5, a death probability of 0.6 or greater resulted in no sticky cells adhering to the grid surface (Figure 5.5B). This suggested that at lower division probabilities, the death probability had the greatest influence over sticky cells adhering to the surface. However, at high division probabilities (R = 0.8 and D = 0.8), cells managed to adhere to the surface for all simulations run (Figure 5.5C). This suggested that if cells have a high probability of dividing, initial surface adhesion can take place. Clinically, this may suggest that if the bacteria have a high growth rate, introducing a mechanism to kill the cells (such as antibiotics) may not always prevent bacteria cells adhering to an implant surface. A study by Theophel et al. [316] studied the simultaneous

cultivation and time-resolved growth analysis of *Enterococcus faecium* (*E. faecium*) in the presence of a range of antibiotics at different concentrations. The authors found that low concentrations of some antibiotics resulted in only partial inhibition of the growth of *E. faecium* and the paper presented extended lag phases in the growth analysis. After the extended lag phase, exposure to several antibiotics led to reversible growth inhibition, which could be compensated for by higher cell densities until the end of the experiment. Exposing *E. faecium* to fosfomycin or fusidic acid even resulted in higher maximum specific growth rates [316]. This study supports the findings of the simulations from the model developed in the present work, whereby the model suggests an increased growth rate could facilitate survival of the bacteria. The mechanism by which this growth behaviour occurs is not known. However, it should be noted that the study by Theophe et al. [316] was conducted in planktonic cultures so cannot be directly compared to the surface adhesion modelled in the cellular automaton.

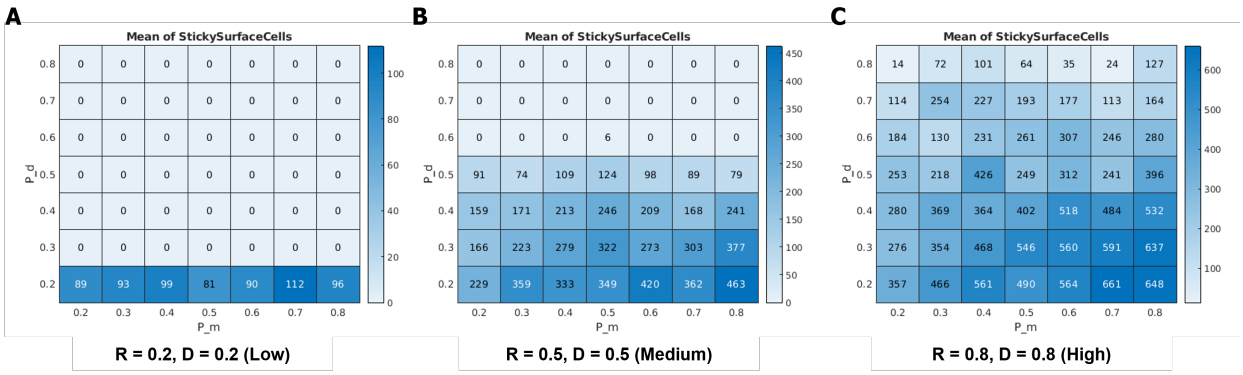


Figure 5.5: Number of sticky cells on the surface at $i$ = 400,000 for a range of values of P_d (death probability) and P_m (migration probability). The sticky cell division probability (R) and non-sticky cell division probability (D) were fixed at (A) 0.2, (B) 0.5, and (C) 0.8.

For non-sticky cells, most input parameter values gave rise to no cells adhering to the surface (See Appendix G). For example, a high death probability (P_d), a high sticky cell division probability (R), and a low migration probability (P_m) all resulted in a non-sticky

surface cell count of zero. This suggested that the conditions had to be optimum in order for a cell that is unable to adhere to a surface without the presence of an early coloniser to adhere. For example, as demonstrated in Figure 5.6, a high division probability of both sticky and non-sticky cells was needed to result in non-sticky cells adhering to the surface. If we consider non-sticky cells to be an invasive pathogenic species (e.g. *Porphyromonas gingivalis*), and sticky cells to be commensal oral species, the model captures cooperative biofilm formation whereby pathogenic species cannot adhere to a surface without the presence of an early coloniser.

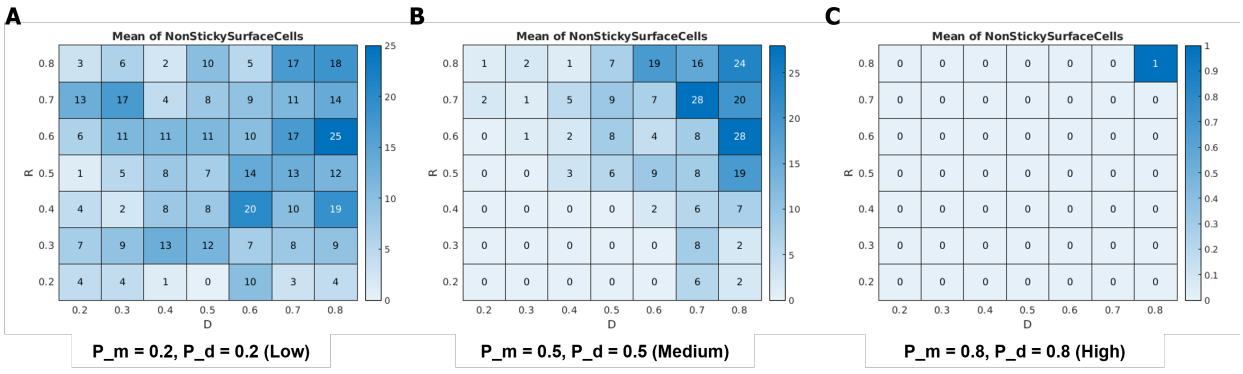


Figure 5.6: Number of non-sticky cells on the surface at $i = 400{,}000$ for a range of values of R (sticky cell division probability) and D (non-sticky cell division probability). The migration probability (P_m) and death probability (P_d) were fixed at (A) 0.2, (B) 0.5, and (C) 0.8.

Death probability had a great influence on the number of sticky cells present in the liquid at $i = 400{,}000$. A medium to high death probability (P_d = 0.5 or P_d = 0.8) typically resulted in zero sticky cells in the liquid compartment. The exception to this was when high migration probability (P_m) and high division probability of the sticky cell (R) were input. This could perhaps have been because the carrying capacity (5,000) was significantly lower than the total number of cells that could adhere to the surface (100,000). *In vitro*, biofilms have been shown to have higher antibiotic resistance than bacteria in planktonic cultures [317]. Whilst the present computational model did not incorporate antimicrobial

agents, heat map analyses suggested the cellular automaton appeared to support these observed *in vitro* behaviours. Even in the presence of antibiotics, the cells are more likely to form biofilms.

In summary, this analysis further aided the understanding of the input parameters on final cell number. Examining the results as heat maps allowed for the parameters to be compared to *in vitro* and *in vivo* scenarios. This knowledge could be tested through *in vitro* experiments by trying to influence the parameters of death probability (for example by using a range of concentration of antimicrobial), migration probability (for example by using different surfaces to form biofilms on) or by controlling division probability (for example by limiting the nutrients available). In this section, the parameter effects have been linked to potential clinical scenarios, in order to demonstrate how models such as the present cellular automaton can support the development of strategies to prevent infection of dental implants. By determining the parameter with the greatest impact on surface cell numbers, this can inform antimicrobial strategies. For example, if death probability has the greatest effect on surface adhesion, then infection prevention strategies should focus on killing cells after dental implant placement. However, if surface migration probability has the greatest impact on cell adhesion, then strategies should focus on the surface properties to try and prevent this occurring.

The data generated in this analysis is multidimensional and additional strategies could be used to attempt to quantify the effect of different input parameters on cell number. Future studies should investigate the possibility of using dimensionality-reduction techniques such as principal component analysis (PCA) and t-distributed Stochastic Neighbour Embedding (t-SNE). Both techniques aim to reduce the dimensionality of complex datasets, increasing interpretability but at the same time minimising information loss [318, 319].

One of the the drawbacks of cellular automata, is that the rules may be arbitrarily

formulated, which can lead to aesthetically driven outputs [174, 185]. Validation is an essential part of computational modelling, and this thesis presented a great opportunity to utilise the results of *in vitro* experiments to enhance the computational model. This validation and fitting process ensured the parameters and rules used in the cellular automaton described are grounded in *in vitro* observations. Therefore, the model was fitted to biofilm and planktonic growth curves. Up until this point, a range of starting parameters and scenarios have been considered. For validation, the model was tailored to a single-species biofilm.

### 5.3.2 Model fitting

In order to determine the input parameters that represented a specific *in vitro* cell adhesion to surfaces, the model was fitted to planktonic and biofilm growth curves of *S. sanguinis*.

#### Planktonic growth curves

As the cellular automaton contained a liquid compartment as well as the grid surface, planktonic growth curves were generated to fit to this aspect of the model. *S. sanguinis* planktonic growth curves were generated as a basis for comparison with biofilm growth. Figure 5.7 shows the resulting curves generated. A logistic growth equation was fitted to both curves, with $R^2$ values of 0.9907 and 0.9226 for absorbance and CFU/mL respectively. The logistic growth curve is described by Equation 5.1 [320]

$$\frac{dP}{dt} = rP(1 - \frac{P}{K}) \tag{5.1}$$

Where $P$ is population size, $t$ is time, $r$ is the growth rate, and $K$ is the carrying capacity.

This equation represents a continuous model, which can be used for the planktonic

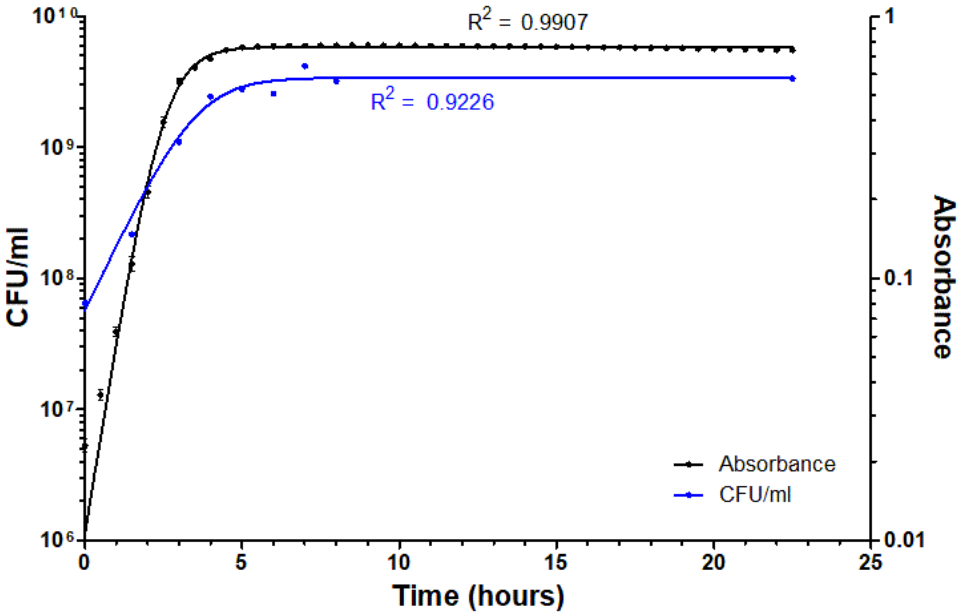


Figure 5.7: Planktonic growth curve of *S. sanguinis*. Two methods were used to produce a growth curve. Absorbance was recorded every 30 minutes for 24 hours by measuring the optical density of the culture at 600 nm wavelength. A serial dilution was performed on the planktonic culture at 0, 1.5, 3, 4, 5, 6, 7, 8, and 24 hours and the CFUs were counted at each time point.

culture because it was assumed to be well-mixed. This does not apply for the biofilm model because spatial considerations become more important. Furthermore, it should be noted that an optical density of zero in theory would be equal to zero CFU/mL, however this is not possible in practice due to the sensitivity of the equipment. Hence the logistic curve fit demonstrated in Figure 5.7 is true above an optical density of 0.05.

### Biofilm growth curves

Single-species biofilms of *S. sanguinis* were used to generate *in vitro* data to fit the model. Figure 5.8 shows the total number of bacteria cells in each biofilm, counted using a haemocytometer. Biofilm growth was rapid over the first 24 hours, then increased at a slower rate

over the following 7 days, representing the log and stationary phases of bacterial growth. Compared to the planktonic cultures, the stationary phase was reached later, at 24 hours for the biofilm and between 5-8 hours for the planktonic culture (Figure 5.7). Slower growth of biofilms has been linked to nutrient limitation for some cells within the biofilm, and also linked to a general stress response initiated by growth within a biofilm that is not observed with planktonic cultures [321]. The key advantage of this slower growth is that slow or no growth is generally accompanied by an increase in resistance to antibiotics [321].

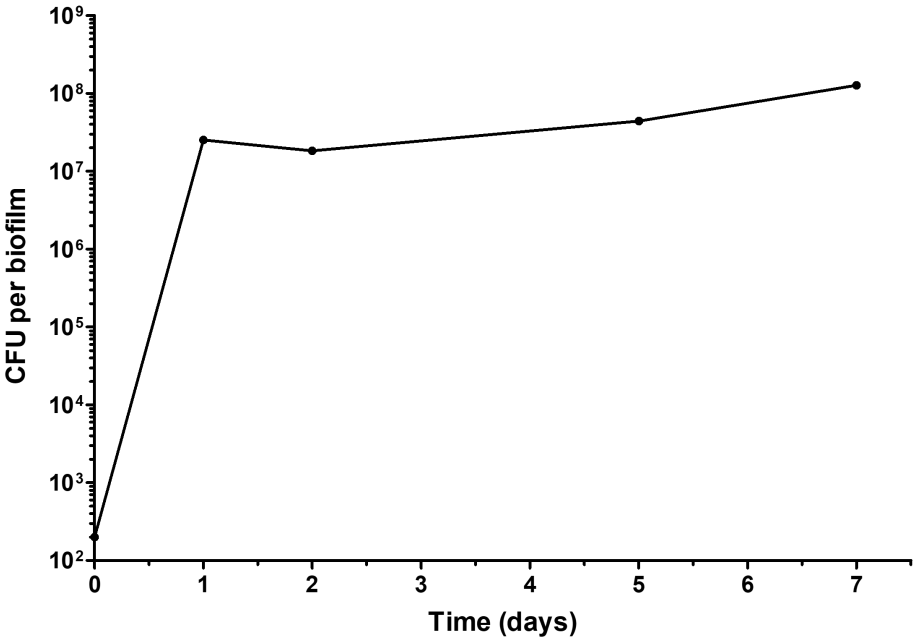


Figure 5.8: Biofilm growth curve of *Streptococcus sanguinis*. Biofilms were analysed at 0, 1, 2, 5 and 7 days (n = 3). Each coverslip with biofilm was placed in 5 mL of fresh BHI broth in a universal tube. The bacteria were removed from the coverslip by sonication in an ultrasonic cleaner for 10 minutes at 50-60 Hz, followed by agitation using a vortex mixer for 5 minutes. A serial dilution was performed using the Miles and Misra method to count the number of colony-forming units (CFU) [256]. This enabled an estimation of the number of live cells found in each biofilm.

Table 5.4: Cell counts entered into model fitting script to identify parameter values for *in vitro* experimental data.

| **Time point (days)** | 0 | 1 | 2 | 5 | 7 |
|---|---|---|---|---|---|
| **Time point (iteration)** | 0.1 | 5,174 | 11,428 | 28,570 | 40,000 |
| **Original mean-average CFU** | N/A | 25,138,889 | 18,333,333 | 44,166,667 | 126,666,667 |
| **Data input into model fitting code** | 1 | 19 | 14 | 34 | 96 |

**Fitting biofilm data to the cellular automaton model**

For the first model fitting, the CFU count for *S. sanguinis* biofilms at 1, 2, 5 and 7 days was equated to total sticky surface cells in the cellular automaton. No non-sticky cells were included in the model fitting to reflect the single-species *in vitro* experimental data that was generated. Several assumptions were made to enable fitting. Firstly, the CFU counted from each biofilm from the *in vitro* experimental data was assumed to represent a single cell from the biofilm: the CFU value was directly equated to biofilm cell count. Secondly, the model allowed only one bacteria cell to bind to one space on the model grid. As one cell of *S. sanguinis* is approximately 1 $\mu$m in diameter, the model grid was therefore assumed to be 100 $\mu m^2$ (0.0001 $mm^2$) in area. As the *in vitro* experimental data was calculated from coverslips of 13 mm diameter (132.73 $mm^2$), the total cell counts from the biofilm growth curve were scaled accordingly. Finally, for the initial fitting attempt, the biofilm was assumed to cover the entire coverslip (100% surface coverage), although this assumption was revised in later fittings. Table 5.4 shows the values used to fit to the model. To use the fitting code, initial parameter guesses needed to be entered and these were selected to be R = 0.75, P_m = 0.01, P_d = 0.01 and K = 5,000.

Figure 5.9 shows the results of the first model fitting, based on the assumptions described previously. The model fitting script identified the parameter values to be R = 0.7, P_m = 0.0025, P_d = 0 and K = 5,211. As can be seen from Figure 5.9, the model appeared to increase linearly, unlike the experimental data. However, based on this figure, it was felt to be a reasonable fit.

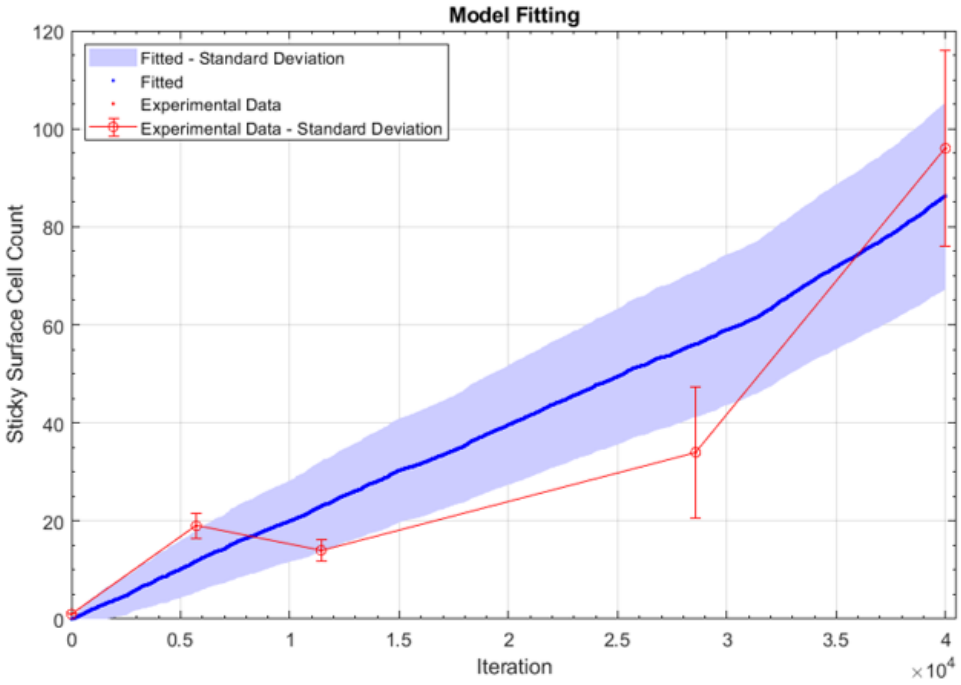


Figure 5.9: Comparison of experimental data (red) and cellular automaton results for sticky surface cells (blue). Output parameters from the model fitting were R = 0.7, P_m = 0.0025, P_d = 0 and K = 5,211. For experimental data, n = 3 (mean ± standard deviation) and for the model fitting, n = 50 (mean ± standard deviation.)

Next, the results from running the cellular automaton using these parameters were plotted, and can be seen in Figure 5.10. This enabled both bound and free cells to be visualised. From this fitting attempt, it appeared that *S. sanguinis* divided rapidly in the liquid compartment, but these cells did not adhere well to the surface over the course of 7 days (under these fitted parameters). The maximum capacity (K) in the liquid is reached at about iteration $i$ = 30,000 (just after day 5 in the experimental data). *S. sanguinis*

is known to be an early coloniser for biofilms and this was therefore an unexpected model output. Though the number of bound cells matched the experimental data well, it was surprising that so many cells remained in the liquid compartment. A migration probability of 0.0025 was extremely low, whilst the division probability of the sticky cells was high at 0.7, which resulted in the large difference between the number of cells in the liquid compartment compared to on the grid surface.

Next, the assumption used in the above model fitting, that 100% of the coverslip was covered in biofilm, was challenged, as this was not observed in the *in vitro* biofilm growth. Biofilm coverage of different amounts of the coverslip was assumed to range from 10% to 100% and new experimental data values were calculated based on this assumption (Table 5.5). Furthermore, it was observed that the death probability from the previous model fitting was zero or close to zero for all outputs and the carrying capacity did not change significantly from the initial guess. To focus the fitting function on the migration probability (P_m) and division probability (R), the carrying capacity (K) and death probability (P_d) were fixed at 0.01 and 5,000 respectively.

Table 5.6 and Figure 5.11 show the results from fitting to the experimental data assuming different surface coverage. Initial parameter guesses of R = 0.75 and P_m = 0.01 were input to the fitting script, with fixed values of K = 5,000 and P_d = 0.01 (fixed values meant that the fitting function would not iterate over these parameters). The results suggested that the surface coverage that best fit the experimental data could fall between 10% and 50%. However, as with the previous fitting experiment, when the full model results were plotted, the number of cells in the liquid compartment was far higher than the number of sticky cells on the surface (Figure 5.12). As before, since *S. sanguinis* is an early coloniser, this result suggested there could be an error in the assumptions used or the choice of model fitting function.

Table 5.5: Cell counts entered into model fitting script to identify parameter values for *in vitro* experimental data, assuming different surface coverages.

| **Time point (days)** | Assumed percentage coverage (%) | 0 | 1 | 2 | 5 | 7 |
|---|---|---|---|---|---|---|
| **Time point (iteration)** | | 0.1 | 5,174 | 11,428 | 28,570 | 40,000 |
| **Original mean-average CFU** | | N/A | 25,138889 | 18,333,333 | 44,166,667 | 126,666,667 |
| **Data input into model fitting code** | 100 | 1 | 19 | 14 | 34 | 96 |
| **Data input into model fitting code** | 75 | 1 | 26 | 19 | 45 | 127 |
| **Data input into model fitting code** | 50 | 1 | 38 | 28 | 67 | 191 |
| **Data input into model fitting code** | 10 | 1 | 190 | 139 | 333 | 955 |

Table 5.6: Cell counts entered into model fitting script to identify parameter values for *in vitro* experimental data.

| **Assumed surface coverage (%)** | **R** | **P_m** |
|---|---|---|
| 100 | 0.7819 | 0.0101 |
| 75 | 0.8010 | 0.0080 |
| 50 | 0.7781 | 0.0096 |
| 10 | 0.7485 | 0.0105 |

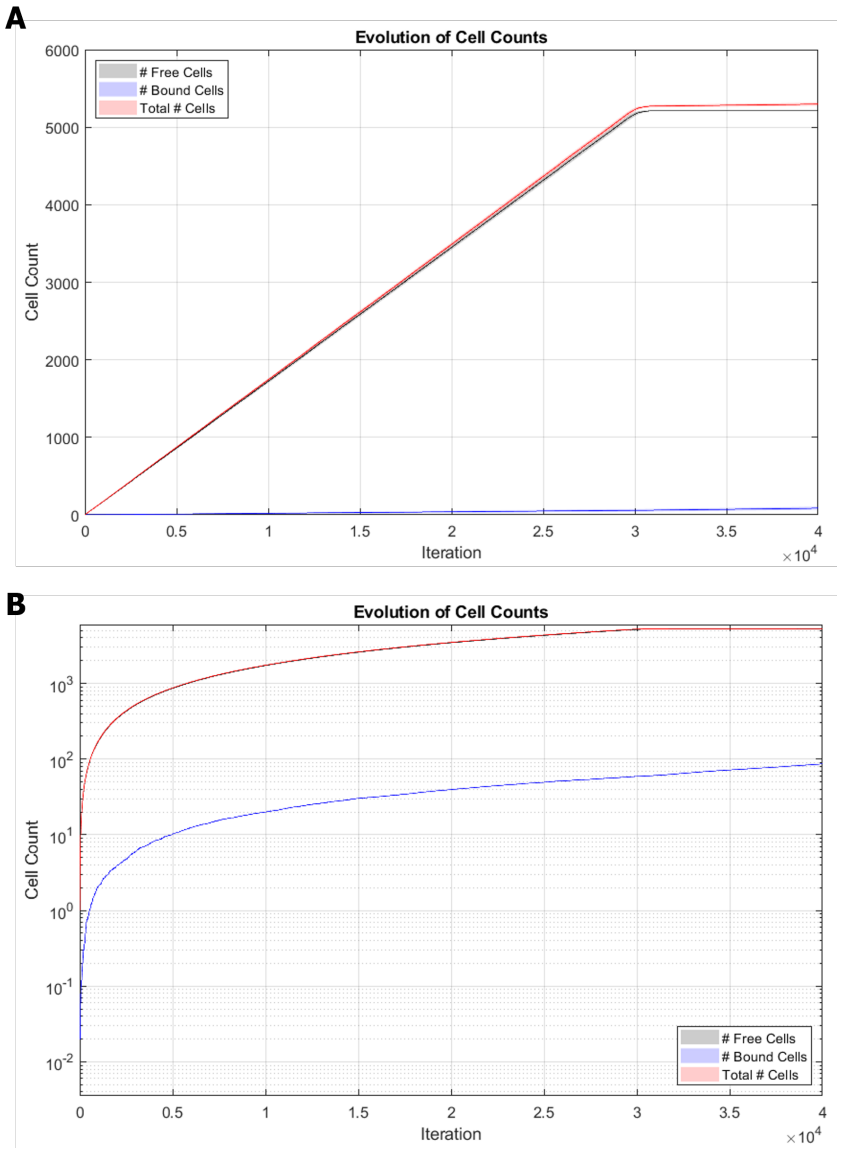


Figure 5.10: Results of cellular automaton using parameters from model fitting: R = 0.7, P_m = 0.0025, P_d = 0 and K = 5211 (n = 50, mean ± standard deviation). (A) Results plotted on a linear y-axis and (B) results plotted on a log10 y-axis. Carrying capacity is not reached until iteration $i = 30{,}000$.

To continue the model fitting process further, the liquid compartment was fit to the planktonic growth curve data, although over a shorter timescale than the biofilm growth curve. Further assumptions were made in order to scale the experimental data to fit the scale of the model. The volume of the liquid compartment was not specified in the model.

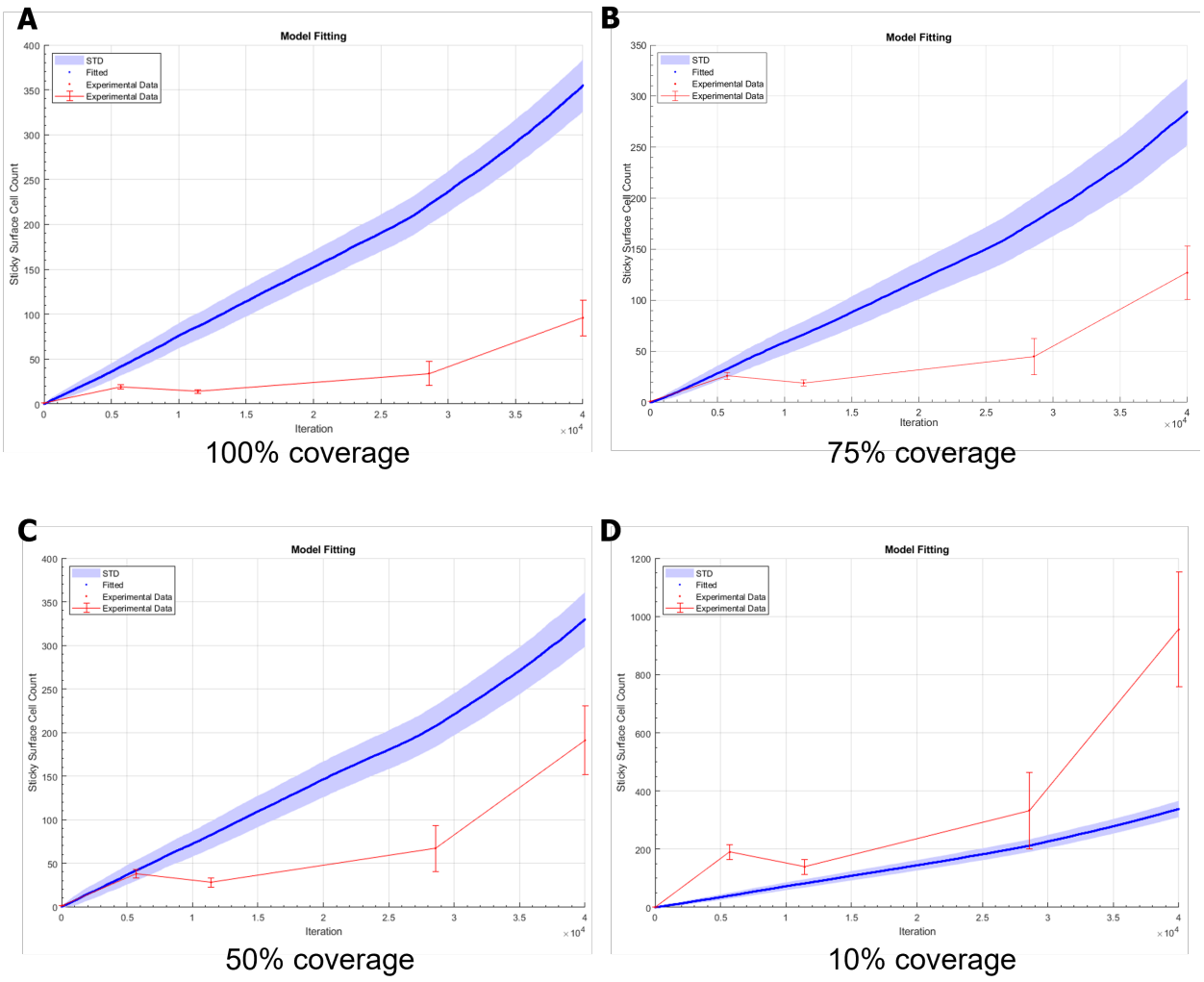


Figure 5.11: Comparison of experimental data (red) and cellular automaton results for sticky surface cells (blue). For experimental data, n = 3 (mean ± standard deviation) and for the model fitting, n = 50 (mean ± standard deviation). Assumed surface coverage used to calculate the experimental data to input into the model fitting script: (A) 100% surface coverage, (B) 75% surface coverage, (C) 50% surface coverage and (D) 10% surface coverage.

To fit the experimental data, it was assumed that the liquid compartment was a cube with the length of each side equal to the length of the grid, and therefore the volume of the liquid compartment was 1,000,000 $\mu m^3$. In the *in vitro* experiment, the volume of planktonic culture in each well was 1 mL, and therefore the CFU per mL (or per well) was scaled

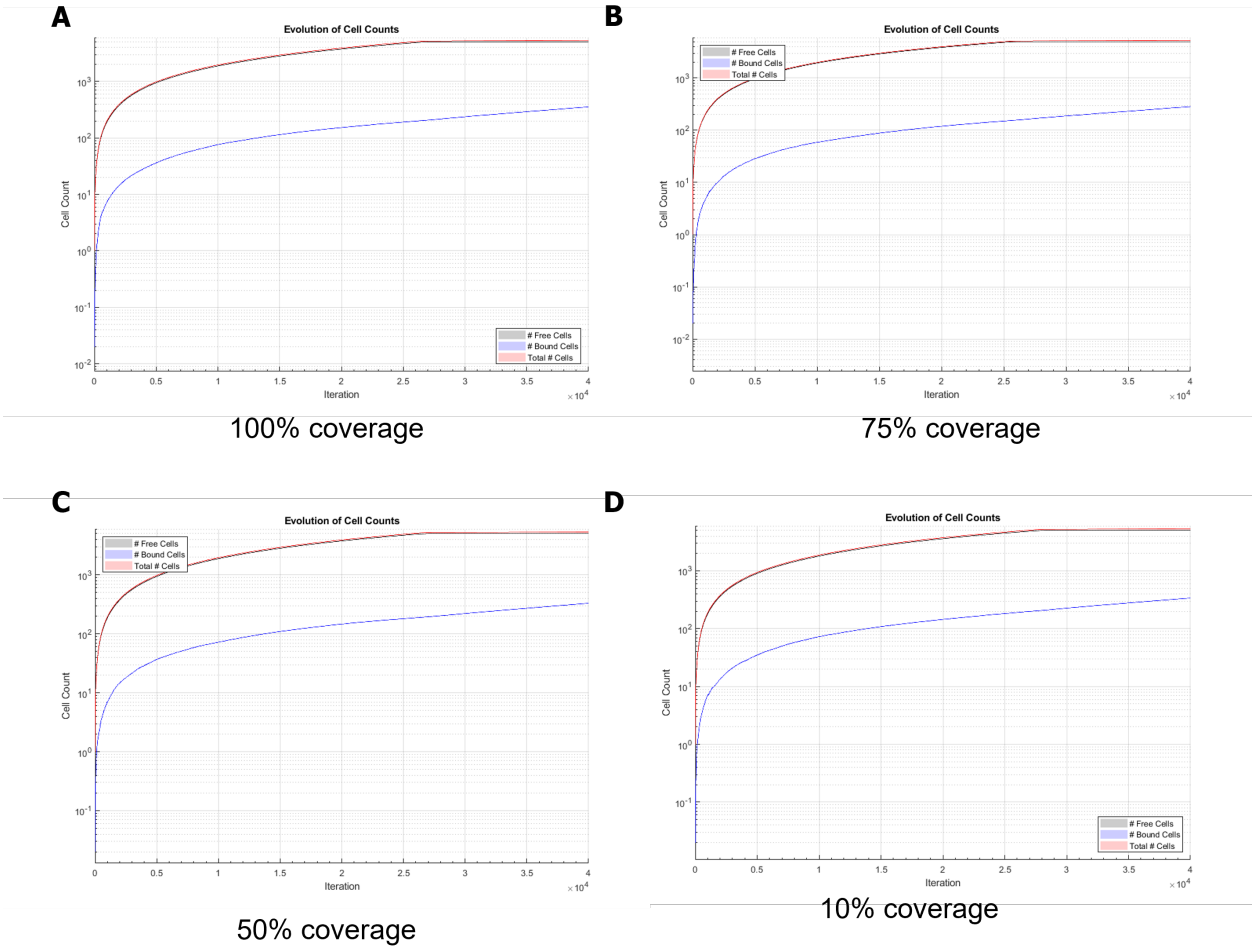


Figure 5.12: Results of cellular automaton using parameters determined from model fitting (n = 50, mean ± standard deviation). Assumed surface coverage used to calculate the experimental data to input into the model fitting script: (A) 100% surface coverage, (B) 75% surface coverage, (C) 50% surface coverage and (D) 10% surface coverage. Carrying capacity is reached between iteration $i$ = 25,000 and iteration $i$ = 28,000 for all surface coverage conditions.

accordingly to fit the size of the environment in the cellular automaton. For this fitting, three parameters were investigated: sticky cell division probability (R), migration probability (P_m) and the carrying capacity (K). The death probability was fixed at 0.01 as per the previous model fittings. Initial parameter guesses were input as R = 0.5, P_m = 0.2 and K = 4,000. The results of the model fitting compared to the experimental data is shown in

Figure 5.13. The results of the full simulation are shown in Figure 5.14.

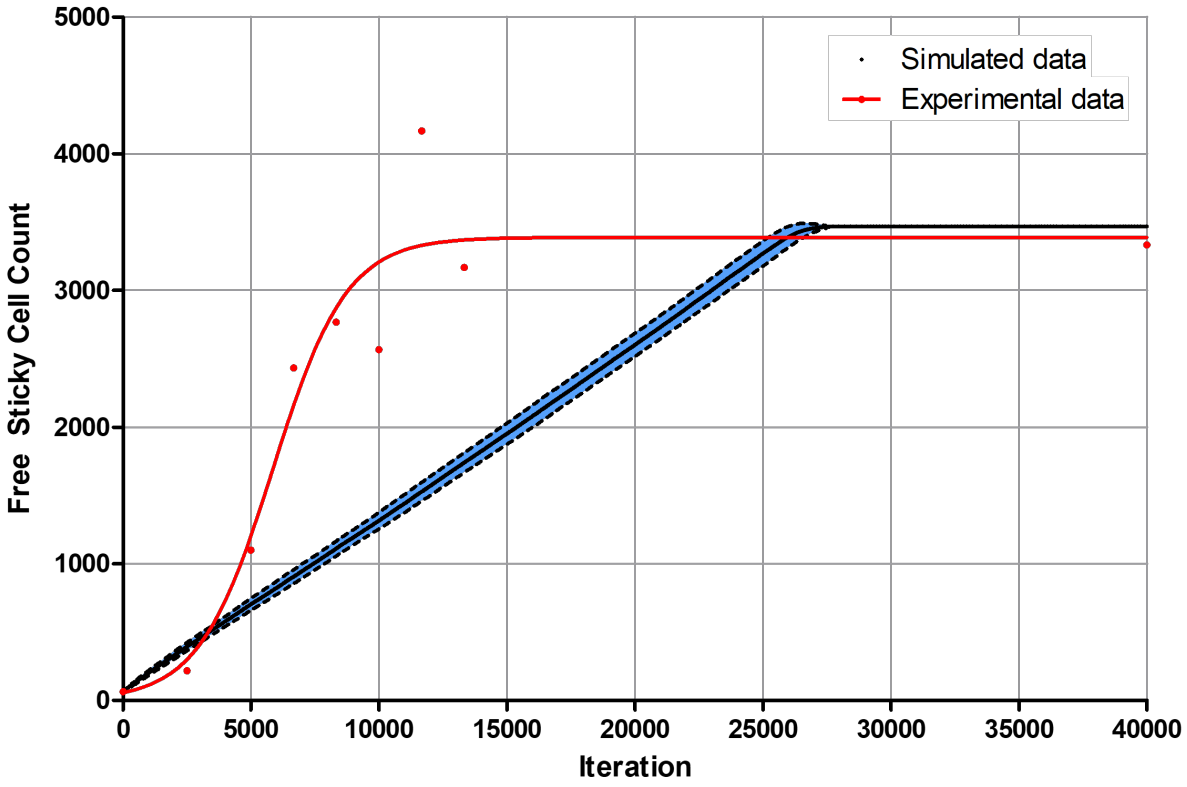


Figure 5.13: Comparison of experimental data (red) and cellular automaton results for free sticky cells in the liquid compartment (blue). For experimental data, n = 1 with a logistical curve fit. For the model fitting, n = 50 (mean ± standard deviation).

Comparing the experimental and simulated data showed that the growth rate of the simulated bacteria was much slower than that of the experimental data. *In vitro*, the stationary phase (or carrying capacity) was reached at iteration $i = 15{,}000$. The simulated liquid compartment did not reach its carrying capacity until $i = 27{,}500$. However, the parameter for division probability of sticky cells obtained from the model fitting was 0.9, indicating that the model could not feasibly achieve a faster rate of growth as the probability of division was close to the maximum value of 1. Figure 5.14 showed that there was a steady increase in the total number of sticky cells adhered to the grid surface throughout

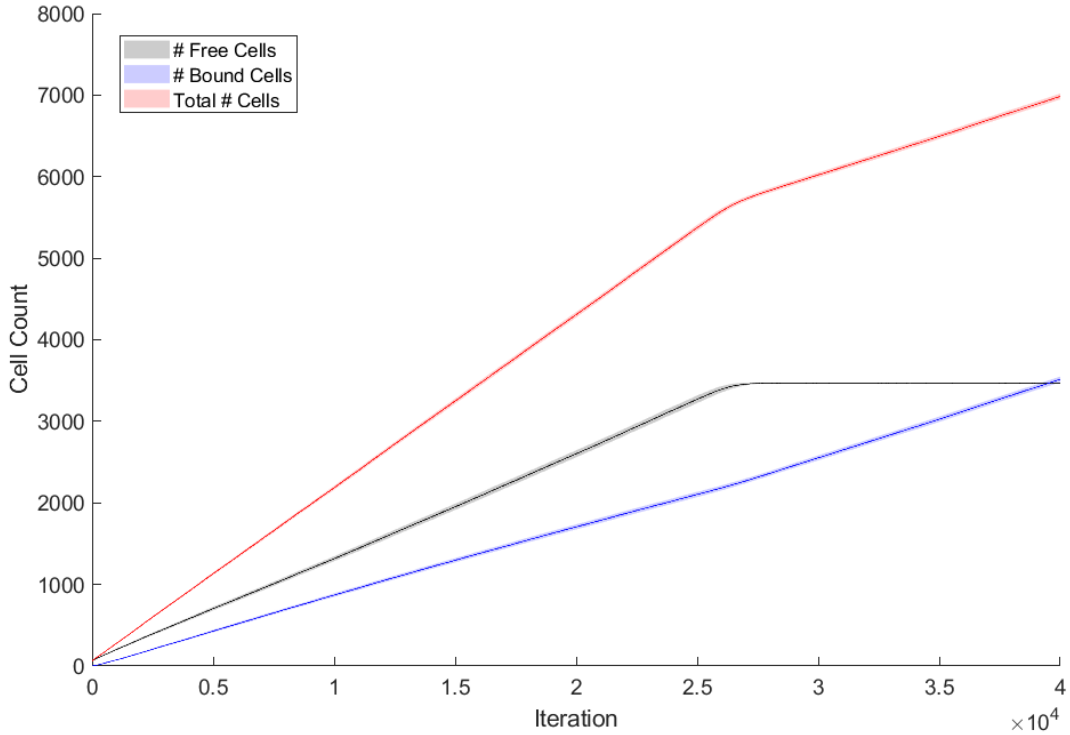


Figure 5.14: Results of cellular automaton using parameters determined from model fitting (n = 50, mean ± standard deviation).

the simulation, even at a low migration probability of 0.2, which was the predicted value of this parameter for the model fitting. Overall, the surface cell count reached 3,000 by the end of the simulation and this is much higher than the sticky surface cell count that was simulated when fitting the model to the biofilm growth curve data, which reached a maximum of 350 when 100% surface coverage was assumed (Figure 5.11). This suggests that the experimental liquid growth curves were better for fitting the simulated data to. This could be for several reasons. Firstly fewer assumptions needed to be made to fit the cellular automaton simulation to the liquid growth curve. Secondly, calculating the number of cells within the biofilm required removal of the biofilm from the coverslip, which could have introduced an additional error. Finally, the biofilms from the *in vitro* experiment were grown over 7 days, forming mature 3D biofilms. This model is best suited to simulating the

initial surface adhesion, and this may be a key factor in the poor fit of the simulated data to the experimental biofilm data.

Fitting the model results to *in vitro* data proved challenging. Due to the complexity of the model, it may be that a global minimum was not reached for some of the parameters and instead the solution to the fitting function is a local minimum. Other non-derivative fitting functions could be considered to try and improve the results of the model solutions.

It should be noted that the inability to achieve a good model fit to experimental data is a common issue in computational modelling and often indicates that there is an element of the *in vitro* or *in vivo* system that is not captured in the model. For this reason, there remain some limitations to the present model. The primary limitation is that the model only forms a 2D biofilm, with a single layer of cells able to adhere to the grid. In the body, biofilms are complex 3D systems, with local variations in their environment. Future development of this model should consider adding the ability for 3D biofilm formation to allow the simulation of early to mid-stage biofilm formation. Secondly, there are only two cell species modelled in this system. Future studies could consider expanding the capabilities of the model to multi-species systems, and comparing cooperative biofilm formation, as presented in this chapter, with competitive species (two sticky species competing for the surface). An additional factor to measure *in vitro* in order to improve the fit could be the biofilm surface coverage, which was explored in Figure 5.11. Calculating coverage is possible using the tool described in Chapter 4, and this could be included as a parameter to be fitted in future work.

Parameter sets were identified that enabled the model to reproduce the quantitative data, but when these fits were later tested it was found that the dynamics of the individual sub-populations did not follow the expected qualitative patterns. This highlights the importance of challenging model fits, something which is too often overlooked in model parameterisation. Analysis of the resulting model behaviour paves the way for future improvements

to the model and model-informed experimental design. This is the natural cyclical approach that should always be adopted in computational modelling of biological systems: the data informs the model which informs the experimental design which again informs the model, and so on. This work provides the first crucial step in that process.

## 5.4 Summary

In this chapter, a cellular automaton model of initial surface adhesion of single and two-species biofilms has been presented. In particular, the effect of different input parameters on the number of cells in the liquid and on the surface was the main focus, with the aim of using the knowledge of these effects to identify strategies for preventing surface adhesion. In addition to exploring the scope of the model and understanding how the event probabilities affect cell number, the cellular automaton was fitted to biofilm and planktonic growth curves generated *in vitro*. The results presented in this chapter show that the model can simulate a range of different cell behaviours by controlling the input parameters (event probabilities). Therefore, this agent-based approach is appropriate for exploring this initial step in biofilm formation. Research objectives 3 and 4 have been addressed, namely, to devise a computational model based on cellular automata for evaluating cell adhesion to implant surfaces and use the computational model combined with experimental data to understand the fundamental parameters that affect cell adhesion.

### 5.4.1 Conclusion

The analysis in this chapter has highlighted that the balance between the rate of migration to the surface, division rate, and death rate of a bacteria species has a significant input on the number of cells adhering to the surface. If the balance of these parameters can be controlled

*in vitro* and *in vivo*, then this could inform the development of strategies for preventing surface colonisation and therefore dental implant infection.

# Chapter Six

# Final discussion and conclusion

The "race to the surface" describes the competition between bacteria and eukaryotic cells for colonisation of an implant device. This concept is particularly pertinent to the oral environment, as both soft and hard tissue types and many hundreds of bacterial species interact with a dental implant material once it is placed in the mouth. The destructive disease peri-implantitis is caused through infection of such an implant by pathogenic bacterial species. This can result in inflammation of the surrounding soft tissues, in some cases leading to irreversible bone loss and often requiring secondary surgery to disinfect and replace the device. Therefore, much research has focused on developing novel materials, surface treatments, coatings, and antimicrobial approaches to try and prevent the occurrence of peri-implantitis, which has been reported to affect between 10 and 22% of patients [22, 23]. However, many of these novel antimicrobial approaches have not progressed to the clinic, and this is due, in part, to the complex environment in which these devices are placed that is difficult to model *in vitro*. The preclinical animal models required to test novel devices and antimicrobial interventions to achieve regulatory approval are expensive and require specific expertise. Therefore, physiologically relevant *in vitro* models may provide additional confidence that pursuing animal studies and regulatory approval may be successful.

As outlined in Chapter 1, many models of the interplay between bacteria and the oral mucosa have been published to try and replicate the complex interactions that occur in the oral environment. These models include cells grown in 2D cultures with planktonic bacteria, which are useful for elucidating underlying biological processes, but do not replicate the 3D environment *in vivo*. The two most common approaches to 3D models of the oral mucosa are collagen-based hydrogel scaffolds and decellularised matrix. Whilst a range of 3D oral mucosa models and biofilm models exist, very few studies have combined the two, as it is challenging to analyse such a system *in vitro*. In addition to these challenges with 2D and 3D *in vitro* models, the soft tissues in the oral cavity have an essential role in dispersing the mechanical forces that occur from eating, talking and saliva flow. Several studies have shown that the mechanical strength of an *in vitro* tissue scaffold can influence cell behaviour [115, 116, 125]. However, the 3D oral mucosa models described in the literature have not yet considered the mechanical properties of such scaffolds.

Noting both the challenge of analysing an experimental system that can assess the interaction between the oral mucosa, oral biofilms, and a dental implant material, along with the lack of studies that have investigated the effects of mechanical stiffness on oral fibroblasts encapsulated within a hydrogel scaffold, the first objective of this research was to address these gaps in modelling the oral microenvironment through the development of a 3D hydrogel tissue model with mechanical properties similar to the native tissue. In addition to the development of this *in vitro* model, a solution was proposed to analyse the interactions that occur when placing this tissue model in the context of an implant and biofilm through the development of an automated image analysis tool. Finally, given the challenges associated with modelling such a complex environment, a computational approach was used to examine the initial stages of surface adhesion during biofilm formation. To achieve these aims, an interdisciplinary approach was vital, and this work combined elements of materials science, cell culture, microbiology, and mathematical modelling.

First, the mechanical properties of porcine oral mucosa under compression were determined to establish a basis for the alignment of a hydrogel scaffold to these properties. Porcine oral mucosa was used as a model for human tissue as, histologically, it displays many similarities to human oral mucosa [214]. A blended alginate and collagen hydrogel scaffold was selected such that alginate could provide the mechanical stiffness required and collagen could provide the biological binding motifs to support cell growth. Exploring alternative hydrogel systems was not a goal of this work, but could be an interesting variable to investigate in the future, especially given there are other hydrogel scaffolds that have been used in oral mucosa models including elastin and fibrin [322, 323].

Following the characterisation of the native tissue, the mechanical stiffness of blended collagen-alginate hydrogels at different concentrations was measured. Through these experiments, the stiffness of the blended hydrogel system was found to align well with that of porcine oral mucosa, specifically at 2.5 mg/mL collagen and 5 mg/mL alginate, and 2.5 mg/mL collagen and 10 mg/mL alginate. As previously discussed, mucosa models presented in the literature have not considered the mechanical properties of the native tissue in their development, which was a unique aspect to this approach. The presence of collagen fibrils in the blended scaffold was identified using scanning electron microscopy, and these fibrils were important to support the adhesion of encapsulated cells. Additionally, the gelling behaviour of the acellular scaffold was examined using rheology, and the results demonstrated that the alginate had fully cross-linked within 20 minutes of adding the cross-linking solution calcium chloride ($CaCl_2$), at a concentration of 150 mM. This is important because minimising the time cells were in contact with calcium ions ensured that cell viability would remain high once fibroblasts and epithelial cells were incorporated into the model. It should be noted that the mechanical properties of the blended scaffolds were measured on acellular gels. It is possible that the presence of cells within the hydrogel could impact on the mechanical stiffness of the model. Therefore, an important future study would be to investigate the me-

chanical stiffness of the full model with fibroblasts and epithelial cells present and compare this with the results of acellular scaffolds.

Following the selection of the blended scaffold concentrations, primary human dermal fibroblasts (HDFs) and H400s (an oral epithelial cell line) were incorporated into the model. HDFs were selected for the initial optimisation of the system as they were cheaper to purchase and more readily available. However, they have been shown to display differences from primary gingival fibroblasts. Furthermore, H400s are an oral epithelial cell line and whilst being originally derived from the relevant tissue, cell lines typically display differences to primary cells in culture. Therefore, an important next step in the development of this model would be to repeat the viability studies with more relevant cell types. However, for the purposes of preliminary model development work, HDFs and H400s were deemed to be a good choice. The protocol for producing the *in vitro* mucosa model involved encapsulating HDFs in a collagen-alginate solution and pipetting the solution into transwells. The collagen was allowed to aggregate first by incubating at 37°C for a minimum of 4 hours, followed by adding $CaCl_2$ to cross-link the alginate component. The encapsulated cells were cultured for 10 days, and then H400s were added to the surface. The epithelial cells were raised to an air-liquid interface after 4 days, and finally the model was cultured for a further 10-14 days. Typically, models of the oral mucosa utilise either a fibroblast-containing collagen gel or a decellularised matrix [104, 112, 118]. Decellularised matrix could provide a similar stiffness to the native tissue, but there are challenges to using this method consistently due to variations caused by different decellularisation methods, insufficient preservation of vasculature and extracellular matrix (ECM) composition, and inhomogeneous recellularisation within the scaffold. Therefore, to ensure consistency and repeatability of studies, hydrogels are a useful approach to *in vitro* models. However, collagen hydrogels have low stiffness, and this is a factor that has been previously shown to significantly influence and control cell function and behaviour [115, 116, 125]. A unique aspect of the model described in this thesis is the

inclusion of the alginate component, which provides mechanical stiffness to the scaffold. With the ultimate goal of introducing an implant material to the mucosa model, a scaffold with increased stiffness compared to the commonly used collagen matrix would be advantageous.

The viability and morphology of the cells within the hydrogel model were examined using live/dead staining and confocal microscopy. Blended collagen-alginate hydrogels were shown to support cell growth, with high cell viability observed. Matrix stiffness was found to influence fibroblast morphology, as fibroblasts encapsulated within scaffold with an alginate concentration of 10 mg/mL displayed a rounded morphology, whilst at 5 mg/mL alginate, they demonstrated a typical elongated spindle shape. This finding supports the idea that scaffold stiffness can influence cell behaviour. The next steps for continuing this line of investigation would be to compare gene expression of primary oral fibroblasts encapsulated within collagen-alginate matrices of differing stiffness. Additionally, it would be interesting to try and understand the effect of matrix stiffness on the ability of cells to form a junction with an implant material within the *in vitro* system.

In the present work, preliminary experiments to investigate the presence of an epithelial layer did not provide concrete evidence that one had formed in the *in vitro* model, either through confocal imaging or histological staining. Therefore, further optimisation of the model is still required to produce a mature epithelium. Previous studies have demonstrated that a stratified epithelium can be obtained with H400s, and therefore this approach was considered to have been an appropriate first step in the development of the 3D *in vitro* system. Cell-specific staining is an approach that may help to identify the presence of H400s in confocal imaging, for example by selectively staining for cytokeratins, E-cadherin, or desmoglein-3 to differentiate these cells from the HDFs under the microscope. Once a stratified epithelium has been identified using the blended collagen-alginate system, a similar investigation into the effect of scaffold stiffness on gene expression would form part of the future work. The development of a new approach to generating an *in vitro* model of the

oral mucosa is valuable to the field, despite the further optimisation required. The use of decellularised matrix as a scaffold for such models, as previously described, has challenges of repeatability due to the differences between tissue sources [234].

With the ultimate goal of bringing the engineered mucosa, biofilm and dental material into one *in vitro* model system, a key challenge for this experimental approach is analysing biofilm growth on implant materials in such a complex system. Therefore, alongside the development of the tissue model, consideration was given to how to best address this problem and a novel image analysis tool was developed for quantifying confocal laser scanning microscopy micrographs of live/dead stained biofilms. The advantage of using CLSM is that it enables 3D visualisation of biofilm structure, without the need to remove the sample from the surface and disrupt the specimen. CLSM in combination with viability staining provides high sensitivity, specificity and resolution. However, obtaining quantitative information from confocal micrographs is challenging. The tool developed in this project calculated percentage viability from live/dead stained biofilm micrographs, and was shown to have low computational time, with 25 micrographs analysed in less than 10 minutes. This allowed for an increased number of samples to be analysed and can therefore improve the robustness of studies investigating biofilm formation on implant surfaces.

Whilst developed for the purpose of analysing biofilm formation in the model described in this research project, this tool has broad application to the wider field, for example for antimicrobial drug and implant surface modification testing in many different industries and research fields. The key advantages of this protocol are that it is written in open-source software, is easy to use, transparent in function and is modifiable. This makes it a useful tool for those with different research backgrounds to enable quantitative analysis of biofilm viability to be performed. It has been demonstrated that the current approach is a reliable measurement of biofilm growth and cell viability assessment, critical for the development and analysis of novel antimicrobial strategies. This has been demonstrated on Ti-6Al-4V as

an example implant material and has proven the tool is effective for such applications.

Finally, acknowledging the range of challenges encountered when analysing the complex oral environment *in vitro*, a computational approach was considered. A cellular automaton model of initial surface adhesion of single and two-species biofilms was presented, a highly-relevant stage in the "race to the surface". *In silico* approaches allow for examination of biological behaviour on different scales, can predict behaviour, and may lead to new experimental approaches. Furthermore, a key advantage of using a mathematical model is that it can characterise complex data in terms of few parameters. The computational model was shown to simulate a range of different cell behaviours by controlling the input parameters and therefore, this approach was considered appropriate for exploring the initial step in biofilm formation. Parameter sets were identified that enabled the model to reproduce quantitative *in vitro* experimental data, but when these fits were later tested it was found that the dynamics of the individual sub-populations did not follow the expected qualitative patterns. Analysis of the resulting model behaviour paves the way for future improvements to the model and model-informed experimental design. Further analysis of the model highlighted that the balance between the rate of migration to the surface, division rate, and death rate of a bacterial species has a significant influence on the number of cells adhering to the surface. If the balance of these parameters can be controlled *in vitro* and *in vivo*, then this could inform the development of strategies for preventing surface colonisation and therefore dental implant infection.

To conclude, the work presented in this thesis supports the development of antimicrobial strategies and novel implant devices to prevent the occurrence of infection of dental implants. An interdisciplinary approach was taken to progress the field towards successful culture of a 3D tissue model, biofilm and implant material in a single well *in vitro*. Physiologically relevant 3D *in vitro* models of the oral environment are important to reduce the need for animal models, in line with a 3Rs strategy. Increasing the complexity of experi-

mental models increases the variables that can affect cell behaviour, however these systems need to advance in order to achieve physiologically representative models that can support the progression of novel antimicrobial approaches and implant designs to *in vivo* testing and, ultimately, to the clinic and benefit of patients.

# Chapter Seven

# Future work

A range of further studies have been identified in order to develop the findings of this research; these are outlined below.

- In Chapter 2, the mechanical properties of the blended scaffolds were measured on acellular gels. It is possible that the presence of cells within the hydrogel could impact on the mechanical stiffness of the model. Therefore, an important future study is to investigate the mechanical stiffness of the model with fibroblasts and epithelial cells present and compare this with the mechanical stiffness of the acellular scaffolds.

- In Chapter 3, the cells utilised to assess the ability of the hydrogel scaffold to support cell growth were human dermal fibroblasts and the oral cancer cell line H400. Therefore, an important next step in the development of this model is to repeat the viability studies with more relevant cell types, specifically primary human gingival fibroblasts and primary human oral keratinocytes.

- The preliminary experiments carried out in Chapter 3 to investigate the presence of an epithelial layer did not provide concrete evidence that one had formed in the *in vitro* model, either through confocal imaging or histological staining. Therefore, further

optimisation of the model is still required to produce a mature epithelium.

- In Chapter 3, an interesting observation was that the matrix stiffness of the scaffold influenced the morphology of encapsulated fibroblasts. The next steps are to compare gene expression of primary oral fibroblasts encapsulated within collagen-alginate matrices of differing stiffness, to further understand the relationship between matrix stiffness and cell characteristics. Additionally, it would be interesting to try and understand the effect of matrix stiffness on the ability of cells to form a junction with an implant material within the *in vitro* system.

- Through the development of a cellular automaton in Chapter 5, parameter sets were identified that enabled the computational model to reproduce quantitative *in vitro* experimental data. However, further interrogation of these parameters found that the dynamics of the individual sub-populations did not follow the expected qualitative patterns observed *in vitro*. Future improvements to the model and model-informed experimental design are an important next step in its development, for example refining the assumptions made in the simulations and model fitting.

- The final research objective listed in Chapter 1 was not completed, namely to develop an *in vitro* system that includes an implant material, biofilm, and 3D oral mucosa model that can be used to examine the "race to the surface". A key next step for this research is to combine the elements described in this research into a single *in vitro* model.

# References


(1) Gristina, A. G. *Science* **1987**, *7*, 16–19.

(2) Arciola, C.; Alvi, F.; An, Y.; Campoccia, D.; Montanaro, L. *The International Journal of Artificial Organs* **2005**, *28*, 1119–1125.

(3) Busscher, H. J.; Van Der Mei, H. C.; Subbiahdoss, G.; Jutte, P. C.; Van Den Dungen, J. J.; Zaat, S. A.; Schultz, M. J.; Grainger, D. W. *Science Translational Medicine* **2012**, *4*, 153RV10.

(4) Mountcastle, S. E.; Cox, S. C.; Sammons, R. L.; Jabbari, S.; Shelton, R. M.; Kuehne, S. A. *Jounral of Oral Microbiology (under review)* **2020**.

(5) Duraccio, D.; Mussano, F.; Faga, M. G. *Journal of Materials Science* **2015**, *50*, 4779–4812.

(6) Misch, C. E. In *Dental Implant Prosthetics (Second Edition)*, Misch, C. E., Ed.; Mosby: St. Louis, 2015, pp 1–25.

(7) Drago, C., *Implant Restorations : A Step-by-Step Guide*; Wiley: Somerset, UNITED STATES, 2014.

(8) Pye, A. D.; Lockhart, D. E.; Dawson, M. P.; Murray, C. A.; Smith, A. J. *Journal of Hospital Infection* **2009**, *72*, 104–110.

(9) Gaviria, L.; Salcido, J. P.; Guda, T.; Ong, J. L. *Journal of the Korean Association of Oral and Maxillofacial Surgeons* **2014**, *40*, 50.

(10) Campbell, J. C. Dental Implant Series Part I: What Are the Most Recent Trends in Tooth Replacement in Dentistry, 2016.

(11) Buser, D.; Sennerby, L.; De Bruyn, H. *Periodontology 2000* **2017**, *73*, 7–21.

(12) White, D. A.; Tsakos, G.; Pitts, N. B.; Fuller, E.; Douglas, G. V.; Murray, J. J.; Steele, J. G. *British Dental Journal* **2012**, *213*, 567–572.

(13) Jayachandran, S.; Walmsley, A. D.; Hill, K. *Journal of Dentistry* **2020**, *99*, 103414.

(14) Atieh, M. A.; Morgaine, K. C.; Duncan, W. J. *Clinical Oral Implants Research* **2016**, *27*, 383–391.

(15) Stanford, C. M. *Journal of the American Dental Association* **2007**, *138*, S34–S40.

(16) Elias, C. N.; Lima, J. H.; Valiev, R.; Meyers, M. A. *JOM* **2008**, *60*, 46–49.

(17) Oldani, C.; Dominguez, A. In *Recent Advances in Arthroplasty*; InTech: 2012.

(18) Ratner, B. D.; Hoffman, A. S.; Schoen, F. J.; Lemons, J. E., *Biomaterials Science*; Elsevier: 2013.

(19) Elias, C. N.; Fernandes, D. J.; Souza, F. M. D.; Monteiro, E. D. S.; Biasi, R. S. D. *Journal of Materials Research and Technology* **2019**, *8*, 1060–1069.

(20) Duan, Y.; Gonzalez, J. A.; Kulkarni, P. A.; Nagy, W. W.; Griggs, J. A. *Dental Materials* **2018**, *34*, 1299–1309.

(21) Goodacre, C. J.; Bernal, G.; Rungcharassaeng, K.; Kan, J. Y. *Journal of Prosthetic Dentistry* **2003**, *90*, 121–132.

(22) Derks, J.; Schaller, D.; Håkansson, J.; Wennström, J. L.; Tomasi, C.; Berglundh, T. *Journal of Dental Research* **2016**, *95*, 43–49.

(23) Alghamdi, J.; Shafik, S.; Al-Mashat, H. *International journal of applied research* **2017**, *3*, 792–797.

(24) Raikar, S.; Talukdar, P.; Kumari, S.; Panda, S. K.; Oommen, V. M.; Prasad, A. *Journal of International Society of Preventive and Community Dentistry* **2017**, *7*, 351–355.

(25) Branemark, P. I. *The Journal of Prosthetic Dentistry* **1983**, *50*, 399–410.

(26) Dhinakarsamy, V.; Jayesh, R. *Journal of Pharmacy and Bioallied Sciences* **2015**, *7*, 228.

(27) Junker, R.; Dimakis, A.; Thoneick, M.; Jansen, J. A. *Clinical Oral Implants Research* **2009**, *20*, 185–206.

(28) Civantos, A.; Martínez-Campos, E.; Ramos, V.; Elvira, C.; Gallardo, A.; Abarrategi, A. *ACS Biomaterials Science and Engineering* **2017**, *3*, 1245–1261.

(29) Villar, C. C.; Huynh-Ba, G.; Mills, M. P.; Cochran, D. L. *Endodontic Topics* **2011**, *25*, 44–62.

(30) Schrott, A. R.; Jimenez, M.; Hwang, J. W.; Fiorellini, J.; Weber, H. P. *Clinical Oral Implants Research* **2009**, *20*, 1170–1177.

(31) Forna, N.; Agop-Forna, D. *Medicine and Pharmacy Reports* **2019**, *92*, S6–S13.

(32) Hasan, A.; Palmer, R. M. *British Dental Journal* **2014**, *216*, 457–461.

(33) Kilian, M.; Chapple, I. L. C.; Hannig, M.; Marsh, P. D.; Meuric, V.; Pedersen, A. M. L.; Tonetti, M. S.; Wade, W. G.; Zaura, E. *Bdj* **2016**, *221*, 657–666.

(34) Atieh, M. A.; Alsabeeha, N. H.; Faggion, C. M.; Duncan, W. J. *Journal of Periodontology* **2012**, *84*, 1–15.

(35) Meffert, R. M. *Critical Reviews in Oral Biology and Medicine* **1996**, *7*, 278–291.

(36) Becker, S. T.; Beck-Broichsitter, B. E.; Graetz, C.; Dörfer, C. E.; Wiltfang, J.; Häsler, R. *Clinical Implant Dentistry and Related Research* **2014**, *16*, 401–411.

(37) Tarnow, D. P. *Journal of Dental Research* **2016**, *95*, 7–8.

(38) Sanz, M.; Chapple, I. L. *Journal of Clinical Periodontology* **2012**, *39*, 202–206.

(39) Heitz-Mayfield, L. J.; Lang, N. P. *Periodontology 2000* **2010**, *53*, 167–181.

(40) Kumar, P. S.; Mason, M. R.; Brooker, M. R.; O'Brien, K. *Journal of Clinical Periodontology* **2012**, *39*, 425–433.

(41) Chandki, R.; Kala, M. *Journal of Oral Implantology* **2012**, *38*, 95–100.

(42) Maruyama, N.; Maruyama, F.; Takeuchi, Y.; Aikawa, C.; Izumi, Y.; Nakagawa, I. *Scientific Reports* **2014**, *4*, 6602.

(43) Claffey, N.; Clarke, E.; Polyzois, I.; Renvert, S. *Journal of Clinical Periodontology* **2008**, *35*, 316–332.

(44) Lindhe, J.; Lang, N. P.; Karring, T., *Clinical Periodontology and Implant Dentistry*, 6th ed.; John Wiley & Sons, Ltd: 2015.

(45) Bartold, P. M.; Walsh, L. J.; Narayanan, A. S. *Periodontology 2000* **2000**, *24*, 28–55.

(46) Kaiser, G. Anatomical Barriers to Infection, Mechanical Removal of Microbes, and Bacterial Antagonism by Normal Body Microbiota, 2019.

(47) Qin, R.; Steel, A.; Fazel, N. *Clinics in Dermatology* **2017**, *35*, 477–483.

(48) Nanci, A.; Ten Cate, A. R., *Ten Cate's oral histology : development, structure, and function.* 8th, illus; Elsevier: 2013, p 379.

(49) Squier, C. A.; Kremer, M. J. *Journal of the National Cancer Institute. Monographs* **2001**, *29*, 7–15.

(50) Chai, W. L.; Moharamzadeh, K.; Brook, I. M.; Emanuelsson, L.; Palmquist, A.; van Noort, R. *Journal of Periodontology* **2010**, *81*, 1187–1195.

(51) Wong, J. W.; Gallant-Behm, C.; Wiebe, C.; Mak, K.; Hart, D. A.; Larjava, H.; Häkkinen, L. *Wound Repair and Regeneration* **2009**, *17*, 717–729.

(52) Mak, K.; Manji, A.; Gallant-Behm, C.; Wiebe, C.; Hart, D. A.; Larjava, H.; Häkkinen, L. *Journal of Dermatological Science* **2009**, *56*, 168–180.

(53) Turabelidze, A.; Guo, S.; Chung, A. Y.; Chen, L.; Dai, Y.; Marucha, P. T.; DiPietro, L. A. *PLoS ONE* **2014**, *9*, ed. by Slominski, A. T., e101480.

(54) Enoch, S.; Moseley, R.; Stephens, P.; Thomas, D. W. *Oral Surgery* **2008**, *1*, 11–21.

(55) Von Den Hoff, J. W.; Maltha, J. C.; Kuijpers-Jagtman, A. M. In *Cleft Lip and Palate: Diagnosis and Management*, 2013, pp 309–324.

(56) Larjava, H.; Koivisto, L.; Häkkinen, L.; Heino, J. *Journal of Dental Research* **2011**, *90*, 1367–1376.

(57) Mah, W.; Jiang, G.; Olver, D.; Cheung, G.; Kim, B.; Larjava, H.; Häkkinen, L. *PLoS ONE* **2014**, *9*, e90715.

(58) Enoch, S.; Peake, M. A.; Wall, I.; Davies, L.; Farrier, J.; Giles, P.; Kipling, D.; Price, P.; Moseley, R.; Thomas, D.; Stephens, P. *Journal of Dental Research* **2010**, *89*, 1407–1413.

(59) Sculean, A.; Gruber, R.; Bosshardt, D. D. *Journal of Clinical Periodontology* **2014**, *41*, S6–S22.

(60) Khoury, S. B.; Thomas, L.; Walters, J. D.; Sheridan, J. F.; Leblebicioglu, B. *Journal of Periodontology* **2008**, *79*, 1904–1912.

(61) Boonsiriseth, K.; Suriyan, N.; Min, K.; Wongsirichat, N. *International Research Journal of Medicine and Medical Sciences* **2014**, *5*, 121–126.

(62) Yamaza, T.; A., M. In *Implant Dentistry - The Most Promising Discipline of Dentistry*; InTech: 2011.

(63) Tomasi, C.; Tessarolo, F.; Caola, I.; Piccoli, F.; Wennström, J. L.; Nollo, G.; Berglundh, T. *Journal of Clinical Periodontology* **2016**, *43*, 816–824.

(64) Dale, B. A. *Periodontology 2000* **2002**, *30*, 70–78.

(65) Milward, M. R.; Chapple, I. L. C.; Wright, H. J.; Millard, J. L.; Matthews, J. B.; Cooper, P. R. *Clinical & Experimental Immunology* **2007**, *148*, 307–324.

(66) Groeger, S.; Meyle, J. *Frontiers in Immunology* **2019**, *10*, 208.

(67) Zhao, Y.; Liu, D.; Huang, W.; Yang, Y.; Ji, M.; Nghiem, L. D.; Trinh, Q. T.; Tran, N. H. *Bioresource Technology* **2019**, *288*, 121619.

(68) De Carvalho, C. C. *Frontiers in Marine Science* **2018**, *5*, 126.

(69) Kip, N.; Van Veen, J. A. *The ISME Journal 2015 9:3* **2014**, *9*, 542–551.

(70) Muhammad, M. H.; Idris, A. L.; Fan, X.; Guo, Y.; Yu, Y.; Jin, X.; Qiu, J.; Guan, X.; Huang, T. *Frontiers in Microbiology* **2020**, *11*, 928.

(71) Subhadra, B.; Kim, D. H.; Woo, K.; Surendran, S.; Choi, C. H. *Materials* **2018**, *11*, DOI: 10.3390/MA11091676.

(72) Huang, R.; Li, M.; Gregory, R. L. *Virulence* **2011**, *2*, 435–444.

(73) Vasudevan, R. *Journal of Microbiology & Experimentation* **2014**, *1*.

(74) Dale, B. A.; Fredericks, L. P. *Current Issues in Molecular Biology* **2005**, *7*, 119–134.

(75) Souza, L. R.; Oliveira, M. V.; Basile, J. R.; Souza, L. N.; Souza, A. C.; Haikal, D. S.; De-Paula, A. M. In *Seminars in Dysphagia*; InTech: 2015.

(76) Schoen, M. H.; Freed, J. R. *Annual Review of Public Health* **1981**, *2*, 71–92.

(77) Parashar, A.; Parashar, S.; Zingade, A.; Gupta, S.; Sanikop, S. *Oral Science International* **2015**, *12*, 37–42.

(78) Kriebel, K.; Hieke, C.; Müller-Hilke, B.; Nakata, M.; Kreikemeyer, B. *Frontiers in Microbiology* **2018**, *9*, 1–14.

(79) Zarco, M. F.; Vess, T. J.; Ginsburg, G. S. *Oral Diseases* **2012**, *18*, 109–120.

(80) Kumar, B.; Kashyap, N.; Avinash, A.; Chevvuri, R.; Sagar, M. K.; Shrikant, K. *International Journal of Contemporary Dental and Medical Reviews* **2017**, 1–6.

(81) Anderson, A. C.; Rothballer, M.; Altenburger, M. J.; Woelber, J. P.; Karygianni, L.; Lagkouvardos, I.; Hellwig, E.; Al-Ahmad, A. *Scientific Reports* **2018**, *8*, 14202.

(82) Carter, M.; Shieh, J. C., *Guide to Research Techniques in Neuroscience*, 2010, p 417.

(83) Goers, L.; Freemont, P.; Polizzi, K. M. *Journal of the Royal Society Interface* **2014**, *11*.

(84) Pan, Y.; Teng, D.; Burke, A. C.; Haase, E. M.; Scannapieco, F. A. *Microbial Pathogenesis* **2009**, *46*, 73–79.

(85) Stathopoulou, P. G.; Benakanakere, M. R.; Galicia, J. C.; Kinane, D. F. *Journal of Clinical Periodontology* **2010**, *37*, 24–29.

(86) Saito, A.; Inagaki, S.; Ishihara, K. *Microbial Pathogenesis* **2009**, *47*, 329–333.

(87) Fteita, D.; Könönen, E.; Gürsoy, M.; Ma, X.; Sintim, H. O.; Gürsoy, U. K. *Anaerobe* **2018**, *54*, 128–135.

(88) Yee, M.; Kim, S.; Sethi, P.; Düzgüneş, N.; Konopka, K. *Anaerobe* **2014**, *28*, 62–67.

(89) Marsh, P. D.; Zaura, E. *Journal of Clinical Periodontology* **2017**, *44*, S12–S22.

(90) Palmer, R. J. *Periodontology 2000* **2014**, *64*, 20–39.

(91) Mintz, K. P.; Fives-Taylor, P. M. *Infection and Immunity* **1994**, *62*, 3672–3678.

(92) Fives-Taylor, P.; Meyer, D.; Mintz, K. *Advances in dental research* **1995**, *9*, 55–62.

(93) Yilmaz, O.; Watanabe, K.; Lamont, R. J. *Cellular Microbiology* **2002**, *4*, 305–314.

(94) Yilmaz, O.; Young, P. A.; Lamont, R. J.; Kenny, G. E. *Microbiology* **2003**, *149*, 2417–2426.

(95) Han, Y. W.; Shi, W.; Huang, G. T.; Kinder Haake, S.; Park, N. H.; Kuramitsu, H.; Genco, R. J. *Infection and immunity* **2000**, *68*, 3140–6.

(96) Gursoy, U. K.; Kononen, E.; Uitto, V. J. *Oral Microbiology and Immunology* **2009**, *24*, 304–309.

(97) Dabija-Wolter, G.; Cimpan, M.-R.; Costea, D. E.; Johannessen, A. C.; Sørnes, S.; Neppelberg, E.; Al-Haroni, M.; Skaug, N.; Bakken, V. *Journal of Periodontology* **2009**, *80*, 1174–1183.

(98) Bodet, C.; Chandad, F.; Grenier, D. *Microbes and Infection* **2005**, *7*, 448–456.

(99) Bodet, C.; Chandad, F.; Grenier, D. *Microbes and Infection* **2006**, *8*, 27–35.

(100) Bates, A. M.; Fischer, C. L.; Abhyankar, V. P.; Johnson, G. K.; Guthmiller, J. M.; Progulske-Fox, A.; Brogden, K. A. *International journal of molecular sciences* **2018**, *19*, 3923.

(101) Diaz, P. I.; Rogers, A. H. *Oral Microbiology and Immunology* **2004**, *19*, 88–94.

(102) Sancilio, S.; Di Giacomo, V.; Di Giulio, M.; Gallorini, M.; Marsich, E.; Travan, A.; Tarusha, L.; Cellini, L.; Cataldi, A. *PLoS ONE* **2014**, *9*, ed. by Al-Ahmad, A., e96520.

(103) Giulio, M. D.; D'Ercole, S.; Zara, S.; Cataldi, A.; Cellini, L. *Apmis* **2012**, *120*, 139.

(104) Gursoy, U. K.; Pöllänen, M.; Könönen, E.; Uitto, V.-J. *Journal of Periodontology* **2010**, *81*, 1084–1091.

(105) Millhouse, E.; Jose, A.; Sherry, L.; Lappin, D. F.; Patel, N.; Middleton, A. M.; Pratten, J.; Culshaw, S.; Ramage, G. *BMC Oral Health* **2014**, *14*, 80.

(106) Belibasakis, G. N.; Thurnheer, T.; Bostanci, N. *PLoS ONE* **2013**, *8*, e81581.

(107) Dickinson, B. C.; Moffatt, C. E.; Hagerty, D.; Whitmore, S. E.; Brown, T. A.; Graves, D. T.; Lamont, R. J. *Molecular Oral Microbiology* **2011**, *26*, 210–220.

(108) Guggenheim, B.; Gmür, R.; Galicia, J. C.; Stathopoulou, P. G.; Benakanakere, M. R.; Meier, A.; Thurnheer, T.; Kinane, D. F. *BMC Microbiology* **2009**, *9*, 280.

(109) Thurnheer, T.; Belibasakis, G. N.; Bostanci, N. *Archives of Oral Biology* **2014**, *59*, 977–986.

(110) Dongari-Bagtzoglou, A.; Kashleva, H. *Nature Protocols* **2006**, *1*, 2012–2018.

(111) Schaller, M.; Zakikhany, K.; Naglik, J. R.; Weindl, G.; Hube, B. *Nature Protocols* **2007**, *1*, 2767–2773.

(112) Pinnock, A.; Murdoch, C.; Moharamzadeh, K.; Whawell, S.; Douglas, C. W. I. *Microbes and Infection* **2014**, *16*, 310–319.

(113) Bao, K.; Akguel, B.; Bostanci, N. *Cells Tissues Organs* **2014**, *199*, 228–237.

(114) Grande, R.; Pacella, S.; Di Giulio, M.; Rapino, M.; Di Valerio, V.; Cellini, L.; Cataldi, A. *Clinical Oral Investigations* **2015**, *19*, 841–849.

(115) Discher, D. E. *Science* **2005**, *310*, 1139–1143.

(116) Engler, A. J.; Sen, S.; Sweeney, L. H.; Discher, D. E. *Cell* **2006**, *126 VN* -, 677–689.

(117) Cukierman, E. *Science (New York, NY)* **2001**, *294*, 1708–1712.

(118) Yadev, N. P.; Murdoch, C.; Saville, S. P.; Thornhill, M. H. *Microbial Pathogenesis* **2011**, *50*, 278–285.

(119) Park, J.; Shokeen, B.; Haake, S. K.; Lux, R. *International Journal of Oral Science* **2016**, *8*, 138–144.

(120) Sakolish, C. M.; Esch, M. B.; Hickman, J. J.; Shuler, M. L.; Mahler, G. J. *EBioMedicine* **2016**, *5*, 30–39.

(121) Merne, M.; Syrjänen, S. *Archives of Dermatological Research* **2003**, *295*, 190–198.

(122) Gursoy, U. K.; Könönen, E. *Journal of oral microbiology* **2012**, *4*.

(123) Duval, K.; Grover, H.; Han, L. H.; Mou, Y.; Pegoraro, A. F.; Fredberg, J.; Chen, Z. *Physiology* **2017**, *32*, 266–277.

(124) Moharamzadeh, K.; Colley, H.; Murdoch, C.; Hearnden, V.; Chai, W.; Brook, I.; Thornhill, M.; MacNeil, S. *Journal of Dental Research* **2012**, *91*, 642–650.

(125) Young, J. L.; Engler, A. J. *Biomaterials* **2011**, *32*, 1002–1009.

(126) Chen, J.; Ahmad, R.; Li, W.; Swain, M.; Li, Q. *Journal of the Royal Society Interface* **2015**, *12*.

(127) Goktas, S.; Dmytryk, J. J.; McFetridge, P. S. *Journal of Periodontology* **2011**, *82*, 1178–1186.

(128) Inoue, K.; Arikawa, H.; Fujii, K.; Shinohara, N.; Kawahata, N. *Dental Materials Journal* **1985**, *4*, 47–53.

(129) Lacoste-Ferré, M. H.; Demont, P.; Dandurand, J.; Dantras, E.; Duran, D.; Lacabanne, C. *Journal of the Mechanical Behavior of Biomedical Materials* **2011**, *4*, 269–274.

(130) Tanaka, E.; Yamano, E.; Dalla-Bona, D. A.; Watanabe, M.; Inubushi, T.; Shirakura, M.; Sano, R.; Takahashi, K.; Van Eijden, T.; Tanne, K. *Journal of Dental Research* **2006**, *85*, 571–575.

(131) Aas, J. A.; Paster, B. J.; Stokes, L. N.; Olsen, I.; Dewhirst, F. E. *Journal of Clinical Microbiology* **2005**, *43*, 5721 LP –5732.

(132) Hall, C. W.; Mah, T. F. *FEMS Microbiology Reviews* **2017**, *41*, 276–301.

(133) Khalaf, H.; Palm, E.; Bengtsson, T. In *Periodontitis - A Useful Reference*, 2017; Chapter 3, pp 45–68.

(134) Wang, H.-Y.; Cheng, J.-W.; Yu, H.-Y.; Lin, L.; Chih, Y.-H.; Pan, Y.-P. *Acta Biomaterialia* **2015**, *25*, 150–161.

(135) La, V. D.; Howell, A. B.; Grenier, D. *Antimicrobial Agents and Chemotherapy* **2010**, *54*, 1778 LP –1784.

(136) Zhou, Y.; Guan, X.; Zhu, W.; Liu, Z.; Wang, X.; Yu, H.; Wang, H. *European Journal of Clinical Microbiology & Infectious Diseases* **2014**, *33*, 211–219.

(137) Matsui, A.; Jin, J. O.; Johnston, C. D.; Yamazaki, H.; Houri-Haddad, Y.; Rittling, S. R. *Infection and Immunity* **2014**, *82*, 4068–4079.

(138) Ramage, G.; Lappin, D. F.; Millhouse, E.; Malcolm, J.; Jose, A.; Yang, J.; Bradshaw, D. J.; Pratten, J. R.; Culshaw, S. *Journal of periodontal research* **2017**, *52*, 325–333.

(139) Subbiahdoss, G.; Kuijer, R.; W Grijpma, D.; van der Mei, H.; Busscher, H. *Acta biomaterialia* **2009**, *5*, 1399–1404.

(140) Dwidar, M.; Leung, B. M.; Yaguchi, T.; Takayama, S.; Mitchell, R. J. *PLoS ONE* **2013**, *8*, ed. by Dague, E., e67165.

(141) Chin, M. Y. H.; Busscher, H. J.; Evans, R.; Noar, J.; Pratten, J. *European Journal of Orthodontics* **2005**, *28*, 1–7.

(142) Rath, H.; Stumpp, S. N.; Stiesch, M. *PLoS ONE* **2017**, *12*, e0172095.

(143) Tolker-Nielsen, T.; Sternberg, C. *Current Protocols in Microbiology* **2011**, *21*, 1–1.

(144) Crusz, S. A.; Popat, R.; Rybtke, M. T.; Cámara, M.; Givskov, M.; Tolker-Nielsen, T.; Diggle, S. P.; Williams, P. *Biofouling* **2012**, *28*, 835–842.

(145) Bao, K.; Papadimitropoulos, A.; Akgül, B.; Belibasakis, G. N.; Bostanci, N. *Virulence* **2015**, *6*, 265–273.

(146) Bao, K.; Belibasakis, G. N.; Selevsek, N.; Grossmann, J.; Bostanci, N. *Scientific Reports* **2015**, *5*, 15999.

(147) Cani, P. D. *Gut* **2018**, *67*, 1716–1725.

(148) Shanahan, F.; Van Sinderen, D.; O'Toole, P. W.; Stanton, C. *Gut* **2017**, *66*, 1709–1717.

(149) Tilg, H.; Adolph, T. E.; Gerner, R. R.; Moschen, A. R. *Cancer Cell* **2018**, *33*, 954–964.

(150) Bahrami, B.; Child, M. W.; Macfarlane, S.; Macfarlane, G. T. *Applied and Environmental Microbiology* **2011**, *77*, 2934–2942.

(151) Park, G. S.; Park, M. H.; Shin, W.; Zhao, C.; Sheikh, S.; Oh, S. J.; Kim, H. J. *Stem Cell Reviews and Reports* **2017**, *13*, 321–334.

(152) Payne, A. N.; Zihler, A.; Chassard, C.; Lacroix, C. *Trends in Biotechnology* **2012**, *30*, 17–25.

(153) Monnappa, A. K.; Bari, W.; Choi, S. Y.; Mitchell, R. J. *Scientific Reports* **2016**, *6*, 33485.

(154) Shaban, L.; Chen, Y.; Fasciano, A. C.; Lin, Y.; Kaplan, D. L.; Kumamoto, C. A.; Mecsas, J. *Anaerobe* **2018**, *50*, 85–92.

(155) Dosh, R. H.; Jordan-Mahy, N.; Sammon, C.; Le Maitre, C. L. *Tissue Engineering - Part B: Reviews* **2018**, *24*, 98–111.

(156) Fatehullah, A.; Tan, S. H.; Barker, N. *Nature Cell Biology* **2016**, *18*, 246–254.

(157) Bartfeld, S.; Bayram, T.; Van De Wetering, M.; Huch, M.; Begthel, H.; Kujala, P.; Vries, R.; Peters, P. J.; Clevers, H. *Gastroenterology* **2015**, *148*, 126–136.

(158) Trujillo-de Santiago, G.; Lobo-Zegers, M. J.; Montes-Fonseca, S. L.; Zhang, Y. S.; Alvarez, M. M. *Microphysiological Systems* **2018**, *1*, 1–1.

(159) Anonye, B. O.; Hassall, J.; Patient, J.; Detamornrat, U.; Aladdad, A. M.; Schüller, S.; Rose, F. R.; Unnikrishnan, M. *Frontiers in Microbiology* **2019**, *10*, 1–15.

(160) Rosenthal, M.; Goldberg, D.; Aiello, A.; Larson, E.; Foxman, B. *Infection, Genetics and Evolution* **2011**, *11*, 839–848.

(161) Rademacher, F.; Simanski, M.; Gläser, R.; Harder, J. *Experimental Dermatology* **2018**, *27*, 489–494.

(162) Klicks, J.; von Molitor, E.; Ertongur-Fauth, T.; Rudolf, R.; Hafner, M. *Journal of Cellular Biotechnology* **2017**, *3*, 21–39.

(163) El Ghalbzouri, A.; Commandeur, S.; Rietveld, M. H.; Mulder, A. A.; Willemze, R. *Biomaterials* **2009**, *30*, 71–78.

(164) Anderson, M. J.; Parks, P. J.; Peterson, M. L. *Journal of Microbiological Methods* **2013**, *92*, 201–208.

(165) Lebeaux, D.; Chauhan, A.; Rendueles, O.; Beloin, C. *Pathogens* **2013**, *2*, 288–356.

(166) Brodland, G. W. *Seminars in Cell and Developmental Biology* **2015**, *47-48*, 62–73.

(167) Ziraldo, C.; Mi, Q.; An, G.; Vodovotz, Y. *Advances in Wound Care* **2013**, *2*, 527–537.

(168) Marcián, P.; Borák, L.; Konečný, O.; Navrátil, P.; Florian, Z. In *Applied Mechanics and Materials*, Trans Tech Publications Ltd: 2013; Vol. 245, pp 57–62.

(169) Lardon, L. A.; Merkey, B. V.; Martins, S.; Dötsch, A.; Picioreanu, C.; Kreft, J.-U.; Smets, B. F. *Environmental Microbiology* **2011**, *13*, 2416–2434.

(170) Duddu, R.; Bordas, S.; Chopp, D.; Moran, B. *International Journal for Numerical Methods in Engineering* **2008**, *74*, 848–870.

(171) Rodriguez, D.; Carpio, A.; Einarsson, B. In *Blucher Mechanical Engineering Proceedings*, 2014.

(172) Hellweger, F. L.; Bucci, V. *Ecological Modelling* **2009**, *220*, 8–22.

(173) Picioreanu, C.; Kreft, J. U.; Van Loosdrecht, M. C. *Applied and Environmental Microbiology* **2004**, *70*, 3024–3040.

(174) Mattei, M. R.; Frunzo, L.; D'Acunto, B.; Pechaud, Y.; Pirozzi, F.; Esposito, G. *Journal of Mathematical Biology* **2018**, *76*, 945–1003.

(175) Stewart, P. S.; Franklin, M. J. *Nature Reviews Microbiology* **2008**, *6*, 199–210.

(176) Wolfram, S. *Nature* **1984**, *311*, 419–424.

(177) Gong, Y. In *IOP Conference Series: Materials Science and Engineering*, 2017, p 242.

(178) Andrews, G. *Cellular Automata and Applications*; tech. rep.

(179) Barker, G. C.; Grimson, M. J. *Binary Comput Microbiol* **1993**, *5*, 132–137.

(180) Chang, I.; Gilbert, E. S.; Eliashberg, N.; Keasling, J. D. *Microbiology* **2003**, *149*, 2859–2871.

(181) Picioreanu, C.; Van Loosdrecht, M. C.; Heijnen, J. J. *Biotechnology and Bioengineering* **1998**, *57*, 718–731.

(182) Pizarro, G.; Griffeath, D.; Noguera, D. R. *Journal of Environmental Engineering* **2001**, *127*, 782–789.

(183) Tang, Y.; Valocchi, A. J. *Water Research* **2013**, *47*, 5729–5742.

(184) Van Gestel, J.; Nowak, M. A. *PLoS Computational Biology* **2016**, *12*, e1004764.

(185) Laspidou, C. S.; Kungolos, A.; Samaras, P. *Desalination* **2010**, *250*, 390–394.

(186) Goldmann, W. H. In *Progress in Molecular Biology and Translational Science*; Elsevier B.V.: 2014; Vol. 126, pp 75–102.

(187) Baruffaldi, D.; Palmara, G.; Pirri, C.; Frascella, F. *ACS Applied Bio Materials* **2021**, *4*, 2233–2250.

(188) Randall, M. J.; Jüngel, A.; Rimann, M.; Wuertz-Kozak, K. *Frontiers in Bioengineering and Biotechnology* **2018**, *6*, 154.

(189) Kim, H. N.; Choi, N. *Biochip Journal* **2019**, *13*, 8–19.

(190) Tam, N. W.; Chung, D.; Baldwin, S. J.; Simmons, J. R.; Xu, L.; Rainey, J. K.; Dellaire, G.; Frampton, J. P. *Journal of Materials Chemistry B* **2020**, *8*, 9718–9733.

(191) Choi, J. J. E.; Zwirner, J.; Ramani, R. S.; Ma, S.; Hussaini, H. M.; Waddell, J. N.; Hammer, N. *Clinical and Experimental Dental Research* **2020**, *6*, 602–611.

(192) Ruedinger, F.; Lavrentieva, A.; Blume, C.; Pepelanova, I.; Scheper, T. *Applied Microbiology and Biotechnology* **2015**, *99*, 623–636.

(193) Tibbitt, M. W.; Anseth, K. S. *Biotechnology and Bioengineering* **2009**, *103*, 655–663.

(194) Lee, K. Y.; Mooney, D. J. *Chemical Reviews* **2001**, *101*, 1869–1879.

(195) Dongari-Bagtzoglou, A.; Kashleva, H. *Microbial Pathogenesis* **2006**, *40*, 271–278.

(196) Tabatabaei, F.; Moharamzadeh, K.; Tayebi, L. *Journal of Oral Biology and Craniofacial Research* **2020**, *10*, 573–577.

(197) De Carvalho Dias, K.; de Sousa, D. L.; Barbugli, P. A.; Cerri, P. S.; Salih, V. M.; Vergani, C. E. *Journal of Microbiological Methods* **2018**, *152*, 52–60.

(198) Smithmyer, M. E.; Sawicki, L. A.; Kloxin, A. M. *Biomaterials Science* **2014**, *2*, 634–650.

(199) Friess, W. *European Journal of Pharmaceutics and Biopharmaceutics* **1998**, *45*, 113–136.

(200) Sarrigiannidis, S. O.; Rey, J. M.; Dobre, O.; González-García, C.; Dalby, M. J.; Salmeron-Sanchez, M. *Materials Today Bio* **2021**, *10*, 100098.

(201) Zhu, Y. K.; Umino, T.; Liu, X. D.; Wang, H. J.; Romberger, D. J.; Spurzem, J. R.; Rennard, S. I. *In Vitro Cellular and Developmental Biology - Animal* **2001**, *37*, 10–16.

(202) Kuo, C. K.; Ma, P. X. *Biomaterials* **2001**, *22*, 511–521.

(203) Moxon, S. R.; Corbett, N. J.; Fisher, K.; Potjewyd, G.; Domingos, M.; Hooper, N. M. *Materials Science and Engineering: C* **2019**, *104*, 109904.

(204) Sun, J.; Tan, H. *Materials* **2013**, *6*, 1285–1309.

(205) Perez, R. A.; Kim, M.; Kim, T. H.; Kim, J. H.; Lee, J. H.; Park, J. H.; Knowles, J. C.; Kim, H. W. *Tissue Engineering - Part A* **2014**, *20*, 103–114.

(206) Lee, M.; Lo, A. C.; Cheung, P. T.; Wong, D.; Chan, B. P. *Biomaterials* **2009**, *30*, 1214–1221.

(207) Liu, W.; Griffith, M.; Li, F. *Journal of Materials Science: Materials in Medicine* **2008**, *19*, 3365–3371.

(208) Bahram, M.; Mohseni, N.; Moghtader, M. In *Emerging Concepts in Analysis and Applications of Hydrogels*; InTech: 2016.

(209) Sun, J.-Y.; Zhao, X.; Illeperuma, W. R. K.; Chaudhuri, O.; Oh, K. H.; Mooney, D. J.; Vlassak, J. J.; Suo, Z. *Nature* **2012**, *489*, 133–136.

(210) Kinikoglu, B.; Hemar, J.; Hasirci, V.; Breton, P.; Damour, O. *Artif Cells Blood Substit Immobil Biotechnol* **2012**, *40*, 271–274.

(211) Paraffin Processing of Tissue | Protocols Online.

(212) Protocols - Formalin Fixation and Paraffin Embedding of Tissues | LSBio.

(213) Fischer, A. H.; Jacobson, K. A.; Rose, J.; Zeller, R. *Cold Spring Harbor Protocols* **2008**, *2008*.

(214) Sa, G.; Xiong, X.; Wu, T.; Yang, J.; He, S.; Zhao, Y. *European Journal of Pharmaceutical Sciences* **2016**, *81*, 10–17.

(215) Thirion-Delalande, C.; Gervais, F.; Fisch, C.; Cuiné, J.; Baron-Bodo, V.; Moingeon, P.; Mascarell, L. *PLoS ONE* **2017**, *12*.

(216) Haslach, H. W. *Biomechanics and Modeling in Mechanobiology* **2005**, *3*, 172–189.

(217) Banerjee, A.; Arha, M.; Choudhary, S.; Ashton, R. S.; Bhatia, S. R.; Schaffer, D. V.; Kane, R. S. *Biomaterials* **2009**, *30*, 4695–4699.

(218) Nunamaker, E. A.; Otto, K. J.; Kipke, D. R. *Journal of the Mechanical Behavior of Biomedical Materials* **2011**, *4*, 16–33.

(219) Kaklamani, G.; Cheneler, D.; Grover, L. M.; Adams, M. J.; Bowen, J. *Journal of the Mechanical Behavior of Biomedical Materials* **2014**, *36*, 135–142.

(220) Jang, J.; Lee, J.; Seol, Y. J.; Jeong, Y. H.; Cho, D. W. *Composites Part B: Engineering* **2013**, *45*, 1216–1221.

(221) Baniasadi, M.; Minary-Jolandan, M. *Materials* **2015**, *8*, 799–814.

(222) Zhou, J.; Zhang, K.; Ma, S.; Liu, T.; Yao, M.; Li, J.; Wang, X.; Guan, F. *E-Polymers* **2019**, *19*, 87–91.

(223) Ghibelli, L.; Cerella, C.; Diederich, M. *International Journal of Cell Biology* **2010**.

(224) Kaberova, Z.; Karpushkin, E.; Nevoralová, M.; Vetrík, M.; Šlouf, M.; Dušková-Smrcková, M. *Polymers* **2020**, *12*, 578.

(225) Subramanian, A.; Rodriguez-Saona, L. In *Infrared Spectroscopy for Food Quality Analysis and Control*, Sun, D.-W., Ed.; Academic Press: San Diego, 2009, pp 145–178.

(226) Kuzmanović, M.; Božanić, D. K.; Milivojević, D.; Ćulafić, D. M.; Stanković, S.; Ballesteros, C.; Gonzalez-Benito, J. *RSC Advances* **2017**, *7*, 53422–53432.

(227) Daemi, H.; Barikani, M. *Scientia Iranica* **2012**, *19*, 2023–2028.

(228) De Campos Vidal, B.; Mello, M. L. S. *Micron* **2011**, *42*, 283–289.

(229) Belbachir, K.; Noreen, R.; Gouspillou, G.; Petibois, C. *Analytical and Bioanalytical Chemistry 2009 395:3* **2009**, *395*, 829–837.

(230) Popa, R. M.; Fetea, F.; Socaciu, C. *Molecules* **2021**, *26*, 4837.

(231) Schädle, T.; Pejcic, B.; Mizaikoff, B. *Analytical Methods* **2016**, *8*, 756–762.

(232) Almansoori, A. A.; Kim, B.; Lee, J. H.; Tran, S. D. *Micromachines* **2020**, *11*, 1–13.

(233) Assunção, M.; Dehghan-Baniani, D.; Yiu, C. H. K.; Später, T.; Beyer, S.; Blocki, A. *Frontiers in Bioengineering and Biotechnology* **2020**, *8*.

(234) KC, P.; Hong, Y.; Zhang, G. *Regenerative Biomaterials* **2019**, *6*, 185.

(235) Tabatabaei, F.; Moharamzadeh, K.; Tayebi, L. *Tissue Engineering - Part B: Reviews* **2020**, *26*, 443–460.

(236) Diaz, P. I.; Xie, Z.; Sobue, T.; Thompson, A.; Biyikoglu, B.; Ricker, A.; Ikonomou, L.; Dongari-Bagtzoglou, A. *Infection and Immunity* **2012**, *80*, 620–632.

(237) Sobue, T.; Bertolini, M.; Thompson, A.; Peterson, D. E.; Diaz, P. I.; Dongari-Bagtzoglou, A. *Molecular Oral Microbiology* **2018**, *33*, 212–223.

(238) Bertolini, M.; Ranjan, A.; Thompson, A.; Diaz, P. I.; Sobue, T.; Maas, K.; Dongari-Bagtzoglou, A. *PLoS Pathogens* **2019**, *15*, e1007717.

(239) Lee, H. G.; Eun, H. C. *Journal of Dermatological Science* **1999**, *21*, 176–182.

(240) Shannon, D. B.; McKeown, S. T.; Lundy, F. T.; Irwin, C. R. *Wound Repair and Regeneration* **2006**, *14*, 172–178.

(241) Bierbaumer, L.; Schwarze, U. Y.; Gruber, R.; Neuhaus, W. *Tissue Barriers* **2018**, *6*.

(242) Klausner, M.; Handa, Y.; Aizawa, S. *In Vitro Cellular and Developmental Biology - Animal* **2021**, *57*, 148–159.

(243) Wayakanon, K.; Thornhill, M. H.; Douglas, C. W.; Lewis, A. L.; Warren, N. J.; Pinnock, A.; Armes, S. P.; Battaglia, G.; Murdoch, C. *FASEB Journal* **2013**, *27*, 4455–4465.

(244) De Ryck, T.; Grootaert, C.; Jaspaert, L.; Kerckhof, F. M.; Van Gele, M.; De Schrijver, J.; Van Den Abbeele, P.; Swift, S.; Bracke, M.; Van De Wiele, T.; Vanhoecke, B. *Applied Microbiology and Biotechnology* **2014**, *98*, 6831–6846.

(245) Décanis, N.; Savignac, K.; Rouabhia, M. *Cytokine* **2009**, *45*, 132–140.

(246) Pöllänen, M. T.; Gursoy, U. K.; Könönen, E.; Uitto, V.-J. *Journal of Periodontology* **2012**, *83*, 1329–1335.

(247) Khan, E. Characterisation of 2D and 3D oral keratinocyte cultures. Ph.D. Thesis, 2012, p 171.

(248) Hunt, N.; Shelton, R.; Henderson, D.; Grover, L. *Tissue engineering. Part A* **2013**, *19*, 905–914.

(249) Hamilton, N. J.; Hynds, R. E.; Gowers, K. H.; Tait, A.; Butler, C. R.; Hopper, C.; Burns, A. J.; Birchall, M. A.; Lowdell, M.; Janes, S. M. *Tissue Eng Part C Methods* **2019**, *25*, 93–102.

(250) Ron, A.; Azeloglu, E. U.; Calizo, R. C.; Hu, M.; Bhattacharya, S.; Chen, Y.; Jayaraman, G.; Lee, S.; Neves-Zaph, S. R.; Li, H.; Gordon, R. E.; He, J. C.; Hone, J. C.; Iyengar, R. *Nature Communications 2017 8:1* **2017**, *8*, 1–15.

(251) Bao, M.; Xie, J.; Piruska, A.; Huck, W. T. S. *Nature Communications 2017 8:1* **2017**, *8*, 1–12.

(252) Khan, E. Characterisation of 2D and 3D oral keratinocyte cultures, Ph.D. Thesis, Birmingham: University of Birmingham, 2012.

(253) Khan, E.; Shelton, R. M.; Cooper, P. R.; Hamburger, J.; Landini, G. *Journal of Biomedical Materials Research Part A* **2012**, *100A*, 3227–3238.

(254) Hearnden, V. Developing tissue engineered models of oral mucosa and oral cancer to study novel therapeutic and diagnostic techniques, Ph.D. Thesis, University of Sheffield, 2010.

(255) Mountcastle, S. E.; Vyas, N.; Villapun, V. M.; Cox, S. C.; Jabbari, S.; Sammons, R. L.; Shelton, R. M.; Walmsley, A. D.; Kuehne, S. A. *npj Biofilms and Microbiomes 2021 7:1* **2021**, *7*, 1–12.

(256) Miles, A. A.; Misra, S. S.; Irwin, J. O. *The Journal of hygiene* **1938**, *38*, 732–49.

(257) Tetz, G. V.; Artemenko, N. K.; Tetz, V. V. *Antimicrobial Agents and Chemotherapy* **2009**, *53*, 1204–1209.

(258) Canty, M. K.; Hansen, L. A.; Tobias, M.; Spencer, S.; Henry, T.; Luke-Marshall, N. R.; Campagnari, A. A.; Ehrensberger, M. T. *mSphere* **2019**, *4*.

(259) Donlan, R. M. *Emerging Infectious Diseases* **2002**, *8*, 881–890.

(260) Rabin, N.; Zheng, Y.; Opoku-Temeng, C.; Du, Y.; Bonsu, E.; Sintim, H. O. *Future Medicinal Chemistry* **2015**, *7*, 493–512.

(261) Haney, E. F.; Trimble, M. J.; Cheng, J. T.; Vallé, Q.; Hancock, R. E. *Biomolecules* **2018**, *8*.

(262) Stiefel, P.; Rosenberg, U.; Schneider, J.; Mauerhofer, S.; Maniura-Weber, K.; Ren, Q. *Applied Microbiology and Biotechnology* **2016**, *100*, 4135–4145.

(263) Shukla, S. K.; Rao, T. S. *bioRxiv* **2017**, 100214.

(264) Zhou, X.; Li, Y., *Atlas of Oral Microbiology: From Healthy Microflora to Disease*; Elsevier Inc.: 2015, p 118.

(265) Welch, K.; Cai, Y.; Strømme, M. *Journal of Functional Biomaterials* **2012**, *3*, 418–431.

(266) Drago, L.; Agrappi, S.; Bortolin, M.; Toscano, M.; Romanò, C. L.; De Vecchi, E. *International Journal of Molecular Sciences* **2016**, *17*.

(267) Schwarz, F.; Papanicolau, P.; Rothamel, D.; Beck, B.; Herten, M.; Becker, J. *Journal of Biomedical Materials Research Part A* **2006**, *77A*, 437–444.

(268) Vickery, K.; Pajkos, A.; Cossart, Y. *American Journal of Infection Control* **2004**, *32*, 170–176.

(269) Li, J.; Hirota, K.; Goto, T.; Yumoto, H.; Miyake, Y.; Ichikawa, T. *Journal of Dentistry* **2012**, *40*, 686–692.

(270) Gomes, L. C.; Mergulhão, F. J. *Scanning* **2017**, *2017*.

(271) Azeredo, J. et al. *Critical Reviews in Microbiology* **2017**, *43*, 313–351.

(272) Oliveira, F.; Lima, C. A.; Brás, S.; França, Â.; Cerca, N. *FEMS Microbiology Letters* **2015**, *362*, ed. by Rumbaugh, K.

(273) Tresse, O.; Lescob, S.; Rho, D. *Journal of Applied Microbiology* **2003**, *94*, 849–855.

(274) Fernández-Barat, L.; Li Bassi, G.; Ferrer, M.; Bosch, A.; Calvo, M.; Vila, J.; Gabarrús, A.; Martínez-Olondris, P.; Rigol, M.; Esperatti, M.; Luque, N.; Torres, A. *FEMS Immunology and Medical Microbiology* **2012**, *65*, 309–317.

(275) Neut, D.; Hendriks, J. G.; Van Horn, J. R.; Van Der Mei, H. C.; Busscher, H. J. *Acta Orthopaedica Scandinavica* **2005**, *76*, 109–114.

(276) Reichhardt, C.; Parsek, M. R. *Frontiers in Microbiology* **2019**, *10*, 677.

(277) Filmtracer LIVE/DEAD Biofilm Viability Kit - Thermo Fisher Scientific.

(278) Skogman, M. E.; Kujala, J.; Busygin, I.; Leino, R.; Vuorela, P. M.; Fallarero, A. *Natural Product Communications* **2012**, *7*, 1173–1176.

(279) Fricke, K.; Koban, I.; Tresp, H.; Jablonowski, L.; Schröder, K.; Kramer, A.; Weltmann, K.-D.; von Woedtke, T.; Kocher, T. *PLoS ONE* **2012**, *7*, ed. by Gasset, M.

(280) Chávez de Paz, L. E.; Hamilton, I. R.; Svensäter, G. *Microbiology* **2008**, *154*, 1927–1938.

(281) Cruz, P. C.; de Andrade, I. M.; Peracini, A.; de Souza-Gugelmin, M. C. M.; Silva-Lovato, C. H.; de Souza, R. F.; Paranhos, H. d. F. O. *Journal of Applied Oral Science* **2011**, *19*, 668–673.

(282) Ahirwar, A. *International Journal of Information Technology and Computer Science* **2013**, *5*, 44–53.

(283) Heydorn, A.; Nielsen, A. T.; Hentzer, M.; Sternberg, C.; Givskov, M.; Ersboll, B. K.; Molin, S. *Microbiology* **2000**, *146*, 2395–2407.

(284) Mueller, L. N.; de Brouwer, J. F.; Almeida, J. S.; Stal, L. J.; Xavier, J. B. *BMC Ecology* **2006**, *6*.

(285) Hartmann, R. et al. *bioRxiv* **2019**, 735423.

(286) Zhang, K.; Melo, M. A. S.; Cheng, L.; Weir, M. D.; Bai, Y.; Xu, H. H. *Dental Materials* **2012**, *28*, 842–852.

(287) Chebath-Taub, D.; Steinberg, D.; Featherstone, J. D.; Feuerstein, O. *Journal of Photochemistry and Photobiology B: Biology* **2012**, *116*, 75–78.

(288) Rosenberg, M.; Azevedo, N. F.; Ivask, A. *Scientific Reports* **2019**, *9*, 1–12.

(289) Mesquita, D. P.; Amaral, A. L.; Ferreira, E. C. *Chemosphere* **2011**, *85*, 643–652.

(290) De Chávez Paz, L. E. *Applied and Environmental Microbiology* **2009**, *75*, 1734–1739.

(291) Luo, T. L.; Eisenberg, M. C.; Hayashi, M. A.; Gonzalez-Cabezas, C.; Foxman, B.; Marrs, C. F.; Rickard, A. H. *Scientific Reports* **2018**, *8*, 13013.

(292) Klinger-Strobel, M.; Suesse, H.; Fischer, D.; Pletz, M. W.; Makarewicz, O. *PLoS ONE* **2016**, *11*.

(293) Larimer, C.; Winder, E.; Jeters, R.; Prowant, M.; Nettleship, I.; Addleman, R. S.; Bonheyo, G. T. *Analytical and Bioanalytical Chemistry* **2016**, *408*, 999–1008.

(294) Pratten, J.; Smith, A. W.; Wilson, M. *The Journal of antimicrobial chemotherapy* **1998**, *42*, 453–9.

(295) Dawson, L. F.; Valiente, E.; Faulds-Pain, A.; Donahue, E. H.; Wren, B. W. *PLoS ONE* **2012**, *7*, ed. by Popoff, M. R.

(296) Sternberg, S. R. *Computer* **1983**, *16*, 22–34.

(297) Lasko, T. A.; Bhagwat, J. G.; Zou, K. H.; Ohno-Machado, L. *Journal of Biomedical Informatics* **2005**, *38*, 404–415.

(298) Villapún, V. M.; Carter, L. N.; Gao, N.; Addison, O.; Webber, M. A.; Shepherd, D. E.; Andrews, J. W.; Lowther, M.; Avery, S.; Glanvill, S. J.; Grover, L. M.; Cox, S. *Additive Manufacturing* **2020**, 101528.

(299) Hajian-Tilaki, K. *Caspian Journal of Internal Medicine* **2013**, *4*, 627–635.

(300) Galdiero, E.; de Alteriis, E.; De Natale, A.; D'Alterio, A.; Siciliano, A.; Guida, M.; Lombardi, L.; Falanga, A.; Galdiero, S. *Scientific Reports* **2020**, *10*, 1–12.

(301) Kleine, D.; Chodorski, J.; Mitra, S.; Schlegel, C.; Huttenlochner, K.; Müller-Renno, C.; Mukherjee, J.; Ziegler, C.; Ulber, R. *Engineering in Life Sciences* **2019**, *19*, elsc.201800176.

(302) Oliveira, W. F.; Silva, P. M.; Silva, R. C.; Silva, G. M.; Machado, G.; Coelho, L. C.; Correia, M. T. *Journal of Hospital Infection* **2018**, *98*, 111–117.

(303) Cox, S. C.; Jamshidi, P.; Eisenstein, N. M.; Webber, M. A.; Burton, H.; Moakes, R. J.; Addison, O.; Attallah, M.; Shepherd, D. E.; Grover, L. M. *ACS Biomaterials Science and Engineering* **2017**, *3*, 1616–1626.

(304) Helou, M.; Kara, S. *International Journal of Computer Integrated Manufacturing* **2018**, *31*, 243–261.

(305) Du Plessis, A.; Yadroitsava, I.; Yadroitsev, I.; le Roux, S. G.; Blaine, D. C. *Virtual and Physical Prototyping* **2018**, *13*, 266–281.

(306) Wiggins, A.; Austerberry, R.; Morrison, D.; Ho, K. M.; Honeybul, S. *Neurosurgery* **2013**, *72*, 248–256.

(307) Wafa, H.; Grimer, R. J.; Reddy, K.; Jeys, L.; Abudu, A.; Carter, S. R.; Tillman, R. M. *Bone and Joint Journal* **2015**, *97-B*, 252–257.

(308) Itabashi, T.; Narita, K.; Ono, A.; Wada, K.; Tanaka, T.; Kumagai, G.; Yamauchi, R.; Nakane, A.; Ishibashi, Y. *Bone and Joint Research* **2017**, *6*, 108–112.

(309) Achinas, S.; Charalampogiannis, N.; Euverink, G. J. W. *Applied Sciences* **2019**, *9*, 2801.

(310) Crawford, R. J.; Webb, H. K.; Truong, V. K.; Hasan, J.; Ivanova, E. P. *Advances in Colloid and Interface Science* **2012**, *179-182*, 142–149.

(311) Efimochkina, N. R.; Bykova, I. B.; Markova, Y. M.; Korotkevich, Y. V.; Stetsenko, V. V.; Minaeva, L. P.; Sheveleva, S. A. *Bulletin of Experimental Biology and Medicine* **2017**, *162*, 474–478.

(312) Segovia-Juarez, J. L.; Ganguli, S.; Kirschner, D. *Journal of Theoretical Biology* **2004**, *231*, 357–376.

(313) Elias, S.; Banin, E. *FEMS Microbiology Reviews* **2012**, *36*, 990–1004.

(314) Wang, L.; Fan, D.; Chen, W.; Terentjev, E. M. *Scientific Reports 2015 5:1* **2015**, *5*, 1–11.

(315) Rendueles, O.; Ghigo, J. M. *FEMS Microbiology Reviews* **2012**, *36*, 972–989.

(316) Theophel, K.; Schacht, V. J.; Schlüter, M.; Schnell, S.; Stingu, C. S.; Schaumann, R.; Bunge, M. *Frontiers in Microbiology* **2014**, *5*, 544.

(317) Sharma, D.; Misba, L.; Khan, A. U. *Antimicrobial Resistance and Infection Control* **2019**, *8*, 1–10.

(318) Jollife, I. T.; Cadima, J. *Philosophical Transactions of the Royal Society A: Mathematical, Physical and Engineering Sciences* **2016**, *374*.

(319) Eshghi, S. T.; Au-Yeung, A.; Takahashi, C.; Bolen, C. R.; Nyachienga, M. N.; Lear, S. P.; Green, C.; Rodney Mathews, W.; O'Gorman, W. E. *Frontiers in Immunology* **2019**, *10*, 1194.

(320) McKendrick, A. G.; Pai, M. K. *Proceedings of the Royal Society of Edinburgh* **1912**, *31*, 649–653.

(321) Mah, T. F. C.; O'Toole, G. A. *Trends in Microbiology* **2001**, *9*, 34–39.

(322) Golinski, P. A.; Gröger, S.; Herrmann, J. M.; Bernd, A.; Meyle, J. *Journal of Periodontal Research* **2011**, *46*, 704–711.

(323) Sanchez-Quevedo, M. C.; Alaminos, M.; Capitan, L. M.; Moreu, G.; Garzon, I.; Crespo, P. V.; Campos, A. *Histology and Histopathology* **2007**, *22*, 631–640.

# Appendix One

# Details of porcine mucosa specimens

Table A.1: Record of porcine oral mucosa samples taken for mechanical testing, and associated location information.

| **Sample Name** | **Animal number** | **Jaw** | **Location** | **Left/Right** |
|---|---|---|---|---|
| P1_Sample2 | 1 | Mandible | Lingual | Right |
| P1_Sample3 | 1 | Mandible | Lingual | Right |
| P3_Sample1 | 3 | Mandible | Lingual | Left |
| P3_Sample2 | 3 | Mandible | Lingual | Left |
| P3_Sample3 | 3 | Mandible | Lingual | Left |
| P3_Sample4 | 3 | Mandible | Lingual | Left |
| P3_Sample5 | 3 | Mandible | Lingual | Left |
| P3_Sample6 | 3 | Mandible | Lingual | Right |
| P3_Sample7 | 3 | Mandible | Lingual | Right |
| P3_Sample9 | 3 | Mandible | Lingual | Right |
| P3_Sample10 | 3 | Mandible | Lingual | Left |
| P3_Sample11 | 3 | Mandible | Lingual | Right |
| P3_Sample12 | 3 | Mandible | Lingual | Right |
| P3_Sample13 | 3 | Mandible | Buccal | Left |
| P3_Sample14 | 3 | Mandible | Buccal | Left |

**Table A.1 continued from previous page**

| | | | | |
|---|---|---|---|---|
| P3_Sample15 | 3 | Mandible | Buccal | Left |
| P3_Sample16 | 3 | Mandible | Buccal | Left |
| P3_Sample17 | 3 | Mandible | Buccal | Right |
| P3_Sample18 | 3 | Mandible | Buccal | Right |
| P3_Sample19 | 3 | Mandible | Buccal | Right |
| P3_Sample20 | 3 | Mandible | Buccal | Right |
| P3_Sample21 | 3 | Maxilla | Palette | Right |
| P3_Sample22 | 3 | Maxilla | Palette | Right |
| P3_Sample23 | 3 | Maxilla | Palette | Right |
| P3_Sample24 | 3 | Maxilla | Buccal | Left |
| P3_Sample25 | 3 | Maxilla | Buccal | Left |
| P3_Sample26 | 3 | Maxilla | Buccal | Left |
| P3_Sample27 | 3 | Maxilla | Buccal | Left |
| P3_Sample28 | 3 | Maxilla | Buccal | Left |
| P3_Sample29 | 3 | Maxilla | Buccal | Right |
| P3_Sample30 | 3 | Maxilla | Buccal | Right |
| P3_Sample31 | 3 | Maxilla | Buccal | Right |
| P3_Sample32 | 3 | Maxilla | Buccal | Right |
| P4_Sample1 | 4 | Mandible | Lingual | Right |
| P4_Sample2 | 4 | Mandible | Lingual | Right |
| P4_Sample2 | 4 | Mandible | Lingual | Right |
| P4_Sample3 | 4 | Mandible | Lingual | Right |
| P4_Sample4 | 4 | Mandible | Lingual | Right |
| P4_Sample5 | 4 | Mandible | Lingual | Left |
| P4_Sample7 | 4 | Mandible | Lingual | Left |

**Table A.1 continued from previous page**

| | | | | |
|---|---|---|---|---|
| P4_Sample8 | 4 | Mandible | Lingual | Left |
| P4_Sample9 | 4 | Mandible | Lingual | Right |
| P4_Sample10 | 4 | Mandible | Buccal | Left |
| P4_Sample11 | 4 | Mandible | Buccal | Left |
| P4_Sample12 | 4 | Mandible | Buccal | Left |
| P4_Sample13 | 4 | Mandible | Buccal | Right |
| P4_Sample14 | 4 | Mandible | Buccal | Right |
| P4_Sample15 | 4 | Mandible | Buccal | Right |
| P4_Sample16 | 4 | Maxilla | Palette | Left |
| P4_Sample17 | 4 | Maxilla | Palette | Left |
| P4_Sample18 | 4 | Maxilla | Palette | Left |
| P4_Sample19 | 4 | Maxilla | Palette | Right |
| P4_Sample20 | 4 | Maxilla | Buccal | Left |
| P4_Sample21 | 4 | Maxilla | Buccal | Left |
| P4_Sample22 | 4 | Maxilla | Buccal | Left |
| P4_Sample23 | 4 | Maxilla | Buccal | Right |
| P4_Sample24 | 4 | Maxilla | Buccal | Right |
| P4_Sample25 | 4 | Maxilla | Buccal | Right |
| P5_Sample1 | 5 | Mandible | Lingual | Left |
| P5_Sample2 | 5 | Mandible | Lingual | Left |
| P5_Sample3 | 5 | Mandible | Lingual | Right |
| P5_Sample4 | 5 | Mandible | Lingual | Right |
| P5_Sample5 | 5 | Mandible | Lingual | Right |
| P5_Sample6 | 5 | Mandible | Lingual | Right |
| P5_Sample7 | 5 | Mandible | Buccal | Left |

**Table A.1 continued from previous page**

| | | | | |
|---|---|---|---|---|
| P5_Sample8 | 5 | Mandible | Buccal | Left |
| P5_Sample9 | 5 | Mandible | Buccal | Left |
| P5_Sample10 | 5 | Mandible | Buccal | Right |
| P5_Sample11 | 5 | Mandible | Buccal | Right |
| P5_Sample12 | 5 | Mandible | Buccal | Right |
| P5_Sample13 | 5 | Mandible | Lingual | Left |
| P5_Sample14 | 5 | Maxilla | Palette | Left |
| P5_Sample15 | 5 | Maxilla | Palette | Left |
| P5_Sample16 | 5 | Maxilla | Palette | Left |
| P5_Sample17 | 5 | Maxilla | Palette | Right |
| P5_Sample18 | 5 | Maxilla | Palette | Right |
| P5_Sample19 | 5 | Maxilla | Buccal | Left |
| P5_Sample20 | 5 | Maxilla | Buccal | Left |
| P5_Sample21 | 5 | Maxilla | Buccal | Left |
| P5_Sample22 | 5 | Maxilla | Buccal | Right |
| P5_Sample23 | 5 | Maxilla | Buccal | Right |

# Appendix Two

# List of bacteria species used in this thesis

Table B.1: List of bacteria species and their origins used in this thesis

| **Species name** | **Abbreviation** | **Strain/Source** |
|---|---|---|
| *Streptococcus sanguinis* | *S. sanguinis* | ATCC 10556 |
| *Pseudomonas aeruginosa* | *P. aeruginosa* | PA01-N, Paul Williams, University of Nottingham |
| *Fusobacterium nucleatum spp. polymorphum* | *F. nucleatum* | ATCC 10953 |
| *Streptococcus gordonii* | *S. gordonii* | NCTC 7865 |
| *Actinomyces naeslundii* | *A. naeslundii* | DSM 17233 |
| *Porphyromonas gingivalis* | *P. gingivalis* | W83 |
| *Staphylococcus epidermidis* | *S. epidermidis* | ATCC 12228 |

# Appendix Three

# Cellular automaton MATLAB script

```
function [Free_Sticky_Cells_Record, Free_Non_Sticky_Cells_Record,↙
Sticky_Surface_Cells_Record, Non_Sticky_Surface_Cells_Record] = GestelNowakModel(T, D, R,↙
P_m, P_d, K, G, Free_Sticky_Cells_init, Free_Non_Sticky_Cells_init);
%% Gestel Novak Model
% Created by Sophie Mountcastle (                    )
% Adapted from code by Dr Paul Roberts (                          )

% This function models two species of bacteria binding to a 2D surface. The
% two species start within a liquid above the surface. Based on the input
% parameters chosen, upon each iteration a cell can perform one action;
% either divide, die, or migrate to the surface. The two species are known
% as 'Sticky' and 'Non-sticky' bacteria. Sticky bacteria can migrate to any
% available space on the surface. Non-sticky bacteria can only migrate to a
% space on the surface directly neighbouring a sticky cell.

%% Input parameters for function

% T = number of time steps/iterations (e.g. 4*10^5)
% D = division rate of non-sticky cell (must be between 0 and 1)
% R = division rate of sticky cell (must be between 0 and 1)
% P_m = migration rate of cell: liquid to surface (must be between 0 and 1)
% P_d = death rate (must be between 0 and 1)
% K = carrying capacity - max number of cells there can be in the liquid (e.g. 5*10^3)
% G = grid size - length of one side of 2D surface (e.g. 100 or 10 - choose an even value↙
for g)
% Free_Sticky_Cells_init = number of starting sticky cells in liquid (e.g. 10^2)
% Free_Non_Sticky_Cells_init = number of starting non-sticky cells in liquid (e.g. 10^2)

% Grid size
GxFull         = G + 2; % Embed the true grid in a larger grid with empty cells around↙
the periphery (1 column either side).
GyFull         = G + 2; % Embed the true grid in a larger grid with empty cells around↙
the periphery (1 row above and below).
Num_Sites      = G^2;
Num_Sites_Full = GxFull*GyFull;
% We must enlarge the grid with a border of ghost cells so that the CA code
% can search neighbouring cells for any cell on the true grid. The ghost
% cells will remain empty for all time.


%% Initial Conditions

Binding_Sites_init = zeros(GyFull,GxFull);
% All the cells are in the fluid compartment initially, such that all binding sites
% on the surface are empty.

% Save Interval
Save_int  = T/10; % (4*10^3) (T/10)
Num_Saves = T/Save_int;

% Solution Vectors and Matrices
```

```
Free_Sticky_Cells     = Free_Sticky_Cells_init;
Free_Non_Sticky_Cells = Free_Non_Sticky_Cells_init;
Binding_Sites         = Binding_Sites_init; % Enlarged matrix

Free_Sticky_Cells_Record        = [Free_Sticky_Cells_init;zeros(T,1)];
Free_Non_Sticky_Cells_Record    = [Free_Non_Sticky_Cells_init;zeros(T,1)];
Sticky_Surface_Cells_Record     = [0;zeros(T,1)];
Non_Sticky_Surface_Cells_Record = [0;zeros(T,1)];
Binding_Sites_Record            = zeros(G,G,Num_Saves+1); % Matrices containing true sites only


% Cell Counts
% Counting Cells on the Surface
Sticky_Surface_Cells     = 0;
Non_Sticky_Surface_Cells = 0;

% Total Number of Cells
Tot_Num_Cells = Free_Sticky_Cells + Free_Non_Sticky_Cells...
    + Sticky_Surface_Cells + Non_Sticky_Surface_Cells;

%%
%%% Cellular Automata Loop

for i = 2:T+1 % + 1 as i = 1 is t = i-1.

    if Tot_Num_Cells > 0 % Come out of the loop when no cells are left.

        % Pick a cell at random
        rnd_cell_choice_para = randi(Tot_Num_Cells);

        % Decide which of 4 actions to take (migration in either direction counts as 1 action)
        % 1. Migrate (L --> S or S --> L), 2. Differentiate, 3. Die, 4. Divide.
        rnd_act_choice_para = randi(4,1);


        %%%%%%% Pick a free sticky cell (if there aren't any it can't pick one)
        %%%%%%%
        if rnd_cell_choice_para <= Free_Sticky_Cells

            %%%%% Migrate L --> S %%%%%
            if rnd_act_choice_para == 1 && rand(1) < P_m

                % Choose a site to bind to, not counting the border of ghost cells
                % surrounding the true sites.
                Site_Num_x = randi([2,GxFull-1],1);
                Site_Num_y = randi([2,GyFull-1],1);

                if Binding_Sites(Site_Num_y,Site_Num_x) == 0 % Check the site is empty
```

```
                    Binding_Sites(Site_Num_y,Site_Num_x) = 1;    % Cell binds to surface
                    Free_Sticky_Cells = Free_Sticky_Cells - 1;   % Cell leaves fluid

                end

            %%%%% Die %%%%%
            elseif rnd_act_choice_para == 3 && rand(1) < P_d

                Free_Sticky_Cells = Free_Sticky_Cells - 1;  % Cell dies

            %%%%% Divide %%%%%
            elseif rnd_act_choice_para == 4 && Free_Sticky_Cells + Free_Non_Sticky_Cells↙
< K && rand(1) <= R

                Free_Sticky_Cells = Free_Sticky_Cells + 1;  % Cell divides

            end

        %%%%%%% Pick a free nonsticky cell (if there aren't any it can't pick one)
        %%%%%%%
        elseif Free_Sticky_Cells < rnd_cell_choice_para && rnd_cell_choice_para <=↙
Free_Sticky_Cells + Free_Non_Sticky_Cells

            %%%%% Migrate L --> S %%%%%
            if rnd_act_choice_para == 1 && rand(1) < P_m

                % Choose a site to bind to, not counting the border of ghost cells
                % surrounding the true sites.
                Site_Num_x = randi([2,GxFull-1],1);
                Site_Num_y = randi([2,GyFull-1],1);

                % Check that the proposed site is empty, check the parity of the row and
                % check for the presence of sticky cells in neighbouring sites.
                if Binding_Sites(Site_Num_y,Site_Num_x) == 0 && mod(Site_Num_y,2) == 1 &&↙
sum([Binding_Sites(Site_Num_y-1,Site_Num_x),    Binding_Sites(Site_Num_y+1,↙
Site_Num_x),...
↙
Binding_Sites(Site_Num_y,Site_Num_x-1),    Binding_Sites(Site_Num_y,Site_Num_x+1),...
↙
Binding_Sites(Site_Num_y-1,Site_Num_x+1),  Binding_Sites(Site_Num_y+1,Site_Num_x+1)] ==↙
1) >= 1 ||... % Odd row (counting ghost rows)
                    Binding_Sites(Site_Num_y,Site_Num_x) == 0 && mod(Site_Num_y,2) == 0 &&↙
sum([Binding_Sites(Site_Num_y-1,Site_Num_x),    Binding_Sites(Site_Num_y+1,↙
Site_Num_x),...
↙
Binding_Sites(Site_Num_y,Site_Num_x-1),    Binding_Sites(Site_Num_y,Site_Num_x+1),...
↙
Binding_Sites(Site_Num_y-1,Site_Num_x-1),  Binding_Sites(Site_Num_y+1,Site_Num_x-1)] ==↙
1) >= 1       % Even row (counting ghost rows)

                    Binding_Sites(Site_Num_y,Site_Num_x) = 2;          % Cell binds to↙
```

```
surface
                    Free_Non_Sticky_Cells = Free_Non_Sticky_Cells - 1; % Cell leaves↙
fluid

                end

            %%%%% Die %%%%%
            elseif rnd_act_choice_para == 3 && rand(1) < P_d

                Free_Non_Sticky_Cells = Free_Non_Sticky_Cells - 1;  % Cell dies

            %%%%% Divide %%%%%
            elseif rnd_act_choice_para == 4 && Free_Sticky_Cells + Free_Non_Sticky_Cells↙
< K && rand(1) <= D

                Free_Non_Sticky_Cells = Free_Non_Sticky_Cells + 1;  % Cell divides

            end

        %%%%%%% Pick a bound sticky cell (if there aren't any it can't pick one)
        %%%%%%%
        elseif Free_Sticky_Cells + Free_Non_Sticky_Cells < rnd_cell_choice_para &&↙
rnd_cell_choice_para <= Free_Sticky_Cells + Free_Non_Sticky_Cells + Sticky_Surface_Cells

            %%%%% Die %%%%%
            if rnd_act_choice_para == 3 && rand(1) < P_d

                % Pick a sticky cell
                Sticky_Cell_Indices = find(Binding_Sites==1);↙
% Entry number in Binding Site array
                [Sticky_Cell_Indices_y,Sticky_Cell_Indices_x] = find(Binding_Sites==1);↙
% x and y indices of entry
                Sticky_Cell_Index_Choice = randi(length(Sticky_Cell_Indices),1);↙
% Choose a sticky cell from amongst those available (recording its index)
                Sticky_Cell_Choice_x_coord = Sticky_Cell_Indices_x↙
(Sticky_Cell_Index_Choice);   % Find the x coordinate/index of the chosen cell
                Sticky_Cell_Choice_y_coord = Sticky_Cell_Indices_y↙
(Sticky_Cell_Index_Choice);   % Find the y coordinate/index of the chosen cell

                % Kill it
                Binding_Sites(Sticky_Cell_Indices(Sticky_Cell_Index_Choice)) = 0;

                % Identify neighbouring Non-Sticky Cells which do not posses
                % other Sticky neighbours and release them into the fluid.

                % Note the coordinates of the sites surrounding the sticky
                % cell
                if mod(Sticky_Cell_Choice_y_coord,2) == 1     % If the sticky cell is in↙
an odd row (counting ghost rows)

                    Sticky_Neighbourhood_x_coord = Sticky_Cell_Choice_x_coord + [0;0;-1;↙
```

```
1;1;1];
                    Sticky_Neighbourhood_y_coord = Sticky_Cell_Choice_y_coord + [-1;1;0;↙
0;-1;1];

                elseif mod(Sticky_Cell_Choice_y_coord,2) == 0 % If the sticky cell is in↙
an even row (counting ghost rows)

                    Sticky_Neighbourhood_x_coord = Sticky_Cell_Choice_x_coord + [0;0;-1;↙
1;-1;-1];
                    Sticky_Neighbourhood_y_coord = Sticky_Cell_Choice_y_coord + [-1;1;0;↙
0;-1;1];

                end


               % Identify which of the neighbouring sites contain
               % Non-Sticky Cells
                Non_Sticky_Cell_Presence_Vec = zeros(6,1);

                for j = 1:6

                    Non_Sticky_Cell_Presence_Vec(j) = Binding_Sites↙
(Sticky_Neighbourhood_y_coord(j),Sticky_Neighbourhood_x_coord(j))==2;

                end

                Non_Sticky_Neighbour_Cell_Indices = find↙
(Non_Sticky_Cell_Presence_Vec==1); % Indices of sites containing Non-Sticky Cells

                Non_Sticky_Neighbour_Cell_x_coord = Sticky_Neighbourhood_x_coord↙
(Non_Sticky_Neighbour_Cell_Indices); % x-coordinates of sites containing Non-Sticky Cells
                Non_Sticky_Neighbour_Cell_y_coord = Sticky_Neighbourhood_y_coord↙
(Non_Sticky_Neighbour_Cell_Indices); % y-coordinates of sites containing Non-Sticky Cells

                Num_Non_Sticky_Neighbour_Cells = length↙
(Non_Sticky_Neighbour_Cell_x_coord);

                for j = 1:Num_Non_Sticky_Neighbour_Cells

                    % If there are no sticky neighbour cells then detach and return to↙
liquid.
                    if mod(Non_Sticky_Neighbour_Cell_y_coord(j),2) == 1 && sum↙
([Binding_Sites(Non_Sticky_Neighbour_Cell_y_coord(j)-1,Non_Sticky_Neighbour_Cell_x_coord↙
(j)),    Binding_Sites(Non_Sticky_Neighbour_Cell_y_coord(j)+1,↙
Non_Sticky_Neighbour_Cell_x_coord(j)),...
↙
Binding_Sites(Non_Sticky_Neighbour_Cell_y_coord(j),Non_Sticky_Neighbour_Cell_x_coord(j)↙
-1),    Binding_Sites(Non_Sticky_Neighbour_Cell_y_coord(j),↙
Non_Sticky_Neighbour_Cell_x_coord(j)+1),...
↙
Binding_Sites(Non_Sticky_Neighbour_Cell_y_coord(j)-1,Non_Sticky_Neighbour_Cell_x_coord(j)↙
```

```
+1),  Binding_Sites(Non_Sticky_Neighbour_Cell_y_coord(j)+1,↙
Non_Sticky_Neighbour_Cell_x_coord(j)+1)] == 1) == 0 ||... % Odd row (counting ghost rows)
                        mod(Non_Sticky_Neighbour_Cell_y_coord(j),2) == 0 && sum↙
([Binding_Sites(Non_Sticky_Neighbour_Cell_y_coord(j)-1,Non_Sticky_Neighbour_Cell_x_coord↙
(j)),    Binding_Sites(Non_Sticky_Neighbour_Cell_y_coord(j)+1,↙
Non_Sticky_Neighbour_Cell_x_coord(j)),...
↙
Binding_Sites(Non_Sticky_Neighbour_Cell_y_coord(j),Non_Sticky_Neighbour_Cell_x_coord(j)↙
-1),    Binding_Sites(Non_Sticky_Neighbour_Cell_y_coord(j),↙
Non_Sticky_Neighbour_Cell_x_coord(j)+1),...
↙
Binding_Sites(Non_Sticky_Neighbour_Cell_y_coord(j)-1,Non_Sticky_Neighbour_Cell_x_coord(j)↙
-1),  Binding_Sites(Non_Sticky_Neighbour_Cell_y_coord(j)+1,↙
Non_Sticky_Neighbour_Cell_x_coord(j)-1)] == 1) == 0       % Even row (counting ghost↙
rows)

                        Binding_Sites(Non_Sticky_Neighbour_Cell_y_coord(j),↙
Non_Sticky_Neighbour_Cell_x_coord(j)) = 0; % Detach Cell
                        Free_Non_Sticky_Cells = Free_Non_Sticky_Cells + 1; % Return Cell↙
to Fluid Compartment

                    end

                end

            %%%%% Divide %%%%%
            elseif rnd_act_choice_para == 4 && rand(1) <= R

                % Pick a sticky cell
                Sticky_Cell_Indices = find(Binding_Sites==1);↙
% Entry number in Binding Site array
                [Sticky_Cell_Indices_y,Sticky_Cell_Indices_x] = find(Binding_Sites==1);↙
% x and y indices of entry
                Sticky_Cell_Index_Choice = randi(length(Sticky_Cell_Indices),1);↙
% Choose a sticky cell from amongst those available (recording its index)
                Sticky_Cell_Choice_x_coord = Sticky_Cell_Indices_x↙
(Sticky_Cell_Index_Choice);   % Find the x coordinate/index of the chosen cell
                Sticky_Cell_Choice_y_coord = Sticky_Cell_Indices_y↙
(Sticky_Cell_Index_Choice);   % Find the y coordinate/index of the chosen cell

                % Note the coordinates of the sites surrounding the sticky
                % cell
                if mod(Sticky_Cell_Choice_y_coord,2) == 1     % If the sticky cell is in↙
an odd row (counting ghost rows)

                    Sticky_Neighbourhood_x_coord = Sticky_Cell_Choice_x_coord + [0;0;-1;↙
1;1;1];
                    Sticky_Neighbourhood_y_coord = Sticky_Cell_Choice_y_coord + [-1;1;0;↙
0;-1;1];

                elseif mod(Sticky_Cell_Choice_y_coord,2) == 0 % If the sticky cell is in↙
```

```
an even row (counting ghost rows)

                    Sticky_Neighbourhood_x_coord = Sticky_Cell_Choice_x_coord + [0;0;-1;↙
1;-1;-1];
                    Sticky_Neighbourhood_y_coord = Sticky_Cell_Choice_y_coord + [-1;1;0;↙
0;-1;1];

                end

                % Remove any coordinates from the ghost border region

                Rejected_x_Coord_indices_1 = find(Sticky_Neighbourhood_x_coord==1); % Find↙
ghost points on the left and right edges
                Rejected_x_Coord_indices_2 = find(Sticky_Neighbourhood_x_coord==GxFull);

                Rejected_y_Coord_indices_1 = find(Sticky_Neighbourhood_y_coord==1); % Find↙
ghost points on the top and bottom edges
                Rejected_y_Coord_indices_2 = find(Sticky_Neighbourhood_y_coord==GyFull);

                % Collect all rejected indices and remove repetitions
                All_Rejected_Coord_indices = unique([Rejected_x_Coord_indices_1;↙
Rejected_x_Coord_indices_2;Rejected_y_Coord_indices_1;Rejected_y_Coord_indices_2]);

                Sticky_Neighbourhood_x_coord(All_Rejected_Coord_indices) = []; % Strip the↙
coordinate vectors of ghost points
                Sticky_Neighbourhood_y_coord(All_Rejected_Coord_indices) = [];

                Num_Valid_Neighbourhood_Coords = length(Sticky_Neighbourhood_x_coord);

                % Identify which of the neighbouring sites are empty
                Empty_Cell_Presence_Vec = zeros(Num_Valid_Neighbourhood_Coords,1);

                for j = 1:Num_Valid_Neighbourhood_Coords

                    Empty_Cell_Presence_Vec(j) = Binding_Sites↙
(Sticky_Neighbourhood_y_coord(j),Sticky_Neighbourhood_x_coord(j))==0;

                end

                Empty_Neighbour_Indices = find(Empty_Cell_Presence_Vec==1); % Indices of↙
empty sites

                Num_Empty_Neighbour_Sites = length(Empty_Neighbour_Indices);

                % 4 Cases: 1. Neighbour sites and fluid free, 2. Only
                % neighbour sites free, 3. Only fluid free, 4. Nothing free
                % (in this last case do nothing).

                if Num_Empty_Neighbour_Sites > 0 && Free_Sticky_Cells +↙
Free_Non_Sticky_Cells < K % Case 1: Neighbour sites and fluid free.
```

```
                    Chosen_Daughter_Site_Num = randi(Num_Empty_Neighbour_Sites+1,1); %↙
Choose a site or the fluid for the daughter cell

                    if Chosen_Daughter_Site_Num == Num_Empty_Neighbour_Sites + 1 % Cell↙
goes to the fluid

                        Free_Sticky_Cells = Free_Sticky_Cells + 1; % Sticky daughter cell↙
is released into the fluid.

                    else % Cell goes to a neighbouring site

                    Chosen_Daughter_Site_Index = Empty_Neighbour_Indices↙
(Chosen_Daughter_Site_Num);          % Find the index of the site
                    Chosen_Daughter_Site_x_coord = Sticky_Neighbourhood_x_coord↙
(Chosen_Daughter_Site_Index); % Find the coordinates of the site
                    Chosen_Daughter_Site_y_coord = Sticky_Neighbourhood_y_coord↙
(Chosen_Daughter_Site_Index);

                    Binding_Sites(Chosen_Daughter_Site_y_coord,↙
Chosen_Daughter_Site_x_coord) = 1; % Sticky daughter cell is released into neighbouring↙
empty site.

                    end

                elseif Num_Empty_Neighbour_Sites > 0 && Free_Sticky_Cells +↙
Free_Non_Sticky_Cells == K % Case 2: Only neighbour sites free.

                    Chosen_Daughter_Site_Num = randi(Num_Empty_Neighbour_Sites,1);↙
% Choose a site for the daughter cell
                    Chosen_Daughter_Site_Index = Empty_Neighbour_Indices↙
(Chosen_Daughter_Site_Num);          % Find the index of the site
                    Chosen_Daughter_Site_x_coord = Sticky_Neighbourhood_x_coord↙
(Chosen_Daughter_Site_Index); % Find the coordinates of the site
                    Chosen_Daughter_Site_y_coord = Sticky_Neighbourhood_y_coord↙
(Chosen_Daughter_Site_Index);

                    Binding_Sites(Chosen_Daughter_Site_y_coord,↙
Chosen_Daughter_Site_x_coord) = 1; % Sticky daughter cell is released into neighbouring↙
empty site.

                elseif Num_Empty_Neighbour_Sites == 0 && Free_Sticky_Cells +↙
Free_Non_Sticky_Cells < K % Case 3: Only fluid free.

                    Free_Sticky_Cells = Free_Sticky_Cells + 1; % Sticky daughter cell is↙
released into the fluid.

                end


            end
```

```
        %%%%%%% Pick a bound non-sticky cell (if there aren't any it can't pick one)
        %%%%%%%
        elseif Free_Sticky_Cells + Free_Non_Sticky_Cells + Sticky_Surface_Cells <↙
rnd_cell_choice_para && rnd_cell_choice_para <= Free_Sticky_Cells + Free_Non_Sticky_Cells↙
+ Sticky_Surface_Cells + Non_Sticky_Surface_Cells

            %%%%% Die %%%%%
            if rnd_act_choice_para == 3 && rand(1) < P_d

                % Pick a Non-Sticky Cell
                Non_Sticky_Cell_Indices = find(Binding_Sites==2);
                Non_Sticky_Cell_Index_Choice = randi(length(Non_Sticky_Cell_Indices),1);
                % Kill it
                Binding_Sites(Non_Sticky_Cell_Indices(Non_Sticky_Cell_Index_Choice)) = 0;

            %%%%% Divide %%%%%
            elseif rnd_act_choice_para == 4 && rand(1) <= D

                % Pick a non-sticky cell
                Non_Sticky_Cell_Indices = find(Binding_Sites==2);↙
% Entry number in Binding Site array
                [Non_Sticky_Cell_Indices_y,Non_Sticky_Cell_Indices_x] = find↙
(Binding_Sites==2);             % x and y indices of entry
                Non_Sticky_Cell_Index_Choice = randi(length(Non_Sticky_Cell_Indices),1);↙
% Choose a non-sticky cell from amongst those available (recording its index)
                Non_Sticky_Cell_Choice_x_coord = Non_Sticky_Cell_Indices_x↙
(Non_Sticky_Cell_Index_Choice);   % Find the x coordinate/index of the chosen cell
                Non_Sticky_Cell_Choice_y_coord = Non_Sticky_Cell_Indices_y↙
(Non_Sticky_Cell_Index_Choice);   % Find the y coordinate/index of the chosen cell

                % Note the coordinates of the sites surrounding the non-sticky
                % cell
                if mod(Non_Sticky_Cell_Choice_y_coord,2) == 1     % If the non-sticky↙
cell is in an odd row (counting ghost rows)

                    Non_Sticky_Neighbourhood_x_coord = Non_Sticky_Cell_Choice_x_coord +↙
[0;0;-1;1;1;1];
                    Non_Sticky_Neighbourhood_y_coord = Non_Sticky_Cell_Choice_y_coord +↙
[-1;1;0;0;-1;1];

                elseif mod(Non_Sticky_Cell_Choice_y_coord,2) == 0 % If the non-sticky↙
cell is in an even row (counting ghost rows)

                    Non_Sticky_Neighbourhood_x_coord = Non_Sticky_Cell_Choice_x_coord +↙
[0;0;-1;1;-1;-1];
                    Non_Sticky_Neighbourhood_y_coord = Non_Sticky_Cell_Choice_y_coord +↙
[-1;1;0;0;-1;1];

                end

               % Remove any coordinates from the ghost border region
```

```
            Rejected_x_Coord_indices_1 = find(Non_Sticky_Neighbourhood_x_coord==1); %↙
Find ghost points on the left and right edges
            Rejected_x_Coord_indices_2 = find↙
(Non_Sticky_Neighbourhood_x_coord==GxFull);

            Rejected_y_Coord_indices_1 = find(Non_Sticky_Neighbourhood_y_coord==1); %↙
Find ghost points on the top and bottom edges
            Rejected_y_Coord_indices_2 = find↙
(Non_Sticky_Neighbourhood_y_coord==GyFull);

            % Collect all rejected indices and remove repetitions
            All_Rejected_Coord_indices = unique([Rejected_x_Coord_indices_1;↙
Rejected_x_Coord_indices_2;Rejected_y_Coord_indices_1;Rejected_y_Coord_indices_2]);

            Non_Sticky_Neighbourhood_x_coord(All_Rejected_Coord_indices) = []; % Strip↙
the coordinate vectors of ghost points
            Non_Sticky_Neighbourhood_y_coord(All_Rejected_Coord_indices) = [];

            Num_Valid_Neighbourhood_Coords = length(Non_Sticky_Neighbourhood_x_coord);

            % Identify which of the neighbouring sites are empty
             Empty_Cell_Presence_Vec = zeros(Num_Valid_Neighbourhood_Coords,1);

             for j = 1:Num_Valid_Neighbourhood_Coords

                 Empty_Cell_Presence_Vec(j) = Binding_Sites↙
(Non_Sticky_Neighbourhood_y_coord(j),Non_Sticky_Neighbourhood_x_coord(j))==0;

             end

             Empty_Neighbour_Indices = find(Empty_Cell_Presence_Vec==1); % Indices of↙
empty sites

             Neighbour_Site_x_coords = Non_Sticky_Neighbourhood_x_coord↙
(Empty_Neighbour_Indices); % Find the coordinates of the valid empty neighbouring sites
             Neighbour_Site_y_coords = Non_Sticky_Neighbourhood_y_coord↙
(Empty_Neighbour_Indices);

             Num_Empty_Neighbour_Sites = length(Empty_Neighbour_Indices); % The number↙
of valid empty neighbouring sites

             Sites_with_Sticky_Neighbours = zeros(1,6);

             for j = 1:Num_Empty_Neighbour_Sites

                 % Remove those entries which don't have any sticky neighbours.
                 if mod(Neighbour_Site_y_coords(j),2) == 1 && sum([Binding_Sites↙
(Neighbour_Site_y_coords(j)-1,Neighbour_Site_x_coords(j)),    Binding_Sites↙
(Neighbour_Site_y_coords(j)+1,Neighbour_Site_x_coords(j)),...
                                                                Binding_Sites↙
```

```
(Neighbour_Site_y_coords(j),Neighbour_Site_x_coords(j)-1),    Binding_Sites↙
(Neighbour_Site_y_coords(j),Neighbour_Site_x_coords(j)+1),...
                                                              Binding_Sites↙
(Neighbour_Site_y_coords(j)-1,Neighbour_Site_x_coords(j)+1),  Binding_Sites↙
(Neighbour_Site_y_coords(j)+1,Neighbour_Site_x_coords(j)+1)] == 1) > 0 ||... % Odd row↙
(counting ghost rows)
                    mod(Neighbour_Site_y_coords(j),2) == 0 && sum([Binding_Sites↙
(Neighbour_Site_y_coords(j)-1,Neighbour_Site_x_coords(j)),    Binding_Sites↙
(Neighbour_Site_y_coords(j)+1,Neighbour_Site_x_coords(j)),...
                                                              Binding_Sites↙
(Neighbour_Site_y_coords(j),Neighbour_Site_x_coords(j)-1),    Binding_Sites↙
(Neighbour_Site_y_coords(j),Neighbour_Site_x_coords(j)+1),...
                                                              Binding_Sites↙
(Neighbour_Site_y_coords(j)-1,Neighbour_Site_x_coords(j)-1),  Binding_Sites↙
(Neighbour_Site_y_coords(j)+1,Neighbour_Site_x_coords(j)-1)] == 1) > 0       % Even row↙
(counting ghost rows)

                        Sites_with_Sticky_Neighbours(j) = 1;

                    end

                end

                Sites_with_Sticky_Neighbours_Indices = find↙
(Sites_with_Sticky_Neighbours==1);

                Neighbour_Site_x_coords = Neighbour_Site_x_coords↙
(Sites_with_Sticky_Neighbours_Indices);
                Neighbour_Site_y_coords = Neighbour_Site_y_coords↙
(Sites_with_Sticky_Neighbours_Indices);

                Num_Valid_Neighbour_Sites = length(Neighbour_Site_x_coords); % The number↙
of valid empty neighbouring sites with sticky neighbours

                % 4 Cases: 1. Neighbour sites and fluid free, 2. Only
                % neighbour sites free, 3. Only fluid free, 4. Nothing free
                % (in this last case do nothing).

                if Num_Valid_Neighbour_Sites > 0 && Free_Sticky_Cells +↙
Free_Non_Sticky_Cells < K % Case 1: Neighbour sites and fluid free.

                    Chosen_Daughter_Site_Num = randi(Num_Valid_Neighbour_Sites+1,1); %↙
Choose a site or the fluid for the daughter cell

                    if Chosen_Daughter_Site_Num == Num_Valid_Neighbour_Sites + 1 % Cell↙
goes to the fluid

                        Free_Non_Sticky_Cells = Free_Non_Sticky_Cells + 1; % Non-sticky↙
daughter cell is released into the fluid.

                    else % Cell goes to a neighbouring site
```

```
                    Chosen_Daughter_Site_x_coord = Neighbour_Site_x_coords↙
(Chosen_Daughter_Site_Num); % Find the coordinates of the site
                    Chosen_Daughter_Site_y_coord = Neighbour_Site_y_coords↙
(Chosen_Daughter_Site_Num);

                    Binding_Sites(Chosen_Daughter_Site_y_coord,↙
Chosen_Daughter_Site_x_coord) = 2; % Nonsticky daughter cell is released into↙
neighbouring empty site.

                    end

                elseif Num_Valid_Neighbour_Sites > 0 && Free_Sticky_Cells +↙
Free_Non_Sticky_Cells == K % Case 2: Only neighbour sites free.

                    Chosen_Daughter_Site_Num = randi(Num_Valid_Neighbour_Sites,1);↙
% Choose a site for the daughter cell
                    Chosen_Daughter_Site_x_coord = Neighbour_Site_x_coords↙
(Chosen_Daughter_Site_Num); % Find the coordinates of the site
                    Chosen_Daughter_Site_y_coord = Neighbour_Site_y_coords↙
(Chosen_Daughter_Site_Num);

                    Binding_Sites(Chosen_Daughter_Site_y_coord,↙
Chosen_Daughter_Site_x_coord) = 2; % Non-sticky daughter cell is released into↙
neighbouring empty site.

                elseif Num_Valid_Neighbour_Sites == 0 && Free_Sticky_Cells +↙
Free_Non_Sticky_Cells < K % Case 3: Only fluid free.

                    Free_Non_Sticky_Cells = Free_Non_Sticky_Cells + 1; % Non-sticky↙
daughter cell is released into the fluid.

                end

            end

        end

        % Remove cells from the fluid if their number exceeds the carrying
        % capacity. Remove cells randomly, with probability in proportion
        % to the fracion of cells that are sticky/non-sticky.
        while Free_Sticky_Cells + Free_Non_Sticky_Cells > K

            if rand(1) < Free_Sticky_Cells/(Free_Sticky_Cells + Free_Non_Sticky_Cells)

                Free_Sticky_Cells = Free_Sticky_Cells - 1;

            else

                Free_Non_Sticky_Cells = Free_Non_Sticky_Cells - 1;
```

```
            end

        end

        % Counting Cells on the Surface
        Sticky_Surface_Cells     = length(find(Binding_Sites==1));
        Non_Sticky_Surface_Cells = length(find(Binding_Sites==2));

        % Total Number of Cells
        Tot_Num_Cells            = Free_Sticky_Cells + Free_Non_Sticky_Cells...
            + Sticky_Surface_Cells + Non_Sticky_Surface_Cells;

        % Record True Binding Sites every Save_int-th iteration
        if mod(i,Save_int) == 0

            Binding_Sites_Record(:,:,1+i/Save_int) = Binding_Sites(2:(GyFull-1),2:↙
(GxFull-1)); % 1+ as the first entry should be the initial condition.

        end

        % Update cell counts
        Free_Sticky_Cells_Record(i)        = Free_Sticky_Cells;
        Free_Non_Sticky_Cells_Record(i)    = Free_Non_Sticky_Cells;
        Sticky_Surface_Cells_Record(i)     = Sticky_Surface_Cells;
        Non_Sticky_Surface_Cells_Record(i) = Non_Sticky_Surface_Cells;

    end

end
```

# Appendix Four

# Cellular automaton MATLAB script with dead cell count

```
function [Free_Sticky_Cells_Record, Dead_Free_Sticky_Cells_Record,↙
Free_Non_Sticky_Cells_Record, Dead_Free_Non_Sticky_Cells_Record,↙
Sticky_Surface_Cells_Record, Dead_Sticky_Surface_Cells_Record,↙
Non_Sticky_Surface_Cells_Record, Dead_Non_Sticky_Surface_Cells_Record] =↙
GestelNowakModel_DeadCells(T, D, q, R, p, P_m, P_d, K, G, Free_Sticky_Cells_init,↙
Free_Non_Sticky_Cells_init);
%% Gestel Novak Model
% Created by Sophie Mountcastle (                    )
% Adapted from code by Dr Paul Roberts (                          )

% This function models two species of bacteria binding to a 2D surface. The
% two species start within a liquid above the surface. Based on the input
% parameters chosen, upon each iteration a cell can perform one action;
% either divide, die, or migrate to the surface. The two species are known
% as 'Sticky' and 'Non-sticky' bacteria. Sticky bacteria can migrate to any
% available space on the surface. Non-sticky bacteria can only migrate to a
% space on the surface directly neighbouring a sticky cell.

%This code is designed to represent the number of bacteria over a single or
%small number of epithelial cells (i.e. a 10x10 Grid is approximately 10x10
%microns).

%% Input parameters for function

%T = 4*10^5; %number of time steps/iterations (e.g. 4*10^5)
%D = 0.5; %division rate of non-sticky cell (must be between 0 and 1)
%q = 1; %a function of D (e.g. for p = 1:T, division rate can be sin(p). Set to 1 if not↙
using a function.)
%R = 0.5; %division rate of sticky cell (must be between 0 and 1)
%p = 1; %a function of R (e.g. for p = 1:T, division rate can be sin(p). Set to 1 if not↙
using a function.)
%P_m = 0.75; %migration rate of cell: liquid to surface (must be between 0 and 1)
%P_d = 0.1; %death rate (must be between 0 and 1)
%K = 5000; %carrying capacity - max number of cells there can be in the liquid (e.g.↙
5*10^3)
%G = 100; %grid size - length of one side of 2D surface (e.g. 100 or 10 - choose an even↙
value for g)
%Free_Sticky_Cells_init = 100; %number of starting sticky cells in liquid (e.g. 10^2)
%Free_Non_Sticky_Cells_init = 100; %number of starting non-sticky cells in liquid (e.g.↙
10^2)
Dead_Free_Sticky_Cells_init = 0;
Dead_Free_Non_Sticky_Cells_init = 0;

% Grid size
GxFull         = G + 2; % Embed the true grid in a larger grid with empty cells around↙
the periphery (1 column either side).
GyFull         = G + 2; % Embed the true grid in a larger grid with empty cells around↙
the periphery (1 row above and below).
Num_Sites      = G^2;
Num_Sites_Full = GxFull*GyFull;
% We must enlarge the grid with a border of ghost cells so that the CA code
```

```
% can search neighbouring cells for any cell on the true grid. The ghost
% cells will remain empty for all time.


%% Initial Conditions

Binding_Sites_init = zeros(GyFull,GxFull);
% All the cells are in the fluid compartment initially, such that all binding sites
% on the surface are empty.

% Save Interval
Save_int  = T/10; % (4*10^3) (T/10)
Num_Saves = T/Save_int;

% Solution Vectors and Matrices
Free_Sticky_Cells           = Free_Sticky_Cells_init;
Dead_Free_Sticky_Cells      = Dead_Free_Sticky_Cells_init;
Free_Non_Sticky_Cells       = Free_Non_Sticky_Cells_init;
Dead_Free_Non_Sticky_Cells  = Dead_Free_Non_Sticky_Cells_init;
Binding_Sites               = Binding_Sites_init; % Enlarged matrix

Free_Sticky_Cells_Record             = [Free_Sticky_Cells_init;zeros(T,1)];
Dead_Free_Sticky_Cells_Record        = [Dead_Free_Sticky_Cells_init;zeros(T,1)];
Free_Non_Sticky_Cells_Record         = [Free_Non_Sticky_Cells_init;zeros(T,1)];
Dead_Free_Non_Sticky_Cells_Record    = [Dead_Free_Non_Sticky_Cells_init;zeros(T,1)];
Sticky_Surface_Cells_Record          = [0;zeros(T,1)];
Dead_Sticky_Surface_Cells_Record     = [0;zeros(T,1)];
Non_Sticky_Surface_Cells_Record      = [0;zeros(T,1)];
Dead_Non_Sticky_Surface_Cells_Record = [0;zeros(T,1)];
Binding_Sites_Record                 = zeros(G,G,Num_Saves+1); % Matrices containing true↙
sites only


% Cell Counts
% Counting Cells on the Surface
Sticky_Surface_Cells          = 0;
Dead_Sticky_Surface_Cells     = 0;
Non_Sticky_Surface_Cells      = 0;
Dead_Non_Sticky_Surface_Cells = 0;

% Total Number of Cells
Tot_Num_Cells = Free_Sticky_Cells + Dead_Free_Sticky_Cells + Free_Non_Sticky_Cells...
    + Dead_Free_Non_Sticky_Cells + Sticky_Surface_Cells + Dead_Sticky_Surface_Cells...
    + Non_Sticky_Surface_Cells + Dead_Non_Sticky_Surface_Cells;

% Total Number of Live Cells
Tot_Num_Live_Cells = Free_Sticky_Cells + Free_Non_Sticky_Cells + Sticky_Surface_Cells...
    + Non_Sticky_Surface_Cells;

% Total Number of Dead Cells
Tot_Num_Dead_Cells = Dead_Free_Sticky_Cells + Dead_Free_Non_Sticky_Cells...
```

```
    + Dead_Sticky_Surface_Cells + Dead_Non_Sticky_Surface_Cells;

%%
%%% Cellular Automata Loop

for i = 2:T+1 % + 1 as i = 1 is t = i-1.

    if Tot_Num_Live_Cells > 0 % Come out of the loop when no live cells are left.

        % Pick a cell at random
        rnd_cell_choice_para = randi(Tot_Num_Live_Cells); %only live cells can perform an↙
action

        % Decide which of 4 actions to take (migration in either direction counts as 1↙
action)
        % 1. Migrate (L --> S or S --> L), 2. Differentiate, 3. Die, 4. Divide.
        rnd_act_choice_para = randi(4,1);


        %%%%%%% Pick a free sticky cell (if there aren't any it can't pick one)
        %%%%%%%
        if rnd_cell_choice_para <= Free_Sticky_Cells

            %%%%% Migrate L --> S %%%%%
            if rnd_act_choice_para == 1 && rand(1) < P_m

                % Choose a site to bind to, not counting the border of ghost cells
                % surrounding the true sites.
                Site_Num_x = randi([2,GxFull-1],1);
                Site_Num_y = randi([2,GyFull-1],1);

                if Binding_Sites(Site_Num_y,Site_Num_x) == 0 % Check the site is empty

                    Binding_Sites(Site_Num_y,Site_Num_x) = 1;    % Cell binds to surface
                    Free_Sticky_Cells = Free_Sticky_Cells - 1;  % Cell leaves fluid

                end

            %%%%% Die %%%%%
            elseif rnd_act_choice_para == 3 && rand(1) < P_d

                Free_Sticky_Cells = Free_Sticky_Cells - 1;  % Cell dies
                Dead_Free_Sticky_Cells = Dead_Free_Sticky_Cells + 1;

            %%%%% Divide %%%%%
            elseif rnd_act_choice_para == 4 && Free_Sticky_Cells +↙
Free_Non_Sticky_Cells...
                    + Dead_Free_Sticky_Cells + Dead_Free_Non_Sticky_Cells < K && rand(1)↙
<= R(p)

                Free_Sticky_Cells = Free_Sticky_Cells + 1;  % Cell divides
```

```
            end

        %%%%%%% Pick a free nonsticky cell (if there aren't any it can't pick one)
        %%%%%%%
        elseif Free_Sticky_Cells < rnd_cell_choice_para && rnd_cell_choice_para <=↙
Free_Sticky_Cells + Free_Non_Sticky_Cells

            %%%%% Migrate L --> S %%%%%
            if rnd_act_choice_para == 1 && rand(1) < P_m

                % Choose a site to bind to, not counting the border of ghost cells
                % surrounding the true sites.
                Site_Num_x = randi([2,GxFull-1],1);
                Site_Num_y = randi([2,GyFull-1],1);

                % Check that the proposed site is empty, check the parity of the row and
                % check for the presence of sticky cells in neighbouring sites.
                if Binding_Sites(Site_Num_y,Site_Num_x) == 0 && mod(Site_Num_y,2) == 1 &&↙
sum([Binding_Sites(Site_Num_y-1,Site_Num_x),    Binding_Sites(Site_Num_y+1,↙
Site_Num_x),...
↙
Binding_Sites(Site_Num_y,Site_Num_x-1),    Binding_Sites(Site_Num_y,Site_Num_x+1),...
↙
Binding_Sites(Site_Num_y-1,Site_Num_x+1),  Binding_Sites(Site_Num_y+1,Site_Num_x+1)] ==↙
1) >= 1 ||... % Odd row (counting ghost rows)
                    Binding_Sites(Site_Num_y,Site_Num_x) == 0 && mod(Site_Num_y,2) == 0 &&↙
sum([Binding_Sites(Site_Num_y-1,Site_Num_x),    Binding_Sites(Site_Num_y+1,↙
Site_Num_x),...
↙
Binding_Sites(Site_Num_y,Site_Num_x-1),    Binding_Sites(Site_Num_y,Site_Num_x+1),...
↙
Binding_Sites(Site_Num_y-1,Site_Num_x-1),  Binding_Sites(Site_Num_y+1,Site_Num_x-1)] ==↙
1) >= 1       % Even row (counting ghost rows)

                    Binding_Sites(Site_Num_y,Site_Num_x) = 2;          % Cell binds to↙
surface
                    Free_Non_Sticky_Cells = Free_Non_Sticky_Cells - 1; % Cell leaves↙
fluid

                end

            %%%%% Die %%%%%
            elseif rnd_act_choice_para == 3 && rand(1) < P_d

                Free_Non_Sticky_Cells = Free_Non_Sticky_Cells - 1;  % Cell dies
                Dead_Free_Non_Sticky_Cells = Dead_Free_Non_Sticky_Cells +1;

            %%%%% Divide %%%%%
            elseif rnd_act_choice_para == 4 && Free_Sticky_Cells +↙
Free_Non_Sticky_Cells...
```

```
                    + Dead_Free_Sticky_Cells + Dead_Free_Non_Sticky_Cells < K && rand(1) <= D(q)

                Free_Non_Sticky_Cells = Free_Non_Sticky_Cells + 1;  % Cell divides

            end

        %%%%%%% Pick a bound sticky cell (if there aren't any it can't pick one)
        %%%%%%%
        elseif Free_Sticky_Cells + Free_Non_Sticky_Cells < rnd_cell_choice_para && rnd_cell_choice_para <= Free_Sticky_Cells + Free_Non_Sticky_Cells + Sticky_Surface_Cells

            %%%%% Die %%%%%
            if rnd_act_choice_para == 3 && rand(1) < P_d

                % Pick a sticky cell
                Sticky_Cell_Indices = find(Binding_Sites==1);
% Entry number in Binding Site array
                [Sticky_Cell_Indices_y,Sticky_Cell_Indices_x] = find(Binding_Sites==1);
% x and y indices of entry
                Sticky_Cell_Index_Choice = randi(length(Sticky_Cell_Indices),1);
% Choose a sticky cell from amongst those available (recording its index)
                Sticky_Cell_Choice_x_coord = Sticky_Cell_Indices_x(Sticky_Cell_Index_Choice);   % Find the x coordinate/index of the chosen cell
                Sticky_Cell_Choice_y_coord = Sticky_Cell_Indices_y(Sticky_Cell_Index_Choice);   % Find the y coordinate/index of the chosen cell

                % Kill it
                Binding_Sites(Sticky_Cell_Indices(Sticky_Cell_Index_Choice)) = 3; %cell stays bound but dies

                % Identify neighbouring Non-Sticky Cells which do not posses
                % other Sticky neighbours and release them into the fluid.

                % Note the coordinates of the sites surrounding the sticky
                % cell
                if mod(Sticky_Cell_Choice_y_coord,2) == 1     % If the sticky cell is in an odd row (counting ghost rows)

                    Sticky_Neighbourhood_x_coord = Sticky_Cell_Choice_x_coord + [0;0;-1;1;1;1];
                    Sticky_Neighbourhood_y_coord = Sticky_Cell_Choice_y_coord + [-1;1;0;0;-1;1];

                elseif mod(Sticky_Cell_Choice_y_coord,2) == 0 % If the sticky cell is in an even row (counting ghost rows)

                    Sticky_Neighbourhood_x_coord = Sticky_Cell_Choice_x_coord + [0;0;-1;1;-1;-1];
                    Sticky_Neighbourhood_y_coord = Sticky_Cell_Choice_y_coord + [-1;1;0;0;-1;1];
```

```
                end


               % Identify which of the neighbouring sites contain
               % Non-Sticky Cells
                Non_Sticky_Cell_Presence_Vec = zeros(6,1);

                for j = 1:6

                    Non_Sticky_Cell_Presence_Vec(j) = Binding_Sites↙
(Sticky_Neighbourhood_y_coord(j),Sticky_Neighbourhood_x_coord(j))==2;

                end

                Non_Sticky_Neighbour_Cell_Indices = find↙
(Non_Sticky_Cell_Presence_Vec==1); % Indices of sites containing Non-Sticky Cells

                Non_Sticky_Neighbour_Cell_x_coord = Sticky_Neighbourhood_x_coord↙
(Non_Sticky_Neighbour_Cell_Indices); % x-coordinates of sites containing Non-Sticky Cells
                Non_Sticky_Neighbour_Cell_y_coord = Sticky_Neighbourhood_y_coord↙
(Non_Sticky_Neighbour_Cell_Indices); % y-coordinates of sites containing Non-Sticky Cells

                Num_Non_Sticky_Neighbour_Cells = length↙
(Non_Sticky_Neighbour_Cell_x_coord);

                for j = 1:Num_Non_Sticky_Neighbour_Cells

                    % If there are no sticky neighbour cells then detach and return to↙
liquid.
                    if mod(Non_Sticky_Neighbour_Cell_y_coord(j),2) == 1 && sum↙
([Binding_Sites(Non_Sticky_Neighbour_Cell_y_coord(j)-1,Non_Sticky_Neighbour_Cell_x_coord↙
(j)),    Binding_Sites(Non_Sticky_Neighbour_Cell_y_coord(j)+1,↙
Non_Sticky_Neighbour_Cell_x_coord(j)),...
↙
Binding_Sites(Non_Sticky_Neighbour_Cell_y_coord(j),Non_Sticky_Neighbour_Cell_x_coord(j)↙
-1),    Binding_Sites(Non_Sticky_Neighbour_Cell_y_coord(j),↙
Non_Sticky_Neighbour_Cell_x_coord(j)+1),...
↙
Binding_Sites(Non_Sticky_Neighbour_Cell_y_coord(j)-1,Non_Sticky_Neighbour_Cell_x_coord(j)↙
+1),  Binding_Sites(Non_Sticky_Neighbour_Cell_y_coord(j)+1,↙
Non_Sticky_Neighbour_Cell_x_coord(j)+1)] == 1) == 0 ||... % Odd row (counting ghost rows)
                        mod(Non_Sticky_Neighbour_Cell_y_coord(j),2) == 0 && sum↙
([Binding_Sites(Non_Sticky_Neighbour_Cell_y_coord(j)-1,Non_Sticky_Neighbour_Cell_x_coord↙
(j)),    Binding_Sites(Non_Sticky_Neighbour_Cell_y_coord(j)+1,↙
Non_Sticky_Neighbour_Cell_x_coord(j)),...
↙
Binding_Sites(Non_Sticky_Neighbour_Cell_y_coord(j),Non_Sticky_Neighbour_Cell_x_coord(j)↙
-1),    Binding_Sites(Non_Sticky_Neighbour_Cell_y_coord(j),↙
Non_Sticky_Neighbour_Cell_x_coord(j)+1),...
↙
```

```
Binding_Sites(Non_Sticky_Neighbour_Cell_y_coord(j)-1,Non_Sticky_Neighbour_Cell_x_coord(j)↙
-1),  Binding_Sites(Non_Sticky_Neighbour_Cell_y_coord(j)+1,↙
Non_Sticky_Neighbour_Cell_x_coord(j)-1)] == 1) == 0       % Even row (counting ghost↙
rows)

                        Binding_Sites(Non_Sticky_Neighbour_Cell_y_coord(j),↙
Non_Sticky_Neighbour_Cell_x_coord(j)) = 0; % Detach Cell
                        Free_Non_Sticky_Cells = Free_Non_Sticky_Cells + 1; % Return Cell↙
to Fluid Compartment

                    end

                end

            %%%%% Divide %%%%%
            elseif rnd_act_choice_para == 4 && rand(1) <= R(p)

                % Pick a sticky cell
                Sticky_Cell_Indices = find(Binding_Sites==1);↙
% Entry number in Binding Site array
                [Sticky_Cell_Indices_y,Sticky_Cell_Indices_x] = find(Binding_Sites==1);↙
% x and y indices of entry
                Sticky_Cell_Index_Choice = randi(length(Sticky_Cell_Indices),1);↙
% Choose a sticky cell from amongst those available (recording its index)
                Sticky_Cell_Choice_x_coord = Sticky_Cell_Indices_x↙
(Sticky_Cell_Index_Choice);   % Find the x coordinate/index of the chosen cell
                Sticky_Cell_Choice_y_coord = Sticky_Cell_Indices_y↙
(Sticky_Cell_Index_Choice);   % Find the y coordinate/index of the chosen cell

                % Note the coordinates of the sites surrounding the sticky
                % cell
                if mod(Sticky_Cell_Choice_y_coord,2) == 1     % If the sticky cell is in↙
an odd row (counting ghost rows)

                    Sticky_Neighbourhood_x_coord = Sticky_Cell_Choice_x_coord + [0;0;-1;↙
1;1;1];
                    Sticky_Neighbourhood_y_coord = Sticky_Cell_Choice_y_coord + [-1;1;0;↙
0;-1;1];

                elseif mod(Sticky_Cell_Choice_y_coord,2) == 0 % If the sticky cell is in↙
an even row (counting ghost rows)

                    Sticky_Neighbourhood_x_coord = Sticky_Cell_Choice_x_coord + [0;0;-1;↙
1;-1;-1];
                    Sticky_Neighbourhood_y_coord = Sticky_Cell_Choice_y_coord + [-1;1;0;↙
0;-1;1];

                end

               % Remove any coordinates from the ghost border region
```

```
                Rejected_x_Coord_indices_1 = find(Sticky_Neighbourhood_x_coord==1); % Find↙
ghost points on the left and right edges
                Rejected_x_Coord_indices_2 = find(Sticky_Neighbourhood_x_coord==GxFull);

                Rejected_y_Coord_indices_1 = find(Sticky_Neighbourhood_y_coord==1); % Find↙
ghost points on the top and bottom edges
                Rejected_y_Coord_indices_2 = find(Sticky_Neighbourhood_y_coord==GyFull);

                % Collect all rejected indices and remove repetitions
                All_Rejected_Coord_indices = unique([Rejected_x_Coord_indices_1;↙
Rejected_x_Coord_indices_2;Rejected_y_Coord_indices_1;Rejected_y_Coord_indices_2]);

                Sticky_Neighbourhood_x_coord(All_Rejected_Coord_indices) = []; % Strip the↙
coordinate vectors of ghost points
                Sticky_Neighbourhood_y_coord(All_Rejected_Coord_indices) = [];

                Num_Valid_Neighbourhood_Coords = length(Sticky_Neighbourhood_x_coord);

                % Identify which of the neighbouring sites are empty
                 Empty_Cell_Presence_Vec = zeros(Num_Valid_Neighbourhood_Coords,1);

                 for j = 1:Num_Valid_Neighbourhood_Coords

                     Empty_Cell_Presence_Vec(j) = Binding_Sites↙
(Sticky_Neighbourhood_y_coord(j),Sticky_Neighbourhood_x_coord(j))==0;

                 end

                 Empty_Neighbour_Indices = find(Empty_Cell_Presence_Vec==1); % Indices of↙
empty sites

                 Num_Empty_Neighbour_Sites = length(Empty_Neighbour_Indices);

                 % 4 Cases: 1. Neighbour sites and fluid free, 2. Only
                 % neighbour sites free, 3. Only fluid free, 4. Nothing free
                 % (in this last case do nothing).

                 if Num_Empty_Neighbour_Sites > 0 && Free_Sticky_Cells +↙
Free_Non_Sticky_Cells < K % Case 1: Neighbour sites and fluid free.

                     Chosen_Daughter_Site_Num = randi(Num_Empty_Neighbour_Sites+1,1); %↙
Choose a site or the fluid for the daughter cell

                     if Chosen_Daughter_Site_Num == Num_Empty_Neighbour_Sites + 1 % Cell↙
goes to the fluid

                         Free_Sticky_Cells = Free_Sticky_Cells + 1; % Sticky daughter cell↙
is released into the fluid.

                     else % Cell goes to a neighbouring site
```

```
                    Chosen_Daughter_Site_Index = Empty_Neighbour_Indices↙
(Chosen_Daughter_Site_Num);          % Find the index of the site
                    Chosen_Daughter_Site_x_coord = Sticky_Neighbourhood_x_coord↙
(Chosen_Daughter_Site_Index); % Find the coordinates of the site
                    Chosen_Daughter_Site_y_coord = Sticky_Neighbourhood_y_coord↙
(Chosen_Daughter_Site_Index);

                    Binding_Sites(Chosen_Daughter_Site_y_coord,↙
Chosen_Daughter_Site_x_coord) = 1; % Sticky daughter cell is released into neighbouring↙
empty site.

                    end

                elseif Num_Empty_Neighbour_Sites > 0 && Free_Sticky_Cells +↙
Free_Non_Sticky_Cells == K % Case 2: Only neighbour sites free.

                    Chosen_Daughter_Site_Num = randi(Num_Empty_Neighbour_Sites,1);↙
% Choose a site for the daughter cell
                    Chosen_Daughter_Site_Index = Empty_Neighbour_Indices↙
(Chosen_Daughter_Site_Num);          % Find the index of the site
                    Chosen_Daughter_Site_x_coord = Sticky_Neighbourhood_x_coord↙
(Chosen_Daughter_Site_Index); % Find the coordinates of the site
                    Chosen_Daughter_Site_y_coord = Sticky_Neighbourhood_y_coord↙
(Chosen_Daughter_Site_Index);

                    Binding_Sites(Chosen_Daughter_Site_y_coord,↙
Chosen_Daughter_Site_x_coord) = 1; % Sticky daughter cell is released into neighbouring↙
empty site.

                elseif Num_Empty_Neighbour_Sites == 0 && Free_Sticky_Cells +↙
Free_Non_Sticky_Cells < K % Case 3: Only fluid free.

                    Free_Sticky_Cells = Free_Sticky_Cells + 1; % Sticky daughter cell is↙
released into the fluid.

                end


            end

        %%%%%%% Pick a bound non-sticky cell (if there aren't any it can't pick one)
        %%%%%%%
        elseif Free_Sticky_Cells + Free_Non_Sticky_Cells + Sticky_Surface_Cells <↙
rnd_cell_choice_para && rnd_cell_choice_para <= Free_Sticky_Cells + Free_Non_Sticky_Cells↙
+ Sticky_Surface_Cells + Non_Sticky_Surface_Cells

            %%%%% Die %%%%%
            if rnd_act_choice_para == 3 && rand(1) < P_d

                % Pick a Non-Sticky Cell
                Non_Sticky_Cell_Indices = find(Binding_Sites==2);
```

```
                Non_Sticky_Cell_Index_Choice = randi(length(Non_Sticky_Cell_Indices),1);
                % Kill it
                Binding_Sites(Non_Sticky_Cell_Indices(Non_Sticky_Cell_Index_Choice)) = 4;

            %%%%% Divide %%%%%
            elseif rnd_act_choice_para == 4 && rand(1) <= D(q)

                % Pick a non-sticky cell
                Non_Sticky_Cell_Indices = find(Binding_Sites==2);
% Entry number in Binding Site array
                [Non_Sticky_Cell_Indices_y,Non_Sticky_Cell_Indices_x] = find
(Binding_Sites==2);             % x and y indices of entry
                Non_Sticky_Cell_Index_Choice = randi(length(Non_Sticky_Cell_Indices),1);
% Choose a non-sticky cell from amongst those available (recording its index)
                Non_Sticky_Cell_Choice_x_coord = Non_Sticky_Cell_Indices_x
(Non_Sticky_Cell_Index_Choice);   % Find the x coordinate/index of the chosen cell
                Non_Sticky_Cell_Choice_y_coord = Non_Sticky_Cell_Indices_y
(Non_Sticky_Cell_Index_Choice);   % Find the y coordinate/index of the chosen cell

                % Note the coordinates of the sites surrounding the non-sticky
                % cell
                if mod(Non_Sticky_Cell_Choice_y_coord,2) == 1     % If the non-sticky
cell is in an odd row (counting ghost rows)

                    Non_Sticky_Neighbourhood_x_coord = Non_Sticky_Cell_Choice_x_coord +
[0;0;-1;1;1;1];
                    Non_Sticky_Neighbourhood_y_coord = Non_Sticky_Cell_Choice_y_coord +
[-1;1;0;0;-1;1];

                elseif mod(Non_Sticky_Cell_Choice_y_coord,2) == 0 % If the non-sticky
cell is in an even row (counting ghost rows)

                    Non_Sticky_Neighbourhood_x_coord = Non_Sticky_Cell_Choice_x_coord +
[0;0;-1;1;-1;-1];
                    Non_Sticky_Neighbourhood_y_coord = Non_Sticky_Cell_Choice_y_coord +
[-1;1;0;0;-1;1];

                end

                % Remove any coordinates from the ghost border region

                Rejected_x_Coord_indices_1 = find(Non_Sticky_Neighbourhood_x_coord==1); %
Find ghost points on the left and right edges
                Rejected_x_Coord_indices_2 = find
(Non_Sticky_Neighbourhood_x_coord==GxFull);

                Rejected_y_Coord_indices_1 = find(Non_Sticky_Neighbourhood_y_coord==1); %
Find ghost points on the top and bottom edges
                Rejected_y_Coord_indices_2 = find
(Non_Sticky_Neighbourhood_y_coord==GyFull);
```

```
                % Collect all rejected indices and remove repetitions
                All_Rejected_Coord_indices = unique([Rejected_x_Coord_indices_1;↙
Rejected_x_Coord_indices_2;Rejected_y_Coord_indices_1;Rejected_y_Coord_indices_2]);

                Non_Sticky_Neighbourhood_x_coord(All_Rejected_Coord_indices) = []; % Strip↙
the coordinate vectors of ghost points
                Non_Sticky_Neighbourhood_y_coord(All_Rejected_Coord_indices) = [];

                Num_Valid_Neighbourhood_Coords = length(Non_Sticky_Neighbourhood_x_coord);

                % Identify which of the neighbouring sites are empty
                 Empty_Cell_Presence_Vec = zeros(Num_Valid_Neighbourhood_Coords,1);

                 for j = 1:Num_Valid_Neighbourhood_Coords

                     Empty_Cell_Presence_Vec(j) = Binding_Sites↙
(Non_Sticky_Neighbourhood_y_coord(j),Non_Sticky_Neighbourhood_x_coord(j))==0;

                 end

                 Empty_Neighbour_Indices = find(Empty_Cell_Presence_Vec==1); % Indices of↙
empty sites

                 Neighbour_Site_x_coords = Non_Sticky_Neighbourhood_x_coord↙
(Empty_Neighbour_Indices); % Find the coordinates of the valid empty neighbouring sites
                 Neighbour_Site_y_coords = Non_Sticky_Neighbourhood_y_coord↙
(Empty_Neighbour_Indices);

                 Num_Empty_Neighbour_Sites = length(Empty_Neighbour_Indices); % The number↙
of valid empty neighbouring sites

                 Sites_with_Sticky_Neighbours = zeros(1,6);

                 for j = 1:Num_Empty_Neighbour_Sites

                     % Remove those entries which don't have any sticky neighbours.
                     if mod(Neighbour_Site_y_coords(j),2) == 1 && sum([Binding_Sites↙
(Neighbour_Site_y_coords(j)-1,Neighbour_Site_x_coords(j)),    Binding_Sites↙
(Neighbour_Site_y_coords(j)+1,Neighbour_Site_x_coords(j)),...
                                                                  Binding_Sites↙
(Neighbour_Site_y_coords(j),Neighbour_Site_x_coords(j)-1),    Binding_Sites↙
(Neighbour_Site_y_coords(j),Neighbour_Site_x_coords(j)+1),...
                                                                  Binding_Sites↙
(Neighbour_Site_y_coords(j)-1,Neighbour_Site_x_coords(j)+1),  Binding_Sites↙
(Neighbour_Site_y_coords(j)+1,Neighbour_Site_x_coords(j)+1)] == 1) > 0 ||... % Odd row↙
(counting ghost rows)
                         mod(Neighbour_Site_y_coords(j),2) == 0 && sum([Binding_Sites↙
(Neighbour_Site_y_coords(j)-1,Neighbour_Site_x_coords(j)),    Binding_Sites↙
(Neighbour_Site_y_coords(j)+1,Neighbour_Site_x_coords(j)),...
                                                                  Binding_Sites↙
(Neighbour_Site_y_coords(j),Neighbour_Site_x_coords(j)-1),    Binding_Sites↙
```

```
(Neighbour_Site_y_coords(j),Neighbour_Site_x_coords(j)+1),...
                                                                    Binding_Sites↙
(Neighbour_Site_y_coords(j)-1,Neighbour_Site_x_coords(j)-1),  Binding_Sites↙
(Neighbour_Site_y_coords(j)+1,Neighbour_Site_x_coords(j)-1)] == 1) > 0       % Even row↙
(counting ghost rows)

                        Sites_with_Sticky_Neighbours(j) = 1;

                    end

                end

                Sites_with_Sticky_Neighbours_Indices = find↙
(Sites_with_Sticky_Neighbours==1);

                Neighbour_Site_x_coords = Neighbour_Site_x_coords↙
(Sites_with_Sticky_Neighbours_Indices);
                Neighbour_Site_y_coords = Neighbour_Site_y_coords↙
(Sites_with_Sticky_Neighbours_Indices);

                Num_Valid_Neighbour_Sites = length(Neighbour_Site_x_coords); % The number↙
of valid empty neighbouring sites with sticky neighbours

                % 4 Cases: 1. Neighbour sites and fluid free, 2. Only
                % neighbour sites free, 3. Only fluid free, 4. Nothing free
                % (in this last case do nothing).

                if Num_Valid_Neighbour_Sites > 0 && Free_Sticky_Cells +↙
Free_Non_Sticky_Cells < K % Case 1: Neighbour sites and fluid free.

                    Chosen_Daughter_Site_Num = randi(Num_Valid_Neighbour_Sites+1,1); %↙
Choose a site or the fluid for the daughter cell

                    if Chosen_Daughter_Site_Num == Num_Valid_Neighbour_Sites + 1 % Cell↙
goes to the fluid

                        Free_Non_Sticky_Cells = Free_Non_Sticky_Cells + 1; % Non-sticky↙
daughter cell is released into the fluid.

                    else % Cell goes to a neighbouring site

                    Chosen_Daughter_Site_x_coord = Neighbour_Site_x_coords↙
(Chosen_Daughter_Site_Num); % Find the coordinates of the site
                    Chosen_Daughter_Site_y_coord = Neighbour_Site_y_coords↙
(Chosen_Daughter_Site_Num);

                    Binding_Sites(Chosen_Daughter_Site_y_coord,↙
Chosen_Daughter_Site_x_coord) = 2; % Nonsticky daughter cell is released into↙
neighbouring empty site.

                    end
```

```
            elseif Num_Valid_Neighbour_Sites > 0 && Free_Sticky_Cells +↙
Free_Non_Sticky_Cells == K % Case 2: Only neighbour sites free.

                Chosen_Daughter_Site_Num = randi(Num_Valid_Neighbour_Sites,1);↙
% Choose a site for the daughter cell
                Chosen_Daughter_Site_x_coord = Neighbour_Site_x_coords↙
(Chosen_Daughter_Site_Num); % Find the coordinates of the site
                Chosen_Daughter_Site_y_coord = Neighbour_Site_y_coords↙
(Chosen_Daughter_Site_Num);

                Binding_Sites(Chosen_Daughter_Site_y_coord,↙
Chosen_Daughter_Site_x_coord) = 2; % Non-sticky daughter cell is released into↙
neighbouring empty site.

            elseif Num_Valid_Neighbour_Sites == 0 && Free_Sticky_Cells +↙
Free_Non_Sticky_Cells < K % Case 3: Only fluid free.

                Free_Non_Sticky_Cells = Free_Non_Sticky_Cells + 1; % Non-sticky↙
daughter cell is released into the fluid.

            end

        end

    end

    % Remove cells from the fluid if their number exceeds the carrying
    % capacity. Remove cells randomly, with probability in proportion
    % to the fracion of cells that are sticky/non-sticky.
    while Free_Sticky_Cells + Dead_Free_Sticky_Cells + Free_Non_Sticky_Cells...
            + Dead_Free_Non_Sticky_Cells > K

        if rand(1) < Free_Sticky_Cells/(Free_Sticky_Cells + Dead_Free_Sticky_Cells...
                + Free_Non_Sticky_Cells + Dead_Free_Non_Sticky_Cells)

            Free_Sticky_Cells = Free_Sticky_Cells - 1;

        else

            Free_Non_Sticky_Cells = Free_Non_Sticky_Cells - 1;

        end

    end

    % Counting Cells on the Surface
    Sticky_Surface_Cells          = length(find(Binding_Sites==1));
    Non_Sticky_Surface_Cells      = length(find(Binding_Sites==2));
    Dead_Sticky_Surface_Cells     = length(find(Binding_Sites==3));
    Dead_Non_Sticky_Surface_Cells = length(find(Binding_Sites==4));
```

```
        % Total Number of Cells
        Tot_Num_Cells = Free_Sticky_Cells + Dead_Free_Sticky_Cells...
            + Free_Non_Sticky_Cells + Dead_Free_Non_Sticky_Cells...
            + Sticky_Surface_Cells + Dead_Sticky_Surface_Cells...
            + Non_Sticky_Surface_Cells + Dead_Non_Sticky_Surface_Cells;

        %Total Number of Live Cells
        Tot_Num_Live_Cells = Free_Sticky_Cells + Free_Non_Sticky_Cells...
            + Sticky_Surface_Cells + Non_Sticky_Surface_Cells;

        %Total Number of Dead Cells
        Tot_Num_Dead_Cells = Dead_Free_Sticky_Cells + Dead_Free_Non_Sticky_Cells...
            + Dead_Sticky_Surface_Cells + Dead_Non_Sticky_Surface_Cells;

        % Record True Binding Sites every Save_int-th iteration
        if mod(i,Save_int) == 0

            Binding_Sites_Record(:,:,1+i/Save_int) = Binding_Sites(2:(GyFull-1),2:↙
(GxFull-1)); % 1+ as the first entry should be the initial condition.

        end

        % Update cell counts
        Free_Sticky_Cells_Record(i)             = Free_Sticky_Cells;
        Dead_Free_Sticky_Cells_Record(i)        = Dead_Free_Sticky_Cells;
        Free_Non_Sticky_Cells_Record(i)         = Free_Non_Sticky_Cells;
        Dead_Free_Non_Sticky_Cells_Record(i)    = Dead_Free_Non_Sticky_Cells;
        Sticky_Surface_Cells_Record(i)          = Sticky_Surface_Cells;
        Dead_Sticky_Surface_Cells_Record(i)     = Dead_Sticky_Surface_Cells;
        Non_Sticky_Surface_Cells_Record(i)      = Non_Sticky_Surface_Cells;
        Dead_Non_Sticky_Surface_Cells_Record(i) = Dead_Non_Sticky_Surface_Cells;

    end

end
```

# Appendix Five

# MATLAB script used to produce heat maps comparing a range of input probabilities

```
disp("Computing input parameters...")
input_value = [];
 for x = 0.2:0.1:0.8
    for y = 0.2:0.1:0.8
         for z = 0.2:0.1:0.8
              for n = 0.2:0.1:0.8
                  input_value = [input_value; [x, y, z, n]];
              end
         end
    end
 end

disp("Input parameters computed.")

parfor iter = 1:length(input_value)
     D = input_value(iter,1);
     R = input_value(iter,2);
     P_m = input_value(iter,3);
     P_d = input_value(iter,4);

     T = 40000;
     K = 5000;
     G = 100;
     Free_Sticky_Cells_init = 100;
     Free_Non_Sticky_Cells_init = 100;

     [Free_Sticky_Cells_Record, Free_Non_Sticky_Cells_Record,↙
Sticky_Surface_Cells_Record, Non_Sticky_Surface_Cells_Record]...
         = GestelNowakModel(T, D, R, P_m, P_d, K, G, Free_Sticky_Cells_init,↙
Free_Non_Sticky_Cells_init);

     filename = ("./results/iteration_" + iter + ".txt");

     input_variables = [D, R, P_m, P_d];
     results = [Free_Sticky_Cells_Record, Free_Non_Sticky_Cells_Record,↙
Sticky_Surface_Cells_Record, Non_Sticky_Surface_Cells_Record];
     data = [input_variables; results];

     writematrix(data, filename);


end
```

```
%Import input and output data and plot heatmaps

%% Load data

file_dir = './results/';
files_to_process=dir([file_dir filesep '*.txt']);
counter = 0;

for x = 1:length(files_to_process)

    file_path = [file_dir files_to_process(x).name];
    data_file = readmatrix(file_path);

    if size(data_file, 2) == 4
        counter = counter + 1;
        results_struct(counter).input_params = data_file(1,:);
        results_struct(counter).output = data_file(10000,:);

    end

end

%% create arrays %
input_array = [];
output_array = [];

for x = 1:size(results_struct, 2)

    if max(isnan([results_struct(x).input_params])) || max(isnan([results_struct(x).↙
output]))

        %skip files with NaN values

    %elseif max(ismember([results_struct(x).output], 0)) || max(ismember([results_struct↙
(x).output], 1))

        %remove zero value input parameter results

    else

        input_array = [input_array; [results_struct(x).input_params]];
        output_array = [output_array; [results_struct(x).output]];

    end
end

%% Collate data for heatmaps
% Note - Non varied parameters fixed at 0.2 to compare other parameters

% Sticky surface cells
% Division probability non-sticky (D) vs division probability sticky (R) (note -P_m and
```

```
% P_d set to 0.2)

D_R_results = [];

counter = 0;

for i = 1:length(input_array);
    if input_array(i,3) == 0.2 && input_array(i,4) == 0.2;
        counter = counter + 1;
        D_R_results(counter,1) = input_array(i,1);
        D_R_results(counter,2) = input_array(i,2);
        D_R_results(counter,3) = output_array(i,3);
    else
        continue
    end
end

%convert to table
T_D_R_results = array2table(D_R_results, 'VariableNames', {'D', 'R',↙
'StickySurfaceCells'});

%plot heatmap of table
figure;
h = heatmap(T_D_R_results, 'D', 'R', 'ColorVariable', 'StickySurfaceCells');
h.YDisplayData = flipud(h.YDisplayData);



% Sticky surface cells
% Migration probability (P_m) vs Death probability (P_d) (note - D and R set to 0.2)

Pm_Pd_results = [];

counter = 0;

for i = 1:length(input_array);
    if input_array(i,1) == 0.2 && input_array(i,2) == 0.2;
        counter = counter + 1;
        Pm_Pd_results(counter,1) = input_array(i,3);
        Pm_Pd_results(counter,2) = input_array(i,4);
        Pm_Pd_results(counter,3) = output_array(i,3);
    else
        continue
    end
end

%convert to table
T_Pm_Pd_results = array2table(Pm_Pd_results, 'VariableNames', {'P_m', 'P_d',↙
'StickySurfaceCells'});

%plot heatmap of table
```

```
figure;
h = heatmap(T_Pm_Pd_results, 'P_m', 'P_d', 'ColorVariable', 'StickySurfaceCells');
h.YDisplayData = flipud(h.YDisplayData);



% Sticky surface cells
% Non-sticky division probability (D) vs Migration probability (P_m) (note - P_d and R↙
set to 0.2)

D_Pm_results = [];

counter = 0;

for i = 1:length(input_array);
    if input_array(i,2) == 0.2 && input_array(i,4) == 0.2;
        counter = counter + 1;
        D_Pm_results(counter,1) = input_array(i,1);
        D_Pm_results(counter,2) = input_array(i,3);
        D_Pm_results(counter,3) = output_array(i,3);
    else
        continue
    end
end

%convert to table
T_D_Pm_results = array2table(D_Pm_results, 'VariableNames', {'D', 'P_m',↙
'StickySurfaceCells'});

%plot heatmap of table
figure;
h = heatmap(T_D_Pm_results, 'D', 'P_m', 'ColorVariable', 'StickySurfaceCells');
h.YDisplayData = flipud(h.YDisplayData);



% Sticky surface cells
% Division probability of sticky cells (R) vs Migration probability (P_m) (note -P_d and↙
D set to 0.2)

R_Pm_results = [];

counter = 0;

for i = 1:length(input_array);
    if input_array(i,1) == 0.2 && input_array(i,4) == 0.2;
        counter = counter + 1;
        R_Pm_results(counter,1) = input_array(i,2);
        R_Pm_results(counter,2) = input_array(i,3);
```

```
        R_Pm_results(counter,3) = output_array(i,3);
    else
        continue
    end
end

%convert to table
T_R_Pm_results = array2table(R_Pm_results, 'VariableNames', {'R', 'P_m',↙
'StickySurfaceCells'});

%plot heatmap of table
figure;
h = heatmap(T_R_Pm_results, 'R', 'P_m', 'ColorVariable', 'StickySurfaceCells');
h.YDisplayData = flipud(h.YDisplayData);



%%

% Full heatmap analysis
% P_m vs P_d (R and D fixed)

Results = [];

counter = 0;

for i = 1:length(input_array);
    if input_array(i,1) == 0.8 && input_array(i,4) == 0.8;
        counter = counter + 1;
        Results(counter,1) = input_array(i,2);
        Results(counter,2) = input_array(i,3);
        Results(counter,3) = output_array(i,2);
    else
        continue
    end
end

%convert to table
Results = array2table(Results, 'VariableNames', {'R', 'P_m', 'FreeNonStickyCells'});

%plot heatmap of table
figure;
h = heatmap(Results, 'R', 'P_m', 'ColorVariable', 'FreeNonStickyCells');
h.YDisplayData = flipud(h.YDisplayData);
```

# Appendix Six

# MATLAB script used to fit *in vitro* experimental data to cellular automaton

```
function model_fitting

%specifiy data
time = [0 5714 11428 28570 40000]; %in 40000 divided by no. days in experimental data
cellCount = [1 384 731 1727 2329];
%w = [0.5 0.2 0.1 0.2]

%initial parameter guesses
%param_guess=[0.75 0.01 0.01 5000]; %[R - sticky, P_m, P_d, K]
param_guess=[0.5 0.2]; %[R - sticky, P_m]

%perform optimisation using fminsearch on the function defined
%below with initial parameter guesses
options = optimset('MaxFunEvals',10000);
fminsearch(@(par) fitfn(par,time,cellCount),param_guess)
%fminsearch(@(par) fitfn(par,time,pop,w),param_guess)

%%%%%%%%%%%%%%%

%define objective function to minimise
function obj=fitfn(params,time,cellCount);
%function obj=odefitfn(params,time,pop,w)

T = 40001; %number of time steps/iterations (e.g. 4*10^5)
D = 0; %division rate of non-sticky cell (must be between 0 and 1)
R = params(1); %division rate of sticky cell (must be between 0 and 1)
P_m = params(2); %migration rate of cell: liquid to surface (must be between 0 and 1)
P_d = 0.05; %params(3); %death rate (must be between 0 and 1)
K = 5000; %params(4); %carrying capacity - max number of cells there can be in the liquid↙
(e.g. 5*10^3)
G = 100; %grid size - length of one side of 2D surface (e.g. 100 or 10 - choose an even↙
value for g)
Free_Sticky_Cells_init = cellCount(1); %number of starting sticky cells in liquid (e.g.↙
10^2)
Free_Non_Sticky_Cells_init = 0; %number of starting non-sticky cells in liquid (e.g.↙
10^2)
%p=1;
%q=1;

    %obtain the solution to the ODEs defined below
    %sol=ode15s(@(t,x,y,z) GestelNowakModel(t, D, R, 1, P_m, P_d, 5000, 100, 200, 0), [0↙
6.083], P_m, P_d);
    [w,x,y,z]=GestelNowakModel(T,D,abs(R),abs(P_m),abs(P_d),abs(K),G,↙
Free_Sticky_Cells_init,Free_Non_Sticky_Cells_init);

    total=w+x+y+z;
    %log10_total=log10(total);
    %model_output=log10_total(time+1);
    model_output = total(time+1);
    obj=norm(y-cellCount); %sticky surface cells
```

%%%%%%%%%%%%%%%

# Appendix Seven

# Details of heat maps generated to investigate computational model parameters

Table G.1: List of heat maps produced for computational model parameter exploration. Variable input parameters (denoted by X in the table) ranged from 0.2 to 0.8 in increments of 0.1. Results can be found in Appendix H.

| **Heat map Name** | **Fixed input parameters** | | | | **Variable input parameters** | | | | **Tracked output parameter** |
|---|---|---|---|---|---|---|---|---|---|
| | **D** | **R** | **P_m** | **P_d** | **D** | **R** | **P_m** | **P_d** | |
| *StickySurfaceCells_PmPd_L* | 0.2 | 0.2 | | | | | X | X | Sticky Surface Cells |
| *StickySurfaceCells_PmPd_M* | 0.5 | 0.5 | | | | | X | X | Sticky Surface Cells |
| *StickySurfaceCells_PmPd_H* | 0.8 | 0.8 | | | | | X | X | Sticky Surface Cells |
| *NonStickySurfaceCells_PmPd_L* | 0.2 | 0.2 | | | | | X | X | Non-sticky Surface Cells |
| *NonStickySurfaceCells_PmPd_M* | 0.5 | 0.5 | | | | | X | X | Non-sticky Surface Cells |
| *NonStickySurfaceCells_PmPd_H* | 0.8 | 0.8 | | | | | X | X | Non-sticky Surface Cells |
| *FreeStickyCells_PmPd_L* | 0.2 | 0.2 | | | | | X | X | Free Sticky Cells |
| *FreeStickyCells_PmPd_M* | 0.5 | 0.5 | | | | | X | X | Free Sticky Cells |
| *FreeStickyCells_PmPd_H* | 0.8 | 0.8 | | | | | X | X | Free Sticky Cells |
| *FreeNonStickyCells_PmPd_L* | 0.2 | 0.2 | | | | | X | X | Free Non-sticky Cells |
| *FreeNonStickyCells_PmPd_M* | 0.5 | 0.5 | | | | | X | X | Free Non-sticky Cells |
| *FreeNonStickyCells_PmPd_H* | 0.8 | 0.8 | | | | | X | X | Free Non-sticky Cells |
| *StickySurfaceCells_DR_L* | | | 0.2 | 0.2 | X | X | | | Sticky Surface Cells |
| *StickySurfaceCells_DR_M* | | | 0.5 | 0.5 | X | X | | | Sticky Surface Cells |
| *StickySurfaceCells_DR_H* | | | 0.8 | 0.8 | X | X | | | Sticky Surface Cells |
| *NonStickySurfaceCells_DR_L* | | | 0.2 | 0.2 | X | X | | | Non-sticky Surface Cells |
| *NonStickySurfaceCells_DR_M* | | | 0.5 | 0.5 | X | X | | | Non-sticky Surface Cells |
| *NonStickySurfaceCells_DR_H* | | | 0.8 | 0.8 | X | X | | | Non-sticky Surface Cells |
| *FreeStickyCells_DR_L* | | | 0.2 | 0.2 | X | X | | | Free Sticky Cells |

**Table G.1 continued from previous page**

| *FreeStickyCells_DR_M* | 0.5 | 0.5 | X | X | | | Free Sticky Cells |
|---|---|---|---|---|---|---|---|
| *FreeStickyCells_DR_H* | 0.8 | 0.8 | X | X | | | Free Sticky Cells |
| *FreeNonStickyCells_DR_L* | 0.2 | 0.2 | X | X | | | Free Non-sticky Cells |
| *FreeNonStickyCells_DR_M* | 0.5 | 0.5 | X | X | | | Free Non-sticky Cells |
| *FreeNonStickyCells_DR_H* | 0.8 | 0.8 | X | X | | | Free Non-sticky Cells |
| *StickySurfaceCells_DPm_L* | 0.2 | 0.2 | X | | X | | Sticky Surface Cells |
| *StickySurfaceCells_DPm_M* | 0.5 | 0.5 | X | | X | | Sticky Surface Cells |
| *StickySurfaceCells_DPm_H* | 0.8 | 0.8 | X | | X | | Sticky Surface Cells |
| *NonStickySurfaceCells_DPm_L* | 0.2 | 0.2 | X | | X | | Non-sticky Surface Cells |
| *NonStickySurfaceCells_DPm_M* | 0.5 | 0.5 | X | | X | | Non-sticky Surface Cells |
| *NonStickySurfaceCells_DPm_H* | 0.8 | 0.8 | X | | X | | Non-sticky Surface Cells |
| *FreeStickyCells_DPm_L* | 0.2 | 0.2 | X | | X | | Free Sticky Cells |
| *FreeStickyCells_DPm_M* | 0.5 | 0.5 | X | | X | | Free Sticky Cells |
| *FreeStickyCells_DPm_H* | 0.8 | 0.8 | X | | X | | Free Sticky Cells |
| *FreeNonStickyCells_DPm_L* | 0.2 | 0.2 | X | | X | | Free Non-sticky Cells |
| *FreeNonStickyCells_DPm_M* | 0.5 | 0.5 | X | | X | | Free Non-sticky Cells |
| *FreeNonStickyCells_DPm_H* | 0.8 | 0.8 | X | | X | | Free Non-sticky Cells |
| *StickySurfaceCells_RPd_L* | 0.2 | 0.2 | | X | | X | Sticky Surface Cells |
| *StickySurfaceCells_RPd_M* | 0.5 | 0.5 | | X | | X | Sticky Surface Cells |
| *StickySurfaceCells_RPd_H* | 0.8 | 0.8 | | X | | X | Sticky Surface Cells |
| *NonStickySurfaceCells_RPd_L* | 0.2 | 0.2 | | X | | X | Non-sticky Surface Cells |
| *NonStickySurfaceCells_RPd_M* | 0.5 | 0.5 | | X | | X | Non-sticky Surface Cells |

**Table G.1 continued from previous page**

| *NonStickySurfaceCells_RPd_H* | 0.8 | | 0.8 | | | | | X | | X | Non-sticky Surface Cells |
|---|---|---|---|---|---|---|---|---|---|---|---|
| *FreeStickyCells_RPd_L* | 0.2 | | 0.2 | | | | | X | | X | Free Sticky Cells |
| *FreeStickyCells_RPd_M* | 0.5 | | 0.5 | | | | | X | | X | Free Sticky Cells |
| *FreeStickyCells_RPd_H* | 0.8 | | 0.8 | | | | | X | | X | Free Sticky Cells |
| *FreeNonStickyCells_RPd_L* | 0.2 | | 0.2 | | | | | X | | X | Free Non-sticky Cells |
| *FreeNonStickyCells_RPd_M* | 0.5 | | 0.5 | | | | | X | | X | Free Non-sticky Cells |
| *FreeNonStickyCells_RPd_H* | 0.8 | | 0.8 | | | | | X | | X | Free Non-sticky Cells |
| *StickySurfaceCells_DPd_L* | | 0.2 | 0.2 | | | X | | | | X | Sticky Surface Cells |
| *StickySurfaceCells_DPd_M* | | 0.5 | 0.5 | | | X | | | | X | Sticky Surface Cells |
| *StickySurfaceCells_DPd_H* | | 0.8 | 0.8 | | | X | | | | X | Sticky Surface Cells |
| *NonStickySurfaceCells_DPd_L* | | 0.2 | 0.2 | | | X | | | | X | Non-sticky Surface Cells |
| *NonStickySurfaceCells_DPd_M* | | 0.5 | 0.5 | | | X | | | | X | Non-sticky Surface Cells |
| *NonStickySurfaceCells_DPd_H* | | 0.8 | 0.8 | | | X | | | | X | Non-sticky Surface Cells |
| *FreeStickyCells_DPd_L* | | 0.2 | 0.2 | | | X | | | | X | Free Sticky Cells |
| *FreeStickyCells_DPd_M* | | 0.5 | 0.5 | | | X | | | | X | Free Sticky Cells |
| *FreeStickyCells_DPd_H* | | 0.8 | 0.8 | | | X | | | | X | Free Sticky Cells |
| *FreeNonStickyCells_DPd_L* | | 0.2 | 0.2 | | | X | | | | X | Free Non-sticky Cells |
| *FreeNonStickyCells_DPd_M* | | 0.5 | 0.5 | | | X | | | | X | Free Non-sticky Cells |
| *FreeNonStickyCells_DPd_H* | | 0.8 | 0.8 | | | X | | | | X | Free Non-sticky Cells |
| *StickySurfaceCells_RPm_L* | 0.2 | | | 0.2 | | | X | X | | | Sticky Surface Cells |
| *StickySurfaceCells_RPm_M* | 0.5 | | | 0.5 | | | X | X | | | Sticky Surface Cells |
| *StickySurfaceCells_RPm_H* | 0.8 | | | 0.8 | | | X | X | | | Sticky Surface Cells |

**Table G.1 continued from previous page**

| | | | | | | | |
|---|---|---|---|---|---|---|---|
| *NonStickySurfaceCells_RPm_L* | 0.2 | | 0.2 | | X | X | Non-sticky Surface Cells |
| *NonStickySurfaceCells_RPm_M* | 0.5 | | 0.5 | | X | X | Non-sticky Surface Cells |
| *NonStickySurfaceCells_RPm_H* | 0.8 | | 0.8 | | X | X | Non-sticky Surface Cells |
| *FreeStickyCells_RPm_L* | 0.2 | | 0.2 | | X | X | Free Sticky Cells |
| *FreeStickyCells_RPm_M* | 0.5 | | 0.5 | | X | X | Free Sticky Cells |
| *FreeStickyCells_RPm_H* | 0.8 | | 0.8 | | X | X | Free Sticky Cells |
| *FreeNonStickyCells_RPm_L* | 0.2 | | 0.2 | | X | X | Free Non-sticky Cells |
| *FreeNonStickyCells_RPm_M* | 0.5 | | 0.5 | | X | X | Free Non-sticky Cells |
| *FreeNonStickyCells_RPm_H* | 0.8 | | 0.8 | | X | X | Free Non-sticky Cells |

# Appendix Eight

# Heat maps

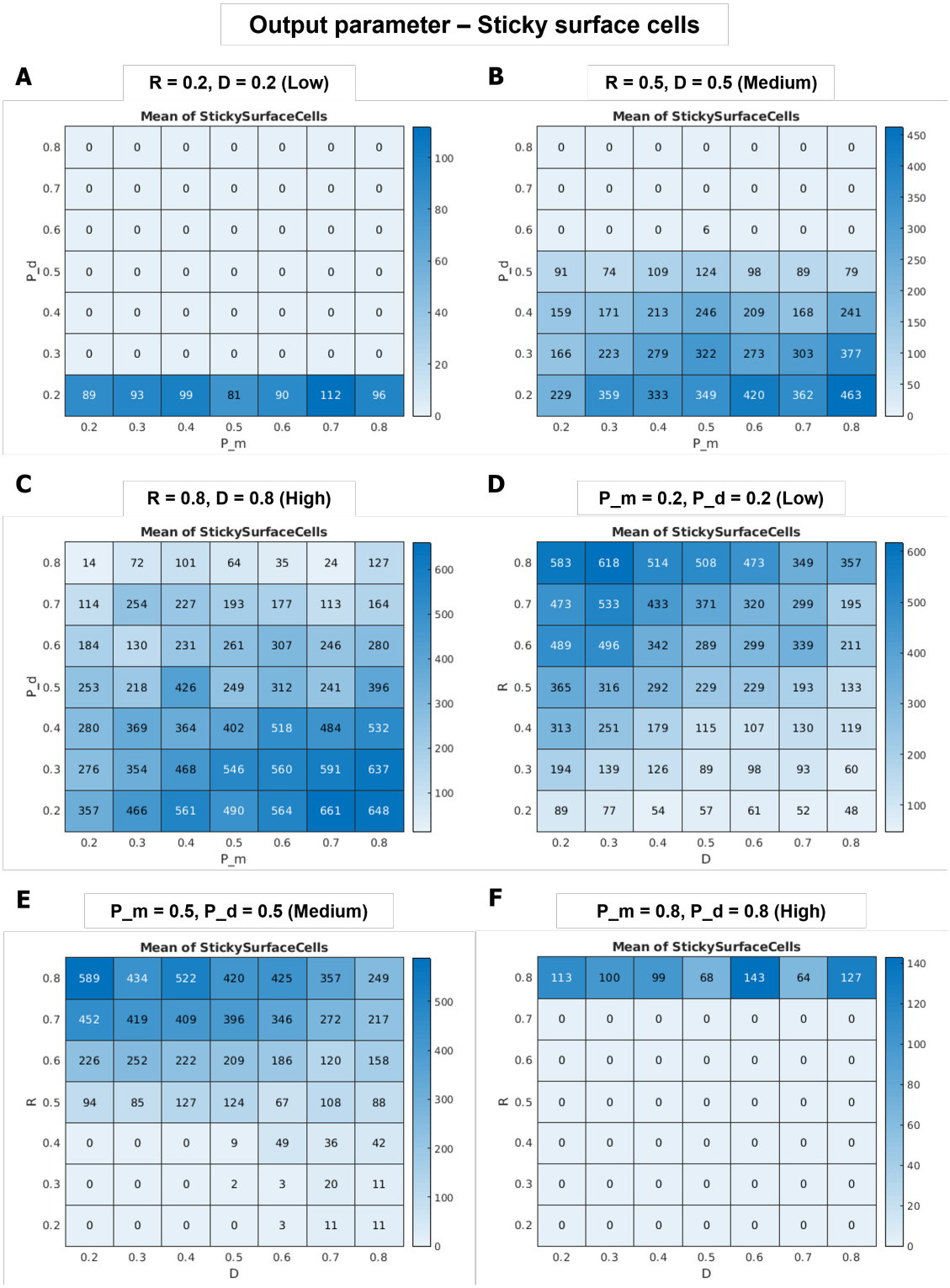


Figure H.1: Output - sticky surface cells.

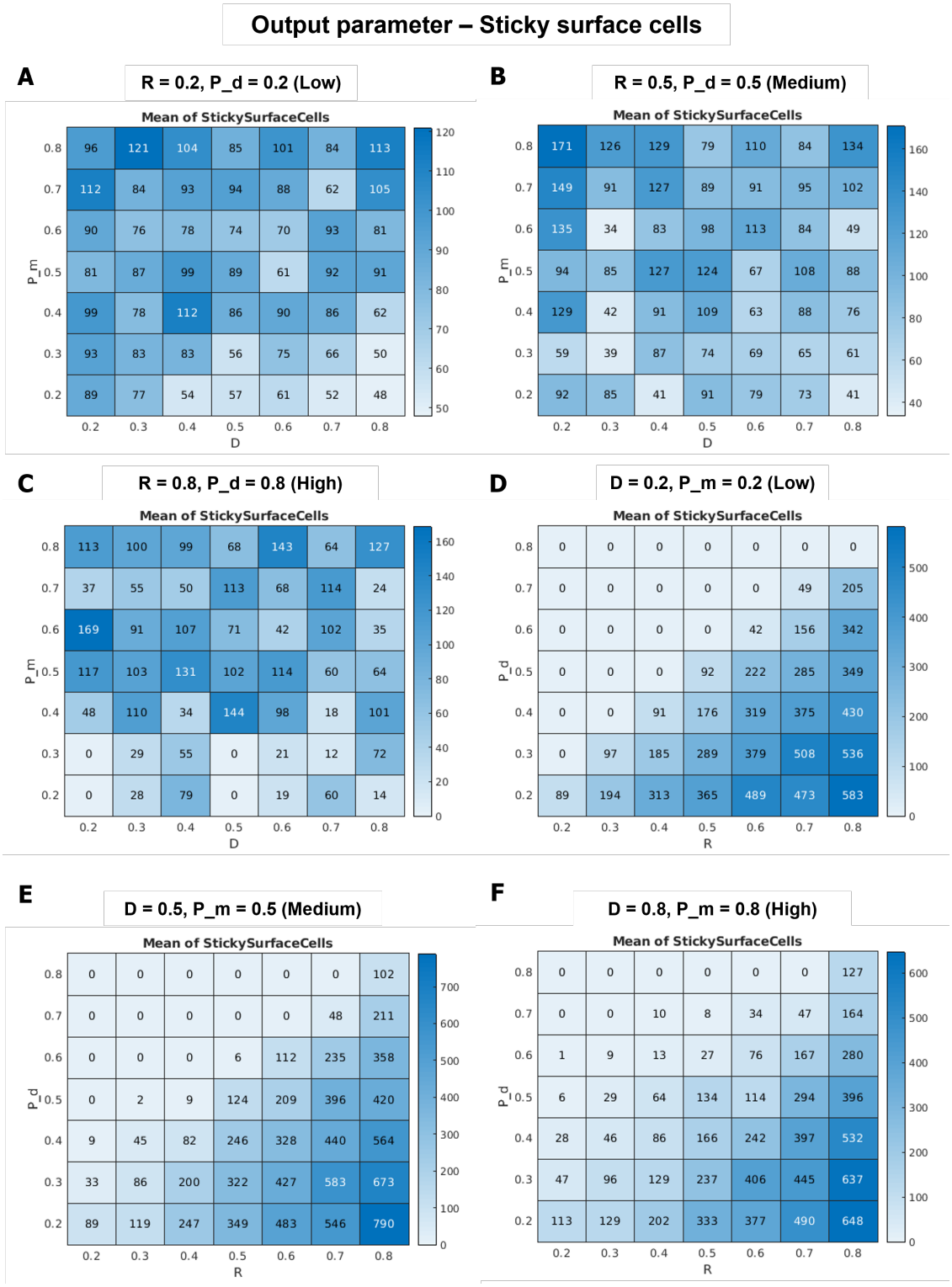


Figure H.2: Output - sticky surface cells.

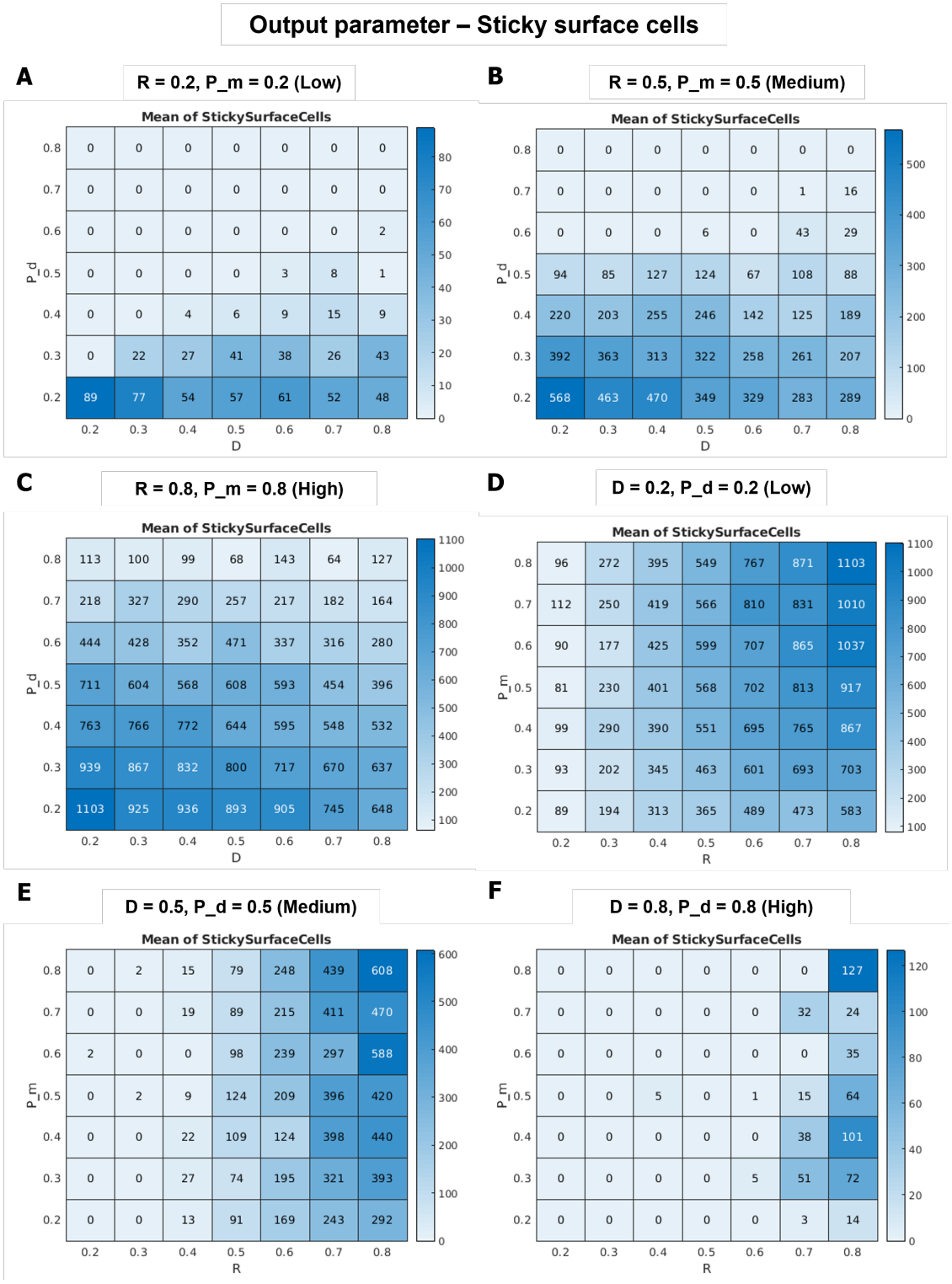


Figure H.3: Output - sticky surface cells.

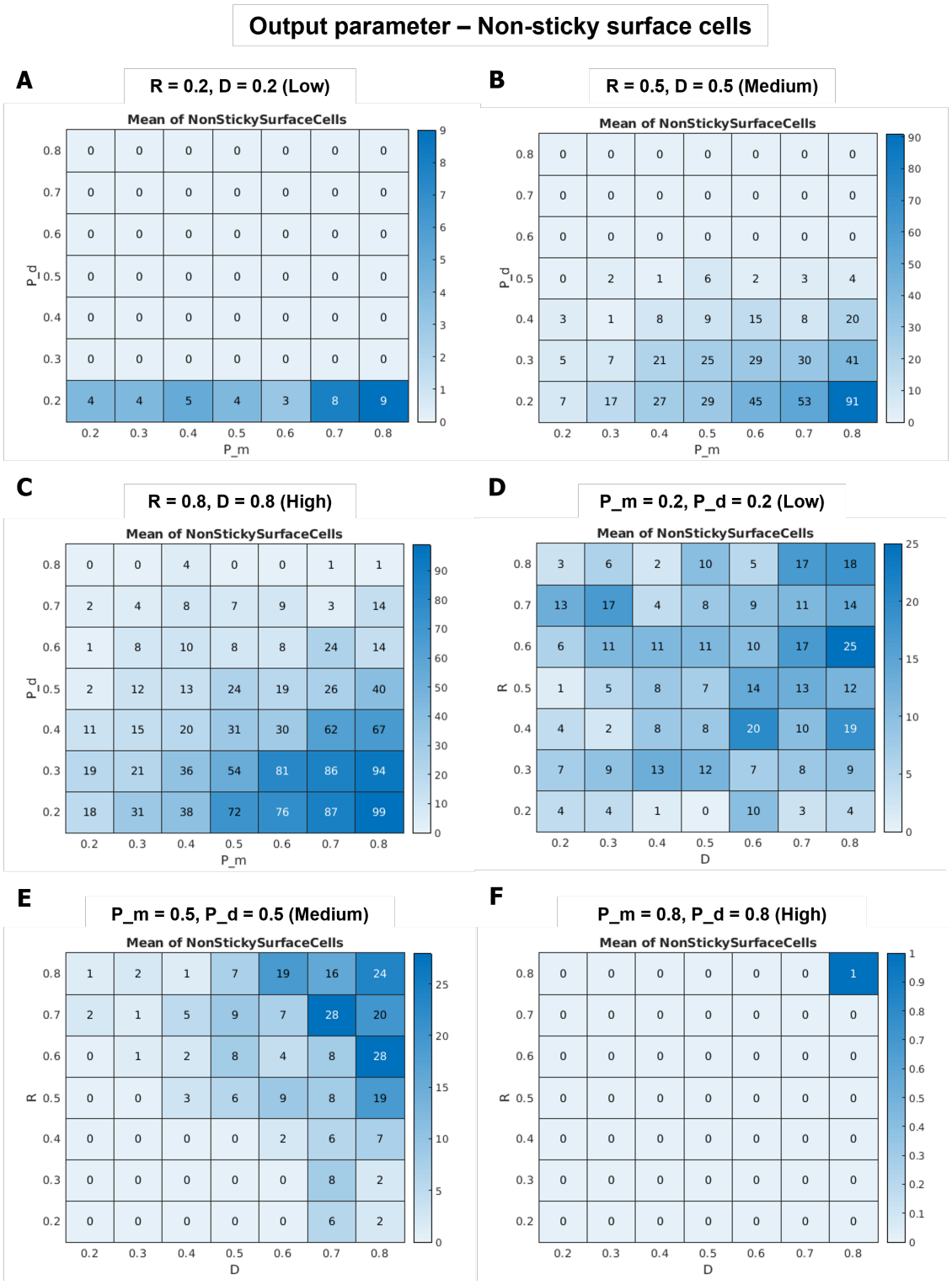


Figure H.4: Output - non-sticky surface cells.

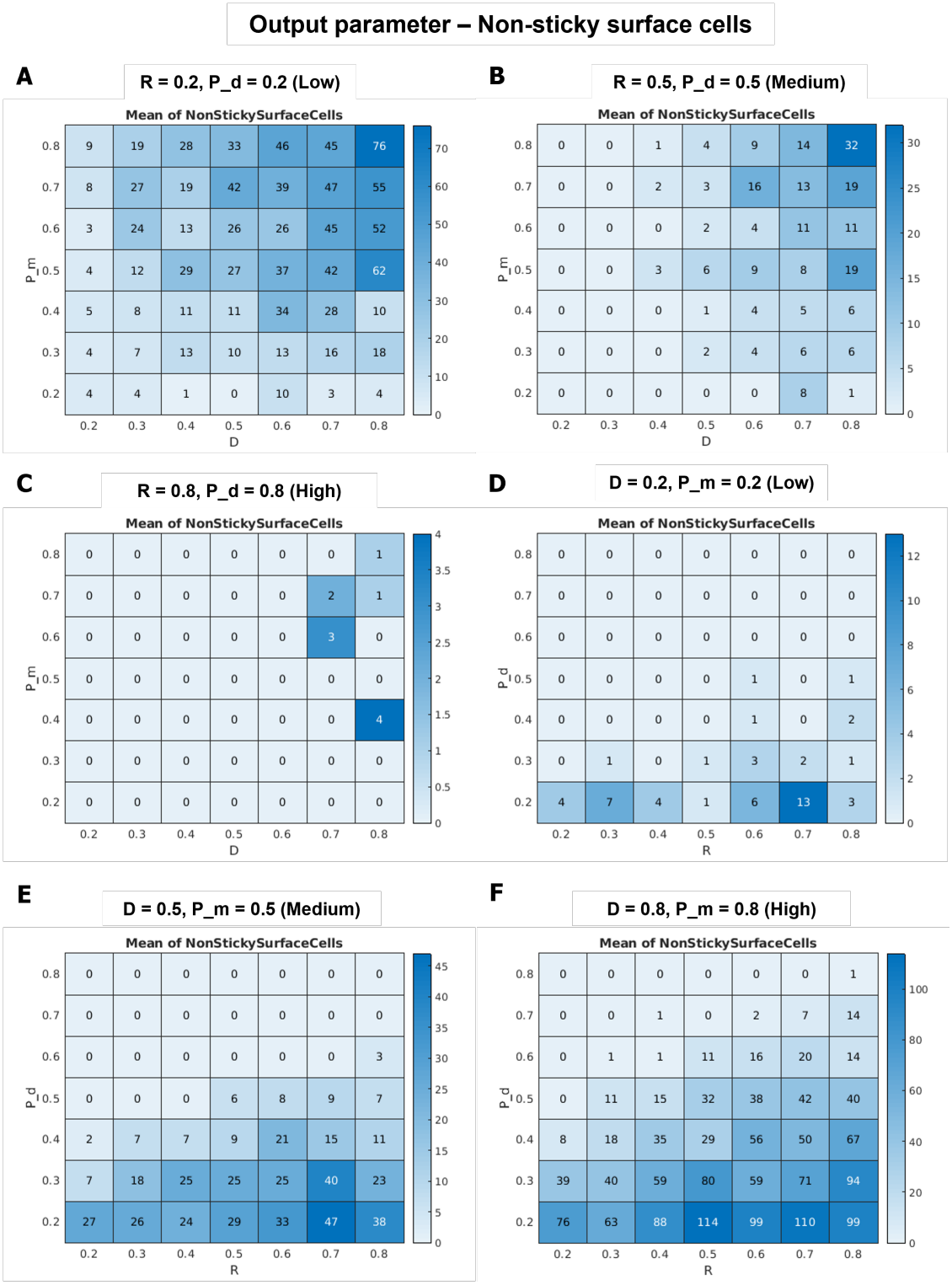


Figure H.5: Output - non-sticky surface cells.

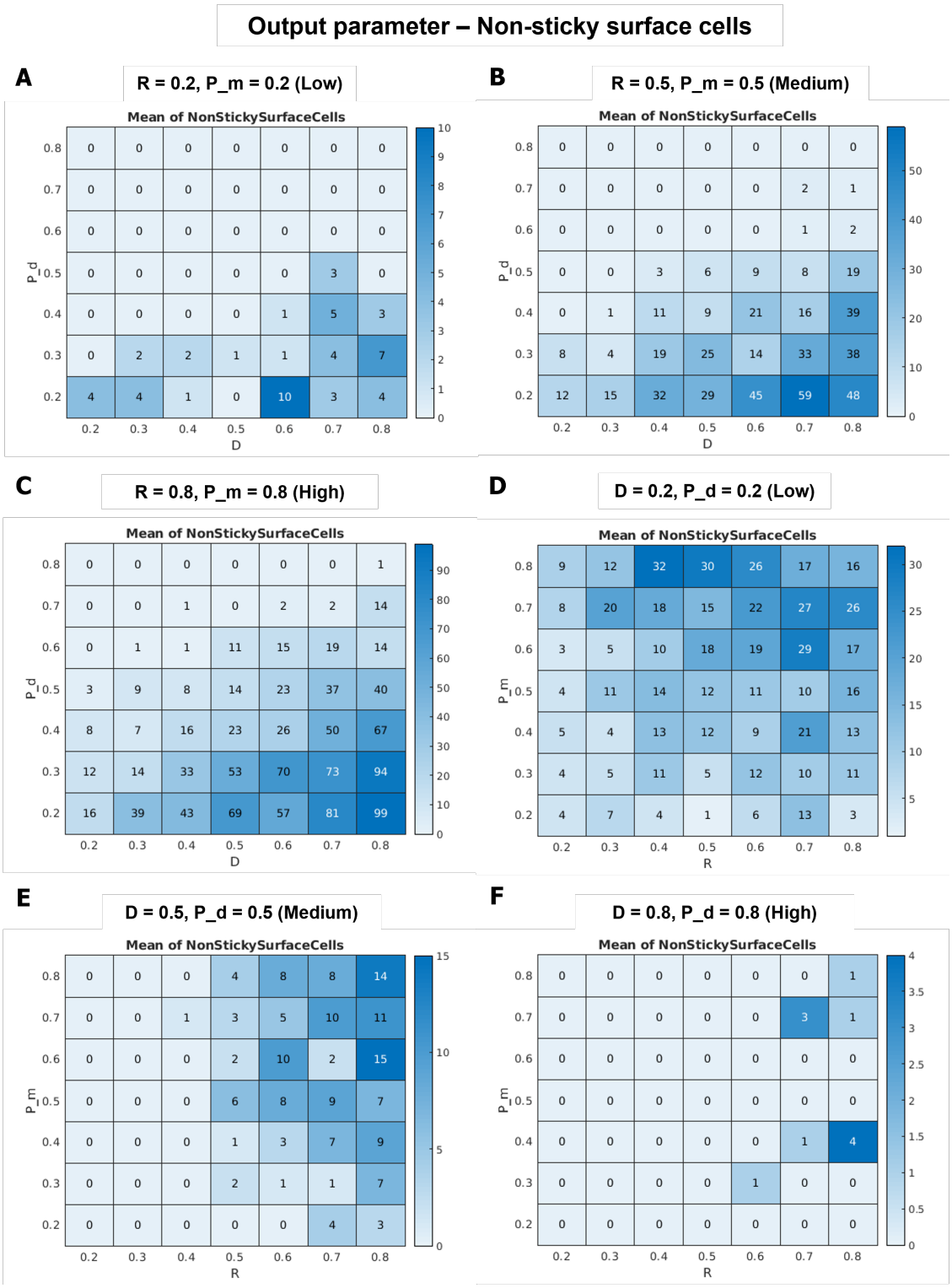


Figure H.6: Output - non-sticky surface cells.

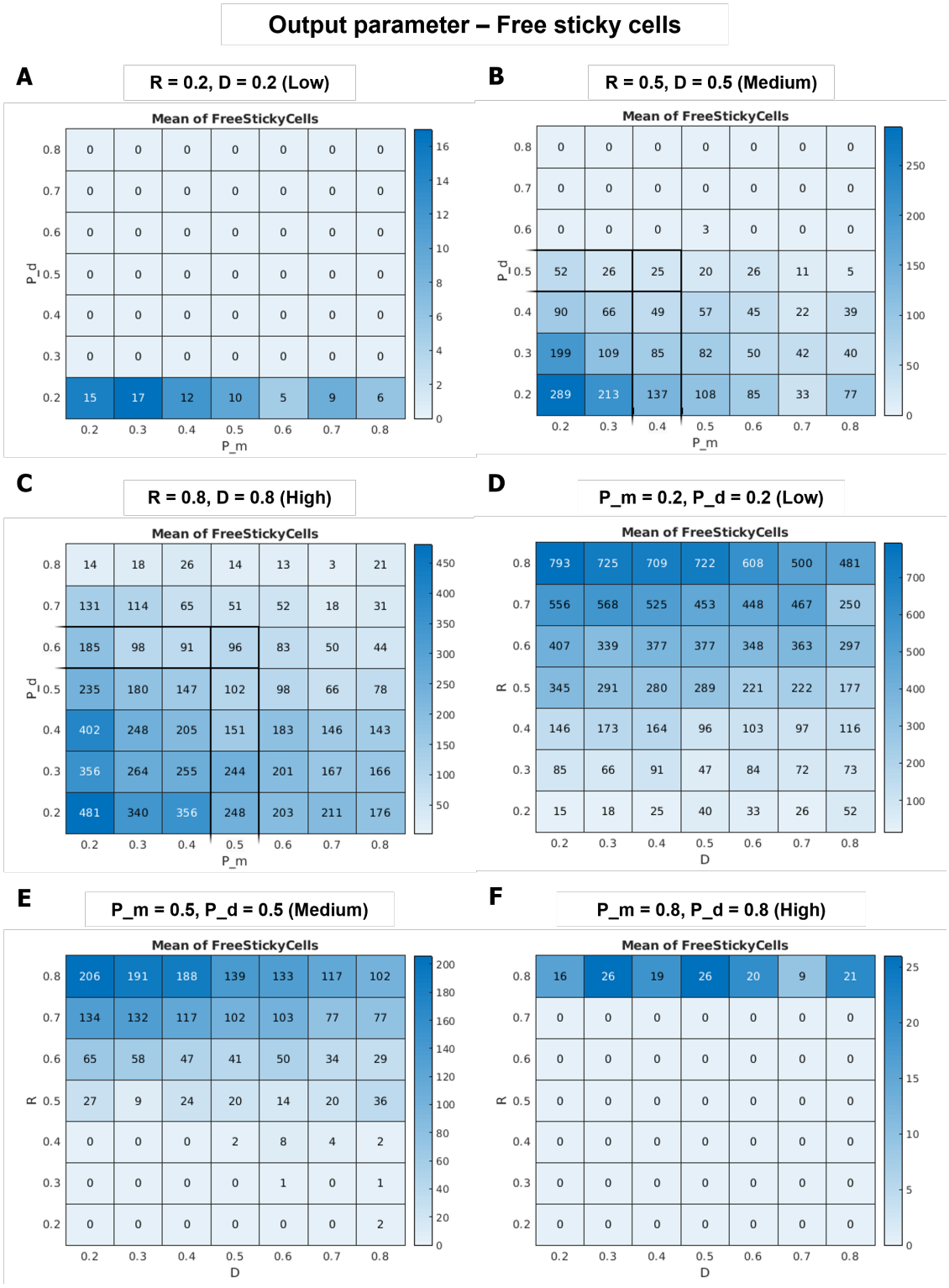


Figure H.7: Output - free sticky cells.

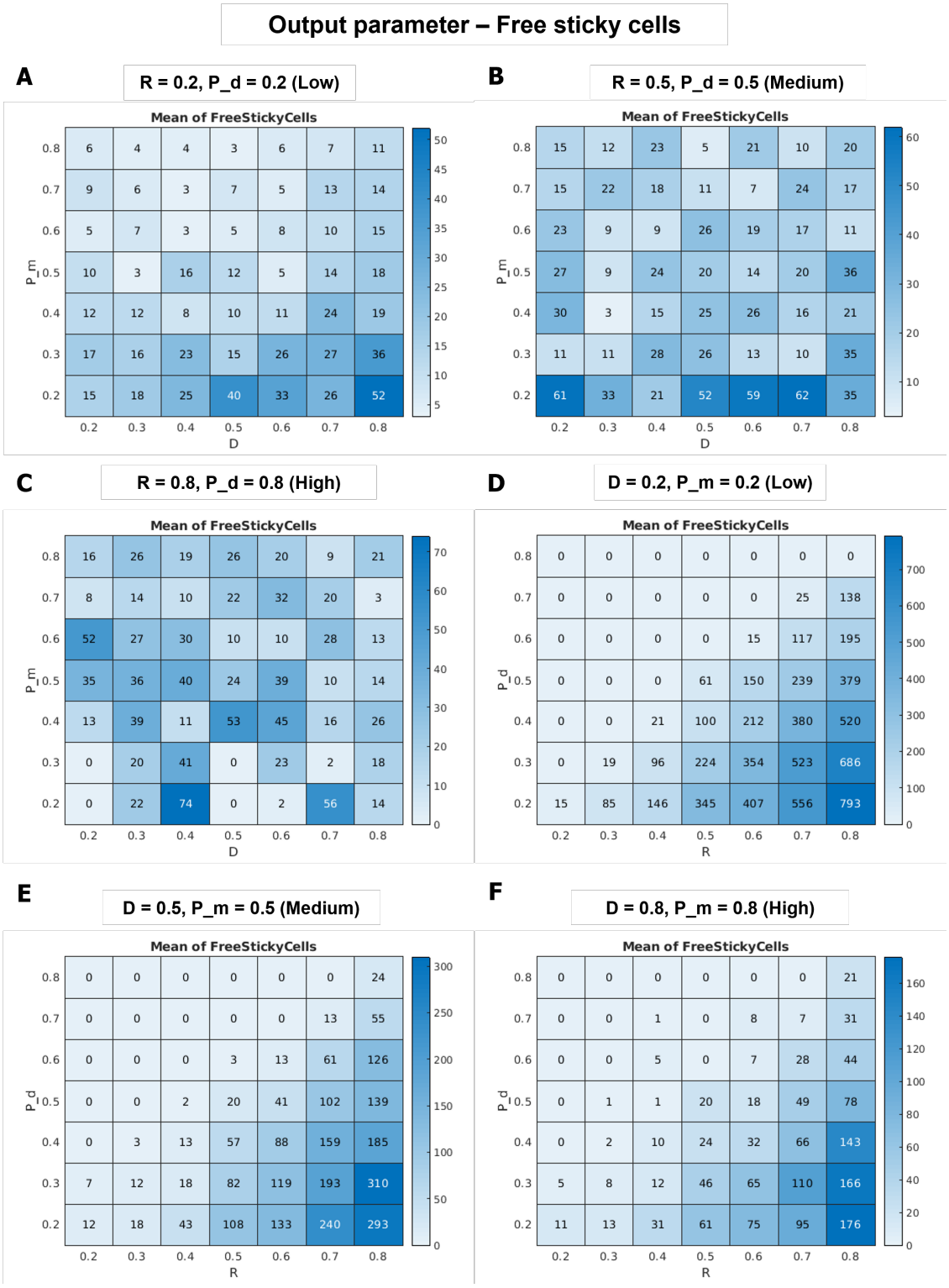


Figure H.8: Output - free sticky cells.

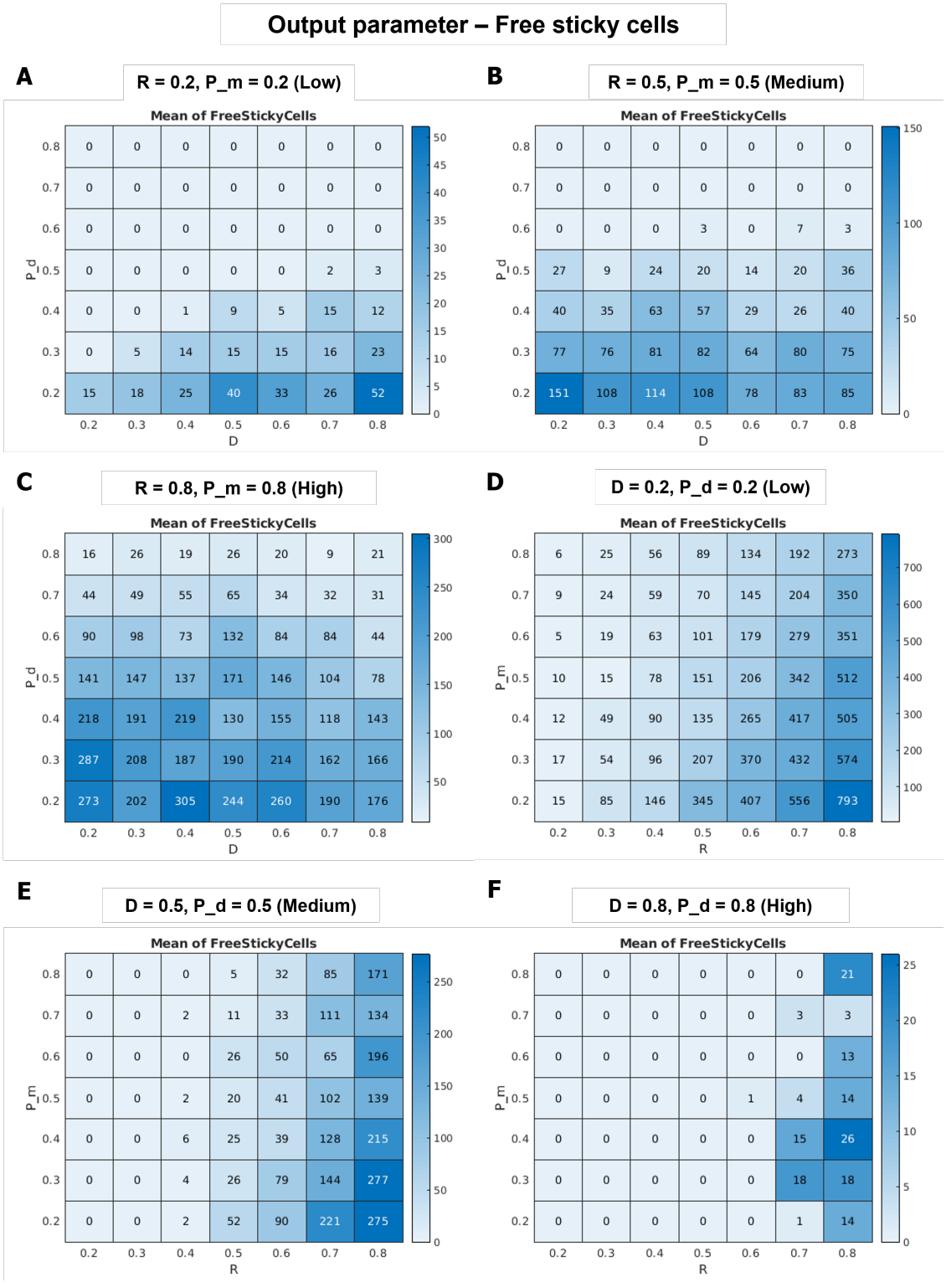


Figure H.9: Output - free sticky cells.

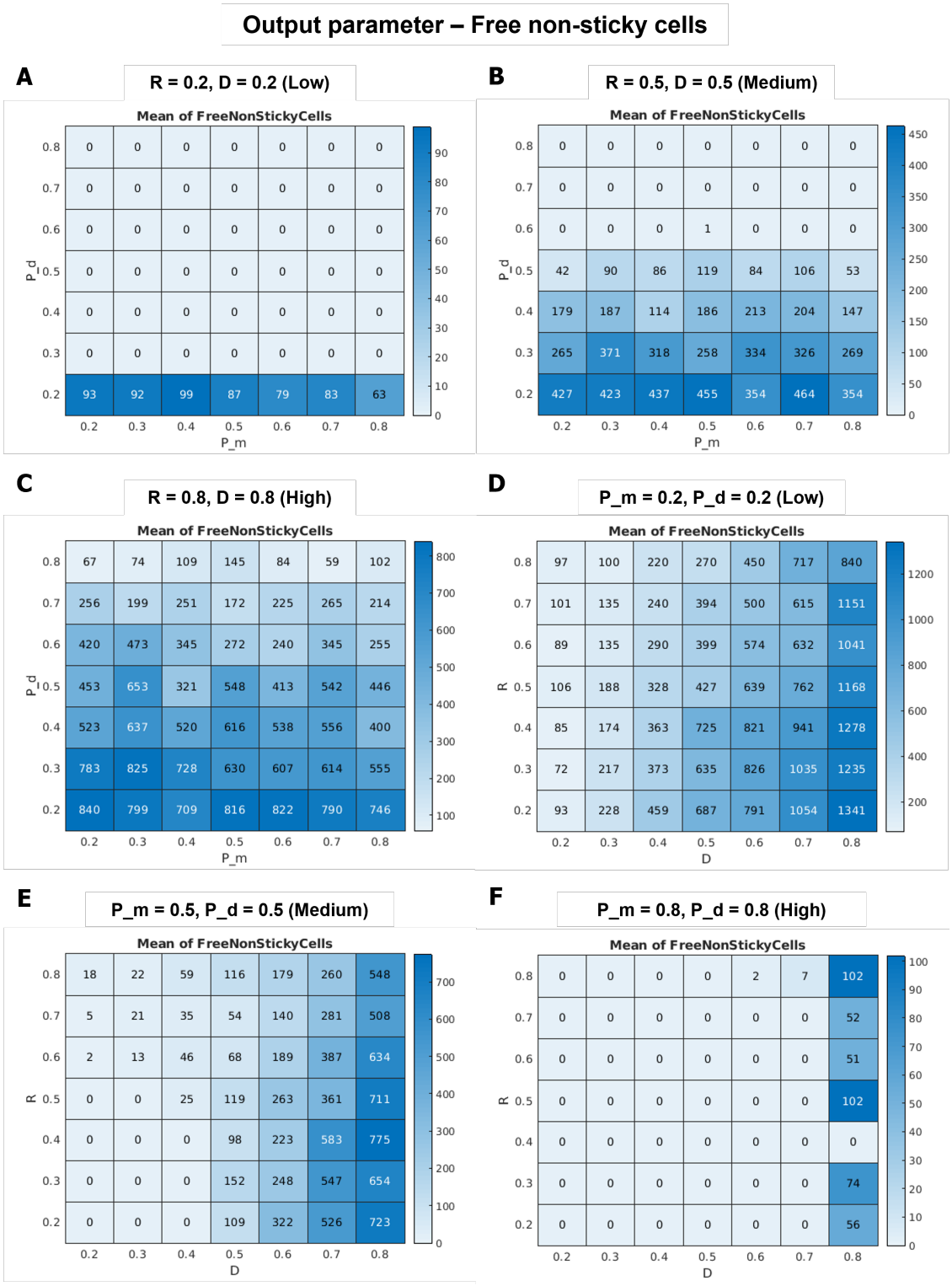


Figure H.10: Output - free non-sticky cells.

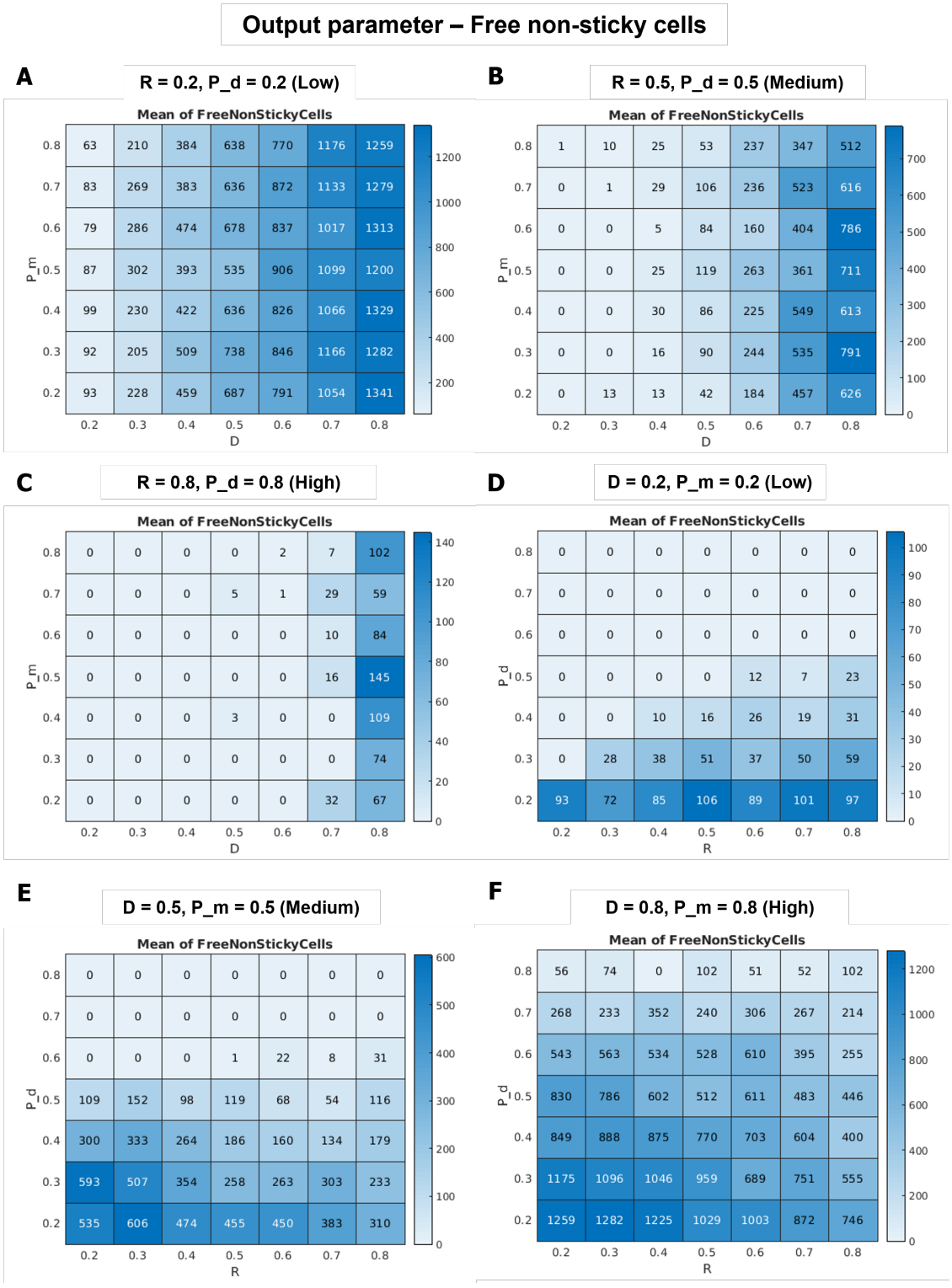


Figure H.11: Output - free non-sticky cells.

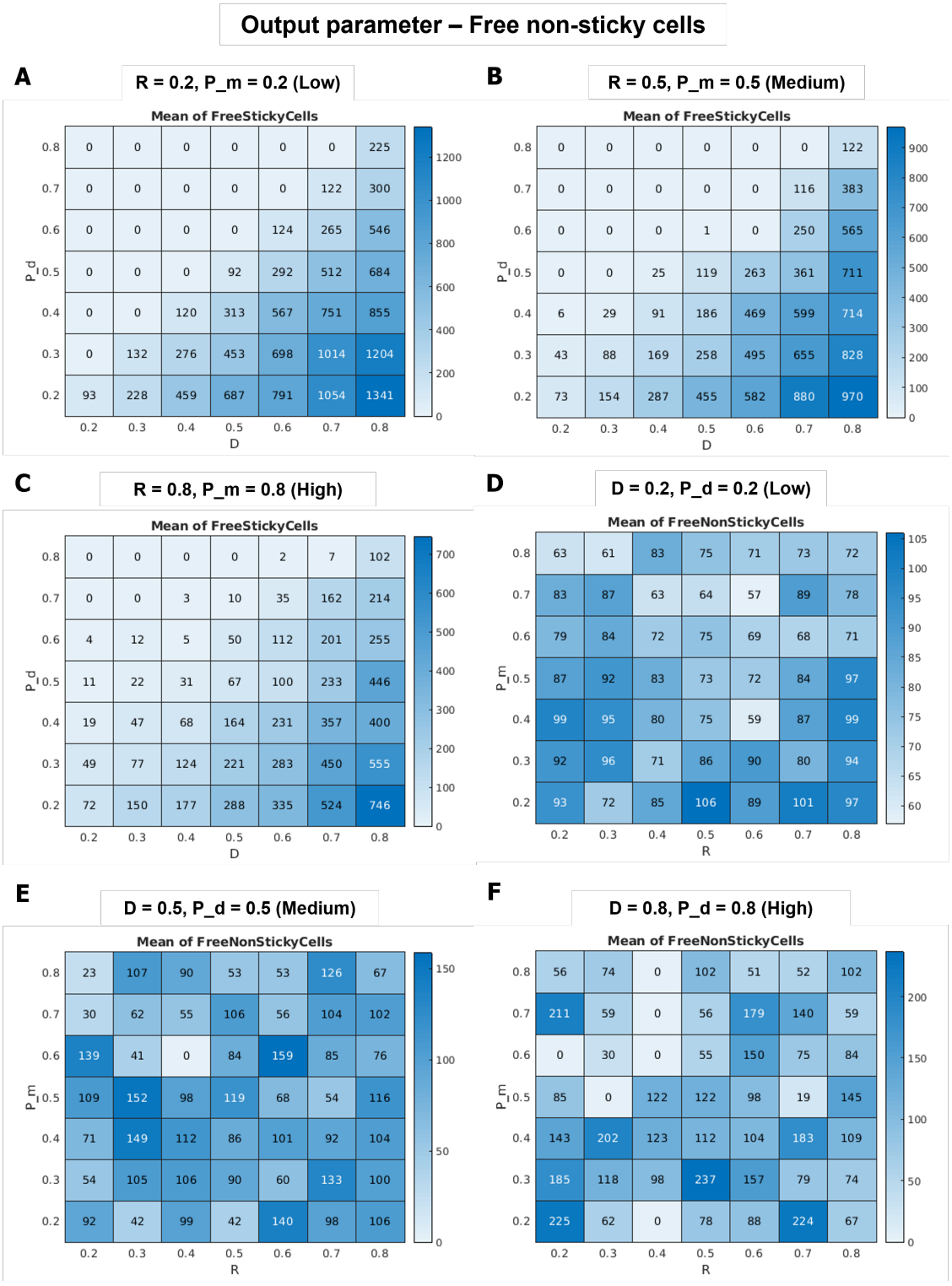


Figure H.12: Output - free non-sticky cells.

# Appendix Nine

# Conference Abstracts

- **Quantifying Biofilm Formation on Biomaterials Surfaces**
  - Sophie E Mountcastle, Nina Vyas, Richard M Shelton, Rachel L Sammons, Sophie C Cox, Sara Jabbari, A Damien Walmsley, Sarah A Kuehne
  - World Congress of Biomaterials 2020, Virtual
  - *Poster presentation*
- **Development of a cellular automaton to study the effect of different parameters on bacterial surface adhesion**
  - Sophie E Mountcastle, Sara Jabbari, Sophie C Cox, Richard M Shelton, Rachel L Sammons, and Sarah A Kuehne
  - $GW_4$ Multidisciplinary Approaches to AMR Virtual Symposium 2020, Virtual
  - *Poster presentation and oral flash talk*
- **Development of a Mechancically Relevant Oral Mucosa Model**
  - Sophie E Mountcastle, Sophie C Cox, Sara Jabbari, Richard M Shelton, Rachel L Sammons, and Sarah A Kuehne
  - BSODR Virtual Prize Competition 2020, Virtual

  - *Poster presentation and oral flash talk*

- **Mimicking the mechanical properties of the oral mucosa: towards the development of a biologically and physically matched oral tissue model**

  - Sophie E Mountcastle, Richard M Shelton, Rachel L Sammons, Sophie C Cox, Sara Jabbari, Sarah A Kuehne

  - 8th International Conference on Mechanics of Biomaterials and Tissues 2019, Hawaii, USA

  - *Oral presentation*

- **Race to the surface: Modelling bacterial and human cell growth on dental implant surfaces**

  - Sophie E Mountcastle, Richard M Shelton, Rachel L Sammons, Sophie C Cox, Sara Jabbari, and Sarah A Kuehne

  - University of Birmingham Research Poster Conference 2019, Birmingham, UK

  - *Poster presentation*

- **A New Method to Quantify Biofilm Formation on Biomaterials Surfaces**

  - Sophie E Mountcastle, Nina Vyas, Richard M Shelton, Rachel L Sammons, Sophie C Cox, Sara Jabbari, A Damien Walmsley, Sarah A Kuehne

  - TCES-UKSB Joint Conference 2019, Nottingham, UK

  - *Poster presentation*

- **Development of an Oral Mucosa Model to Evaluate Implant Integration**

  - Sophie E Mountcastle, Victoria E Seville, Richard M Shelton, Rachel L Sammons, Sophie C Cox, Sara Jabbari, and Sarah A Kuehne

  - OMIG PGR Prize Symposium 2019, Newcastle, UK
  - *Oral presentation*

- **Towards the development of a mechanically and biologically relevant oral mucosa model to evaluate tissue integration approaches for dental implants**
  - Sophie Mountcastle, Richard M Shelton, Rachel L Sammons, Sophie C Cox, Sara Jabbari, and Sarah A Kuenhe
  - RSC Biomaterials Annual Conference 2019, Liverpool, UK
  - *Poster presentation*

- **Viscoelastic and histomorphological characterisation of human osteochondral tissue**
  - Sophie Mountcastle, Ben Mellors, Bernard Lawless, Megan Cooke, Natasha Fell, Daniel Espino, Simon Wyn-Jones, Sophie Cox
  - World Congress of Biomechanics 2018, Dublin, Republic of Ireland
  - *Oral presentation*

# Appendix Ten

# Awards, Grants and Prizes

**Awards and prizes**

- 2020: GW4 AMR Symposium, Awarded 1st Prize for best flash talk.
- 2019: University of Birmingham Research Poster Conference, Awarded "Best Poster" prize.
- 2019: University of Birmingham, School of Chemical Engineering 3-Minute Thesis Competition, Awarded 1st Prize.

**Grants**

- 2019: Awarded an £800 travel grant from the Royal Society of Chemistry Materials Group to attend the 8th International Mechanics of Biomaterials and Tissues Conference in Hawaii, USA.

# Appendix Eleven

# List of Publications

**First-author**

- Sophie E Mountcastle, Nina Vyas, Victor M Villapun, Sophie C Cox, Sara Jabbari, Rachel L Salmons, Richard M Shelton, A Damien Walmsely, and Sarah A Kuehne. **Biofilm Viability Checker: An open-source tool for automated biofilm viability analysis from confocal microscopy images** (2021). *npj Biofilms and Microbiomes.* https://doi.org/10.1038/s41522-021-00214-7

  – Invited to contribute to Nature Microbiology Blog "Behind the Paper" series: https://microbiologycommunity.nature.com/posts/biofilm-viability-checker-creating-a-tool-to-calculate-biofilm-viability-from-confocal-microscopy-images

- Sophie E Mountcastle, Sophie C Cox, Rachel L Sammons, Sara Jabbari, Richard M Shelton, and Sarah A Kuehne. **A review of co-culture models to study the oral microenvironment and disease** (2020). *Journal of Oral Microbiology.* https://doi.org/10.1080/20002297.2020.1773122

- Sophie E Mountcastle, Piers Allen, Ben O L Mellors, Bernard M Lawless, Megan E Cooke, Carolina E Lavecchia, Natasha L A Fell, Daniel M Espino, Simon W Jones, and Sophie C Cox. **Dynamic viscoelastic characterisation of human osteochondral**

**tissue: understanding the effect of the cartilage-bone interface** (2019). *BMC Musculoskeletal Disorders.* https://doi.org/10.1186/s12891-019-2959-4

**Contributing-author**

- Paola Ginestra, Leonardo Riva, Elisabetta Ceretti, David Lobo, Sophie Mountcastle, Victor Villapun, Sophie Cox, Liam Grover, Moataz Attallah, Owen Addison, Duncan Shepherd, and Mark Webber. **Surface finish of Additively Manufactured Metals: biofilm formation and cellular attachment** (2021).

# Appendix Twelve

# First-Author Publications

JOURNAL OF ORAL MICROBIOLOGY
2020, VOL. 12, 1773122
https://doi.org/10.1080/20002297.2020.1773122

Taylor & Francis
Taylor & Francis Group

OPEN ACCESS Check for updates

# A review of co-culture models to study the oral microenvironment and disease

Sophie E Mountcastle[a,b], Sophie C Cox[c], Rachel L Sammons[b], Sara Jabbari[d,e], Richard M Shelton[b] and Sarah A Kuehne[b,e]

[a]EPSRC Centre for Doctoral Training in Physical Sciences for Health, University of Birmingham, Birmingham, UK; [b]School of Dentistry, University of Birmingham, Birmingham, UK; [c]School of Chemical Engineering, University of Birmingham, Birmingham, UK; [d]School of Mathematics, University of Birmingham, Birmingham, UK; [e]Institute of Microbiology and Infection, University of Birmingham, Birmingham, UK

**ABSTRACT**

Co-cultures allow for the study of cell–cell interactions between different eukaryotic species or with bacteria. Such an approach has enabled researchers to more closely mimic complex tissue structures. This review is focused on co-culture systems modelling the oral cavity, which have been used to evaluate this unique cellular environment and understand disease progression. Over time, these systems have developed significantly from simple 2D eukaryotic cultures and planktonic bacteria to more complex 3D tissue engineered structures and biofilms. Careful selection and design of the co-culture along with critical parameters, such as seeding density and choice of analysis method, have resulted in several advances. This review provides a comparison of existing co-culture systems for the oral environment, with emphasis on progression of 3D models and the opportunity to harness techniques from other fields to improve current methods. While filling a gap in navigating this literature, this review ultimately supports the development of this vital technique in the field of oral biology.

**ARTICLE HISTORY**
Received 3 September 2019
Revised 25 April 2020
Accepted 19 May 2020

**KEYWORDS**
Co-culture; oral disease; oral cavity; biofilms; NC3Rs; 3D-*in vitro* models

## Introduction

The oral cavity is a complex environment that contains many microbial species that thrive in the warm, moist conditions [1] (Figure 1a). Furthermore, different regions of the oral cavity are made up of several cell types and tissues, both soft (mucosa, connective tissue, smooth muscle) and hard (enamel, dentine, bone) [2,3] (Figure 1b). Changes in the soft tissues can indicate disease, for example periodontitis (severe gum disease) and oral cancer, and reveal systemic conditions such as diabetes or vitamin deficiency [3]. Equally, the mineralised structures within the mouth may bear signs of disease, including dental caries, that might result in significant hard tissue loss or damage [4]. The composition of microbial species in the mouth can either cause or intensify many of these diseases [5], thus demonstrating the importance of balance within this complex multicellular environment.

The microorganisms present in the oral cavity attach to surfaces in communities called biofilms; highly regulated and organised interspecies habitats that provide defence against competitors and adapt to changes in the wider environment [5]. These communities are essential for many metabolic, physiological, and immunological functions. They support food digestion, regulation of the host immune system, maintenance of mucosa barrier function, detoxification of environmental chemicals, and prevent invasion of disease-promoting species [5]. However, a shift in the species present in the oral microbiome can unsettle the local environment, switching from a healthy to disease state [6]. Saliva also plays a key role in the oral cavity in maintaining homeostasis and defending from disease, as well as containing proteins, minerals, and antimicrobial enzymes that control biofilm formation and activity [7,8]. Evidently, understanding the processes and interactions that occur in the oral cavity, in both healthy and disease states as well as the shift between the two, is vital to furthering our knowledge of disease progression and the discovery of new treatments.

For both human and bacterial cells, utilising single species for *in vitro* modelling of the oral cavity does not fully represent the *in vivo* conditions (Figure 1). This presents a key question for researchers in this field regarding how best to study the oral cavity, both for understanding disease pathogenesis and evaluating novel therapeutics. Challenges in studying this complex environment are not just limited to the presence of many cell types and bacterial species, but also the substantial variations in microbiota between individuals [9]. Mimicking these various degrees of complexity remains difficult and therefore *in vivo*

**CONTACT** Sarah A Kuehne s.a.kuehne@bham.ac.uk School of Dentistry, University of Birmingham, 5 Mill Pool Way, Birmingham B5 7EG, UK

© 2020 The Author(s). Published by Informa UK Limited, trading as Taylor & Francis Group.
This is an Open Access article distributed under the terms of the Creative Commons Attribution License (http://creativecommons.org/licenses/by/4.0/), which permits unrestricted use, distribution, and reproduction in any medium, provided the original work is properly cited.

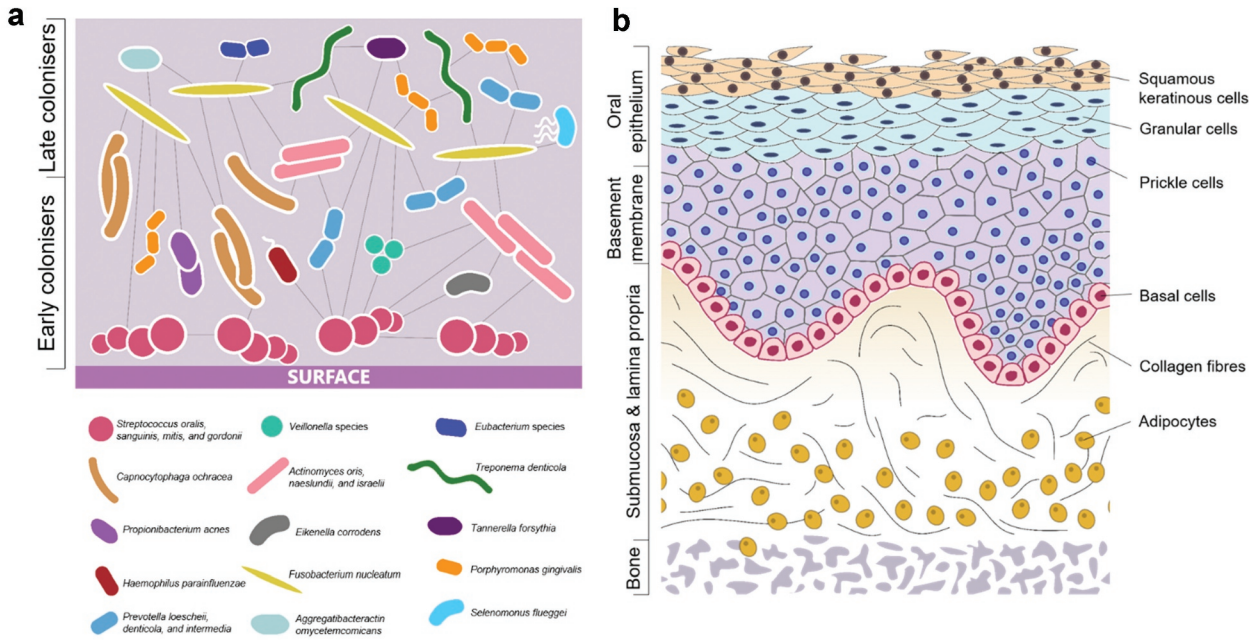


**Figure 1.** (a) Common bacterial species present in pathogenic oral biofilms and their communication between species (adapted from Parashar et al. [92]). (b) Cells and tissue types present in the oral mucosa, demonstrating complexity of 3D structure.

studies remain the gold standard for observing processes in oral pathogenesis. However, clinical *in vivo* studies and animal models bring their own obstacles; they are expensive, labour intensive, and can generate ethical concerns. In addition, human and animal oral microbiota may not be the same and therefore can be difficult to compare. As such, the use of co-culture models to mimic *in vivo* conditions has been recognised as a valuable approach to further our understanding of the relationship between eukaryotic and bacterial cells and is especially applicable to the oral cavity.

Co-culture techniques allow a variety of cell types to be cultivated together, enabling examination of cell–cell interactions [10]. These systems may refer to the culture of two or more eukaryotic cell types together, or eukaryotic and prokaryotic cells. The effectiveness of co-cultures is heavily determined by the choice of experimental setup. Cell–cell interactions in co-cultures are strongly influenced by the extracellular environment, which in turn is influenced by the employed protocol [11]. There are numerous factors that need to be optimised to ensure these systems are representative of the native oral cavity, such as the number of cell populations. Having more than two species can result in unstable systems due to multiple reaction pathways, which may be difficult to monitor, analyse, and interpret [11].

Studying the relationship between the oral microbiome and eukaryotic cells is essential to understanding disease progression and evaluating the effect of new treatments. Many studies have published co-culture methodologies, but to the authors' knowledge, these techniques have not been directly compared, making it challenging to identify and optimise the most appropriate system for a research question. Hence, this review discusses the use of co-culture *in vitro* models to study the oral environment, the progression of these models in complexity, and the disadvantages and benefits of using a range of published methods (Table 1). In addition, the lessons and approaches that can be adapted from other fields that regularly utilise co-cultures are considered with the aim of providing future insights for development. Searches were performed across Science Direct, ProQuest, and the Directory of Open Access Journals [12–14] for papers that reported co-culture studies containing both eukaryotic and bacterial cell species.

## 2D cell culture

The simplest oral environment co-culture systems apply planktonic bacteria to a monolayer of confluent eukaryotic cells [15–18] (Figure 2a). Compared with more complex approaches, these basic models have an advantage in that cellular response to bacteria can be attributed to specific interactions allowing for direct comparison between species, both bacterial and cellular. For example, the inflammatory response of epithelial cells to different bacterial species may be compared [16] or different eukaryotic cell lines may be challenged with the same oral pathogenic species, such as *Porphyromonas gingivalis* (*P. gingivalis*), a key contributor to the pathogenesis of periodontitis [19]. However, it is known that interactions between

**Table 1.** Summary of co-culture methodologies, common protocols employed, and the advantages and disadvantages of each model system.

| Method | Summary of protocol | Advantages | Disadvantages | References |
|---|---|---|---|---|
| 2D monospecies co-culture with planktonic bacteria | • Seed eukaryotic cells into well plate.<br>• Culture until confluent monolayer formed, with media changes every 1–2 days.<br>• Prepare bacteria overnight culture.<br>• Centrifuge overnight and re-suspend bacteria in eukaryotic cell culture media to achieve desired concentration.<br>• Add media containing bacterial suspension to monolayers and perform assays at desired time points. | • Can use simple assays to investigate<br>• Can attribute direct cellular responses from interactions with bacteria<br>• Reproducible with reduced batch-to-batch variation<br>• Supports homogenous growth<br>• All cells have equal access to nutrients | • Not representative of *in vivo* tissue structure<br>• Does not account for immune cells<br>• Does not account for many cues found *in vivo*, including mechanical signalling<br>• Cannot monitor interaction between cell types, in particular, the immune system<br>• Does not represent the complex bacterial biofilms present in the oral cavity | [15–17,19,33,34] |
| 2D multispecies co-culture with planktonic bacteria | • Seed appropriate ratio of eukaryotic cells into well plate.<br>• Culture until confluent, with media changes every 1–2 days.<br>• Prepare bacteria overnight culture.<br>• Centrifuge overnight and re-suspend bacteria in eukaryotic cell culture media to achieve desired concentration.<br>• Add media containing bacterial suspension to cell culture and perform assays at desired time points. | • Can monitor the interaction between cell types<br>• Reproducible with reduced batch-to-batch variation<br>• Supports homogenous growth<br>• All cells have equal access to nutrients | • May require optimisation due to different nutrient requirements<br>• Not representative of *in vivo* tissue structure<br>• Traditional assays cannot always determine between cell species<br>• Does not account for many cues found *in vivo*, including mechanical signalling<br>• Does not represent the complex bacterial biofilms present in the oral cavity | [29,30] |
| 2D co-culture with biofilm | • Seed appropriate ratio of eukaryotic cells into well plate.<br>• Culture until confluent, with media changes every 1–2 days.<br>• Prepare bacteria overnight culture.<br>• To form biofilm, seed overnight culture onto coverslips placed in the bottom of a well plate. Change media every 1–2 days.<br>• At chosen time point, once biofilm has formed, remove media and attach coverslip to base of transwell insert.<br>• Place insert into cell-culture plate.<br>• Perform assays at desired time points. | • Can monitor the interaction between cell types<br>• Reproducible with reduced batch-to-batch variation<br>• Supports homogenous growth<br>• All cells have equal access to nutrients<br>• More clinically relevant, as biofilms show increased antibiotic resistance to planktonic cultures. | • Bacteria can overrun eukaryotic cells if co-culture system is not carefully designed | [46,55–57,66,67] |
| 3D tissue engineered co-culture with planktonic bacteria | • For collagen-based system, mix fibroblasts with collagen gel and pipette into transwell inserts. Set gel in incubator at 37°C for 1 hr.<br>• Seed epithelial cells onto surface of gel. Seed monolayer of epithelial cells into separate well plate to monitor confluence. Culture cells until confluent monolayer formed.<br>• Raise cells to air-liquid interface and culture for 7–10 days to allow stratified epithelium to form.<br>• Prepare bacteria overnight culture.<br>• Centrifuge overnight and re-suspend bacteria in eukaryotic cell culture media to achieve desired concentration.<br>• Add media containing bacterial suspension to 3D cell culture and perform assays at desired time points. | • More representative of *in vivo* environment<br>• Can study cell-cell signalling<br>• Two mucosa models well established in literature – collagen-based and decellularised matrix | • Can be challenging to achieve cell numbers required for multiple models<br>• Require specifically enriched media<br>• Significant optimisation may be needed<br>• More resource-intensive<br>• More difficult to produce replicates<br>• Models may not be fully representative of native tissue structure<br>• Does not represent the complex bacterial biofilms present in the oral cavity | [41–44,46,47] |

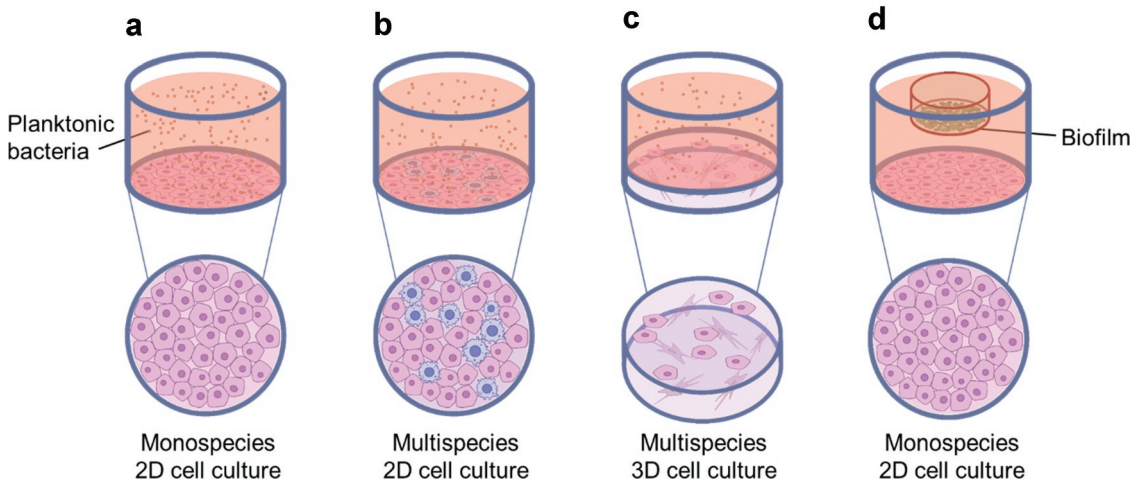


**Figure 2.** Common co-culture systems reported in the literature (a) monospecies 2D cell culture with planktonic bacteria applied; (b) multispecies 2D cell culture with planktonic bacteria applied; (c) multispecies 3D cell culture, typically a collagen-based or decellularised matrix containing fibroblasts, with planktonic bacteria applied; and (d) monospecies 2D cell culture with biofilm applied, typically suspended from a well insert.

different bacteria can affect disease progression [20,21] and therefore applying single species cannot elucidate more complex physiological interactions.

A number of innovative studies utilised 2D co-culture systems to study the adhesion and invasion of epithelial cells by key oral pathogens. *Aggregatibacter actinomycetemcomitans* (*a. actinomycetemcomitans*, formerly *Actinobacillus actinomycetemcomitans*) is a bacterium associated with aggressive periodontitis. Mintz and Fives-Taylor [22,23] applied *a. actinomycetemcomitans* to an oral cancer cell line under different conditions and highlighted that adhesion is affected by both host (saliva, serum) and culture (pH) conditions. Using a similar approach, Yilmaz et al. [24] cultured primary gingival epithelial cells and introduced *P. gingivalis* and its fimbriae-deficient mutant, demonstrating that *P. gingivalis* fimbriae promote adhesion to gingival epithelial cells through interaction with β1 integrins. In a later study, Yilmaz et al. [25] showed that *P. gingivalis* is capable of targeting specific epithelial cell pathways during invasion and can adapt to an intracellular environment. They suggested that disease may ensue from a disruption of the balance between the bacteria and host cells by factors that may trigger virulence or lead to host-immune-mediated tissue damage [25]. Studies like these are essential to determine key proteins and interactions involved in oral pathogenesis, which could potentially provide targets for future treatments.

In addition to looking at a specific bacterium, 2D co-culture systems can be effectively used to compare the response of host cells when challenged with different oral pathogens. Han et al. [26] individually applied six key Gram-negative anaerobic bacteria associated with periodontal diseases to human gingival epithelial cells to compare their ability to adhere and invade, as well as measuring levels of interleukin-8 (a proinflammatory cytokine) secretion from the human cells. Their findings demonstrated that whilst all bacteria species were able to adhere to oral epithelial cells, only *Fusobacterium nucleatum* (*F. nucleatum*) was highly invasive, to levels comparable with *P. gingivalis* [26]. Not only can comparisons be made between different bacteria species using multiple 2D co-cultures, but the ability of different strains to adhere and invade oral epithelial cells can be investigated. The *Prevotella intermedia* (*P. intermedia*) group are made up of three strains (*P. intermedia, Prevotella nigrescens*, and *Prevotella pallens*) and are connected with oral disease pathogenesis. Gursoy et al. [27] showed that *P. intermedia* and *P. nigrescens* type strains can adhere to and invade epithelial cells, the capability of *P. intermedia* being highest. Another key publication in which strains were compared, was the work of Dabija-Wolter et al. [28] who examined the invasion of human gingival fibroblasts by three different *F. nucleatum* strains using a 2D co-culture system. In order to evaluate the amount of bacteria present inside the fibroblasts after infection, live bacteria were fluorescently stained prior to being introduced into the co-culture, and this allowed for visualisation using confocal laser scanning microscopy and quantification using flow cytometry. The studies described use a range of assays and analytical techniques to determine key interactions between host cells and pathogenic bacteria, showing the importance of simple 2D co-culture systems, as well as the influence of strain, cell type, and culture conditions.

To elevate 2D co-cultures and gain further insight into *in vivo* interactions, multiple eukaryotic species can be cultured together (Figure 2B). In two studies by Bodet et al. [29,30], epithelial cells were cultured alongside macrophages to gain a better understanding of the interplay between these two cell types in

the presence of *P. gingivalis*. Careful optimisation of the ratio between cell types is essential and consideration should be given to the analytical techniques applied. In these studies, Bodet et al. [29,30] were unable to identify which cells had a greater role in IL-6 and IL-8 secretion. This highlights that more complex assays, such as flow cytometry, may be required to target each cell type. Recently, a three-cell co-culture was described whereby dendritic cells, gingival epithelial keratinocytes, and T-cells were cultured in a three-cell transwell co-culture plate, essentially allowing for three mono-layers to be cultured in the same well and therefore allowing interactions to be determined when challenged with *P. gingivalis* [31]. Different single- and co-cultures were prepared to compare the production of matrix metalloproteases (MMPs) in response to the pathogen. Interestingly, the cellular reaction changed when T-cells were present with a reduction in MMP9 and a reduced immune response, which indicated that multiple cell types could influence MMP expression, thus providing further evidence of the complex cell-cell signalling occurring *in vivo*.

Not only can 2D co-cultures elucidate information on interactions between oral eukaryotic cells, they can also be used to evaluate microbial communication. Several authors have employed 2D co-cultures to study the effect of multiple oral bacterial species on the invasion of gingival epithelial cells by respiratory pathogens [15] and *P. gingivalis* [17]. Findings suggested that commensal oral species could modulate invasion. Providing careful consideration is given to the controls used, a 2D co-culture system with multiple bacterial species can determine very useful information on the pathogenesis of oral disease. From the *in vitro* study described [15], the authors suggest that increased presence of oral bacteria in the throat could prevent invasion of respiratory pathogens. However, it is important to recognise that these co-culture models are not physiologically representative, due to a lack of host immune system and the use of monolayer cell cultures. Therefore, extrapolating the results of such studies to *in vivo* conditions should be done with care.

Interactions of anaerobic species with human cells raise challenges in culturing these bacteria with oxygen-requiring epithelial cells. One of the limitations in the literature described is the culture of *P. gingivalis* in aerobic conditions. Bodet et al. [29,30] and Saito et al. [17] did not report viability of *P. gingivalis* under the growth conditions applied when co-cultured with their respective oral mucosa model. The growth of *P. gingivalis* under oxygenated environments has been shown to affect its physiology and result in changes in expression of different proteins, including virulence factors [32]. Gursoy et al. [27] also highlighted the tolerance of *P. intermedia* strains to oxygen exposure as a limitation of their co-culture study. The test conditions applied were aerobic, and the type strain had been handled in laboratory conditions for longer than the clinical isolates. Consequently, increased tolerance to oxygen exposure of the type strain may have explained their findings of increased adhesion. It is vital to assess and report the effect of the aerobic growth conditions used on anaerobic species for the duration of the experiment.

Simple 2D co-cultures prove useful for testing responses to a dental material, for example, implants or resins. Human gingival fibroblasts can be cultured directly onto the surfaces of these materials, with planktonic oral species added subsequently to investigate their effect. Using this method, oral bacteria have been shown to modulate toxicity of dental resins on human gingival fibroblasts (HGFs) [33]. It is also possible to adapt these 2D co-cultures to enable high throughput studies to be performed in 96-well plates. For example, a study by Giulio et al. [34] reported the effect of dental resin monomers on HGFs in the presence of *Streptococcus mitis* (*S. mitis*) and demonstrated there was no reduction in bacterial adhesion to the eukaryotic cells. Simple 2D cultures also allow for the interaction between cells and dental resin materials (e.g. HEMA) to be studied in the presence of oral microbes, an important interaction to understand in the context of the oral environment [35].

A key factor to consider when using a co-culture system containing eukaryotic cells is their origin. A range of cell types have been used in the studies described, including primary human gingival epithelial cells [16,24–26] and fibroblasts [33,34], immortalised human gingival cell lines [18], oral carcinoma cell lines [15,17,22,23,26], and skin keratinocyte cell lines [27,29,30]. Some studies did not take the source of their human cells into account when discussing their findings. However, oral keratinocytes and fibroblasts show distinct characteristics to those derived from the skin [36,37]. In addition, whilst cell lines are a convenient choice for these *in vitro* systems as they are highly proliferative and easier to culture, they often have phenotypic, morphological, and genetic differences to their primary tissue origin. Primary cells, on the other hand, maintain many of the markers and functions seen *in vivo* and are therefore useful for elucidating responses from human cells when challenged with oral pathogenic bacteria.

The publications described have demonstrated that a simple 2D co-culture model ensures that subsequent assays and analyses are easier to perform and less complex analytical techniques can be used. They also allow for specific interactions to be identified, which is important when investigating disease progression and potentially identifying new therapies for oral pathogenesis. However, there are challenges associated with using simpler models. In particular, neglecting the effects of the host immune system and

not representing the 3D structure of *in vivo* tissues mean these models lack certain signals that are present in the body (Table 1).

## 3D cell culture

As we have gained an understanding of the importance of cues from the surrounding environment, such as mechanical and biological signalling between cell types [38–40], there has been a move to mimic the structure of the tissue in which the eukaryotic cells are located (Figure 2C). *Candida albicans* (*C. albicans*) is a commensal yeast that can shift to become pathogenic in immunosuppressed individuals and is therefore an important oral pathogen. A number of 3D *in vitro* culture systems have been developed to mimic the oral mucosa in order to study the interaction between epithelial cells and *C. albicans* [41,42]. The 3D models commonly utilised in these investigations comprise a fibroblast-containing collagen gel with oral keratinocytes cultured on the surface at the air-liquid interface. An alternative to the collagen model is the use of decellularised matrix as a 3D scaffold. Interestingly, Yadev et al. [43] demonstrated that a 3D tissue engineered oral mucosa model of human keratinocytes and a fibroblast-containing matrix displayed more similar immunohistological and proliferation characteristics to normal mucosa when compared with a 2D oral cell line. In this study, full-thickness oral mucosa models were prepared from decellularised human matrix and compared with collagen-based 3D mucosa models purchased from SkinEthic Laboratories (Nice, France) and MatTek Corporation (Ashland, MA).

Surprisingly, there are relatively few 3D oral mucosa co-culture studies that have been applied to model bacteria relevant to oral disease. Of those that have, Pinnock et al. [44] reported significant differences in the response of oral mucosa models to *P. gingivalis*, compared with monolayer cultures of epithelial cells. This study described their use of a collagen-fibroblast gel with surface epithelial cells cultured at the air-liquid interface, with the application of *P. gingivalis* in planktonic culture. Subsequently, it was shown that utilising 3D co-culture systems was important in order to fully discern cellular responses to infection and confirmed that the interaction between cell types played an important role. Another key study that supported the significance of 3D co-cultures in the field of oral pathogenesis investigated the bacterial species *F. nucleatum*, which is known to form a bridge between early and late colonisers in the formation of dental plaque (a common oral biofilm) [45]. Gursoy et al. [46] used a collagen-based 3D mucosa model and applied planktonic cultures of *F. nucleatum* to determine the bacteria's ability to attach to and invade epithelial cells. Like Pinnock et al. [44], they also highlighted the difference in response between the 3D co-culture and a simple monolayer of epithelial cells. Given the strong evidence of an interplay between epithelial cells and fibroblasts in response to infection, there is a clear need for future studies to consider the application of 3D mucosa models to studies of oral disease pathogenesis [44,46]. Furthermore, it is worth highlighting that both Pinnock et al. [44] and Gursoy et al. [46] reported that the viability of the anaerobic species they utilised (*P. gingivalis* and *F. nucleatum* respectively) was not reduced under aerobic growth conditions for the duration of their infection co-culture model. It is essential to examine the oxygen tolerance for anaerobic species when applying them to oxygen-requiring epithelium models to ensure physiology is not affected. One of the challenges with developing 3D cultures is that primary cells have relatively short lifespans, as they lose their *in vivo* phenotype after a few passages, and therefore may not offer sufficient cell numbers to use in multiple 3D co-cultures [47]. Furthermore, enriched media specific to each cell type are often required; without this, primary cells can display an altered phenotype and metabolic function [48]. To combat these drawbacks, immortalised cell lines of human gingival keratinocytes (HGKs) and human gingival fibroblasts (HGFs) have been established. Promisingly, Bao et al. [47] have demonstrated that immortalised HGKs still formed a stratified epithelial layer and both HGKs and HGFs displayed cell-specific markers similar to those found in human gingival tissues. The need for reproducibility makes the use of cell lines desirable, although it must be noted that there is a pay-off between reproducibility and physiological relevance, with Yadev at al. highlighting that the commercially available epithelial cell line TR146 does not form a fully differentiated epithelium [43].

As with 2D co-culture systems, the origin of the human eukaryotic cells in a 3D mucosa model is an important aspect to consider when analysing the cellular response to bacteria. A range of cell sources were utilised in the co-culture studies described. These included primary cells from gingival biopsies [43,44], immortalised gingival keratinocyte and fibroblast cell lines [46,47], oral carcinoma cell lines [42,43], human skin epithelial cell lines [41,46] and 3T3 cells (mouse embryonic fibroblast cell line) [41]. Not only do these cells exhibit different phenotypes and morphologies but moreover, the choice of fibroblast origin can influence the characteristics of the keratinocytes in a 3D model. Merne & Syrjänen [49] highlighted the importance of standardising the matrix, both in terms of extracellular matrix components and in the source of fibroblasts used. Where possible, human eukaryotic cells should be utilised

since they are the most physiologically relevant with regards to the *in vivo* tissue of interest.

An additional factor that needs to be taken into account regarding the application of oral pathogens in 2D and 3D co-cultures is the strain of bacteria utilised. Many of the studies cited throughout this review do not detail the origin of the bacteria used. However, it has been previously shown that there is a difference in keratinocyte response between clinical and type strains of *a. actinomycetemcomitans* [50]. Therefore, it is important to appreciate that strains of the same bacterial species may have varying characteristics. It is advisable, where possible, to use clinical strains as well as type strains to conduct co-culture studies in order to compare them with their standards.

The choice to use a 3D culture needs to be a carefully considered decision, as there is currently no universal system available and therefore significant optimisation may be required [51]. Moreover, 2D cell culture approaches can still provide useful information to enhance our understanding of *in vivo* processes. As well as being easier to reproduce and less resource-intensive, 2D cell cultures support homogenous growth and equal access to nutrients for all cells present, whilst cells embedded in a 3D system may not have access to sufficient nutrients [51]. Despite the challenges that come with 3D systems, the studies cited demonstrate that 3D co-cultures are highly valuable, as monolayer culture systems do not fully represent the high complexity of the oral cavity (Table 1). A review of 3D oral mucosa models by Moharamzadeh et al. [52] described the different approaches that have been taken and the advantages and limitations of each, as well as the range of applications for these systems. As protocols and analysis methods continue to improve, these 3D techniques will become more accessible within the oral field.

## Biofilms

The studies described thus far have utilised bacteria in the form of planktonic cultures, applied within nutrient media to the 2D and 3D cell cultures. Often only one or two bacterial species are considered in these studies, compared to the 700 species that have been detected in the oral cavity [53]. Bacteria in the mouth mostly exist in the form of polymicrobial biofilms, which are particularly relevant when looking at plaque-related pathogenesis [5]. Furthermore, species growing in biofilms have been shown to have higher resistance to antibiotics when compared with planktonic bacteria [54]. This highlights that applying biofilm models in co-culture studies is particularly relevant to mimicking the oral cavity, both for studying disease progression and evaluating antimicrobial approaches. Millhouse et al. [55] showed there is interplay between a complex biofilm and oral epithelial cells, determined through changes in pro-inflammatory mediators. Other studies have similarly revealed pro-inflammatory responses of epithelial cells after challenge with biofilms [56,57]. These investigations demonstrated that specific interactions occur between bacteria in a biofilm, as well as with the host cells, yet these interactions are not present in a planktonic culture. Therefore, it may be concluded that the application of biofilms in co-culture studies with oral eukaryotic cells is essential to unearth the complexity of these microenvironments.

Biofilm models are useful to evaluate anti-inflammatory and antimicrobial techniques, treatments, and compounds. Traditionally, the efficacy of novel antimicrobial compounds is assessed on pathogens in planktonic and biofilm states and subsequently these compounds are applied to oral eukaryotic cells to identify any cytotoxic (or beneficial) effects. This approach is very common in *P. gingivalis* research, as this pathogen is known to induce a response in several oral cell types including epithelial cells, osteoblasts, and fibroblasts [58]. Hence, many studies have an interest in the oral cellular response to novel antimicrobial compounds, as well as the effect on *P. gingivalis* itself [59–61]. However, an area this approach does not address is the interaction between the pathogen and oral eukaryotic cells in the presence of the antimicrobial under investigation.

*P. intermedia* is another potential periodontal pathogen associated with the shift from health to disease in a biofilm and has been shown to increase the immune response at the site of infection [62]. Fteita et al. [18] demonstrated that the chemically synthesised quorum-sensing (QS) molecule butyl-dihydroxy-2, 3-pentanedione, an analogue of autoinducer-2 which is commonly produced by many gram-positive and gram-negative species, was able to reduce cytokine expression of a human gingival keratinocyte cell line and simultaneously inhibit biofilm growth of *P. intermedia*. Without observing the entire system in one *in vitro* study, this synergistic effect may have been missed. To further support the importance of evaluating biofilms and oral cells in co-culture, a study by Ramage et al. [63] applied both single- and multi-species biofilms to an oral epithelial cell line (OKF6/TERT2) and the results implied immune-function changes when varying biofilm composition. They reported the dependence of the immune response on the type of bacterial challenge, further highlighting the complexity of the oral cavity and the need to investigate several different interactions to understand disease pathogenesis and identify novel therapeutic targets.

A challenge with using biofilms in a co-culture is the highly different growth rates between the bacteria and eukaryotic cells [64]. High numbers of bacteria in cell culture can cause rapid nutrient depletion and changes in pH, subsequently hindering the growth of eukaryotic cells [65]. Biofilms contain larger numbers of bacteria compared with planktonic cultures, where the concentration of bacteria can be easily adjusted through dilutions. Hence, it can be useful to adopt a methodology whereby the biofilm does not come directly into contact with the eukaryotic cells, or where flow is present to reduce the bacteria numbers in the co-culture system (Figure 2D). Different approaches have been taken to achieve this. Guggenheim et al. [66] and Thurnheer et al. [67] grew a multispecies biofilm on a hydroxyapatite (HA) disc and placed this upside-down on a ring support that was layered onto a gingival epithelial cell monolayer culture. In contrast, Millhouse et al. [55] and Ramage et al. [63] attached the coverslip on which the biofilm was grown to the base of a transwell culture insert, which was placed within the well plate. Hence, the biofilm was suspended approximately 0.5 cm above the monolayer culture and did not directly come into contact with the oral epithelial cells in the bottom of the well (Table 1). An alternative approach to introducing bacteria is to use a flow chamber. These have been used in some studies to evaluate biofilm formation on implant surfaces [68,69]. To grow biofilms in flow chambers the hydrodynamic conditions must be carefully controlled, ideally akin to saliva flow in the mouth [70]. A review of different biofilm flow methodologies has been described elsewhere [70,71]. Relevant to this review, a recent study utilised a flow chamber to compare adhesion of bacteria versus human gingival fibroblasts on titanium surfaces and determined that the smoothest surface best supported fibroblast adhesion and reduced biofilm formation [69]. These findings highlight that dynamic culture systems remain a promising avenue for further exploration. This is of particular relevance to those studying the oral cavity since it enables the system to mimic saliva flow, thus creating an environment more closely aligned to *in vivo* conditions.

Due to the complexity of analysing both 3D tissue models and biofilms, very few studies have attempted to combine the two in a single system. The most simple reported method, published by Gursoy et al. [46], applied biofilms of *F. nucleatum* grown on coverslips directly onto epithelial cells grown on fibroblast-containing collagen matrices. By comparing the application of planktonic species with biofilms, they were able to determine differences between the ways bacteria behaved in these different states, with biofilm bacteria causing significantly greater epithelial cell death than when applied in planktonic form. This study also demonstrated that cells from biofilms of *F. nucleatum* were able to invade the collagen matrix of the mucosal model, highlighting the benefits of choosing a complex system to model the *in vivo* environment. However, the biofilm was directly in contact with the mucosal model and hence this may have increased the magnitude of the effects observed. A more complex approach to modelling the interaction between oral biofilms and oral tissues is to utilise a perfusion bioreactor system [72,73]. Bao et al. were the first to use one of these systems to study periodontal infections and later also used it to characterise the global proteome regulations present in the host-biofilm model. One of the benefits of using a perfusion bioreactor is that immune cells such as monocytes can be incorporated to generate an environment that is potentially more physiologically relevant. However, the cost of a bioreactor system can be a significant barrier to using this technique. Overall, the research described provides clear evidence that understanding the interactions occurring within an oral biofilm will enhance our understanding of the pathogenesis of oral disease, and novel approaches to introducing biofilms to host cells are key to achieving this.

## Perspectives from other fields

### *Gut microbiology*

The human intestines exhibit a multifaceted microbiota, with an abundance of host-microbe, microbe-microbe, and environmental interactions [74]. This complexity creates many similar challenges to researchers working in the oral field. Links between the gut microbiome and obesity, diabetes, liver disease, cancer, and neurodegenerative diseases [75,76] have now been established, which has driven considerable growth in this research area. Similar approaches to the co-culture models described herein have been utilised in this field, including monolayer/planktonic cultures [77–80] and 3D/planktonic cultures [81,82]. Reported methods to generate an *in vitro* environment that better represents the *in vivo* surroundings of the digestive tract include bioreactors [79], 3D organoid cultures [83,84], and organ-on-a-chip systems [85], all of which are described in detail by a review published in 2017 [78]. As with certain anaerobic bacteria in the oral field, interactions of anaerobic gut species with the intestinal mucosa are less-frequently studied due to challenges in culturing anaerobes with the oxygen-requiring epithelium. Anonye et al. [86] reported for the first time the use of a dual environment vertical diffusion chamber (VDC) to study the effect of *Clostridioides difficile* (*C. difficile*) on a 3D gut epithelium model. The use of a VDC allowed for monitoring this interaction over a longer time frame and the study reported that *C. difficile* adhered more effectively to

epithelial cells grown on the surface of the 3D model than on single epithelial monolayers. VDC could similarly be employed in the field of oral microbiology to better study the effect of anaerobic pathogens such as *P. gingivalis* and *F. nucleatum*, key species identified in the progression of periodontitis.

### Skin microflora

The skin is inhabited by a multitude of microorganisms, with many factors including genetics, environmental characteristics, and host demographics having an influence on the composition of the microflora and consequently on the shift from health to disease [87]. There are a number of 3D skin models established, including some that are available to purchase, which have a fully differentiated epithelium [88]. These models have typically been used in toxicity studies and drug testing applications [89]; however, due to the similarities in structure between skin and oral mucosa, lessons can be taken from some of the advanced approaches to 3D dermal models. For example, El Ghalbzouri et al. [90] demonstrated that collagen secretion by human fibroblasts provided a long-term functional human dermal matrix, and that this could be cultured for nearly three times as long as traditionally used rat-tail collagen matrices. This methodology could be beneficial in the oral field, as the short timespan that primary gingival fibroblasts can be cultured is a limiting factor for longer-term studies of periodontal disease. A similar technique frequently applied in the dermal field is to seed keratinocytes onto decellularised matrix. Anderson et al. [91] were interested in the formation of a biofilm phenotype of MRSA, to mimic a natural infection. They used decellularised porcine vaginal mucosa to generate a stratified, squamous epithelium, an advantage of which is that it is inexpensive and easily reproducible. The same study compared planktonic application of *Staphylococcus aureus* (*S. aureus*) with the formation of a biofilm directly on the skin model and demonstrated the importance of closely mimicking natural biofilm infections. In summary, 3D skin models are becoming increasingly useful in the study of the human dermal microbiota. Some of the novel advances made in this area, in particular the production of 3D extracellular matrix from human fibroblasts, could be translated to the oral mucosa to improve the reproducibility and accessibility of current techniques.

## Conclusions

Significant progress has been made towards the development of physiologically relevant models of the oral environment, from simple 2D co-cultures to more complex 3D tissue constructs and from the application of planktonic bacteria to multispecies biofilms. These advances have led to a greater increase in our understanding of the interactions taking place in the oral cavity, and thus deepening our knowledge of how periodontal diseases progress. However, current *in vitro* models have limitations, either due to their simplicity or complexity. Whilst able to identify specific interactions between cell types, simple 2D cultures cannot be used to determine the more complex cell–cell interactions that occur in the oral cavity, for example, between bacterial species and with the host immune system. On the other hand, due to the analytical complexity or equipment costs, very few studies have successfully introduced biofilms to a 3D organotypic mucosa model. Selecting a co-culture system with an appropriate degree of physiological relevance to answer the research question is essential. As a growing number of studies utilise more complex models, many analytical techniques and 3D mucosa models are being optimised. Utilising knowledge from multiple disciplines, including biology, engineering, and mathematics, is likely to become important in furthering the field due to the multifaceted nature of co-culture systems. Additionally, *in silico* models of interactions in the oral cavity may become of increasing significance for simulating more complex environments, though *in vitro* and *in vivo* data will still be required to make computational approaches reliable. Adapting and applying techniques from other fields facing similar challenges can enhance the methodologies currently available in the study of the oral cavity. Systems that combine these approaches will ensure advancement in the field. As such, this will enhance our understanding of disease progression and enable the evaluation of the effects of new antimicrobial compounds and novel therapies.

## Disclosure statement

The authors declare that they have no competing interests.

## Funding

EPSRC provided funding through a studentship at the Centre for Doctoral Training in Physical Sciences for Health [EP/L016346/1]. The funding body had no involvement in the writing of the manuscript and in the decision to submit the manuscript for publication.

## Authors' contributions

Article preparation (SM, SC). Critical revision of the manuscript and final approval (all authors).

## References

[1] Dale BA, Fredericks LP. Antimicrobial peptides in the oral environment: expression and function in health and disease. Curr Issues Mol Biol. 2005;7:119–134.

[2] Souza LR, Oliveira MVM, Basile JR, et al. Anatomical and physiopathological aspects of oral cavity and oropharynx components related to oropharyngeal dysphagia. In: Seminars in Dysphagia. InTech; 2015. doi:10.5772/60766.
[3] Squier CA, Kremer MJ. Biology of oral mucosa and esophagus. J Natl Cancer Inst Monogr. 2001;29:7–15.
[4] Schoen MH, Freed JR. Prevention of dental disease: caries and periodontal disease. Annu Rev Public Health. 1981;2:71–92.
[5] Kilian M, Chapple ILC, Hannig M, et al. The oral microbiome – an update for oral healthcare professionals. Bdj. 2016;221:657–666.
[6] Kriebel K, Hieke C, Müller-Hilke B, et al. Oral biofilms from symbiotic to pathogenic interactions and associated disease - Connection of periodontitis and rheumatic arthritis by peptidylarginine deiminase. Front Microbiol. 2018;9(JAN):1–14.
[7] Zarco MF, Vess TJ, Ginsburg GS. The oral microbiome in health and disease and the potential impact on personalized dental medicine. Oral Dis. 2012;18:109–120.
[8] Kumar B, Kashyap N, Avinash a, et al. The composition, function and role of saliva in maintaining oral health: a review. Int J Contemp Dent Med Rev. 2017; 1–6.
[9] Anderson AC, Rothballer M, Altenburger MJ, et al. In-vivo shift of the microbiota in oral biofilm in response to frequent sucrose consumption. Sci Rep. 2018;8:14202.
[10] Carter M, Shieh JC. Guide to research techniques in neuroscience. 2010.
[11] Goers L, Freemont P, Polizzi KM. Co-culture systems and technologies: taking synthetic biology to the next level. J R Soc Interface. 2014;11. DOI:10.1098/rsif.2014.0065
[12] Science Direct. ScienceDirect.com | science, health and medical journals, full text articles and books. [cited 2019 Jul 4]. Availabe from: http://www.sciencedirect.com/
[13] ProQuest. ProQuest | databases, EBooks and technology for research. [cited 2019 Jul 4]. Available from: https://www.proquest.com/
[14] Directory of Open Access Journals. Directory of open access journals (DOAJ). doi:10.5260/chara.18.3.25.
[15] Pan Y, Teng D, Burke AC, et al. Oral bacteria modulate invasion and induction of apoptosis in HEp-2 cells by *Pseudomonas aeruginosa*. Microb Pathog. 2009;46:73–79.
[16] Stathopoulou PG, Benakanakere MR, Galicia JC, et al. Epithelial cell pro-inflammatory cytokine response differs across dental plaque bacterial species. J Clin Periodontol. 2010;37:24–29.
[17] Saito a, Inagaki S, Ishihara K. Differential ability of periodontopathic bacteria to modulate invasion of human gingival epithelial cells by *Porphyromonas gingivalis*. Microb Pathog. 2009;47:329–333.
[18] Fteita D, Könönen E, Gürsoy M, et al. Quorum sensing molecules regulate epithelial cytokine response and biofilm-related virulence of three *Prevotella* species. Anaerobe. 2018;54:128–135.
[19] Yee M, Kim S, Sethi P, et al. *Porphyromonas gingivalis* stimulates IL-6 and IL-8 secretion in GMSM-K, HSC-3 and H413 oral epithelial cells. Anaerobe. 2014;28:62–67.
[20] Marsh PD, Zaura E. Dental biofilm: ecological interactions in health and disease. J Clin Periodontol. 2017;44:S12–22.
[21] Palmer RJ. Composition and development of oral bacterial communities. Periodontol 2000. 2014;64:20–39.
[22] Mintz KP, Fives-Taylor PM. Adhesion of *Actinobacillus actinomycetemcomitans* to a human oral cell line. Infect Immun. 1994;62:3672–3678. [cited 2019 Nov 25]. Available: http://www.ncbi.nlm.nih.gov/pubmed/8063383
[23] Fives-Taylor P, Meyer D, Mintz K. Characteristics of *Actinobacillus actinomycetemcomitans* invasion of and adhesion to cultured epithelial cells. Adv Dent Res. 1995;9:55–62.
[24] Yilmaz O, Watanabe K, Lamont RJ. Involvement of integrins in fimbriae-mediated binding and invasion by *Porphyromonas gingivalis*. Cell Microbiol. 2002;4:305–314.
[25] Yilmaz O, Young PA, Lamont RJ, et al. Gingival epithelial cell signalling and cytoskeletal responses to *Porphyromonas gingivalis* invasion. Microbiology. 2003;149:2417–2426.
[26] Han YW, Shi W, Huang GT, et al. Interactions between periodontal bacteria and human oral epithelial cells: *fusobacterium nucleatum* adheres to and invades epithelial cells. Infect Immun. 2000;68:3140–3146.
[27] Gursoy UK, Kononen E, Uitto VJ. *Prevotella intermedia* ATCC 25611 targets host cell lamellipodia in epithelial cell adhesion and invasion. Oral Microbiol Immunol. 2009;24:304–309.
[28] Dabija-Wolter G, Cimpan M-R, Costea DE, et al. *Fusobacterium nucleatum* enters normal human oral fibroblasts In Vitro. J Periodontol. 2009;80:1174–1183.
[29] Bodet C, Chandad F, Grenier D. Modulation of cytokine production by *Porphyromonas gingivalis* in a macrophage and epithelial cell co-culture model. Microbes Infect. 2005;7:448–456.
[30] Bodet C, Chandad F, Grenier D. Inflammatory responses of a macrophage/epithelial cell co-culture model to mono and mixed infections with *Porphyromonas gingivalis, Treponema denticola*, and *Tannerella forsythia*. Microbes Infect. 2006;8:27–35.
[31] Bates AM, Fischer CL, Abhyankar VP, et al. Matrix metalloproteinase response of dendritic cell, gingival epithelial keratinocyte, and T-cell transwell Co-Cultures treated with *Porphyromonas gingivalis* Hemagglutinin-B. Int J Mol Sci. 2018;19:3923.
[32] Diaz PI, Rogers AH. The effect of oxygen on the growth and physiology of *Porphyromonas gingivalis*. Oral Microbiol Immunol. 2004;19:88–94.
[33] Sancilio S, Di Giacomo V, Di Giulio M, et al. Biological responses of human gingival fibroblasts (HGFs) in an innovative co-culture model with *Streptococcus mitis* to thermosets coated with a silver polysaccharide antimicrobial system. PLoS One. 2014;9:e96520.
[34] Giulio MD, D'Ercole S, Zara S, et al. *Streptococcus mitis*/human gingival fibroblasts co-culture: the best natural association in answer to the 2-hydroxyethyl methacrylate release. Apmis. 2012;120:139.
[35] Grande R, Pacella S, Di Giulio M, et al. NF-kB mediated down-regulation of collagen synthesis upon HEMA (2-hydroxyethyl methacrylate) treatment of primary human gingival fibroblast/*Streptococcus mutans* co-cultured cells. Clin Oral Investig. 2015;19:841–849.
[36] Mah W, Jiang G, Olver D, et al. Human gingival fibroblasts display a non-fibrotic phenotype distinct from skin fibroblasts in three-dimensional cultures. PLoS One. 2014;9:e90715.
[37] Turabelidze a, Guo S, Chung AY, et al. Intrinsic differences between oral and skin keratinocytes. PLoS One. 2014;9:e101480.

[38] Discher DE. Tissue cells feel and respond to the stiffness of their substrate. Science. 2005;310:1139–1143.
[39] Engler AJ, Sen S, Sweeney LH, et al. Matrix elasticity directs stem cell lineage specification supplementary Information. Cell. 2006;126(VN):677–689.
[40] Cukierman E. Taking cell-matrix adhesions to the third dimension. Science. 2001;294:1708–1712.
[41] Dongari-Bagtzoglou a, Kashleva H. Development of a highly reproducible three-dimensional organotypic model of the oral mucosa. Nat Protoc. 2006;1:2012–2018.
[42] Schaller M, Zakikhany K, Naglik JR, et al. Models of oral and vaginal candidiasis based on in vitro reconstituted human epithelia. Nat Protoc. 2007;1:2767–2773.
[43] Yadev NP, Murdoch C, Saville SP, et al. Evaluation of tissue engineered models of the oral mucosa to investigate oral candidiasis. Microb Pathog. 2011;50:278–285.
[44] Pinnock a, Murdoch C, Moharamzadeh K, et al. Characterisation and optimisation of organotypic oral mucosal models to study *Porphyromonas gingivalis* invasion. Microbes Infect. 2014;16:310–319.
[45] Park J, Shokeen B, Haake SK, et al. Characterization of *Fusobacterium nucleatum* ATCC 23726 adhesins involved in strain-specific attachment to *Porphyromonas gingivalis*. Int J Oral Sci. 2016;8:138–144.
[46] Gursoy UK, Pöllänen M, Könönen E, et al. Biofilm formation enhances the oxygen tolerance and invasiveness of *Fusobacterium nucleatum* in an oral mucosa culture model. J Periodontol. 2010;81:1084–1091.
[47] Bao K, Akguel B, Bostanci N. Establishment and characterization of immortalized gingival epithelial and fibroblastic cell lines for the development of organotypic cultures. Cells Tissues Organs. 2014;199:228–237.
[48] Sakolish CM, Esch MB, Hickman JJ, et al. Modeling barrier tissues In Vitro: methods, achievements, and challenges. EBioMedicine. 2016;5:30–39.
[49] Merne M, Syrjäne S. The mesenchymal substrate influences the epithelial phenotype in a three-dimensional cell culture. Arch Dermatol Res. 2003;295:190–198.
[50] Gursoy UK, Könönen E. Understanding the roles of gingival beta-defensins. J Oral Microbiol. 2012;4. DOI:10.3402/jom.v4i0.15127
[51] Duval K, Grover H, Han LH, et al. Modeling physiological events in 2D vs. 3D cell culture. Physiology. 2017;32:266–277.
[52] Moharamzadeh K, Colley H, Murdoch C, et al. Tissue-engineered oral mucosa. J Dent Res. 2012;91:642–650.
[53] Aas JA, Paster BJ, Stokes LN, et al. Defining the normal bacterial flora of the oral cavity. J Clin Microbiol. 2005;43(5721):LP–5732.
[54] Hall CW, Mah TF. Molecular mechanisms of biofilm-based antibiotic resistance and tolerance in pathogenic bacteria. FEMS Microbiol Rev. 2017;41:276–301.
[55] Millhouse E, Jose a, Sherry L, et al. Development of an in vitro periodontal biofilm model for assessing antimicrobial and host modulatory effects of bioactive molecules. BMC Oral Health. 2014;14:80.
[56] Belibasakis GN, Thurnheer T, Bostanci N. Interleukin-8 responses of multi-layer gingival epithelia to subgingival biofilms: role of the "red complex" species. PLoS One. 2013;8:e81581.
[57] Dickinson BC, Moffatt CE, Hagerty D, et al. Interaction of oral bacteria with gingival epithelial cell multilayers. Mol Oral Microbiol. 2011;26:210–220.
[58] Khalaf H, Palm E, Bengtsson T. Cellular response mechanisms in *Porphyromonas gingivalis* Infection. In: Periodontitis - a useful reference. 2017. p. 45–68.
[59] Wang H-Y, Cheng J-W, Yu H-Y, et al. Efficacy of a novel antimicrobial peptide against periodontal pathogens in both planktonic and polymicrobial biofilm states. Acta Biomater. 2015;25:150–161.
[60] La VD, Howell AB, Grenier D. Anti-*Porphyromonas gingivalis* and anti-inflammatory activities of a-type cranberry proanthocyanidins. Antimicrob Agents Chemother. 2010;54:1778LP–1784.
[61] Zhou Y, Guan X, Zhu W, et al. Capsaicin inhibits *Porphyromonas gingivalis* growth, biofilm formation, gingivomucosal inflammatory cytokine secretion, and in vitro osteoclastogenesis. Eur J Clin Microbiol Infect Dis. 2014;33:211–219.
[62] Matsui a, Jin JO, Johnston CD, et al. Pathogenic bacterial species associated with endodontic infection evade innate immune control by disabling neutrophils. Infect Immun. 2014;82:4068–4079.
[63] Ramage G, Lappin DF, Millhouse E, et al. The epithelial cell response to health and disease associated oral biofilm models. J Periodontal Res. 2017;52:325–333.
[64] Subbiahdoss G, Kuijer R, W Grijpma D, et al. Microbial biofilm growth vs. Tissue integration: "The race for the surface" experimentally studied. 2009.
[65] Dwidar M, Leung BM, Yaguchi T, et al. Patterning bacterial communities on epithelial cells. PLoS One. 2013;8:e67165.
[66] Guggenheim B, Gmür R, Galicia JC, et al. In vitro modeling of host-parasite interactions: the "subgingival" biofilm challenge of primary human epithelial cells. BMC Microbiol. 2009;9:280.
[67] Thurnheer T, Belibasakis GN, Bostanci N. Colonisation of gingival epithelia by subgingival biofilms in vitro: role of "red complex" bacteria. Arch Oral Biol. 2014;59:977–986.
[68] Chin MYH, Busscher HJ, Evans R, et al. Early biofilm formation and the effects of antimicrobial agents on orthodontic bonding materials in a parallel plate flow chamber. Eur J Orthod. 2005;28:1–7.
[69] Rath H, Stumpp SN, Stiesch M. Development of a flow chamber system for the reproducible in vitro analysis of biofilm formation on implant materials. PLoS One. 2017;12:e0172095.
[70] Tolker-Nielsen T, Sternberg C. Growing and analyzing biofilms in flow chambers. Curr Protoc Microbiol. 2011;21:1B.2.1–1B.2.17.
[71] Crusz SA, Popat R, Rybtke MT, et al. Bursting the bubble on bacterial biofilms: a flow cell methodology. Biofouling. 2012;28:835–842.
[72] Bao K, Papadimitropoulos a, Akgül B, et al. Establishment of an oral infection model resembling the periodontal pocket in a perfusion bioreactor system. Virulence. 2015;6:265–273.
[73] Bao K, Belibasakis GN, Selevsek N, et al. Proteomic profiling of host-biofilm interactions in an oral infection model resembling the periodontal pocket. Sci Rep. 2015;5:15999.
[74] Cani PD. Human gut microbiome: hopes, threats and promises. Gut. 2018;67:1716–1725.
[75] Shanahan F, Van Sinderen D, O'Toole PW, et al. Feeding the microbiota: transducer of nutrient signals for the host. Gut. 2017;66:1709–1717.

npj | Biofilms and Microbiomes

www.nature.com/npjbiofilms

ARTICLE OPEN

Check for updates

# Biofilm viability checker: An open-source tool for automated biofilm viability analysis from confocal microscopy images

Sophie E. Mountcastle[1,2,6], Nina Vyas[2,6], Victor M. Villapun[3], Sophie C. Cox[3], Sara Jabbari[4], Rachel L. Sammons[2], Richard M. Shelton[2], A. Damien Walmsley[2] and Sarah A. Kuehne[2,5]✉

Quantifying biofilm formation on surfaces is challenging because traditional microbiological methods, such as total colony-forming units (CFUs), often rely on manual counting. These are laborious, resource intensive techniques, more susceptible to human error. Confocal laser scanning microscopy (CLSM) is a high-resolution technique that allows 3D visualisation of biofilm architecture. In combination with a live/dead stain, it can be used to quantify biofilm viability on both transparent and opaque surfaces. However, there is little consensus on the appropriate methodology to apply in confocal micrograph processing. In this study, we report the development of an image analysis approach to repeatably quantify biofilm viability and surface coverage. We also demonstrate its use for a range of bacterial species and translational applications. This protocol has been created with ease of use and accessibility in mind, to enable researchers who do not specialise in computational techniques to be confident in applying these methods to analyse biofilm micrographs. Furthermore, the simplicity of the method enables the user to adapt it for their bespoke needs. Validation experiments demonstrate the automated analysis is robust and accurate across a range of bacterial species and an improvement on traditional microbiological analysis. Furthermore, application to translational case studies show the automated method is a reliable measurement of biomass and cell viability. This approach will ensure image analysis is an accessible option for those in the microbiology and biomaterials field, improve current detection approaches and ultimately support the development of novel strategies for preventing biofilm formation by ensuring comparability across studies.

*npj Biofilms and Microbiomes* (2021)7:44 ; https://doi.org/10.1038/s41522-021-00214-7

## INTRODUCTION

Biofilms are defined as 'aggregates of microorganisms in which cells are embedded in a self-produced matrix of extracellular substances that are adherent to a surface'[1]. Compared with planktonic bacteria, those present in biofilms can survive harsher environments and demonstrate increased resistance to antimicrobials[2]. Biofilms account for up to 80% of implant-related infections as, unintentionally, medical implants provide excellent surfaces for formation of these 3D bacterial communities[3]. Device-related infections are particularly difficult to eradicate and often result in the need for restorative surgeries[4]. Furthermore, there is also an increased concern regarding the presence and spread of antimicrobial-resistant strains in biofilms[5]. It is therefore vital to consider these complex structures when evaluating antimicrobial activity in the development of functional biomaterials and new antibacterial approaches to tackle device-related infections.

To investigate the effect of novel antimicrobials and surface functionalisation, quantification of biofilm development and viability following such treatment is essential. Traditionally in microbiology, analysis of biofilms is performed through serial dilution of a culture to count the number of colony-forming units (CFUs), or alternatively using crystal violet stain along with spectrophotometry[6–10]. Whilst these traditional methods have their applications and advantages, a move towards more direct quantitative analyses of biofilms that reduce operator variability is recommended. Furthermore, neither CFU-plating nor crystal violet staining allow for detailed visualisation of biofilm architecture. Understanding 3D structure is important because extracellular polymeric substances (EPS) can contribute to antimicrobial resistance properties of biofilms by impeding transport of some antibiotics[11,12]. Disruption of biofilm architecture to expose cells and increase the efficacy of antimicrobial drugs is a potential approach to tackle device-related infections, and therefore is an important aspect to consider[13].

In contrast, direct imaging of biofilms using microscopy techniques provides information on their structural characteristics, which can in turn determine whether an intervention has been successful in disrupting biofilm formation. Confocal laser scanning microscopy (CLSM) selectively excites fluorescence signals from different planes within a sample, acquiring images point by point with localised laser excitation at specific wavelengths. CLSM is a useful technique as it enables 3D visualisation of biofilm structure by excluding signals from adjacent planes. A second benefit of CLSM is the versatility offered by fluorescent stains added to a sample, allowing further information to be obtained; for example, the presence of extracellular DNA, exopolysaccharides and biofilm viability. CLSM with viability staining provides high sensitivity, specificity and resolution[14]. Of the fluorescent stain protocols available, live/dead staining is a conventional method of evaluating biofilm formation in microbiology for a wide variety of applications including oral, bone and gut microbes[15–20]. A live/dead stain provides a fluorescence assay of bacterial viability, based on membrane integrity. Most commonly, SYTO® 9 acts as the green fluorescent nucleic acid stain, labelling bacteria with intact cell membranes, and propidium iodide forms the red-fluorescent nucleic acid stain, penetrating only bacteria with

[1]EPSRC Centre for Doctoral Training in Physical Sciences for Health, University of Birmingham, Edgbaston, Birmingham, UK. [2]School of Dentistry, University of Birmingham, 5 Mill Pool Way, Birmingham, UK. [3]School of Chemical Engineering, University of Birmingham, Edgbaston, Birmingham, UK. [4]School of Mathematics, University of Birmingham, Edgbaston, Birmingham, UK. [5]Institute for Microbiology and Infection, University of Birmingham, Edgbaston, Birmingham, UK. [6]These authors contributed equally: Sophie E. Mountcastle, Nina Vyas. ✉email: s.a.kuehne@bham.ac.uk

Published in partnership with Nanyang Technological University

npj nature partner journals

damaged membranes[21]. Examples of the application of CLSM and fluorescent staining to biofilms include examining *Pseudomonas aeruginosa* (*P. aeruginosa*) biofilm formation on antibiotic-loaded bone cement[19], observing the effect of antimicrobial therapy on biofilm formation in endotracheal tubes[18] and screening cinchona alkaloids for anti-biofilm activity against *Staphylococcus aureus* (*S. aureus*)[22].

Despite the varied and wide-ranging use of CLSM and live/dead staining to investigate biofilm formation, there is little consensus regarding evaluation of the resulting micrographs. Specifically, there is no consistent method applied for quantifying live/dead bacteria from the confocal images reported in the literature. Some groups use CLSM to simply visualise the biofilm and qualitatively interpret the results, or conduct manual segmentation by using a global threshold or delineating the cells in the images manually[16,23,24]. Simple segmentation methods such as these are time consuming and may result in inconsistencies due to user subjectivity. Other studies elect not to report in full their chosen segmentation algorithm or validate its accuracy[19,25–27]. One useful way of validating accuracy is to perform a sensitivity and specificity analysis that determines whether an algorithm can successfully detect a pixel that corresponds with bacteria and a pixel that corresponds with background, respectively[28]. While more robust segmentation protocols have been reported, they are not always accessible or reproducible if the method lacks detail and they may be particularly challenging to implement for non-experts. Many studies use bespoke software such as Imaris[25], COMSTAT[29], PHLIP[30] and most recently BiofilmQ[31]. These can make CLSM micrograph analysis easier to navigate through a user-interface. BiofilmQ can measure features from biofilm images to extract information such as fluorescence intensity, biofilm density and surface area. However, it is not specifically developed for cell viability measurements of biofilms, and currently there is no option for morphological operations, which were used in the macro developed in the current study. Whilst the algorithms used in some bespoke software are made available, an understanding of the settings in each package and how these impact on the data is required. These settings should be reported for a study to be repeated. Furthermore, it is necessary to report any image pre-processing as this will affect comparability across literature.

In addition to navigating the range of segmentation methods and software available, the commonly used stain for bacterial biofilm viability, the FilmTracer™ LIVE/DEAD® Biofilm Viability Kit (Invitrogen, USA)[21], can give erroneous results if images are not analysed correctly. Depending on the contrast of the red and green channel images, bacteria which are dead can appear yellow in images (due to red and green being superimposed on each other)[32,33]. A further challenge with the FilmTracer™ LIVE/DEAD® Bacterial and Biofilm Viability Kits is that propidium iodide can stain extracellular DNA that is present in biofilms[34]. Therefore, qualitative observation of live/dead stained biofilms could lead to misleading conclusions since the contrast of each channel is manually adjusted by the user. If automated image analysis is used to analyse the red and green channels separately this would give more objective quantitation with no possibility of the two channels being superimposed. Although numerous studies have published new image analysis techniques for biofilms[35–39], many microbiological studies that use image processing still do not report the exact methods used, including the type of threshold applied. Such information is critical to determining accuracy of the study and ensuring reproducibility. Ultimately this leads to the conclusion that the current suite of image processing tools available for biofilm analysis is difficult to access and cumbersome for non-specialists with no significant programming experience. This highlights a gap for an open-source image analysis tool designed specifically to assess biofilms which balances accessibility, transparency and accuracy.

This work aims to develop a robust but easy to use automated image analysis technique to quantify biofilm formation from confocal micrographs, which accounts for the errors identified with SYTO® 9 and propidium iodide stains. A new image analysis method is proposed that incorporates image pre-processing and automated thresholding, using the open-access software Fiji (ImageJ, US National Institutes of Health, Bethesda, Maryland, USA). To the authors' knowledge, no prior studies have directly compared the results of confocal micrograph image analysis with those of counting CFUs and therefore this was undertaken in the present work. Alongside method comparison, sensitivity and specificity of the automated image analysis was carried out to evaluate its accuracy. Further validation of the method was conducted on Gram-positive and Gram-negative species of different cell morphologies: *P. aeruginosa*, *Lactobacillus casei*, and a multi-species biofilm consisting of *Fusobacterium nucleatum, Actinomyces naeslundii, Streptococcus gordonii* and *Porphyromonas gingivalis*. A unique aspect of this work is the use of translationally relevant case studies to trial the automated image segmentation protocol, the results of which will also be presented. This analysis method will prove useful by ensuring reproducibility across studies, by offering a faster analysis approach than traditional microbiological methods enabling higher sample numbers, and finally by reducing human error compared with CFU-counting or manual image segmentation. Ultimately, this work will support the development of much needed approaches to prevent and treat costly infections.

## RESULTS

### Validation of image analysis protocol

To assess the reliability and accuracy of the automated protocol developed (Fig. 1), a series of analyses were performed. This included sensitivity and specificity analysis[28], a comparison with traditional microbiological techniques and the application of the protocol to a variety of bacterial species with varying morphologies (Fig. 2).

The sensitivity and specificity of the image analysis method was determined using receiver-operating characteristic (ROC) analysis (Fig. 2a). A ROC curve is a plot of sensitivity (true positive rate) versus 1 − specificity (false positive rate). The greater the algorithm's ability to correctly identify pixels in an image, the closer the curve sits to the upper left-hand corner of the graph[40]. A ROC curve lying on the diagonal reflects a performance that is no better than identifying pixels by chance. The ROC analysis in the present study demonstrated that the specificity for both red and green channels was high, with means of 99.9 and 81.7%, respectively. However, the sensitivity of the automated image analysis method in the red channel varied, ranging from 6.1 to 100.0%.

Figure 2b shows the resulting quantification of *Streptococcus sanguinis* (*S. sanguinis*) biofilm over time using the automated image analysis method developed in this work and CFU-plating combined with counting using a haemocytometer. Both methods demonstrated viability decreased with biofilm age, however, the rate at which this occurred varied significantly between the two methods. It should be noted that the traditional methods induced greater errors, with a coefficient of variation (CV) ranging from 17.0 to 78.1%, compared with 4.24 to 11.5% for image analysis, and this was likely due to the manual nature of the method. Manual analysis of CFU plating and cell counts using a haemocytometer typically result in wider errors due to the subjectivity of the user defining what is considered a cell, and from volume and dilution errors.

To confirm that the developed analysis could be performed on biofilms of species with different morphologies, the ImageJ macro was applied to 24-h *P. aeruginosa* and 7-day *L. casei*

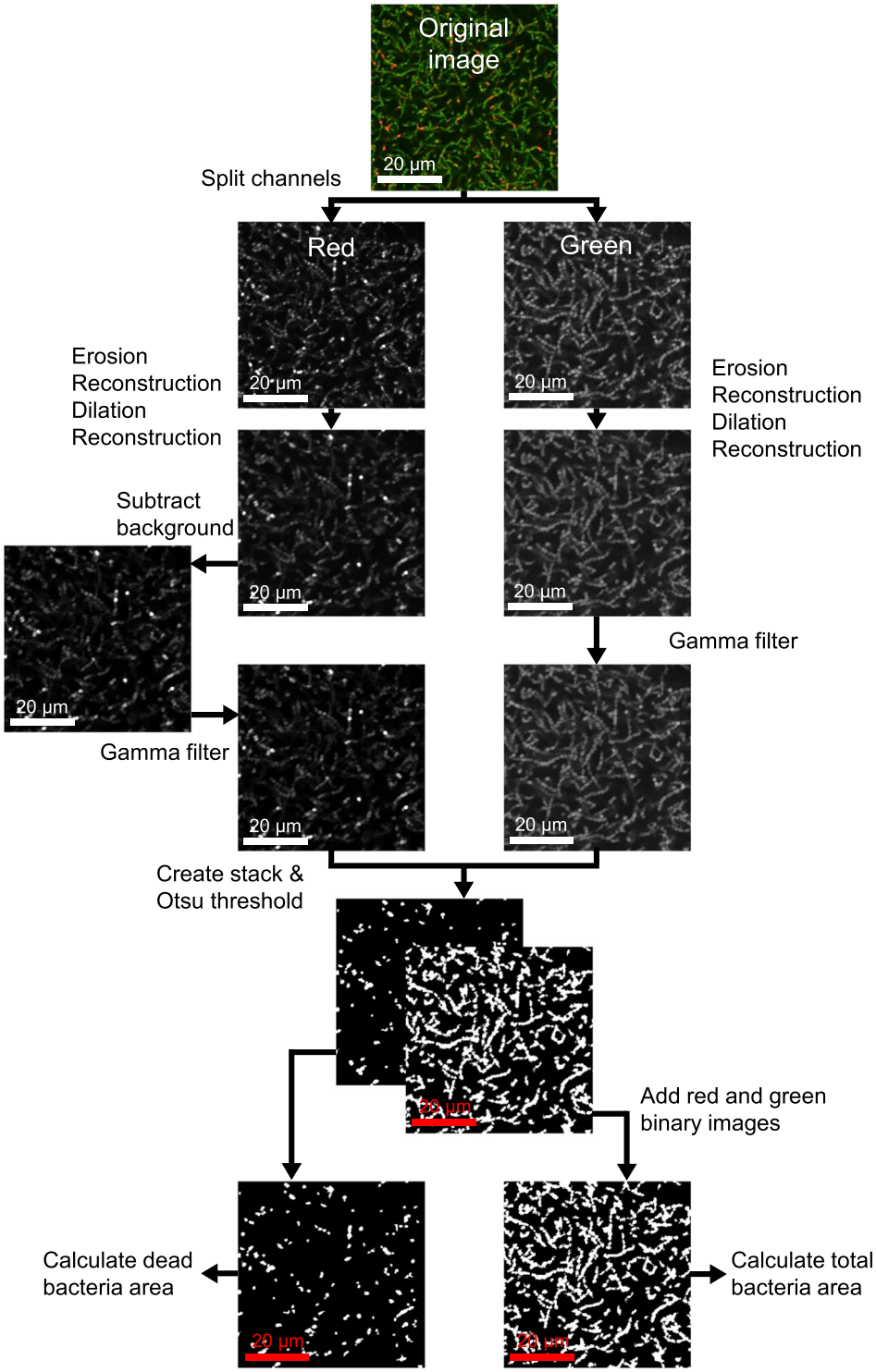


**Fig. 1 Image analysis steps used in ImageJ to calculate bacterial viability from a confocal image of biofilm with LIVE/DEAD stain.** Images taken from a representative *S. sanguinis* biofilm cultured for 48 h (20 µm scale bar). See Supplementary Information to implement the automated analysis.

biofilms, and to further challenge it, a 5-day multi-species biofilm consisting of *F. nucleatum ssp polymorphum*, *A. naeslundii*, *S. gordonii* and *P. gingivalis* (Fig. 2c–f). *L. casei* and *P. aeruginosa* were selected due to their rod-shaped cell morphologies, to contrast with the cocci-shaped *S. sanguinis*. The protocol was applied to a multi-species biofilm containing a range of morphologies to ensure it could accurately determine biofilm viability and coverage in more challenging and complex images. Figure 2c–f show that the analysis protocol successfully identified live and dead bacteria of different morphologies. Through qualitative observation of the outline of stained bacteria (Fig. 2c–f), this was evidenced by very few bacteria being incorrectly identified as background by the automated segmentation method.

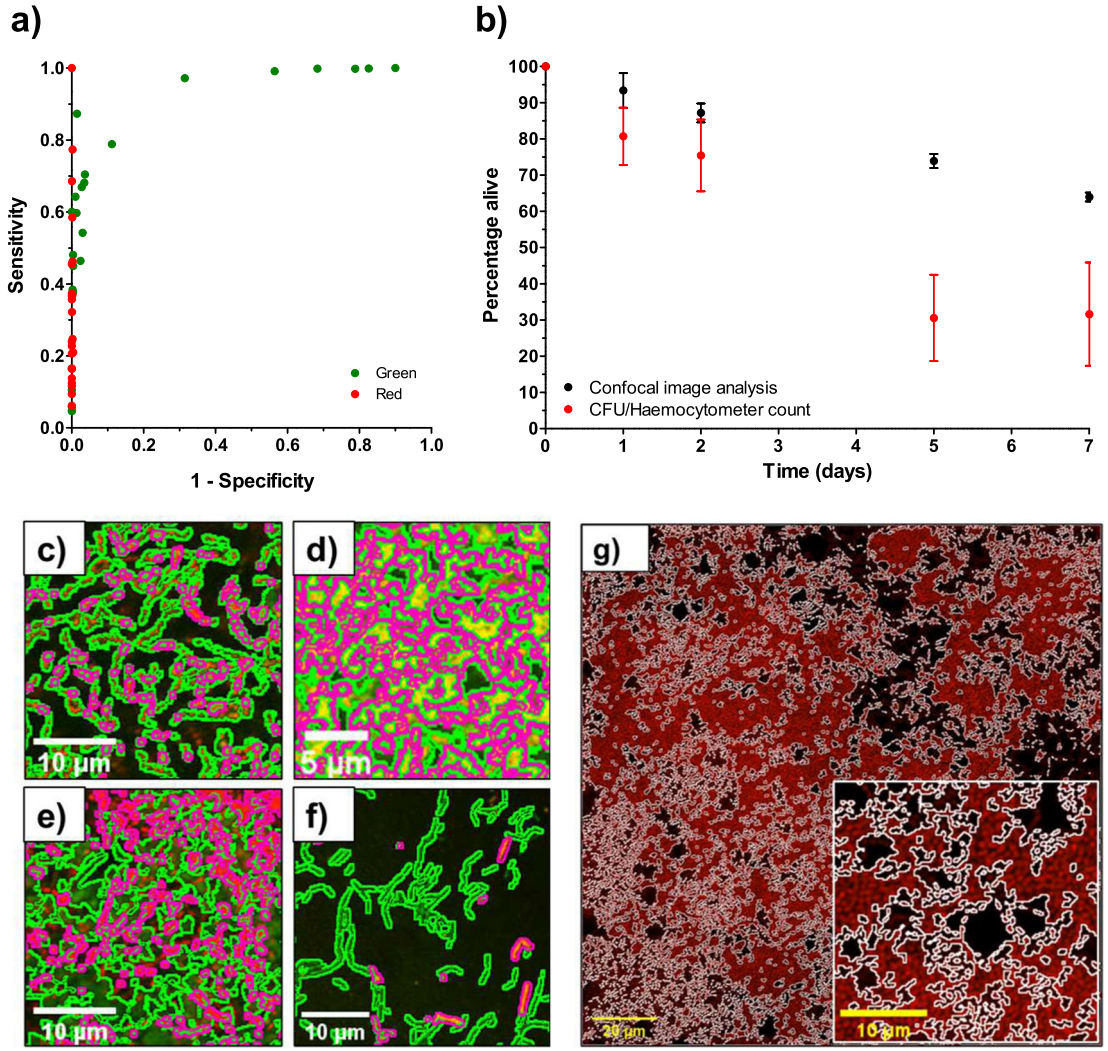


**Fig. 2 Results of validation of automatic image analysis protocol. a** ROC curve demonstrating sensitivity and specificity of the image analysis protocol. Green points represent sensitivity and specificity of the green channel (total cells) and red points represent sensitivity and specificity of the red channel (dead cells). **b** Comparison of image analysis and biological methods. Figure shows mean ± standard deviation (for image analysis, five confocal images were analysed of each of five biological replicates, $N = 5$ and for biological methods, three biological replicates were analysed, $N = 3$). To obtain the percentage viability using biological methods, live cells were counted using a serial dilution and CFU-plating. Total cell count was obtained using a haemocytometer. **c**–**f** Sample images of a variety of single-species biofilms demonstrating result of automated image analysis. The green outline indicates the total bacteria area and the magenta outline indicates the dead bacteria area. **c** *S. sanguinis* (10 µm scale bar), **d** *P. aeruginosa* (5 µm scale bar), **e** multi-species biofilm consisting of *F. nucleatum*, *A. naeslundii*, *S. gordonii* and *P. gingivalis* (10 µm scale bar), **f** *L. casei* (10 µm scale bar). **g** Representative micrograph of an *S. sanguinis* biofilm treated with 5% CPC to demonstrate the ability of the macro to handle extreme conditions (Full image 20 µm scale bar, small image 10 µm scale bar). The magenta line shows the result of the segmentation of the red channel. The resulting output from the macro is 0% viability.

It is important to ensure that any image analysis method can cope with a wide range of conditions. In the development of antimicrobial techniques and novel implant surface coatings, it is expected that conditions which include no viable cells in biofilms will be analysed. To ensure that the protocol handles such conditions, the macro was applied to *S. sanguinis* biofilms treated with the antimicrobial cetylpyridinium chloride (CPC) at bactericidal levels (Fig. 2g). The macro consistently produced results of 0% alive ($n = 6$) for all biofilms treated with CPC. This confirmed it was reliable across a range of biofilm viabilities.

### Translation of image analysis method to research applications

The aim of the present research was to develop an accurate image analysis protocol that will aid in the development of novel antimicrobial therapies and implant devices. To investigate the potential of this protocol, it was applied in three key experiments. First, to demonstrate it could provide useful data to examine the effectiveness of antimicrobial compounds, a simple mouthwash study was performed. In this experiment, a commercial mouthwash was applied to biofilms of two species: *P. aeruginosa*, a pathogen which is known to have increased antibiotic resistance[41], and the commensal oral bacteria, *S. sanguinis*[42]. Secondly, biofilms of *Staphylococcus epidermidis* (*S. epidermidis*) were grown on additively manufactured (AM) Ti-6Al-4V coupons to understand the effect of manufacturing protocols on the viability of a frequently detected pathogen in implant infections[43,44]. Finally, to demonstrate the information that can be obtained regarding the 3D architecture of biofilms, the automated protocol was applied to z-stacks taken from 1-day- and 7-day-old *S. sanguinis* biofilms, the results of which are described below.

Applying mouthwash to biofilms of two different species showcased that mouthwash had a limited effect on the biofilms of *P. aeruginosa* when compared with water-treated samples ($p = 0.93$)

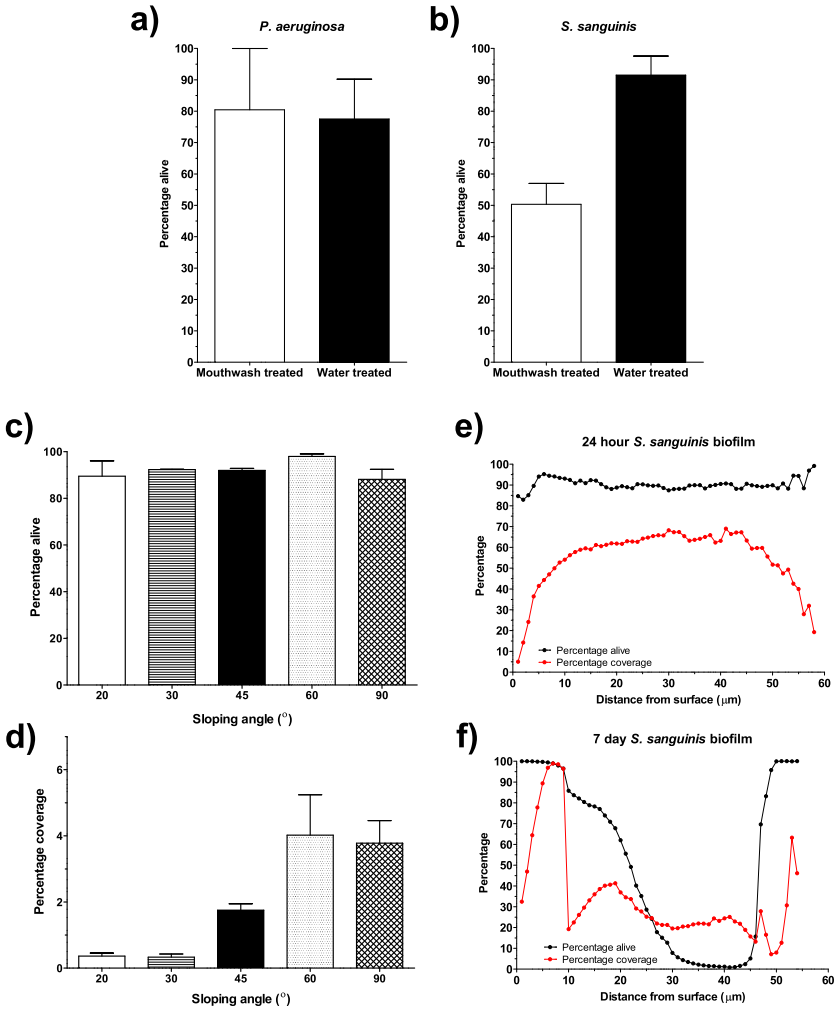


**Fig. 3 Translation of image analysis method to research applications. a**, **b** Simple mouthwash study comparing biofilms of **a** *P. aeruginosa* and **B** *S. sanguinis* treated with mouthwash or water ($n = 3$ for all conditions). **c**, **d** Analysis of *S. epidermidis* biofilms grown on additively manufactured coupons at different sloping angles: **c** Percentage alive and **d** Percentage coverage. **e**, **f** Biofilm coverage and viability with increasing distance from coverslip for **e** a 24-h biofilm of *S. sanguinis* and **f** 7-day biofilm of *S. sanguinis*. Z-stacks were taken at 1 μm increments from the surface (the first plane in which bacteria were identified), and hence the distance from the surface is equivalent to the biofilm thickness.

(Fig. 3a). Whilst there was no significant difference identified between the mouthwash-treated and water-treated biofilms of *S. sanguinis*, the *p* value was much lower ($p = 0.08$) (Fig. 3b). It is expected that a larger study would support the effectiveness of the mouthwash treatment at reducing the percentage of live bacteria in *S. sanguinis* biofilms, as evidenced by other literature[45,46]. This was not the objective of the present study, rather the aim was to demonstrate the application of the automated image analysis. The findings of this experiment agreed with other work that has highlighted the resistance of *P. aeruginosa* to a range of broad-spectrum antibiotics found in commercial mouthwashes[47,48].

A second area of research that is highly important in the field of antimicrobial resistance is the development of novel materials, coatings, and surface treatments for medical and dental implants. To showcase the applicability of the current approach in the development of novel medical devices, two properties of *S. epidermidis* biofilms on AM titanium implants manufactured with different orientations (20° to 90° from the normal plane, see Supplementary Fig. 2) were investigated, namely cell viability and coverage (Fig. 3c, d). Orientation of AM samples significantly modified the resulting average roughness from 8 μm up to 18 μm, for 20° and 90° respectively, as shown in previous works[44]. Nevertheless, the number of live bacteria expressed as a percentage of total bacteria showed no significant difference ($p = 0.07$) between surfaces (Fig. 3c). In contrast, when percentage coverage was analysed (as it relates to biomass), it demonstrated that increasing the sloping angle resulted in a significant increase in percentage coverage of the biofilm ($p = 0.02$) (Fig. 3d). The difference between viability and coverage indicated that albeit an increase in biomass developed on the surface of the samples, the percentage of living cells is not dependent on surface modification. This could be the result of the selected alloy lacking any antimicrobial effect[49], coupled with the larger surface area and shear force protection offered by the peaks and valleys present in the rougher samples, leading to more favourable growth conditions[50,51].

The analysis protocol can be used to investigate biofilm composition from coverslip to biofilm surface by applying it to each image of a confocal z-stack. In addition, the total number of pixels that correspond with bacteria (live or dead) can also be used to calculate biomass as 'percentage coverage', i.e. the number of stained pixels as a percentage of total pixels in the image. This was carried out for an *S. sanguinis* biofilm cultured for 1 and 7 days on a Thermanox coverslip (Fig. 3e, f, respectively). For the 24-h biofilm, viability remained consistent throughout, ranging between 82.9 and 99.18%. However, the coverage

increased in the centre of the biofilm, peaking at 69.0% at 41 µm from the coverslip, and decreased towards the surface, ending at 19.24% at 58 µm from the coverslip. In contrast, viability varied significantly across the 7-day biofilm. Low viability was observed in the centre, with values lower than 50% for distances between 23 to 46 µm from the coverslip surface. In contrast, high viability was detected at the coverslip interface (99%) and on the biofilm surface (100%). The reduction in viability in the centre of the biofilm may be due to nutrients being limited and unable to reach those species in the centre or could be caused by an oxygen gradient throughout the biofilm. Percentage coverage, which relates to biomass, also decreased in the centre of the older biofilm, dropping below 45% between 10 and 52 µm from the coverslip, which may have been linked to the fact that viability had decreased significantly.

## DISCUSSION

The aim of this study was to develop a method to analyse confocal micrographs of live/dead stained biofilms. The method was designed to be simple and accessible to a range of researchers that work on the development of antimicrobial strategies related to biofilms, including microbiologists and materials scientists. Therefore, the analysis protocol was written in the open-source software ImageJ and the method requires no preliminary image preparation or modification. The ImageJ macro, alongside a fully detailed description of how to execute the algorithm to enable researchers to implement this protocol, is available in Fig. 1 and the Supplementary Information. The algorithm was effective and accurate on a range of biofilms, including different bacterial morphologies, such as cocci (*S. sanguinis*) and rod-shaped (*L. casei*) bacteria, and different biofilm ages (from 24 h up to 7 days). A full workflow is provided alongside a series of validation methods in this study, and furthermore includes application of the code to translational case studies, which is an advantage compared with other literature that include analysis of CLSM micrographs of biofilms.

Over the past two decades, many researchers have attempted to tackle the problem of automated analysis of biofilm micrographs, including developing commercial and free software tools[29–31]. Depending on the size of the cells, the quality and resolution of the image, and thickness or density of the biofilm, two approaches to automated quantification can be taken: (1) by detecting and counting discrete objects or cells or (2) by making assumptions regarding the manner in which the properties of the entire image relate to the biofilm characteristics. In this study, the latter approach was taken, and the number of pixels stained red and green were used to quantify the number of viable (live) cells as a percentage of total cells. The reason for selecting this method was driven by the small cell size and common overlapping of bacteria in biofilm images, even in high-resolution CLSM micrographs. Furthermore, detecting discrete cells can be challenging if they have different morphologies. Therefore, making assumptions about the relationship between pixel count and bacteria viability ensured that the automated approach was accurate and applicable to a range of cell morphologies. The total number of pixels that correspond with bacteria (live or dead) can also be used to calculate biomass as 'percentage coverage', i.e. the number of stained pixels as a percentage of total pixels in the image.

A number of studies that utilise CLSM to analyse biofilm formation simply visualise the biofilm and report qualitative results, or conduct manual segmentation of the micrographs[16,23,24]. The challenge with these approaches makes comparison with other literature difficult due to the subjective data. Neither of these methods take into consideration any non-specific staining or extracellular matrix staining that may occur when using the FilmTracer™ LIVE/DEAD® Biofilm Viability Kit[34]. Furthermore, segmentation methods that involve manually selecting the cells in an image are time consuming and may result in inconsistent segmentation. To address these challenges, the image analysis protocol presented in this study demonstrated consistent and repeatable results. This was evidenced by a small standard deviation with a CV between 4.24 and 11.5% in the large biofilm study with over 100 images of 20 biofilms (Fig. 2b).

A further limitation of studies that implement CLSM micrograph analysis is that many elect not to report in full the chosen segmentation algorithm or validate its accuracy, negatively influencing reproducibility and comparison[19,25–27,52,53]. It is vital that the validity of an image segmentation algorithm is demonstrated across different species, on 'extreme' cases such as all-dead biofilms, and by comparing with separate techniques. In this study we carried out a series of validation steps to demonstrate that the protocol was effective and accurate. This included performing a sensitivity and specificity analysis to compare the automated results with manual segmentation of the images. This manual segmentation represented a 'ground truth' state, although it should be noted that the manual segmentation was conducted on the original images with no pre-processing and therefore background fluorescence and extracellular matrix staining had not been accounted for. The ROC study showed good sensitivity and specificity for the green channel (total bacteria), 60.3 and 81.7%, respectively, and very good specificity of 99.9% for the red channel (dead bacteria), although the sensitivity for the red channel had a wider range (Fig. 2a). This was likely to arise from the additional steps implemented to remove background noise in the red channel necessary to prevent the analysis from including red areas that were not bacteria. Reduced sensitivity in the red channel was needed due to the challenge of extracellular matrix staining that occurred and therefore the potential to underestimate the percentage of live cells[32–34]. Furthermore, the ROC curve was calculated by comparing the resulting binary images after running the automated analysis with manually segmented sections of images (determined by manually delineating all bacteria) that underwent no pre-processing. During manual segmentation it is likely that low-level background fluorescence combined with the red propidium iodide stain marking EPS, results in the 'ground truth' images used to calculate the ROC curve including pixels that are not bacteria. This also contributes to the lower sensitivity of the automated analysis in the red channel.

Very few prior studies have directly compared image analysis with traditional quantification methods. As an example of those that have, Larimer et al. (2016) compared the cell coverage determined by image analysis with cell coverage determined by measuring the optical density of the biofilm[39]. In the current study we compared cell viability determined using image analysis with that determined using CFU-plating and cell counting, which helped to build confidence in the presented approach. Figure 2b demonstrates that the overall trend in live cell percentage varied between the image analysis and manual counting methods. Using traditional techniques such as CFU-plating and counting cells using a haemocytometer resulted in larger errors as the age of the biofilm increased, rising from a CV of 17.0% at 24 h to a CV of 78.1% at 7 days. It also lead to a lower percentage of live cells at later time points compared with the automated image analysis data; for example, the mean percentage alive at 7 days calculated by image analysis was 63.9%, whereas from traditional techniques it was determined to be only 31.6%. This could have been due to the increased number of cells present in the larger, older biofilms, making counting the cells manually less accurate. Figure 2b suggests that automated image analysis was likely to be more accurate and therefore a better method to identify statistically significant variations between biofilm growth conditions when researching antimicrobial approaches. Other benefits to the image analysis method presented are detailed in Table 1.

**Table 1.** Summary of advantages and disadvantages of image analysis and CFU-plating combined with counting cell in a haemocytometer to quantify biofilm formation.

| Method | Approach | Advantages | Disadvantages |
|---|---|---|---|
| Fiji macro (ImageJ) | ■ Correct for uneven fluorescence intensities<br>■ Remove noise<br>■ Segment bacteria from background using Otsu threshold<br>■ Record number of pixels for total bacteria<br>■ Apply same process for red channel only to determine dead bacteria count. | ✓ Open-source software<br>✓ Can run macro on multiple images at once<br>✓ Time taken to run image analysis on 25 CLSM micrographs is <10 min. | ✗ Requires some data manipulation after running the automated segmentation to calculate biofilm viability from pixel count.<br>✗ Workflow may need altering to observe larger mammalian cells or for alternative staining protocols. |
| Biological methods | ■ Determine number of live cells from CFU-plating.<br>■ Determine total cell number using haemocytometer. | ✓ No specific software required<br>✓ Actual cell number determined rather than inferred from pixel number. | ✗ Time-consuming<br>✗ Resource-intensive<br>✗ Susceptible to human error<br>✗ Challenging for larger, increased density biofilms as further dilution required to analyse. |

Some of the more frequently used software packages developed specifically for biofilm analysis, such as COMSTAT and BiofilmQ, have an easy to use graphical user interface that make them popular for use. However, one main drawback of both of these packages is that they do not have options to apply filters and morphological operators as with those used in the current study[29,31], which allow for accurate detection of the bacteria in the image whilst neglecting EPS and non-specific staining, commonly found in biofilms. In addition, these software packages rely on the user deciding if pre-processing of the images is necessary, deciding which operators to apply and implementing any pre-processing, which is difficult for those with no prior knowledge of image analysis. In the present work, morphological operators and filters were included in the automated protocol to remove background fluorescence and account for potential staining of the extracellular matrix or e-DNA, particularly in the red channel. Furthermore, ImageJ is open-source and familiar to many researchers. Presenting the full macro created in this study (see Supplementary Information) enables users to adjust the gamma values, structuring element size and add or remove steps in the image pre-processing according to their data.

Numerous studies have been published that develop new image analysis methods for biofilm micrographs, however, many present several hurdles before they can be applied by non-specialists. For example, they are often created in proprietary software such as MATLAB[35–37] or in programming languages such as C++ [38], which make them difficult to use for researchers with little or no programming experience. In some studies, the chosen image segmentation technique was applied to low resolution images where individual bacteria were not visible[39]. In the present research, high resolution (x40 magnification, numerical aperture 1.30) images were used to ensure the segmentations were accurate. Some published studies that use open-source software have not included the code to allow for easy replication by other scientists wishing to use their method. One of the key strengths of this work is that a copy of the code, instructions on how to implement it and an overview of the image analysis protocol are all provided to ensure reproducibility (see Fig. 1 and Supplementary Information)[14]. This allows for users to understand the code and easily modify it to fit the data being analysed. For example, if a different staining protocol is used, the pre-processing steps can be removed or adjusted so as not to account for the issues identified with the FilmTracer™ LIVE/DEAD® Biofilm Viability Kit. A further strength of the protocol presented is that it has low computational time, with 25 micrographs analysed in less than 10 min (Table 1). This allows for an increased number of samples to be analysed and can ultimately improve the robustness of studies investigating antimicrobial techniques to reduce implant-related infection.

There are, however, several limitations to using a method based on CLSM micrographs. Firstly, it is not possible to evaluate the entire biofilm at once; in this study imaging was performed at x40 magnification to obtain high resolution images of individual bacteria in the biofilm. Averaging data from across the biofilm sample and increasing the number of repeats can limit the impact of this. In this work, five images were taken across five samples for each biofilm condition in Fig. 2b. As the analysis protocol in ImageJ can process many images quickly, increasing the number of samples to account for the limited range of the confocal images was straightforward. Linked to this, a second limitation of the work presented its application to poorer quality micrographs. For example, if a sample is not completely flat when imaged using the CLSM, an area of the image may be over or under exposed and this can affect the resulting analysis. It is advisable to take appropriate steps to ensure optimal imaging of the samples. These include ensuring the fluorescent dye has sufficient signal to avoid noise caused by increasing the contrast artificially, ensuring the sample stays horizontal during sample preparation and imaging using a high numerical aperture/magnification to obtain high resolution images. Individual bacteria should be visible in the micrographs being analysed and it is recommended that a minimum magnification of x40 be used to implement the described method. It should also be noted that the results of the analysis will be more subjective if the user selects the location on the biofilm for the image to be taken. User subjectivity can be reduced significantly by taking a high number of images at random locations across the biofilm; a minimum of five per sample is recommended. A final challenge where this workflow demonstrated limitations was that the macro had been tailored specifically for bacterial biofilms and for fluorescent images that were stained with the FilmTracer™ LIVE/DEAD® Biofilm Viability Kit. For this reason, the additional steps taken to reduce the error caused by SYTO® 9 would affect the results if a different fluorescent stain is used by over-reporting viability. Whilst there is potential for the macro to be applied to other confocal images, the workflow may need altering to examine larger mammalian cells or alternative staining protocols. However, this should be possible for users with some image analysis experience, as each step of the macro has been described within the code.

Despite the limitations of the proposed approach, it is important to reiterate that CLSM and automated micrograph analysis can prove very useful for researchers working on antimicrobial strategies. The study of antimicrobial strategies to tackle device-related infections is a vital area of research due to

the global challenge of antimicrobial resistance[54,55]. Comprehensive efforts are needed to minimise the pace of resistance by studying novel antimicrobial agents and much research is being conducted to develop novel antimicrobial techniques[56]. Current reported image analysis methods for CSLM images of biofilms do not often demonstrate their application to a range of translational research. In the present work, the protocol was applied to three key areas that can benefit from automated CLSM micrograph analysis. The effect of antimicrobial compounds being developed on biofilms is highly important, given the increased resistance shown by bacteria in these complex 3D environments, as well as the knowledge that most bacteria exist in biofilm communities[57]. This is particularly crucial in the oral field, where broad-spectrum antibiotics are used in consumer products, such as toothpaste and mouthwash (e.g. chlorhexidine and CPC) and in the clinic to treat infection (e.g. amoxicillin and metronidazole)[58–61]. Applying the image analysis protocol to a small study on commercial mouthwash demonstrated that *P. aeruginosa* was resistant to the mouthwash. Studies that have previously reported the effect of broad-spectrum antimicrobials on oral pathogens typically identify the minimum inhibitory concentration (MIC) using a CFU-plating technique, measure optical density or report zones of inhibition[47,60]. However, these methods rely on individual interpretation so may be subjective, provide limited information on cell viability and typically result in high standard deviations for small sample numbers. Utilising the proposed analysis protocol in research to investigate new antimicrobial compounds would be effective at identifying potential novel therapeutics. It has benefits over traditional techniques as it produced low error from small sample numbers; in the present study the mean CV was 26.2% from $n = 3$. Furthermore, automated segmentation would ensure reproducibility and comparability across the literature.

A second area of research where preventing infection is paramount in implants and medical devices. Infection of implants can result in costly restorative surgeries and can also increase the failure rate of subsequent implant placement[62]. A specific example comes in the form of AM or bespoke implantable devices. These technologies are capable of producing personalised complex geometries while introducing features to enhance osseointegration (a structural and functional connection with the natural bone), reduce stress shielding and incorporate therapeutically loaded materials[63–65]. Nevertheless, clinical cases requiring such devices are commonly associated with complex interventions, typically arising from traumatic injuries, which may significantly raise infection rates by up to 23–40% for personalised cranioplasties[66,67]. Thus, much research is being conducted to reduce the occurrences of biofilm-related implant infections. One strategy to limit colonisation and proliferation of bacterial species results from careful selection of surface finish for AM materials to ensure the implant allows for osseointegration but prevents biofilm formation[44]. Villapún et al. (2020) demonstrated that in situ roughness control can be achieved through changing the orientation at which an implant is manufactured, with maximum mammalian cell adhesion and minimum *S. epidermidis* growth for printing angles between 20° to 30° to the normal plane[44]. To further assess the applicability of the CSLM image analysis protocol, Ti-6Al-4V coupons were AM and *S. epidermidis* biofilms were grown on the coupons[44]. The resulting biofilms were stained, imaged and two properties investigated through the image analysis protocol, namely viability (percentage alive) and biomass (percentage coverage), Fig. 3c, d, respectively. The percentage of live cells showed no significant changes with sloping angle modification; however, it was determined that an increase in sloping angle resulted in a rise in biomass for angles higher than 30°. This indicated that the growth of *S. epidermidis* biofilm was constrained, however there was no potential antimicrobial effect enacted from the metallic surface. The rise in biomass concurred with crystal violet and confocal image results reported by Villapún et al. (2020), while the lack of contact killing was expected from a bacteriostatic alloy such as Ti-6Al-4V[44]. Crystal violet staining can complicate the analysis of biofilm formation and potentially introduce artefacts during the recovery of the dye[68]. In contrast, confocal imaging is a more versatile method that can quantify biofilm viability and biomass accurately. The current automated method allows for subjectivity to be removed when interpreting CLSM micrographs and can generate additional information regarding cell viability when compared with crystal violet staining methods. Whilst viability did not change with surface roughness in this experiment, viability is a key parameter to obtain in future studies of this nature, where surface functionalisation may induce a bactericidal response that would not be picked up from crystal violet staining alone.

Finally, the translation of the presented method has a further application investigated in this research. One of the advantages of CLSM imaging is that it can generate an understanding of the 3D structure of a biofilm using z-stacks. Not only can this provide information about biofilm thickness and biomass, but the application of the image analysis protocol can elucidate information about biofilm composition throughout. Figure 3e, f show the viability and percentage coverage of an image stack taken of 1-day-old and 7-day-old *S. sanguinis* biofilms. For the younger biofilm, the percentage of live cells remained consistent and above 80% throughout its depth. However, in comparison the viability of the 7-day-old biofilm was reduced significantly in the centre and increased towards the surface. This could have been due to limited nutrients reaching the centre of the biofilm, combined with an oxygen gradient that increased towards the surface, thus resulting in cell death. The reduced coverage identified in the centre of the 7-day biofilm compared with the 24-h biofilm could be explained due to biofilm age. More mature biofilms that have increased EPS compared to early-stage biofilms may prevent the live/dead stain diffusing through to the centre, and this may explain the reduced coverage at the centre of the biofilms. Gaining an insight into the 3D structure of a biofilm, combined with information on viability, can enhance the understanding of the effect of antimicrobial compounds and materials. CLSM is an optimal tool for this as it has a large vertical range that can image a biofilm of up to 60 µm thickness, and fluorescence staining can provide information on viability. Applying the automated method described in this study to biofilms grown on modified surfaces could provide further information on how the modification is affecting the biofilm structure throughout. Gaining an understanding of biofilm composition is especially important when studying implant-related infections. This method could be applied to biofilms formed on modified implant surfaces to quantify antimicrobial effects. The advantage of the proposed segmentation method is that multiple images can be analysed very quickly and consistently, as well as ensuring each image within a single z-stack is treated the same, increasing comparability across samples.

In summary, this paper presents an image analysis protocol for quantifying CLSM micrographs of live/dead stained biofilms. The protocol was validated by comparing with other methods and on different species, and its use as an adjunct to traditional microbiology techniques was demonstrated, for example to support results from semi-quantitative methods such as crystal violet staining. Importantly, the method can be translated to antimicrobial drug and surface modification testing in many different industries and research fields. The key advantages of this protocol are that it is written in open-source software, is easy to use, transparent in function and is modifiable unlike other available software. This makes it a useful tool for those with different research backgrounds to enable quantitative analysis of biofilm viability to be performed. It has been demonstrated that the current approach is a reliable measurement of biofilm growth and cell viability assessment, critical for the development and

analysis of novel antimicrobial strategies. Ultimately, this work will support the development of much needed approaches to prevent and treat costly infections.

## METHODS

All chemicals are Sigma Aldrich (Dorset, UK) unless otherwise specified.

### Artificial saliva preparation

Artificial saliva was prepared by adding the following sequentially to 1 L of reverse osmosis (RO) water, stirring throughout:[69]

- 0.25 g/L sodium chloride (NaCl)
- 0.2 g/L potassium chloride (KCl)
- 0.2 g/L calcium chloride ($CaCl_2$)
- 2 g/L yeast extract
- 1 g/L lab lemco powder
- 2.5 g/L hog gastric mucin (Type III, partially purified)
- 5 g/L protease peptone

The solution was stirred for 1 h at room temperature (25 °C), then autoclaved to sterilise. After autoclaving, 1.25 mL of 40% (w/v) sterile-filtered urea was added (0.22 µm filter). The artificial saliva was wrapped in foil to exclude light and prevent protein degradation. Artificial saliva was stored at 4 °C and used no later than 1 week after preparation.

### *S. sanguinis* biofilm growth

Frozen stock of *S. sanguinis* (ATCC 10556) was streaked onto a tryptone soya agar (TSA) plate and incubated at 37 °C, 5% $CO_2$ for 48 h. Using the colonies grown on the agar plate, an overnight culture of *S. sanguinis* was prepared in 5 mL brain heart infusion (BHI) broth and incubated at 37 °C overnight, agitating at 100 rpm for the duration. A serial dilution in BHI broth containing 1% sucrose (w/v) was performed with the overnight culture, from $10^9$ (an optical density of ~0.5) to $10^3$ cells/mL. Individual Thermanox coverslips (Nunc, Thermo Fisher Scientific) were placed in the bottom of each well in 24-well culture plates (Nunc, Thermo Fisher Scientific). Prior to adding the planktonic culture, 1 mL of artificial saliva was added to each well containing a cover slip and left for 15 min before being removed; this was to aid initial adhesion of the bacteria. Subsequently, *S. sanguinis* monospecies biofilms were prepared by adding 1 mL of the $10^3$ dilution to each well containing a coverslip. The plates containing the biofilms were incubated for up to 7 days at 37 °C, 5% $CO_2$, shaking at 100 rpm, with a change in BHI broth every 24 h, to ensure a well-established biofilm had developed. At 0, 1, 3, 5 and 7 days, analysis of biofilm growth was performed.

### Cell counting

Any remaining BHI broth from the *S. sanguinis* biofilms was removed from each well and each coverslip with biofilm was placed in 5 mL of fresh BHI broth in a universal tube. The bacteria were removed from the coverslip by sonication in an ultrasonic cleaner (In-Ceram, Vitasonic) for 10 min at 50–60 Hz, followed by agitation using a vortex mixer for 5 min. A serial dilution was performed using the Miles and Misra method to count the number of CFUs[10]. This enabled an estimation of the number of live cells found in the biofilm. To quantify the total number of cells in each biofilm, 10 µL of the lowest dilution from the serial dilution was transferred to a haemocytometer and the number of bacteria were counted in each of the corner squares.

### Fluorescent staining

For live/dead staining of *S. sanguinis* biofilms, any remaining broth was removed from each well and five coverslips were transferred to a fresh 24-well plate. A working solution of fluorescent stains was prepared by adding 3 µL of SYTO® 9 stain and 3 µL of propidium iodide stain (FilmTracer™ LIVE/DEAD® Biofilm Viability Kit, Invitrogen, USA) to 1 mL of filter-sterilised water in a foil-covered container. About 200 µL of staining solution was added onto each biofilm sample, gently so as not to disturb the biofilm. Samples were incubated for 30 min at room temperature, protected from light, before being rinsed with 200 µL filter-sterilised water. Each coverslip was then placed face up onto a clean, dry microscope slide and a drop of mounting medium added (ProLong Gold Antifade, ThermoFisher Scientific, Massachusetts, USA). A 22 mm diameter glass coverslip was used to fix the sample in place[70]. Samples were stored protected from light at room temperature (25 °C).

### Confocal laser scanning microscopy (CLSM)

Samples were imaged with CLSM (LSM 700, Zeiss, Germany) using a x40 oil immersion objective (Zeiss Objective EC Plan-Neofluar 40X/1.30 Oil DIC M27, FWD = 0.21 mm). The two stains were first imaged separately to control for any cross bleed between channels. The excitation/emission was 488 nm/<550 nm for SYTO® 9 and 555 nm/>550 nm for propidium iodide. Five random locations were scanned on each biofilm sample, resulting in 25 total images for each experimental condition. Three z-stacks were taken for each condition to calculate the biofilm thickness and for 3D visualisation and analysis. Z-stacks were taken at 1 µm increments from the surface (the first plane in which bacteria were identified).

### Image analysis

The percentage of viable and dead bacteria in each image was determined from the CLSM images. The percentage of viable bacterial was evaluated by calculating the number of pixels corresponding with the total bacteria in the image (green + red), then calculating the number of pixels corresponding with the dead (red) bacteria in the image, and finally subtracting to find the number of pixels corresponding with live bacteria. The live bacteria were quantified as a percentage of the total bacteria in each image. The image analysis method was carried out using Fiji (ImageJ, US National Institutes of Health, Bethesda, Maryland, USA) (Fig. 1). This was chosen due to it being open-source software, and therefore freely available. It should be noted that this macro calculates viability based on the assumption that the image contains a single-species biofilm, and therefore the area of red and green bacteria are proportional to the number of red and green bacteria, respectively. It is still possible to use this macro to analyse multi-species biofilms, although the output should be considered as percentage of live cell area, rather than viability.

*Workflow*.

1. First, the green and red channels were separated.
2. A series of erosion, reconstruction and dilation steps were performed on each channel using a disk structuring element of size 3.
3. An additional step was applied to the red channel to compensate for the staining of extracellular DNA that can result in under-estimation of the number of live cells[34]. The 'Subtract Background' command was applied to the red channel. This is based on a 'rolling ball' algorithm and removes smooth continuous backgrounds from images[71].
4. A non-linear histogram adjustment was applied to both channels using the Gamma command to correct for uneven fluorescence intensities. This allowed faint bacteria to become brighter, while the bright bacteria remained at the same intensity. The gamma value was set at 1.5.
5. The resulting images were pulled into a stack and segmented using Otsu's threshold, with the threshold value selected based on the histogram from both images[37].
6. The number of white pixels in the red channel was recorded from the segmented images to determine the area of dead bacteria.
7. The binary images were combined, and the total number of white pixels was recorded to determine the area of all bacteria.
8. Finally, the total area of bacteria and area of red bacteria were used to determine the percentage of viable cells. The area of all pixels can also be utilised to determine the percentage coverage of the image, which can be a useful alternative to measuring biofilm mass.

### Sensitivity and specificity analysis

A ROC curve is a performance measurement for classification problems[72]. It defines how well a model is capable of distinguishing between classes; in the current study it defined how accurate the automated process was at determining when a pixel was green or when a pixel was red. The true positive rate (TPR) or sensitivity was plotted on the y-axis and the false positive rate (FPR) or '1 – specificity' was plotted on the x-axis[72]. To determine the 'ground truth', small sections of confocal micrographs of *S. sanguinis* biofilms were selected (three sections per image, for a total of eight images) and manually segmented in Fiji (by manually delineating all bacteria in each image) (ImageJ, US National Institutes of Health, Bethesda,

Maryland, USA). The eight images included two images from each timepoint (1, 2, 5 and 7-day biofilms). The automated image analysis script was run on the 24 image sections and the resulting segmentation was compared with the 'ground truth' segmentation results using Eqs. 1–3:

$$\text{TPR or Sensitivity} = \frac{\text{Number of true positive pixels}}{\text{Number of true positive pixels} + \text{Number of false negative pixels}} \quad (1)$$

$$\text{Specificity} = \frac{\text{Number of true negative pixels}}{\text{Number of true negative pixels} + \text{Number of false positive pixels}} \quad (2)$$

$$\text{FPR} = 1 - \text{Specificity} = \frac{\text{Number of false positive pixels}}{\text{Number of true positive pixels} + \text{Number of false positive pixels}} \quad (3)$$

All calculations were made in MATLAB (R2018a, MathWorks Inc., USA).

## Validation of image analysis protocol on single-species biofilms

P. aeruginosa *biofilm growth*. A frozen stock of PA01-N was used to grow *P. aeruginosa* colonies on BHI agar at 37 °C, 5% $CO_2$. Overnight cultures were grown by inoculating 5 mL of BHI broth with three colonies of PA01 and incubating at 37 °C, continuously shaking at 100 rpm for 18 h. The overnight culture was diluted using BHI broth to an optical density of 0.01 (at 600 nm), of which, 1 mL was placed in a well of a 24-well plate containing a coverslip (13 mm diameter, Thermo Scientific™ Nunc™ Thermanox™) and was performed in triplicate. The plate was then incubated for 3 h at 37 °C, shaking at 80 rpm to allow cells to adhere to the coverslip. The culture was removed from the wells and replaced with 1 mL of BHI broth, which was incubated for 24 h at 37 °C, shaking at 80 rpm. The fluorescent staining protocol was conducted as described above.

*Multi-species* F. nucleatum *ssp. polymorphum biofilm growth*. The multi-species biofilm consisted of the strains *F. nucleatum* (ATCC 10953), *A. naeslundii* (DSM 17233), *S. gordonii* (NCTC 7865) and *P. gingivalis* (W83). Overnight cultures of *F. nucleatum* were prepared in Schaedler Anaerobic broth and grown anaerobically at 37 °C. *A. naeslundii*, *P. gingivalis* and *S. gordonii* cultures were prepared in BHI broth. Bacteria were grown anaerobically at 37 °C, except *S. gordonii*, which was grown at 37 °C in 5% $CO_2$. The overnight cultures were diluted with PBS (0.01 M) to an optical density of 0.5 for *S. gordonii* and 0.2 for all other species (at 600 nm). To form the biofilms, 500 µL of *A. naeslundii* and *S. gordonii* were pipetted into a well of a 24-well plate onto a coverslip (13 mm diameter, Thermo Scientific™ Nunc™ Thermanox™), and incubated with 500 µL of artificial saliva for 24 h at 37 °C. The planktonic culture was then replaced with 500 µL of *F. nucleatum* and 500 µL of artificial saliva and cultured for a further 24 h. Finally, the planktonic culture was replaced with 500 µL of *P. gingivalis* and 1.5 mL of artificial saliva. Biofilms were incubated at 37 °C until 5 days old.

L. casei *biofilm growth*. For the *L. casei* (NCTC 16341) biofilms, frozen stock of *L. casei* was streaked onto a De Man, Rogosa and Sharpe (MRS) agar plate and incubated at 37 °C, 5% $CO_2$ for 48 h. Using the colonies grown on the agar plate, an overnight culture of *L. casei* was prepared in 10 mL MRS broth and incubated at 37 °C overnight, agitating at 100 rpm for the duration. A serial dilution in MRS broth was performed with the overnight culture, from $10^9$ to $10^3$ cells/mL. Individual Thermanox coverslips (Nunc, Thermo Fisher Scientific) were placed in the bottom of each well in 24-well culture plates (Nunc, Thermo Fisher Scientific). One microlitre of the $10^3$ dilution was added to each well containing a coverslip. The plates containing the biofilms were incubated for 7 days at 37 °C, 5% $CO_2$, shaking at 100 rpm, with a change in MRS broth every 48 h. The fluorescent staining protocol was conducted as described above.

## Validation of protocol on all-dead biofilms

Five 2-day-old biofilms of *S. sanguinis* (grown as detailed above) were treated with the antimicrobial CPC (0.05% w/v) to act as a negative control for cell viability to test the image analysis protocols. One microlitre of 0.05% (w/v) CPC was added to biofilms for 5 min before fluorescent staining. As well as image analysis, a serial dilution and plating was performed to conform the viability of the antibiotic-treated biofilm. CPC treatment reduced the mean number of cells from 19 million CFU/mL to 1800 CFU/mL. Hence, the images generated under the confocal could be assumed to be 99.99% dead for the purpose of validating the image analysis protocol.

## Mouthwash study

*P. aeruginosa* (strain PA01-N) and *S. sanguinis* (ATCC 10556) were cultured overnight in Tryptone Soya broth and BHI broth, respectively. Each culture was diluted to ~$10^3$ cells/mL. Individual Thermanox coverslips (Nunc, Thermo Fisher Scientific) were placed in the bottom of each well in 24-well culture plates (Nunc, Thermo Fisher Scientific). Prior to adding the planktonic culture, 1 mL of artificial saliva was added to each well containing a cover slip and left for 15 min before being removed. To grow the monospecies biofilms, 2 mL of diluted culture was added to each well and the plate was incubated at 37 °C, shaking at 40 rpm for 48 h. After incubation, the broth was removed, and the coverslips (with biofilms adhered) were placed in a clean 24-well plate. One microlitre of filter-sterilised Listerine® was used to rinse the biofilms by immersing them for 1 min. For the control group, the biofilms were rinsed with 1 mL sterile water for the same duration. The biofilms were then stained and imaged as described above.

## Biofilm formation on AM materials

*Base material manufacturing*. Ti-6Al-4V 10 x 10 x 3 mm coupons with an array of sloping angles (20, 30, 45, 60 and 90°) were fabricated with a laser powder bed fusion additive manufacture system (RenAM 500 M, Renishaw PLC, UK). A powder layer thickness of 30 µm, laser power of 200 W, a point distance of 55 µm, exposure time of 50 µs, a hatch distance of 0.105 mm and a spot size of 70–75 µm were selected[44].

*Bacterial colonisation assays*. Bacterial colonisation on AM sample surfaces was studied by culturing *S. epidermidis* (ATCC 12228) biofilms. Samples were degreased with acetone, disinfected by autoclaving, immersed in pure ethanol for 5 min and dried under UV light. An overnight culture of *S. epidermidis* was diluted in sterile Mueller Hinton broth to a density of ~$10^3$ CFU/mL and 1 mL was inoculated onto a 24-well plate containing the samples. After 24 h, all samples were moved to a new 24-well plate, washed gently three times with 10 mM phosphate buffered saline (PBS) and fixed with 2.5% (v/v) glutaraldehyde in PBS for 1 h[44].

*Bacterial imaging*. One sample for each sloping angle was washed gently three times with 10 mM PBS. Samples were stained with 200 µL of SYTO® 9 and propidium iodide solution (FilmTracer™ LIVE/DEAD® Biofilm Viability Kit, Invitrogen, USA) and incubated for 30 min. Imaging was carried out using a Zeiss LSM 710 confocal microscope (Carl Zeiss GmbH, Germany) at x10 magnification[44].

## Statistical analysis

All statistical analyses were conducted in GraphPad Prism (v. 5.03). For the mouthwash study, a paired *t*-test was conducted to compare the two conditions: mouthwash-treated and water-treated. For the AM material study, a Kruskal–Wallis test (one-way ANOVA) was used to determine any significant differences between the sloping angles. For all analyses, $p < 0.05$ was considered statistically significant.

## Reporting Summary

Further information on research design is available in the Nature Research Reporting Summary linked to this article.

## DATA AVAILABILITY

The datasets used and/or analysed during the current study are available from the corresponding author on reasonable request.

## CODE AVAILABILITY

The macro is available from: https://github.com/sophie-mountcastle/Biofilm-Viability-Checker/.

Received: 8 September 2020; Accepted: 12 March 2021;
Published online: 14 May 2021

## REFERENCES

1. Flemming, H. C. et al. Biofilms: an emergent form of bacterial life. *Nat. Rev. Microbiol.* **14**, 563–575 (2016).
2. Mah, T. F. C. & O'Toole, G. A. Mechanisms of biofilm resistance to antimicrobial agents. *Trends Microbiol.* **9**, 34–39 (2001).
3. Khatoon, Z., McTiernan, C. D., Suuronen, E. J., Mah, T.-F. & Alarcon, E. I. Bacterial biofilm formation on implantable devices and approaches to its treatment and prevention. *Heliyon* **4**, e01067 (2018).
4. Lebeaux, D., Ghigo, J.-M. & Beloin, C. Biofilm-related infections: bridging the gap between clinical management and fundamental aspects of recalcitrance toward antibiotics. *Microbiol. Mol. Biol. Rev.* **78**, 510–543 (2014).
5. Høiby, N., Bjarnsholt, T., Givskov, M., Molin, S. & Ciofu, O. Antibiotic resistance of bacterial biofilms. *Int. J. Antimicrob. Agents* **35**, 322–332 (2010).
6. Haney, E. F., Trimble, M. J., Cheng, J. T., Vall,, Q. & Hancock, R. E. W. Critical assessment of methods to quantify biofilm growth and evaluate antibiofilm activity of host defence peptides. *Biomolecules* **8**, 29 (2018).
7. Stiefel, P. et al. Is biofilm removal properly WWome@1234? Comparison of different quantification methods in a 96-well plate system. *Appl. Microbiol. Biotechnol.* **100**, 4135–4145 (2016).
8. Shukla, S. K. & Rao, T. S. An improved crystal violet assay for biofilm quantification in 96-well microtitre plate. Preprint at *bioRxiv* https://doi.org/10.1101/100214 (2017).
9. Zhou, X. & Li, Y. *Atlas of Oral Microbiology: From Healthy Microflora to Disease* (Elsevier Inc., 2015).
10. Miles, A. A., Misra, S. S. & Irwin, J. O. The estimation of the bactericidal power of the blood. *J. Hyg.* **38**, 732–49 (1938).
11. Donlan, R. M. Biofilms: microbial life on surfaces. *Emerg. Infect. Dis.* **8**, 881–890 (2002).
12. Díaz-Pascual, F. et al. Breakdown of vibrio cholerae biofilm architecture induced by antibiotics disrupts community barrier function. *Nat. Microbiol.* **4**, 2136–2145 (2019).
13. Rabin, N. et al. Biofilm formation mechanisms and targets for developing antibiofilm agents. *Future Med. Chem.* **7**, 493–512 (2015).
14. Drago, L. et al. How to study biofilms after microbial colonization of materials used in orthopaedic implants. *Int. J. Mol. Sci.* **17**, 293 (2016).
15. Welch, K., Cai, Y. & Strømme, M. A method for quantitative determination of biofilm viability. *J. Funct. Biomater.* **3**, 418–431 (2012).
16. Oliveira, F., Lima, C. A., Brás, S., França, Â. & Cerca, N. Evidence for inter- and intraspecies biofilm formation variability among a small group of coagulase-negative staphylococci. *FEMS Microbiol. Lett.* **362**, fnv175 (2015).
17. Tresse, O., Lescob, S. & Rho, D. Dynamics of living and dead bacterial cells within a mixed-species biofilm during toluene degradation in a biotrickling filter. *J. Appl. Microbiol.* **94**, 849–855 (2003).
18. Fernández-Barat, L. et al. Direct analysis of bacterial viability in endotracheal tube biofilm from a pig model of methicillin-resistant Staphylococcus aureus pneumonia following antimicrobial therapy. *FEMS Immunol. Med. Microbiol.* **65**, 309–317 (2012).
19. Neut, D., Hendriks, J. G. E., Van Horn, J. R., Van Der Mei, H. C. & Busscher, H. J. Pseudomonas aeruginosa biofilm formation and slime excretion on antibiotic-loaded bone cement. *Acta Orthop. Scand.* **76**, 109–114 (2005).
20. Reichhardt, C. & Parsek, M. R. Confocal laser scanning microscopy for analysis of Pseudomonas aeruginosa biofilm architecture and matrix localization. *Front. Microbiol.* **10**, 677 (2019).
21. Thermo Fisher Scientific. *Filmtracer LIVE/DEAD Biofilm Viability Kit* (Thermo Fisher Scientific, accessed 2 July 2019); https://www.thermofisher.com/order/catalog/product/L10316?SID=srch-srp-L10316.
22. Skogman, M. E. et al. Evaluation of antibacterial and anti-biofilm activities of cinchona alkaloid derivatives against Staphylococcus aureus. *Nat. Prod. Commun.* **7**, 1173–1176 (2012).
23. Vickery, K., Pajkos, A. & Cossart, Y. Removal of biofilm from endoscopes: evaluation of detergent efficiency. *Am. J. Infect. Control* **32**, 170–176 (2004).
24. Fricke, K. et al. Atmospheric pressure plasma: a high-performance tool for the efficient removal of biofilms. *PLoS ONE* **7**, e42539 (2012).
25. Chávez de Paz, L. E., Hamilton, I. R. & Svensäter, G. Oral bacteria in biofilms exhibit slow reactivation from nutrient deprivation. *Microbiology* **154**, 1927–1938 (2008).
26. Schwarz, F. et al. Influence of plaque biofilm removal on reestablishment of the biocompatibility of contaminated titanium surfaces. *J. Biomed. Mater. Res. Part A* **77A**, 437–444 (2006).
27. Cruz, P. C. et al. The effectiveness of chemical denture cleansers and ultrasonic device in bio film removal from complete dentures. *J. Appl. Oral. Sci.* **19**, 668–673 (2011).
28. Ahirwar, A. Study of techniques used for medical image segmentation and computation of statistical test for region classification of brain MRI. *Int. J. Inf. Technol. Comput. Sci.* **5**, 44–53 (2013).
29. Heydorn, A. et al. Quantification of biofilm structures by the novel computer program COMSTAT. *Microbiology* **146**, 2395–2407 (2000).
30. Mueller, L. N., de Brouwer, J. F., Almeida, J. S., Stal, L. J. & Xavier, J. B. Analysis of a marine phototrophic biofilm by confocal laser scanning microscopy using the new image quantification software *PHLIP. BMC Ecol.* 6(1), (2006).
31. Hartmann, R. et al. Quantitative image analysis of microbial communities with BiofilmQ. *Nat. Microbiol.* **6**, 151–156 (2021).
32. Zhang, K. et al. Effect of quaternary ammonium and silver nanoparticle-containing adhesives on dentin bond strength and dental plaque microcosm biofilms. *Dent. Mater.* **28**, 842–852 (2012).
33. Chebath-Taub, D., Steinberg, D., Featherstone, J. D. B. & Feuerstein, O. Influence of blue light on Streptococcus mutans re-organization in biofilm. *J. Photochem. Photobiol. B Biol.* **116**, 75–78 (2012).
34. Rosenberg, M., Azevedo, N. F. & Ivask, A. Propidium iodide staining underestimates viability of adherent bacterial cells. *Sci. Rep.* **9**, 1–12 (2019).
35. Mesquita, D. P., Amaral, A. L. & Ferreira, E. C. Identifying different types of bulking in an activated sludge system through quantitative image analysis. *Chemosphere* **85**, 643–652 (2011).
36. De Chávez Paz, L. E. Image analysis software based on color segmentation for characterization of viability and physiological activity of biofilms. *Appl. Environ. Microbiol.* **75**, 1734–1739 (2009).
37. Luo, T. L. et al. A sensitive thresholding method for confocal laser scanning microscope image stacks of microbial biofilms. *Sci. Rep.* **8**, 13013 (2018).
38. Klinger-Strobel, M., Suesse, H., Fischer, D., Pletz, M. W. & Makarewicz, O. A novel computerized cell count algorithm for biofilm analysis. *PLoS ONE* **11**, e0154937 (2016).
39. Larimer, C. et al. A method for rapid quantitative assessment of biofilms with biomolecular staining and image analysis. *Anal. Bioanal. Chem.* **408**, 999–1008 (2016).
40. Hajian-Tilaki, K. Receiver operating characteristic (ROC) curve analysis for medical diagnostic test evaluation. *Casp. J. Intern. Med.* **4**, 627–635 (2013).
41. Bassetti, M., Vena, A., Croxatto, A., Righi, E. & Guery, B. How to manage Pseudomonas aeruginosa infections. *Drugs Context* **7**, 212527 (2018).
42. Zhu, B., Macleod, L. C., Kitten, T. & Xu, P. Streptococcus sanguinis biofilm formation & interaction with oral pathogens. *Future Microbiol.* **13**, 915 (2018).
43. Oliveira, W. F. et al. Staphylococcus aureus and Staphylococcus epidermidis infections on implants. *J. Hospital Infect.* **98**, 111–117 (2018).
44. Villapún, V. M. et al. A design approach to facilitate selective attachment of bacteria and mammalian cells to additively manufactured implants. *Addit. Manuf.* https://doi.org/10.1016/j.addma.2020.101528 (2020).
45. Evans, A., Leishman, S. J., Walsh, L. U. & Seow, W. K. Inhibitory effects of antiseptic mouthrinses on Streptococcus mutans, Streptococcus sanguinis and Lactobacillus acidophilus. *Aust. Dent. J.* **60**, 247–254 (2015).
46. Millward, T. A. & Wilson, M. The effect of chlorhexidine on Streptococcus sanguis biofilms. *Microbios* **58**, 155–164 (1989).
47. Masadeh, M. M., Gharaibeh, S. F., Alzoubi, K. H., Al-Azzam, S. I. & Obeidat, W. M. Antimicrobial activity of common mouthwash solutions on multidrug-resistance bacterial biofilms. *J. Clin. Med. Res.* **5**, 389 (2013).
48. Cieplik, F. et al. et alwResistance toward chlorhexidine in oral bacteria-is there cause for concern? Front. *Microbiol* **10**, 587 (2019).
49. Itabashi, T. et al. Bactericidal and antimicrobial effects of pure titanium and titanium alloy treated with short-term, low-energy UV irradiation. *Bone Jt. Res.* **6**, 108–112 (2017).
50. Achinas, S., Charalampogiannis, N. & Euverink, G. J. W. A brief recap of microbial adhesion and biofilms. *Appl. Sci.* **9**, 2801 (2019).
51. Crawford, R. J., Webb, H. K., Truong, V. K., Hasan, J. & Ivanova, E. P. Surface topographical factors influencing bacterial attachment. *Adv. Colloid Interface Sci.* **179–182**, 142–149 (2012).
52. Galdiero, E. et al. Eradication of Candida albicans persister cell biofilm by the membranotropic peptide gH625. *Sci. Rep.* **10**, 1–12 (2020).
53. Kleine, D. et al. Monitoring of biofilms grown on differentially structured metallic surfaces using confocal laser scanning microscopy. *Eng. Life Sci.* **19**, elsc.201800176 (2019).
54. Aslam, B. et al. Antibiotic resistance: a rundown of a global crisis. *Infect. Drug Resist.* **11**, 1645–1658 (2018).
55. Laws, M., Shaaban, A. & Rahman, K. M. Antibiotic resistance breakers: current approaches and future directions. *FEMS Microbiol. Rev.* **43**, 490–516 (2019).
56. Hall, T. et al. A call for action to the biomaterial community to tackle antimicrobial resistance. *Biomater. Sci* **8**, 4951–4974 (2020).

57. Sharma, D., Misba, L. & Khan, A. U. Antibiotics versus biofilm: an emerging battleground in microbial communities. *Antimicrob. Resist. Infect. Control* **8**, 1–10 (2019).
58. Oberoi, S. S., Dhingra, C., Sharma, G. & Sardana, D. Antibiotics in dental practice: how justified are we. *Int. Dent. J.* **65**, 4–10 (2015).
59. Pitten, F., Splieth, C. & Kramer, A. Prophylactic and therapeutic application of antimicrobial agents in the oral cavity. *Pharmazie* **55**, 635–639 (2000).
60. Saleem, H. G. M., Seers, C. A., Sabri, A. N. & Reynolds, E. C. Dental plaque bacteria with reduced susceptibility to chlorhexidine are multidrug resistant. *BMC Microbiol.* **16**, 214 (2016).
61. Thornhill, M. H., Dayer, M. J., Durkin, M. J., Lockhart, P. B. & Baddour, L. M. Oral antibiotic prescribing by NHS dentists in England 2010-2017. *Br. Dent. J.* **227**, 1044–1050 (2019).
62. Busscher, H. J. et al. Biomaterial-associated infection: locating the finish line in the race for the surface. *Sci. Transl. Med.* **4**, 153rv10 (2012).
63. Cox, S. C. et al. Surface finish has a critical influence on biofilm formation and mammalian cell attachment to additively manufactured prosthetics. *ACS Biomater. Sci. Eng.* **3**, 1616–1626 (2017).
64. Helou, M. & Kara, S. Design, analysis and manufacturing of lattice structures: an overview. *Int. J. Comput. Integr. Manuf.* **31**, 243–261 (2018).
65. du Plessis, A., Yadroitsava, I., Yadroitsev, I., le Roux, S. G. & Blaine, D. C. Numerical comparison of lattice unit cell designs for medical implants by additive manufacturing. *Virtual Phys. Prototyp.* **13**, 266–281 (2018).
66. Wiggins, A., Austerberry, R., Morrison, D., Ho, K. M. & Honeybul, S. Cranioplasty with custom-made titanium plates-14 years experience. *Neurosurgery* **72**, 248–256 (2013).
67. Wafa, H. et al. Retrospective evaluation of the incidence of early periprosthetic infection with silver-treated endoprostheses in high-risk patients: case-control study. *Bone Jt. J.* **97-B**, 252–257 (2015).
68. Efimochkina, N. R. et al. Formation of biofilms by foodborne pathogens and development of laboratory in vitro model for the study of campylobacter genus bacteria based on these biofilms. *Bull. Exp. Biol. Med.* **162**, 474–478 (2017).
69. Pratten, J., Smith, A. W. & Wilson, M. Response of single species biofilms and microcosm dental plaques to pulsing with chlorhexidine. *J. Antimicrob. Chemother.* **42**, 453–9 (1998).
70. Dawson, L. F., Valiente, E., Faulds-Pain, A., Donahue, E. H. & Wren, B. W. Characterisation of Clostridium difficile biofilm formation, a role for Spo0A. *PLoS ONE* **7**, e50527 (2012).
71. Sternberg, S. R. Biomedical image processing. *Computer* **16**, 22–34 (1983).
72. Lasko, T. A., Bhagwat, J. G., Zou, K. H. & Ohno-Machado, L. The use of receiver operating characteristic curves in biomedical informatics. *J. Biomed. Inform.* **38**, 404–415 (2005).

## ACKNOWLEDGEMENTS

The authors would like to thank Sandeep Shirgill and Imaan Griffiths for providing images of *P. aeruginosa* and multi-species *F. nucleatum* biofilms for testing the image analysis protocol, and Qianyin Mai for providing images of mouthwash treated biofilms. We acknowledge the use of BioRender® (BioRender.com) during image preparation of Supplementary Fig. 1. EPSRC provided funding through a studentship at the Centre for Doctoral Training in Physical Sciences for Health (EP/L016346/1) and through the grants EP/P015743/1 and EP/P02341X/1 (Process Design to Prevent Prosthetic Infections, PREVENT). The funding body were not involved in the writing of the manuscript and in the decision to submit the manuscript for publication.

## AUTHOR CONTRIBUTIONS

S.E.M. and N.V. contributed equally to this work. Study conception and design (S.E.M. and N.V.). Acquisition of data (S.E.M., N.V. and V.M.V.). Computational method development (S.E.M. and N.V.). Analysis and interpretation of data (all authors). Article preparation (S.E.M. and N.V.). Critical revision of the manuscript and final approval (all authors).

## COMPETING INTERESTS

The authors declare no competing interests.

## ADDITIONAL INFORMATION

**Supplementary information** The online version contains supplementary material available at https://doi.org/10.1038/s41522-021-00214-7.

**Correspondence** and requests for materials should be addressed to S.A.K.

**Reprints and permission information** is available at http://www.nature.com/reprints

**Publisher's note** Springer Nature remains neutral with regard to jurisdictional claims in published maps and institutional affiliations.

**Open Access** This article is licensed under a Creative Commons Attribution 4.0 International License, which permits use, sharing, adaptation, distribution and reproduction in any medium or format, as long as you give appropriate credit to the original author(s) and the source, provide a link to the Creative Commons license, and indicate if changes were made. The images or other third party material in this article are included in the article's Creative Commons license, unless indicated otherwise in a credit line to the material. If material is not included in the article's Creative Commons license and your intended use is not permitted by statutory regulation or exceeds the permitted use, you will need to obtain permission directly from the copyright holder. To view a copy of this license, visit http://creativecommons.org/licenses/by/4.0/.

© The Author(s) 2021

Mountcastle et al. BMC Musculoskeletal Disorders (2019) 20:575
https://doi.org/10.1186/s12891-019-2959-4

BMC Musculoskeletal Disorders

RESEARCH ARTICLE Open Access

# Dynamic viscoelastic characterisation of human osteochondral tissue: understanding the effect of the cartilage-bone interface

Sophie E. Mountcastle[1,2], Piers Allen[1], Ben O. L. Mellors[1], Bernard M. Lawless[3], Megan E. Cooke[1,2,4], Carolina E. Lavecchia[3], Natasha L. A. Fell[3], Daniel M. Espino[3], Simon W. Jones[4] and Sophie C. Cox[2*]

## Abstract

**Background:** Despite it being known that subchondral bone affects the viscoelasticity of cartilage, there has been little research into the mechanical properties of osteochondral tissue as a whole system. This study aims to unearth new knowledge concerning the dynamic behaviour of human subchondral bone and how energy is transferred through the cartilage-bone interface.

**Methods:** Dynamic mechanical analysis was used to determine the frequency-dependent (1–90 Hz) viscoelastic properties of the osteochondral unit (cartilage-bone system) as well as isolated cartilage and bone specimens extracted from human femoral heads obtained from patients undergoing total hip replacement surgery, with a mean age of 78 years ($N = 5$, $n = 22$). Bone mineral density (BMD) was also determined for samples using micro-computed tomography as a marker of tissue health.

**Results:** Cartilage storage and loss moduli along with bone storage modulus were found to increase logarithmically ($p < 0.05$) with frequency. The mean cartilage storage modulus was 34.4 ± 3.35 MPa and loss modulus was 6.17 ± 0.48 MPa (mean ± standard deviation). In contrast, bone loss modulus decreased logarithmically between 1 and 90 Hz ($p < 0.05$). The storage stiffness of the cartilage-bone-core was found to be frequency-dependent with a mean value of 1016 ± 54.0 $N.mm^{-1}$, while the loss stiffness was determined to be frequency-independent at 78.84 ± 2.48 $N.mm^{-1}$. Notably, a statistically significant ($p < 0.05$) linear correlation was found between the total energy dissipated from the isolated cartilage specimens, and the BMD of the isolated bone specimens at all frequencies except at 90 Hz ($p = 0.09$).

**Conclusions:** The viscoelastic properties of the cartilage-bone core were significantly different to the tissues in isolation ($p < 0.05$). Results from this study demonstrate that the functionality of these tissues arises because they operate as a unit. This is evidenced through the link between cartilage energy dissipated and bone BMD. The results may provide insights into the functionality of the osteochondral unit, which may offer further understanding of disease progression, such as osteoarthritis (OA). Furthermore, the results emphasise the importance of studying human tissue, as bovine models do not always display the same trends.

**Keywords:** Articular cartilage, Dynamic mechanical analysis, Osteoarthritis, Subchondral bone, Viscoelasticity

* Correspondence: s.c.cox@bham.ac.uk
[2]School of Chemical Engineering, College of Engineering and Physical Sciences, University of Birmingham, Edgbaston, Birmingham B15 2TT, UK
Full list of author information is available at the end of the article

© The Author(s). 2019 **Open Access** This article is distributed under the terms of the Creative Commons Attribution 4.0 International License (http://creativecommons.org/licenses/by/4.0/), which permits unrestricted use, distribution, and reproduction in any medium, provided you give appropriate credit to the original author(s) and the source, provide a link to the Creative Commons license, and indicate if changes were made. The Creative Commons Public Domain Dedication waiver (http://creativecommons.org/publicdomain/zero/1.0/) applies to the data made available in this article, unless otherwise stated.

## Background

The cartilage-bone interface in articulating joints is key to moderating the transmission of tensile, compressive, and shear forces from the articular cartilage to the subchondral bone [1]. The complex organisation of collagen fibres within cartilage, in part, enables it to store and dissipate energy [2], and articular cartilage is considered to be a frequency-dependent viscoelastic structure [3–6]. Studies that have analysed this interface have primarily focused on its structure and composition, characterising the calcified cartilage and underlying tidemark where collagen type I and II integrate [7–10]. More recently, biological signalling between articular cartilage and subchondral bone have been identified through vascular microchannels that traverse the subchondral bone and calcified cartilage, allowing diffusion of small molecules [11].

The viscoelastic properties of isolated articular cartilage have been well-characterised. Edelsten et al. demonstrated that cartilage behaves non-linearly under high-speed loading [12]. More recently, Lawless et al. [13] focused on observations of isolated cartilage under load at frequencies across a physiological range (1–92 Hz [3]) and determined that the storage and loss moduli were frequency-dependent. Despite providing valuable results on the behaviour of articular cartilage under dynamic loading, both these studies looked at cartilage in isolation and therefore were not able to offer insight on the behaviour of the cartilage-bone system as a whole.

In the last decade, it has been shown that severe impacts to articulating joints are known to result in damage to the bone rather than the cartilage [14]. High-impact loading has been suggested as a major risk factor of osteoarthritis (OA), and subchondral bone has been identified as having a role in the progression of the disease [15–17]. While it is known that both subchondral bone and loading frequency have a significant effect on cartilage viscoelasticity [13, 18], there is currently a gap in our understanding of subchondral bone's response to loading, independent of cartilage. Recent work by Fell et al. endeavoured to rectify this by conducting an analysis of the mechanical properties of bovine cartilage and bone [19]. Interestingly, a linear correlation between bone mineral density (BMD) and cartilage viscoelasticity was identified, suggesting there is an important relationship between the two tissues at the interface. However, to date, there are no studies of this nature conducted in human tissue.

The mechanical properties of osteochondral tissues are evidently very complex. In addition to the studies previously described that have measured cartilage viscoelasticity directly, mathematical models have been developed to elucidate further information on how articular cartilage functions in vivo. For example, local temperature changes in cartilage under load have been assessed through the development of a model to determine temperature increase from cartilage intrinsic viscoelasticity [20]. Modelling cartilage allows for properties that are difficult to measure directly in vivo to be examined. However, there are disputes regarding some mathematical models of cartilage. For instance, as proposed by Huyghe et al. [21], triphasic theory may not respect the laws of thermodynamics. Given the complexity of both tissues, studying and modelling cartilage or bone in isolation does not provide a complete picture of either tissue's capacity to store and dissipate energy [19]. Whilst there are studies that have identified the mechanical properties of animal cartilage, both on and off bone [13, 18], the role of the cartilage-bone interface in the dissipation of energy has not previously been investigated in human tissue, nor has it been incorporated into mathematical models of articular cartilage.

The aim of this study is to characterise the viscoelastic properties of human osteochondral tissues and assess the dissipation of energy by these tissues. More specifically, an approach that characterises viscoelastic behaviour of the osteochondral core and isolated tissues in a physiological frequency range has advantages in being able to assess the significance of the interactions between the two tissues. Therefore, energy dissipation has been analysed for osteochondral tissues. By using dynamic mechanical analysis (DMA), the viscoelastic properties of the human cartilage-bone unit were directly compared to the subchondral bone and articular cartilage. Furthermore, the bone mineral density (BMD) of the subchondral bone was determined, by micro-computed tomography (μ-CT), to identify any relationships with its mechanical properties, or the viscoelastic properties of cartilage.

## Methods

### Specimen preparation

Femoral heads ($N = 5$) (Table 1) were obtained from patients undergoing total hip replacement surgery following fracture of the neck of femur. Patients had no reported history of joint pain or OA disease prior to fracture of the femoral neck. Furthermore, chondropathy assessment of femoral head cartilage integrity revealed

**Table 1** Specimen information

| Specimen Name | L/R Hip | Age | Gender | Weight |
|---|---|---|---|---|
| RHH214 | R | 76 | M | OW |
| RHH217 | R | 72 | F | NW |
| RHH220 | L | 85 | M | NW |
| RHH238 | L | 85 | F | OW |
| RHH239 | R | 71 | M | NW |

*R* Right, *L* Left, *M* Male, *F* Female, *OW* Overweight, *NW* Normal Weight
Weights categorised from patient BMI: 18.5 to 24.9 = NW, 25 to 29.9 = OW

the absence of any cartilage lesions or erosions that might have indicated signs of OA damage. Thus, the cartilage was deemed to be healthy. Ethical approval was provided by the United Kingdom National Research Ethics Service (East of Scotland Research Ethics Service, 11/ES/1044) and consent for the use of their tissue for research was given by the patients. Upon arrival, specimens were stored at -80 °C, which has been previously shown not to affect the viscoelastic properties of the specimens [22]. While each specimen was frozen, a total of 22 cartilage-bone blocks approximately 14 × 14 mm in area ($n = 22$) were obtained using a surgical saw (Fig. 1a). The depth of the block varied depending on the specimen. Prior to testing, the specimens were macroscopically examined, and only intact specimens were thawed in Ringer's solution at 4 °C overnight [13].

### Micro-computed tomography (μ-CT)

Specimens were scanned as 14 × 14 mm blocks to prevent swarf created during sample sectioning from affecting the subsequent analysis of μ-CT data. Specimens were secured in a low X-ray attenuation tube and individually scanned using a Skyscan 1172 scanner (Bruker Micro-CT, Belgium). A 180° scan was performed with 80 kV maximum X-ray energy and 8 W beam power, using an aluminium and copper filter, with a pixel size of 12.03 μm. The data was reconstructed using NRecon V1.6.10.2 (Bruker Micro-CT, Belgium) using a beam hardening correction of 30%, a ring artefact correction of 4.0, and a smoothing value of 2.0. Bone mineral density (BMD) was calibrated from the attenuation coefficient using CT-analyser software V1.15.4.0 (CTAn) (Bruker Micro-CT, Belgium). Two phantom rods made

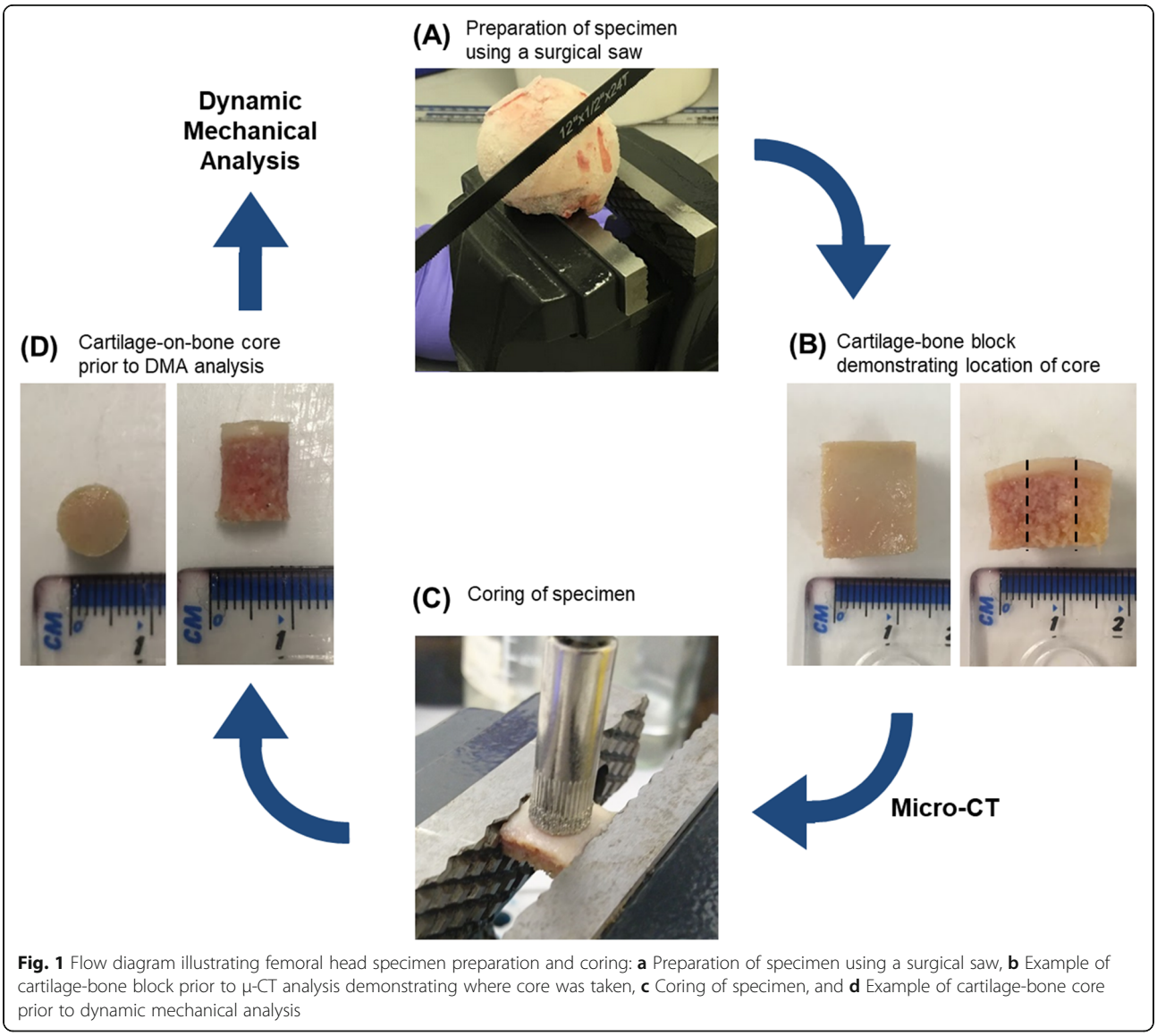


**Fig. 1** Flow diagram illustrating femoral head specimen preparation and coring: **a** Preparation of specimen using a surgical saw, **b** Example of cartilage-bone block prior to μ-CT analysis demonstrating where core was taken, **c** Coring of specimen, and **d** Example of cartilage-bone core prior to dynamic mechanical analysis

up of epoxy resin with embedded fine calcium hydroxylapatite (CaHA) powder at concentrations of 0.25 and 0.75 $g.cm^{-3}$ were scanned and reconstructed using the same parameters as used for the human specimens. BMD values of a cylindrical volume of interest the same size as the sample used for subsequent mechanical analysis (8 mm diameter) for each reconstructed dataset were calculated according to a standard method [23].

### Specimen coring

Following thawing, sectioning of the specimen, and μ-CT scanning, a core 8 mm in diameter was taken from each specimen using a pillar drill with a diamond-coated drill bit (Fig. 1c). After harvesting this cartilage-bone core, the specimen was hydrated in Ringer's solution for 30 min, as per previous studies [4, 5]. Samples were reviewed for macroscopic damage after coring and only samples with intact surfaces were tested, as surface cracks alter the mechanical properties of cartilage. The effect of the curvature evident in the cartilage-bone block (Fig. 1b) was considered to be negligible once a core was taken (Fig. 1d) and therefore not taken into account in subsequent analyses in this study.

### Dynamic mechanical analysis (DMA)

Dynamic Mechanical Analysis (DMA) subjects a specimen to a sinusoidal load and measures its out-of-phase displacement response [24]. This enables the calculation of a structure, or a material's, viscoelastic properties [25]. The viscoelastic properties of all specimens were determined using a Bose ElectroForce 3200 with WinTest 4.1 software (Bose ElectroForce Group, New Castle, Delaware, USA, now TA Instruments). This method has been previously used to determine the viscoelastic properties of bovine and human cartilage [4, 19, 26], and bovine cartilage on bone [6, 13, 18, 19, 27].

By using a cylindrical compression platen (20 mm diameter) under unconfined conditions, a sinusoidally compressive load ranging between 37.7–85.5 N was applied to all specimens, following a preload of 4 N. This induced a stress range between 0.75–1.7 MPa, as 1.7 MPa is estimated cartilage stress during walking [27]. All specimens were tested in air at room temperature; as results in literature suggest that dehydration should not occur over the short duration of each frequency-sweep [4]. The sinusoidal force was applied using a frequency-sweep of: 1, 8, 10, 12, 30, 50, 70, and 90 Hz. The specimens were subjected to two preload conditions: 25 Hz for 1500 cycles and 50 Hz for 3000 cycles, as cartilage requires application of a series of loading cycles to reach a steady state [6, 28]. After DMA was performed on the osteochondral core, full-thickness cartilage was then removed from the subchondral bone using a scalpel and hydrated in Ringer's solution for 30 min. Following inspection to ensure there was no damage to the sample, the same DMA procedure as described above was subsequently performed on the isolated subchondral bone and isolated cartilage specimens.

For each frequency sweep conducted, the WinTest DMA software performed a Fourier analysis of the load and displacement sinusoidal waves. From this, the magnitudes of the load ($F^*$), displacement ($d^*$), phase angle ($\delta$), and frequency ($f$) were determined, further described elsewhere [25]. The complex stiffness ($k^*$) was then calculated (Eq. 1).

$$k^* = \frac{F^*}{d^*} \tag{1}$$

By using the complex stiffness ($k^*$) and phase angle ($\delta$), the storage stiffness ($k'$) and loss stiffness ($k''$) were calculated (Eqs. 2 and 3) [25, 29].

$$k' = k^*(\cos\delta) \tag{2}$$

$$k'' = k^*(\sin\delta) \tag{3}$$

Using a shape factor, S, calculated from the diameter ($d$) and height ($h$) of the specimen (Eq. 4), the storage ($E'$) and loss ($E''$) moduli can be determined (Eqs. 5 and 6) [4].

$$S = \frac{\pi d^2}{4h} \tag{4}$$

$$E' = \frac{k^* \cos\delta}{S} \tag{5}$$

$$E'' = \frac{k^* \sin\delta}{S} \tag{6}$$

$E'$ and $E''$ were calculated for isolated cartilage and subchondral bone specimens. As the cartilage-bone cores were complex multi-structures, $k'$ *and* $k''$ were calculated for those specimens. This enabled evaluation of the properties of the overall system with those of the individual tissues. All results are presented against the requested frequency used for DMA for ease of comparison, however actual frequencies measured varied by ±1 Hz.

### Thickness testing

Following DMA, and after removing the cartilage from the bone using a surgical scalpel, the cartilage specimens were hydrated in Ringer's solution for 30 min, consistent with a previous study [3]. Following hydration, cartilage thickness was determined using an established needle technique accurate to 1 μm resolution [4, 30]. An analogue Vernier calliper was used to calculate the thickness of bone specimens by taking three measurements from each specimen and calculating the mean

thickness (resolution of 0.1 mm). Mean average thicknesses of each specimen type can be found in Table 2.

### Energy dissipation calculation

Energy dissipation was calculated using Matlab R2018a (Matlab R2018a, MathWorks, Inc., Natick, Massachusetts, USA). Time, force, and displacement data was collected during DMA. Plotting displacement vs force at a given frequency for each specimen produced a hysteresis loop (Fig. 2a). For each complete loop, the area between the arcs was assumed to be the total energy dissipated for that DMA cycle. This was calculated by finding a polynomial approximation of each arc, which was then solved for the range zero to the maximal displacement of that cycle. The area below each polynomial arc was approximated by the trapezoid rule [31] (Fig. 2b); the difference between the two arcs equated to the energy dissipated for that cycle. Finally, the values across all cycles were averaged, resulting in the total energy dissipation per cycle for each specimen at a given frequency.

### Statistical analysis

Statistical analyses were performed using GraphPad Prism 5.03 (GraphPad Software Inc., San Diego, California, USA). 95% confidence intervals were calculated ($N = 5$, $n = 23$); the number of independent patients from which specimens were collected was 5, and between 4 and 5 specimens were measured from each patient. Logarithmic regression curves were fitted to material viscoelastic ($E'$ and $E''$) and structure stiffness ($k'$ and $k''$) data, where a significant trend was identified ($p < 0.05$) (Eq. 7). Wilcoxon Rank-Sum tests were used to assess whether the cartilage and bone specimens had significantly different material properties ($p < 0.05$). Kruskal-Wallis one-way analysis of variance (ANOVA) tests determined whether structural stiffness variations between the cartilage, bone, and osteochondral cores were significantly different ($p < 0.05$). Tukey's multiple comparison tests were used to determine the structural stiffness variations that were significantly different between specimen types.

$$E' = A \ \log_e(f) + B \ for \ 1 \le f \le 90 \ Hz \quad (7)$$

## Results

Of the 23 specimens tested, the results of two were rejected since the cartilage thickness (2.6 and 2.7 mm) lay far outside the normal physiological range of 1–2 mm [32] and may be representative of degenerated cartilage [33]. Peirce's criterion was used to eliminate the two values [34].

### Viscoelastic properties of isolated cartilage and bone specimens

#### *Storage modulus (E')*

For isolated tissue specimens, $E'$ was found to be frequency-dependent and differed significantly ($p < 0.001$) between cartilage and bone specimens (Fig. 3a). The mean value of E' was 34.4 ± 3.35 MPa for cartilage, while for bone it was considerably higher, 170 ± 4.76 MPa. A logarithmic relationship for $E'$ was observed with respect to frequency for both specimens (Eq. 7), with storage modulus increasing with frequency (Fig. 3a).

#### *Loss modulus (E")*

Loss modulus was also found to be frequency-dependent and differed significantly ($p < 0.001$) between cartilage and bone specimens (Fig. 3b). A logarithmic relationship for both specimens was observed with respect to frequency (Eq. 7). For cartilage, the mean $E''$ was 6.17 ± 0.48 MPa and for bone, $E''$ was 9.02 ± 1.07 MPa. The loss modulus for cartilage increased with increasing frequency, while for bone it decreased with increasing frequency (Fig. 3b).

### Viscoelastic properties of cartilage-bone cores

#### *Storage stiffness (k')*

Cartilage-bone cores, cartilage, and bone specimens were found to be frequency-dependent with respect to $k'$ (Eq. 7, Fig. 4a). Consistently, $k'$ was observed to increase with frequency for all specimens, with the mean cartilage-bone specimen result as 1016 ± 54.0 $N.mm^{-1}$, cartilage 1217 ± 117 $N.mm^{-1}$, and bone 1455 ± 40.7 $N.mm^{-1}$. For $k'$, differences between all three specimen types (cartilage-bone core, cartilage, and bone), were found to be statistically significant ($p < 0.001$).

#### *Loss stiffness (k")*

Loss stiffness was frequency-dependent for cartilage and bone specimens (Eq. 7) with a mean value of 218 ± 16.1 $N.mm^{-1}$ for cartilage and 79.8 ± 9.77 $N.mm^{-1}$ for bone. However, loss stiffness was found to be frequency-independent for the cartilage-bone-system (Fig. 4b). A significant difference ($p < 0.001$) was observed between

**Table 2** Specimen thicknesses. Data displayed to 3 significant figures

| Specimen type | n number | Mean average thickness (mm) | Standard deviation (mm) |
|---|---|---|---|
| Cartilage-bone core | 18 | 7.43 | ± 2.17 |
| Cartilage | 20 | 1.48 | ± 0.43 |
| Bone | 18 | 5.94 | ± 2.09 |

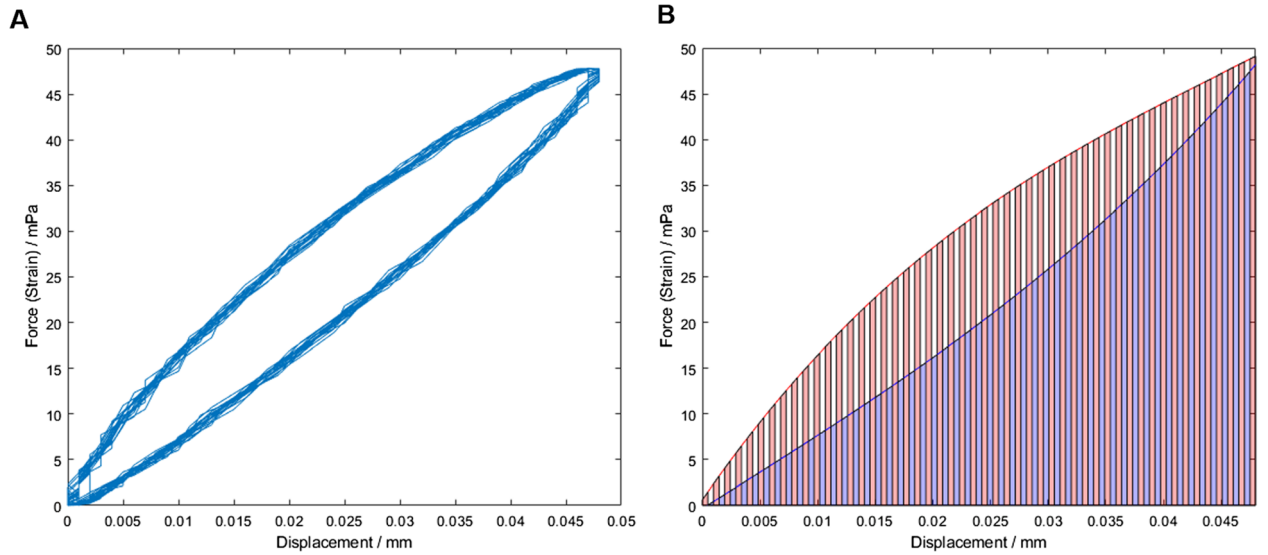


**Fig. 2** Cartilage hysteresis. Force is given as increase in force during loading cycle. **a** Example of hysteresis loop generated for a single specimen at 30 Hz. **b** Approximation of the area between the upper and lower arcs of each cycle calculated using the trapezoidal rule. The difference between the two areas was determined as the total energy dissipated during that cycle of DMA

$k$" values for the cartilage-bone core and cartilage specimens, as well as between isolated cartilage and bone specimens. However, there was no significant difference ($p > 0.05$) found for $k$" between the cartilage-bone-system and isolated bone specimens.

### Total energy dissipated

Energy dissipated was found to be frequency-dependent for all three specimen types (Eq. 8) with a mean value of $0.143 \pm 0.101$ J for bone specimens, $0.339 \pm 0.111$ J for cartilage specimens, and $0.2184 \pm 0.094$ J for cartilage-bone cores (Fig. 5). A significant difference ($p < 0.05$) was found between the total energy dissipated for all three groups.

$$energy\ dissipated = A\ (f) + B\ for\ 1 \le f \le 90\ Hz \qquad (8)$$

### Histomorphological analysis

The mean BMD ($\rho$) for all bone specimens tested was $+0.286 \pm 0.081$ g.cm$^{-3}$. Regression analysis of BMD and

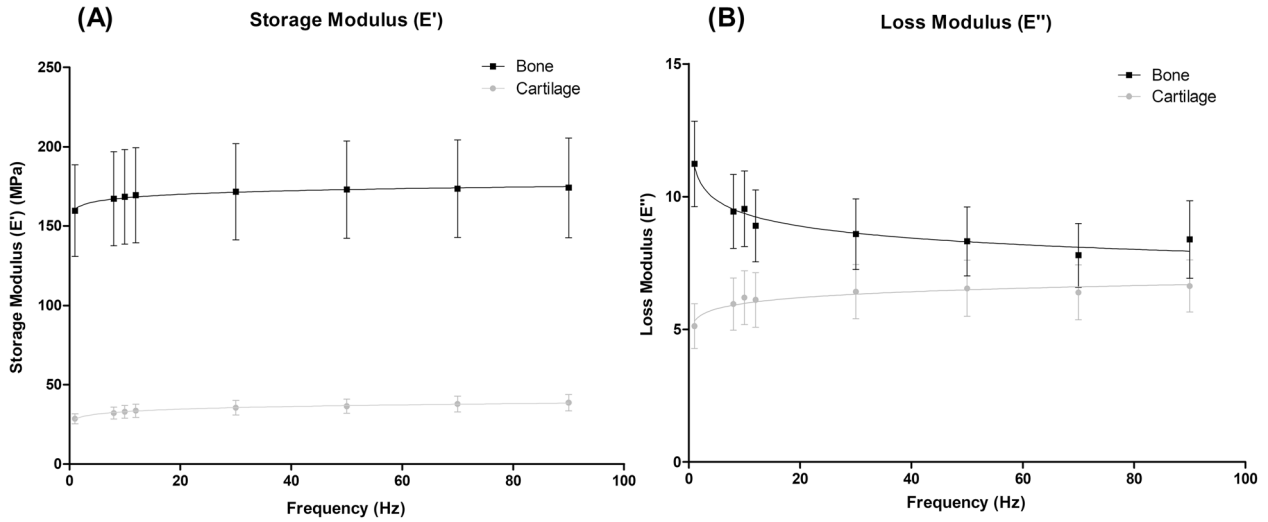


**Fig. 3** Storage (**a**) and loss (**b**) moduli for isolated cartilage and bone specimens plotted against frequency from 1 to 90 Hz (mean ± 95% confidence intervals, ($N = 5$) with natural logarithmic regression trendlines). In total, 19 cartilage and 18 bone specimens from five femoral heads were tested. Results are displayed on a linear scale

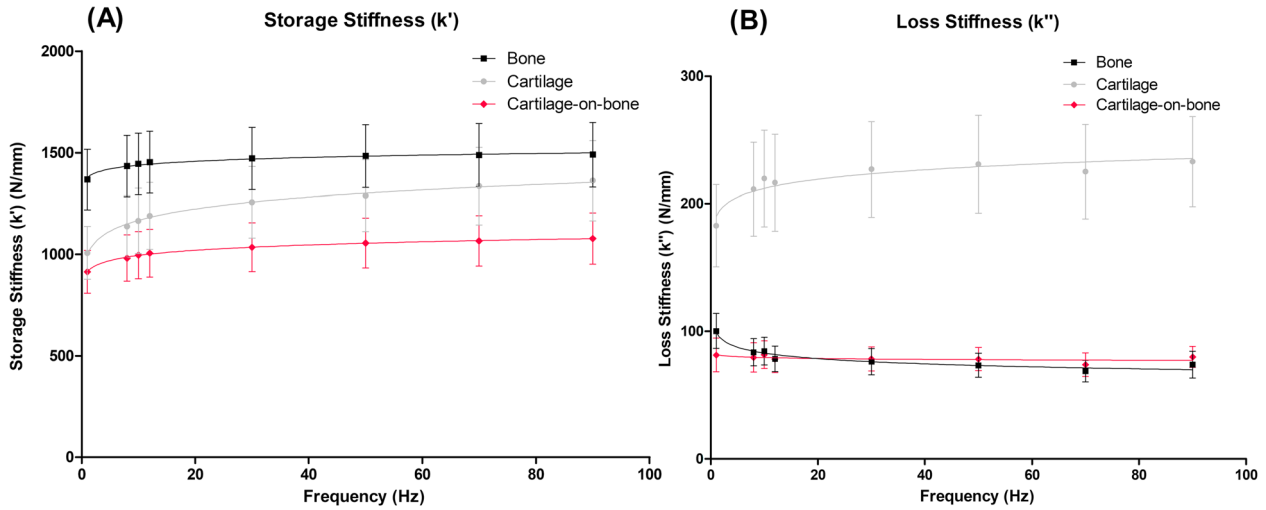


**Fig. 4** Storage (**a**) and loss (**b**) stiffness for the cartilage-bone-system, isolated cartilage, and isolated bone specimens plotted against frequency from 1 to 90 Hz (mean ± 95% confidence intervals, ($N = 5$) with natural logarithmic regression trendlines). In total, 19 cartilage-bone cores, 19 cartilage, and 18 bone specimens from five femoral heads were tested. Results are displayed on a linear scale

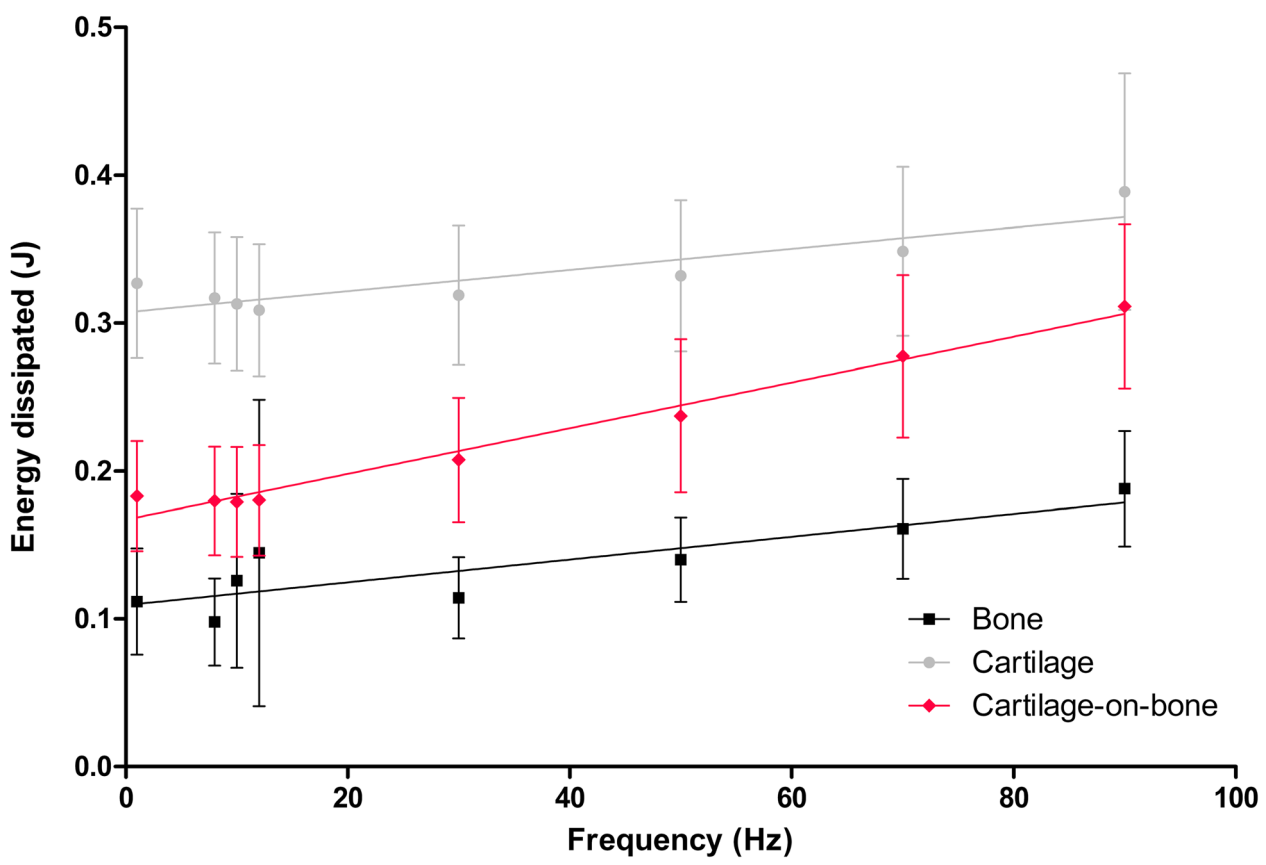


**Fig. 5** Total energy dissipated for cartilage-bone cores, cartilage, and bone specimens plotted against frequency from 1 to 90 Hz (mean ± 95% confidence intervals, ($N = 5$) with linear regression trendlines). In total, 19 cartilage-bone cores, 19 cartilage, and 18 bone specimens from five femoral heads were tested. Results are displayed on a linear scale

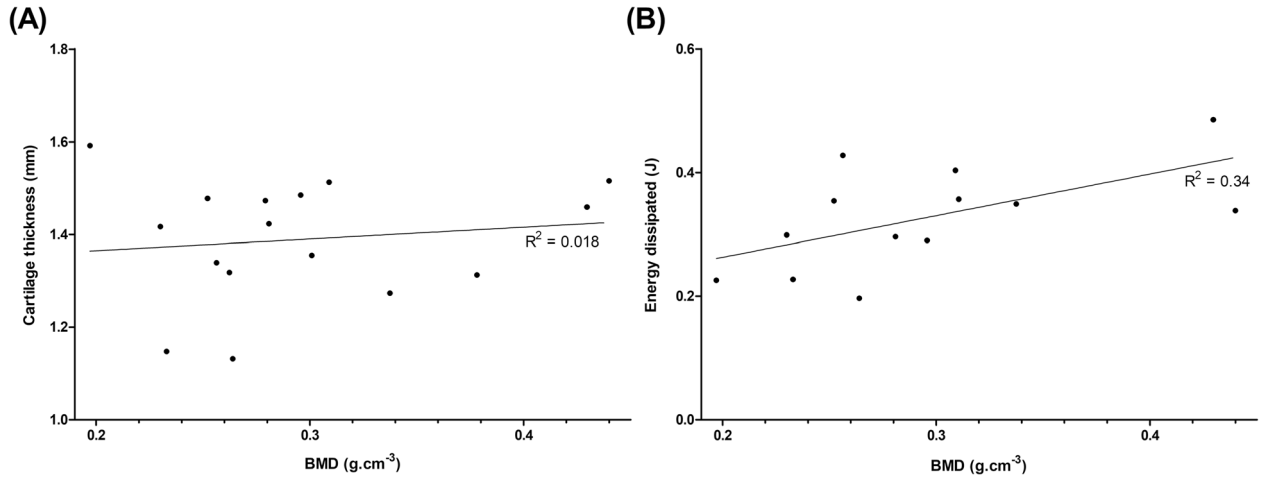


**Fig. 6 a** Isolated cartilage thickness plotted against BMD (linear regression (solid line), ($N = 5$)). In total, 16 specimens from five femoral heads were tested. **b** Linear regression analysis of BMD and total energy dissipated from cartilage at 1 Hz (linear regression trendline, ($N = 5$)). In total, 13 specimens from five femoral heads were tested. Results displayed on a linear scale

cartilage thickness values did not reveal any significant relationship ($p = 0.62$) (Fig. 6a). Linear regression analysis (Eq. 9) was performed on BMD ($\rho$) and mean total energy dissipated from cartilage specimens (Fig. 6b, Table 3). The relationship between these properties was found to be statistically significant ($p < 0.05$) at all frequencies except at 90 Hz ($p = 0.09$).

$$Energy\ dissipated = A\ (\rho) + B \tag{9}$$

No significant relationships existed between BMD and the storage or loss moduli of the cartilage, or the storage and loss moduli of the bone. Furthermore, there were no significant relationships found between total energy dissipated and the thickness of the isolated cartilage, isolated bone, or the osteochondral specimens respectively.

**Table 3** $R^2$ and *p*-values from linear regression analysis of BMD ($n = 13$) and total energy dissipated from isolated cartilage specimens ($n = 13$) for each frequency. Data displayed to 2 significant figures

| Frequency (Hz) | *p*-value | $R^2$ |
|---|---|---|
| 1 | 0.035 | 0.34 |
| 8 | 0.017 | 0.39 |
| 10 | 0.021 | 0.37 |
| 12 | 0.017 | 0.39 |
| 30 | 0.021 | 0.37 |
| 50 | 0.032 | 0.33 |
| 70 | 0.046 | 0.29 |
| 90 | 0.093 | 0.22 |

## Discussion

This study established the viscoelastic behaviour of isolated cartilage and bone specimens in compression, and compared it with the osteochondral core, an analogy not previously conducted with human tissue. Cartilage-bone cores, isolated cartilage, and subchondral bone specimens were determined to be viscoelastic across all frequencies tested. Significant differences in behaviour of the core compared with the isolated specimens for *k'* and *k"* were identified. Most notably, cartilage-bone specimens displayed a frequency-independent trend for *k'* unlike isolated specimens, which were frequency-dependent. Previous research has focused on cartilage or cartilage-bone specimens alone [4, 6, 13, 18] and has not looked at the independent properties of human subchondral bone. DMA testing of human subchondral bone was conducted in the present work and the results highlight a significant difference in the viscoelastic properties of bone in comparison to cartilage; *E"* was shown to increase with increasing frequency for cartilage yet decrease with increasing frequency for bone. This data emphasises the complex mechanical properties of osteochondral tissues and in particular demonstrates the significance of the cartilage-bone interface.

A previous study by Temple et al. characterised the viscoelastic properties of human articular cartilage and revealed that this tissue behaves in a frequency-dependent manner, fitting a logarithmic function, thus supporting the findings of this study [4]. They reported storage and loss moduli for articular cartilage from human femoral heads to be 31.9–43.3 MPa and 5.3–8.5 MPa respectively. This is in line with reported mean storage and loss moduli in the present analysis of 34.4 ± 3.35 MPa and 6.17 ± 0.48 MPa respectively. In addition,

Jeffrey & Aspden [35] calculated a 'dynamic' modulus for human articular cartilage from femoral heads by applying an impact load. The resulting dynamic modulus of human articular cartilage at stresses of 10 MPa and 23 MPa was reported to be 64 ± 13 MPa and 85.1 ± 4.9 MPa respectively. This is higher than the values reported for cartilage storage modulus in this study, although it is important to note that the induced stresses applied by Jeffrey & Aspden [35] were much higher, and higher stress is known to increase the storage modulus [13]. The present study has demonstrated that both storage and loss modulus for cartilage increase with increasing frequency. Notably, more energy is stored by both cartilage and bone tissues than is dissipated, with the effect most apparent at higher frequencies. It was determined that *E"* was an order of magnitude lower than *E'* for bone across all frequencies tested. Similarly, *E"* for cartilage was lower than *E'* between 1 and 90 Hz, as confirmed by other authors [4]. A small subset of the population is known to have high heel-strike rise times during gait, which induce forces at high frequencies (as high as 92 Hz) on the lower limbs [3]. Initially hypothesised by Radin et al. [36], high-frequency loading on the lower limbs has been identified as a marker of early onset osteoarthritis (OA), a degenerative disease that results in cartilage loss [37]. This study demonstrated increased energy storage for both cartilage and bone at higher frequencies, with energy dissipation determined to be an order of magnitude lower than energy storage. This behaviour could be a contributing factor to disease progression due to damaging stress concentrations. This is significant, as subchondral bone tissue in particular is likely to incur damage due to its increased ability to store energy yet decreased ability to dissipate it. However, as bone has a higher regenerative capacity than cartilage [38], this may be a mechanism for preventing cartilage damage, as the bone is more readily able to heal.

Bovine articular cartilage is considered a good model for human articular cartilage, as it displays similar trends in viscoelastic properties [4]. A recent study by Fell et al. [19] determined the viscoelastic properties of bovine cartilage and subchondral bone. They reported mean storage and loss moduli of bovine cartilage to be 45 MPa and 5.5 MPa respectively, whilst isolated bovine subchondral bone was found to have a mean storage modulus of 110 MPa and a mean loss modulus of 5 MPa. The storage modulus for bovine cartilage was therefore 1.3 times higher than isolated human cartilage in this study, which had a mean of 34.4 MPa. However, the bovine storage moduli for bone and loss moduli for cartilage reported by Fell et al. [19] were found to be lower than the respective results for the isolated human specimens in this study, though in the same order of magnitude. A possible reason for this is that the bovine tissues were obtained from the knee joint, whereas the human specimens were from the hip. Therefore, anatomical region is important when investigating and comparing the mechanical properties of osteochondral tissues.

Similar trends to the results in the present study were displayed by Fell et al. [19] for cartilage and bone storage and loss moduli (1–90 Hz). Of note, the loss modulus trends found in bovine tissue were also evident in human tissue (Fig. 3b). Whilst the trends were similar for bovine and human osteochondral tissue, Fell et al. evidenced a 'crossover' of the cartilage and bone loss modulus values [19]. At 1 Hz, bone had a higher loss modulus than cartilage, but at frequencies above 8 Hz this was reversed with cartilage samples exhibiting a higher loss modulus than bone. The authors suggested this might be a mechanism to prevent cartilage damage, as cartilage will dissipate more energy than bone under high-frequency loading. However, this trend was not noted in human osteochondral tissue, where bone had a higher loss modulus than cartilage at all frequencies tested (Fig. 3b). This data raises the hypothesis that cartilage damage in OA patients could be due to an inability of cartilage to dissipate energy into the bone under high-frequency loading, but further experimental work would be required to evidence this. A comparison of the trends seen here with Fell et al. demonstrates the importance of studying human osteochondral tissue since it is clear that animal models do not always display the same trends [4]. The present study is the first to report viscoelastic properties of human articular cartilage, subchondral bone, and the osteochondral core using Dynamic Mechanical Analysis.

As well as investigating isolated tissues, this research aimed to better understand the osteochondral core as a whole system. Storage stiffness for the cartilage-bone system was logarithmically frequency dependent and lower than cartilage and bone for all frequencies tested (Fig. 4). Loss stiffness for the cartilage-bone system was independent of frequency and lower than isolated specimens across the range of frequencies tested. These results are in line with previous work, which looked solely at bovine cartilage-bone cores and found loss stiffness to be frequency-independent [13, 18]. The difference in behaviour of cartilage isolated from and attached to subchondral bone is emphasised here and has demonstrated that cartilage should not be considered in isolation when determining properties representative of in vivo behaviour. The data obtained in our study supports the development and testing of whole tissue-replacement systems as opposed to cartilage replacement materials in isolation.

Prior studies of bovine cartilage both on- and off-bone found the loss modulus of on-bone cartilage to be frequency-independent, whereas cartilage off-bone has a frequency-dependent modulus [13, 18]. Lawless et al.

[13] found that there was no dependency of the storage stiffness on the presence or absence of the underlying subchondral bone, and therefore proposed that on-bone cartilage may be more predisposed to failure than off-bone cartilage due to the storage/loss ratio being higher for cartilage on-bone. The findings of the present study report the same frequency-independence for cartilage on-bone loss modulus, with isolated cartilage displaying a frequency-dependent trend. Thus, findings reported in prior studies support the current results, although it should be noted that the aim of the present study was focused on the viscoelasticity of subchondral bone and the role of the cartilage-bone interface, rather than the cartilage itself. Hence, a more detailed discussion on the viscoelastic properties of cartilage both on- and off-bone is provided elsewhere [13].

In order to explain the difference in behaviour between isolated cartilage and the cartilage-bone-system system, Edelsten et al. [12] suggested that cartilage attached to subchondral bone is more constrained in its deformation, and this may lead to it appearing stiffer and more elastic than when in isolation. Experimentally, this result has been verified as *k"* becomes frequency-independent under load [12, 13]. However, the trends in *E'* and *E"* in isolated bone identified in this study (Fig. 3) may infer an additional explanation. Bone was found to be positively frequency-dependent for storage and negatively frequency-dependent for loss moduli. Therefore, the constraining effects of the bone could not be the sole reason for the frequency independence of *k"* for the cartilage-bone-system. A decrease in loss stiffness indicates a decrease in the energy dissipated, suggesting that bone does not dissipate as much energy to the surrounding tissue at higher frequencies. This may prevent the load energy being returned to the cartilage, which could be a further mechanism to prevent cartilage damage. While observing equine osteochondral cores under high-impact, Malekipour et al. identified that bone can absorb a much higher amount of impact energy than cartilage [39]. Furthermore, it is often bone that breaks during high-impact loading, as the main mechanism by which it absorbs energy is through trabeculae fracture [39]. Although this may be desirable, as bone has a greater propensity to heal than cartilage, this may put the joint at risk of long-term damage. Clearly, the interface between the two tissues plays an essential role in transferring the load energy through the cartilage and into the bone.

A significant difference was identified between loss stiffness values for the cartilage-bone system and cartilage specimens. In contrast, when comparing the cartilage-bone system and bone specimens this was not observed, signifying that the loss stiffness of the osteochondral core is more closely aligned to the loss stiffness of bone than of isolated cartilage. This suggests a key property to consider is the energy transfer, including dissipation of energy, through the osteochondral junction. In order to characterise this in the present study, the total energy dissipated from the cartilage at each frequency during DMA was calculated. The benefit of this approach is the entire system is considered as a whole by determining absolute values rather than material properties. The results demonstrated that cartilage dissipated higher total energy than bone and the cartilage-bone system across all frequencies tested (Fig. 5). While expected, as one of the key roles of articular cartilage is to dissipate energy into the underlying bone, to the best of the authors knowledge this is the first report of such a relationship from human tissue analysis.

It has been hypothesised that high heel-strike rise times during gait causes a predisposition to the onset of OA [6, 36]. This high-impact loading, combined with a reduced ability to dissipate energy at high frequencies, is likely to cause damage to the bone, leading to subchondral bone remodelling and therefore a higher BMD. Prior to work by Fell et al. [19], no previous studies had attempted to link bone histomorphology with viscoelastic properties of osteochondral tissues. The study on bovine osteochondral cores identified a significant relationship between subchondral bone BMD and cartilage loss stiffness [19]. Correlations between cartilage thickness with BMD and subchondral bone plate thickness were also unearthed. This suggests that cartilage health is interrelated with the histomorphological properties of the subchondral bone. The results of the present study demonstrated a statistically significant ($p < 0.05$) link at all frequencies except at 90 Hz ($p = 0.09$) between the total energy dissipated by isolated cartilage specimens and BMD (Fig. 6b). This supports the findings by Fell et al. and validates the hypothesis that the dissipation of energy through to the subchondral bone provides mechanical signals, which can alter the structure of the tissue, for example a remodelling of the trabeculae [40]. It should be noted that although the goodness of fit is low between the BMD and total energy dissipated from the cartilage, they are comparable to R and $R^2$ values presented in other BMD studies [19, 41, 42].

There are a small number of limitations within the present study. One of the key challenges with human tissue is that specimens can have wide variation due to factors such as age, weight, and gender, which are known to have an effect on the health of these tissues. In addition, the patients who donated their tissue for this study are of an advanced age and therefore may not be representative of younger adults. Furthermore, it has been previously reported that bovine cartilage stiffens with age [43]. Whilst the tissues in the present study are obtained from older adults, the joints showed no sign of

OA joint damage upon chondropathy assessment and are representative of cartilage that has maintained health throughout its lifespan. The high variation between specimens, combined with reduced specimen numbers due to tissue availability, is likely to be the reason that a significant link between BMD and cartilage viscoelasticity was not established in the present study, despite being demonstrated in bovine tissue [19]. It should also be noted that the cartilage surface in the sample blocks exhibited a slight curvature (Fig. 1b). To minimise the impact of this on mechanical test data, cores were taken from flatter regions of the block, and hence it was not accounted for. There are advantages and disadvantages to using stiffness measurements, as reported in this study. The calculation of storage and loss moduli is dependent on thickness, and therefore any limitations associated with thickness measurements are included in moduli, but are not included in stiffness [44], however, direct comparison of stiffness can only be made for the same shape and size of specimens. As moduli and stiffness are fundamentally different measurements, it limits the comparability across literature, although their trends with frequency of loading can be compared because the modulus is simply the stiffness divided by a constant (i.e. a shape factor) [13]. The primary reason for choosing to report stiffness in this study is that the osteochondral cores were a structure consisting of both soft and hard tissues. A separate limitation during DMA testing of biological tissues is damping if these are tested in a fluid medium. To avoid potential damping due to fluid in this study, the samples were not submerged in fluid and, therefore, the dissipation of energy reported was solely due to the cartilage tissue. Damping has been previously shown to have little effect between samples tested in air and in Ringer's solution [13].

The complexity of the frequency-dependent viscoelastic properties of cartilage and bone described in this study demonstrate that there is a sophisticated interaction between these two tissues in regard to storage and dissipation of energy. High-frequency loading results in an increased storage of energy in the subchondral bone, a likely mechanism to prevent cartilage damage, which is a factor that should be further investigated in relation to the progression of OA. The results obtained in this study provide details of native tissue behaviour in vitro at physiologically relevant frequency ranges, the first reported values in human osteochondral tissue under dynamic loading.

## Conclusions

This study demonstrates that subchondral bone is viscoelastic over a physiological frequency range (1–90 Hz). Storage and loss moduli for cartilage and storage modulus for bone increase with increasing frequency, while the loss modulus of bone decreases. Loss stiffness for the cartilage-bone-system is frequency-independent yet for isolated specimens it was shown to be frequency-dependent. Finally, a statistically significant link has been identified between cartilage energy dissipated and bone histomorphology. From these results, the importance of characterising the properties of articular cartilage both isolated from, and attached to, subchondral bone is clearly highlighted. Overall, this work demonstrates the significance of the bone-cartilage interface, in particular for energy storage and dissipation.

### Abbreviations

BMD: Bone mineral density; CaHA: Calcium hydroxylapatite; DMA: Dynamic mechanical analysis; OA: Osteoarthritis; μ-CT: Micro-computed tomography

### Acknowledgements

The authors thank the members of the Healthcare Technologies Institute and Department of Mechanical Engineering at the University of Birmingham for their technical support. We also thank the Institute of Inflammation and Ageing at the University of Birmingham for providing the specimens.

### Authors' contributions

Study conception and design (SC, DE, SJ, SM). Acquisition of data (SM, BM, BL, MC, NF, CL). Computational method development (PA). Analysis and interpretation of data (all authors). Article preparation (SM, SC). Critical revision of the manuscript and final approval (all authors).

### Funding

EPSRC provided funding through a studentship at the Centre for Doctoral Training in Physical Sciences for Health (EP/ L016346/1). The materials testing equipment used in this study was funded by Arthritis Research UK, now a part of Versus Arthritis (Grant number: H0671). The funding bodies had no involvement in the design of the study; collection, analysis and interpretation of data; in the writing of the manuscript; and in the decision to submit the manuscript for publication.

### Availability of data and materials

The datasets used and/or analysed during the current study are available from the corresponding author on reasonable request.

### Ethics approval and consent to participate

Ethical approval was provided by the United Kingdom National Research Ethics Service (East of Scotland Research Ethics Service, 11/ES/1044) and informed written consent for the use of their tissue for research was given by all patients.

### Consent for publication

Not applicable.

### Competing interests

The authors declare that they have no competing interests.

### Author details

[1]EPSRC Centre for Doctoral Training in Physical Sciences for Health, University of Birmingham, Edgbaston, Birmingham B15 2TT, UK. [2]School of Chemical Engineering, College of Engineering and Physical Sciences, University of Birmingham, Edgbaston, Birmingham B15 2TT, UK. [3]Department of Mechanical Engineering, University of Birmingham, Edgbaston, Birmingham B15 2TT, UK. [4]Centre for Musculoskeletal Ageing Research, Queen Elizabeth Hospital, University of Birmingham, Edgbaston, Birmingham B15 2TT, UK.

Received: 16 May 2019 Accepted: 20 November 2019
Published online: 30 November 2019

## References


1. Hoemann CD, Ph D, Sc M, Lascau-coman V, Sc M, Chen G, et al. The cartilage-bone interface. J Knee Surg. 2012;1:85–97. https://doi.org/10.1055/s-0032-1319782.
2. Moger CJ, Barrett R, Bleuet P, Bradley DA, Ellis RE, Green EM, et al. Regional variations of collagen orientation in normal and diseased articular cartilage and subchondral bone determined using small angle X-ray scattering (SAXS). Osteoarthr Cartil. 2007;15:682–7. https://doi.org/10.1016/j.joca.2006.12.006.
3. Shepherd DET, Seedhom BB. A technique for measuring the compressive modulus of articular cartilage under physiological loading rates with preliminary results. Proc Inst Mech Eng Part H J Eng Med. 1997;211:155–65. https://doi.org/10.1243/0954411971534278.
4. Temple DK, Cederlund AA, Lawless BM, Aspden RM, Espino DM. Viscoelastic properties of human and bovine articular cartilage: a comparison of frequency-dependent trends. BMC Musculoskelet Disord. 2016;17:419. https://doi.org/10.1186/s12891-016-1279-1.
5. Sadeghi H, Lawless BM, Espino DM, Shepherd DET. Effect of frequency on crack growth in articular cartilage. J Mech Behav Biomed Mater. 2018;77:40–6. https://doi.org/10.1016/j.jmbbm.2017.08.036.
6. Sadeghi H, Espino DM, Shepherd DE. Variation in viscoelastic properties of bovine articular cartilage below, up to and above healthy gait-relevant loading frequencies. Proc Inst Mech Eng Part H J Eng Med. 2015;229:115–23. https://doi.org/10.1177/0954411915570372.
7. Wang F, Ying Z, Duan X, Tan H, Yang B, Guo L, et al. Histomorphometric analysis of adult articular calcified cartilage zone. J Struct Biol. 2009;168:359–65. https://doi.org/10.1016/j.jsb.2009.08.010.
8. Hunziker EB, Quinn TM, Hauselmann HJ. Quantitative structural organization of normal adult human articular cartilage. Osteoarthr Cartil. 2002;10:564–72.
9. Rey C, Beshah K, Griffin R, Glimcher MJ. Structural studies of the mineral phase of calcifying cartilage. J Bone Miner Res. 1991;6:515–25. https://doi.org/10.1002/jbmr.5650060514.
10. Kaabar W, Laklouk A, Bunk O, Baily M, Farquharson MJ, Bradley D. Compositional and structural studies of the bone-cartilage interface using PIXE and SAXS techniques. Nucl Instruments Methods Phys Res Sect A Accel Spectrometers, Detect Assoc Equip. 2010;619:78–82. https://doi.org/10.1016/j.nima.2010.01.040.
11. Findlay DM, Kuliwaba JS. Bone-cartilage crosstalk: a conversation for understanding osteoarthritis. Bone Res. 2016;4:16028. https://doi.org/10.1038/boneres.2016.28.
12. Edelsten L, Jeffrey JE, Burgin LV, Aspden RM. Viscoelastic deformation of articular cartilage during impact loading. Soft Matter. 2010;6:5206. https://doi.org/10.1039/c0sm00097c.
13. Lawless BM, Sadeghi H, Temple DK, Dhaliwal H, Espino DM, Hukins DWL. Viscoelasticity of articular cartilage: Analysing the effect of induced stress and the restraint of bone in a dynamic environment. J Mech Behav Biomed Mater. 2017;75:293–301. https://doi.org/10.1016/j.jmbbm.2017.07.040.
14. Burgin LV, Aspden RM. Impact testing to determine the mechanical properties of articular cartilage in isolation and on bone. J Mater Sci Mater Med. 2008;19:703–11. https://doi.org/10.1007/s10856-007-3187-2.
15. Mahjoub M, Berenbaum F, Houard X. Why subchondral bone in osteoarthritis? The importance of the cartilage bone interface in osteoarthritis. Osteoporos Int. 2012;23:841–6. https://doi.org/10.1007/s00198-012-2161-0.
16. Li G, Yin J, Gao J, Cheng TS, Pavlos NJ, Zhang C, et al. Subchondral bone in osteoarthritis: insight into risk factors and microstructural changes. Arthritis Res Ther. 2013;15:223. https://doi.org/10.1186/ar4405.
17. Lories RJ, Luyten FP. The bone–cartilage unit in osteoarthritis. Nat Rev Rheumatol. 2011;7:43–9. https://doi.org/10.1038/nrrheum.2010.197.
18. Fulcher GR, Hukins DW, Shepherd DE. Viscoelastic properties of bovine articular cartilage attached to subchondral bone at high frequencies. BMC Musculoskelet Disord. 2009;10:61. https://doi.org/10.1186/1471-2474-10-61.
19. Fell NLA, Lawless BM, Cox SC, Cooke ME, Eisenstein NM, Shepherd DET, et al. The role of subchondral bone, and its histomorphology, on the dynamic viscoelasticity of cartilage, bone and osteochondral cores. Osteoarthr Cartil. 2018. https://doi.org/10.1016/J.JOCA.2018.12.006.
20. Abdel-Sayed P, Moghadam MN, Salomir R, Tchernin D, Pioletti DP. Intrinsic viscoelasticity increases temperature in knee cartilage under physiological loading. J Mech Behav Biomed Mater. 2014;30:123–30. https://doi.org/10.1016/J.JMBBM.2013.10.025.
21. Huyghe JM, Wilson W, Malakpoor K. On the thermodynamical admissibility of the triphasic theory of charged hydrated tissues. J Biomech Eng. 2009;131:044504. https://doi.org/10.1115/1.3049531.
22. Szarko M, Muldrew K, Bertram JE. Freeze-thaw treatment effects on the dynamic mechanical properties of articular cartilage. BMC Musculoskelet Disord. 2010;11:231. https://doi.org/10.1186/1471-2474-11-231.
23. Bruker. Bone mineral density (BMD) and tissue mineral density (TMD) calibration and measurement by micro-CT using Bruker-MicroCT CT-Analyser. https://medicine.temple.edu/sites/medicine/files/files/ct_analyzer.pdf.
24. Menard KP. Dynamic mechanical analysis : a practical introduction: CRC Press; 2008. https://www.crcpress.com/Dynamic-Mechanical-Analysis-A-Practical-Introduction-Second-Edition/Menard/p/book/9781420053128.
25. Lawless BM, Barnes SC, Espino DM, Shepherd DET. Viscoelastic properties of a spinal posterior dynamic stabilisation device. J Mech Behav Biomed Mater. 2016;59:519–26. https://doi.org/10.1016/j.jmbbm.2016.03.011.
26. Cooke ME, Lawless BM, Jones SW, Grover LM. Loss of proteoglycan content primes articular cartilage for mechanically induced damage. Osteoarthr Cartil. 2018;26:S371. https://doi.org/10.1016/j.joca.2018.02.731.
27. Yao JQ, Seedhom BB. Mechanical conditioning of articular cartilage to prevalent stresses. Br J Rheumatol. 1993;32:956–65 http://www.ncbi.nlm.nih.gov/pubmed/8220934. .
28. Verteramo A, Seedhom BB. Effect of a single impact loading on the structure and mechanical properties of articular cartilage. J Biomech. 2007;40:3580–9. https://doi.org/10.1016/j.jbiomech.2007.06.002.
29. Barnes SC, Shepherd DET, Espino DM, Bryan RT. Frequency dependent viscoelastic properties of porcine bladder. J Mech Behav Biomed Mater. 2014;42C:168–76. https://doi.org/10.1016/j.jmbbm.2014.11.017.
30. Swann AC, Seedhom BB. Improved techniques for measuring the indentation and thickness of articular cartilage. Proc Inst Mech Eng Part H J Eng Med. 1989;203:143–50. https://doi.org/10.1243/PIME_PROC_1989_203_026_01.
31. Atkinson KE. An introduction to numerical analysis. https://www.wiley.com/en-us/An+Introduction+to+Numerical+Analysis%2C+2nd+Edition-p-9780471624899. .
32. Shepherd DE, Seedhom BB. Thickness of human articular cartilage in joints of the lower limb. Ann Rheum Dis. 1999;58:27–34 http://www.ncbi.nlm.nih.gov/pubmed/10343537. .
33. Espino DM, Shepherd DE, Hukins DW. Viscoelastic properties of bovine knee joint articular cartilage: dependency on thickness and loading frequency. BMC Musculoskelet Disord. 2014;15:205. https://doi.org/10.1186/1471-2474-15-205.
34. Ross SM. Peirce's criterion for the elimination of suspect experimental data. J Eng Technol. 2003.
35. Jeffrey JE, Aspden RM. The biophysical effects of a single impact load on human and bovine articular cartilage. Proc Inst Mech Eng Part H J Eng Med. 2006;220:677–86.
36. Radin EL, Yang KH, Riegger C, Kish VL, O'Connor JJ. Relationship between lower limb dynamics and knee joint pain. J Orthop Res. 1991;9:398–405. https://doi.org/10.1002/jor.1100090312.
37. Cooke ME, Lawless BM, Jones SW, Grover LM. Matrix degradation in osteoarthritis primes the superficial region of cartilage for mechanical damage. Acta Biomater. 2018.
38. Zhang L, Hu J, Athanasiou KA. The role of tissue engineering in articular cartilage repair and regeneration. Crit Rev Biomed Eng. 2009;37:1–57 http://www.ncbi.nlm.nih.gov/pubmed/20201770. .
39. Malekipour F, Whitton C, Oetomo D, Lee PVS. Shock absorbing ability of articular cartilage and subchondral bone under impact compression. J Mech Behav Biomed Mater. 2013;26:127–35. https://doi.org/10.1016/j.jmbbm.2013.05.005.
40. Li Z, Liu S-Y, Xu L, Xu S-Y, Ni G-X. Effects of treadmill running with different intensity on rat subchondral bone. Sci Rep. 2017;7:1977. https://doi.org/10.1038/s41598-017-02126-z.
41. Novitskaya E, Chen P-Y, Hamed E, Jun L, Lubarda V, Jasiuk I, et al. Recent advances on the measurement and calculation of the elastic moduli of cortical and trabecular bone: a review. Theor Appl Mech. 2011;38:209–97.
42. Wachter NJ, Augat P, Krischak GD, Sarkar MR, Mentzel M, Kinzl L, et al. Prediction of strength of cortical bone in vitro by microcomputed tomography. Clin Biomech. 2001;16:252–6.

43. Charlebois M, McKee MD, Buschmann MD. Nonlinear tensile properties of bovine articular cartilage and their variation with age and depth. J Biomech Eng. 2004;126:129–37. https://doi.org/10.1115/1.1688771.
44. Pearson B, Espino DM. Effect of hydration on the frequency-dependent viscoelastic properties of articular cartilage. Proc Inst Mech Eng Part H J Eng Med. 2013;227:1246–52.

## Publisher's Note

Springer Nature remains neutral with regard to jurisdictional claims in published maps and institutional affiliations.

**Ready to submit your research? Choose BMC and benefit from:**

- fast, convenient online submission
- thorough peer review by experienced researchers in your field
- rapid publication on acceptance
- support for research data, including large and complex data types
- gold Open Access which fosters wider collaboration and increased citations
- maximum visibility for your research: over 100M website views per year

**At BMC, research is always in progress.**

**Learn more** biomedcentral.com/submissions